THE EFFECTS OF HUMIDITY AND SOLUBLE WATER CONTENT ON THE LUBRICITY TESTING OF A N-HEXADECANE AND PALMITIC ACID TEST FLUID.

Jacobus Langenhoven

THE EFFECTS OF HUMIDITY AND SOLUBLE WATER CONTENT ON THE LUBRICITY TESTING OF A N-HEXADECANE AND PALMITIC ACID TEST FLUID.

By

Jacobus Langenhoven

A dissertation in partial fulfilment of the requirements for the degree

Master of Engineering (Chemical Engineering)

In the

Department of Chemical Engineering

University of Pretoria

Pretoria

30 November 2014

THE EFFECTS OF HUMIDITY AND SOLUBLE WATER CONTENT ON THE LUBRICITY TESTING OF A N-HEXADECANE AND PALMITIC ACID TEST FLUID.

Synopsis

Liquid fuel lubricity testing is known to be sensitive to the humidity of the surrounding atmosphere. The effect reported does however not seem to be universal for all diesel types according to available literature. This study was limited to the use of n-hexadecane as base fluid with addition of between 100 - 2000 ppm of palmitic acid (PA) as lubricity enhancer. The fuel spectrum was kept simple to allow a more fundamental approach by limiting the extent of possible chemical reactions. Both wear and seizure load testing were performed.

The effect of water on both tests was found to be:

- Wear and friction increased with higher soluble water content. Water therefore interferes with the action of the lubricating additive leading to decreased performance.
- It is known that hydroxyl groups, from dissociative chemisorption of water, act as active sites for adsorption. It is however postulated that the associative chemisorption and/or physisorption of water interferes by either reducing the active site availability or reducing activity to ligand exchange.
- No iron oxyhydroxides (FeOOH) were detected on the wear scars or tracks using Raman spectroscopy. The adsorbed water therefore likely only interact with the surface due to their low concentrations (10 ~ 50 ppm).

For wear testing the following additional observations were made:

- The electric contact resistance (ECR) took longer to increase at higher soluble water content, for all PA concentrations. The equilibrium values attained were also lower, when values were within the measurement range. This again highlights the reduced lubricity performance at higher soluble water content.
- Wear scar appearance and colour were uniquely affected at each concentration of PA
- Similar trends were observed at 60 °C and 80 °C. At the higher temperature:
    - Wear scar diameters increased.
    - Friction coefficients decreased and had less variance.
    - ECR values were similar, but took longer to increase to a steady value.

For seizure load testing the following additional observations were made:

- At higher water content, the oscillation-stroke on the test machine used tended to deviate more, before the actual seizure point was reached.
- The effects of soluble water were more noticeable at lower PA concentrations.

Keywords: seizure load, wear testing, adsorption

Acknowledgements

The author would like to thank the following people and organizations in particular:

- Professor Philip de Vaal for his guidance and support during this project.
- SASOL Limited for the support in making this project a possibility.
- Thank you also to the National Research Foundation for the funding provided.
- Professor Egmont Rohwer, Dr Stefan de Goede and Dr Linda Prinsloo for the guidance they provided.

Contents

Nomenclature

A	constant	-
A_t	true area of contact	m^2
a_1	constant	-
B	constant	-
b_1	constant	-
C	constant	-
Ca	concentration of species A	ppm
Ca_s	surface concentration of species A	ppm
Ca_0	initial concentration of species A	ppm
c_1	constant	-
c_2	constant	-
D	diffusion coefficient	cm^2/s
D_{AB}	diffusion coefficient	cm^2/s
E_a^{dess}	desorption energy	kJ/mol
E_a^{diss}	dissociation energy	kJ/mol
E^{ads}	adsorption energy	kJ/mol
F	frictional force	N
F_a	friction force due to adhesion	N
f_{ab}	micro-poughing / micro-cutting index	-
F_d	friction force due to deformation	N
ΔG_{ads}	free energy of adsorption	kJ/mol

ΔG_f^0	standard free Gibbs energy of formation	kJ/mol
ΔG_f^0 products	standard free Gibbs energy of formation products	kJ/mol
ΔG_f^0 reactants	standard free Gibbs energy of formation reactants	kJ/mol
ΔG_r^0	standard free Gibbs energy of reaction	kJ/mol
ΔG_r	Gibbs free energy of reaction	kJ/mol
H	Henry's law constant	atm
ΔH_f^0	enthalpy of formation	kJ/mol
$\Delta H_{reaction}^0$	enthalpy of reaction	kJ/mol
H_s	hardness of the softer surface	N/m^2
K	equilibrium constant	
K_A	constant	
K_{ads}	equilibrium constant (adsorption)	
K_b	Boltzman constant	J/K
L	diffusion length	cm
n	constant (fitting parameter)	-
p	constant	-
P_i	partial gas phase pressure	kPa
P_{tot}	total gas phase pressure	kPa
p_y	plastic flow stress	N/m^2
Q	reaction quotient	
R_{solute}	solute radius	m
R	universal gas constant	kJ/kmol.K
S	solubility limit	ppm
S_D	total sliding distance	m
ΔS_f^0	entropy of formation	kJ/kmol.K
T	temperature	K or °C
T_B	boiling temperature	K
t	time	s

V	wear volume	m^3
W	normal force	N
X_{aq}	adsorbate equilibrium concentration	
x_i	liquid phase mole fraction	-
Y	normalized change in concentration	-
y_i	gas mole fraction	-
Y0	initial normalized change in concentration	-
ƶ	position	cm

Greek:

α	angle of attack	
α_c	critical angle of attack	
ε_r	relative permittivity	-
η	solvent shear viscosity	kg/m.s
θ	change in concentration	ppm
λ	constant	
σ	resistance	Ω.cm
τ	shear stress	N/m^2
τ_t	temperature parameter	K/100
μ	friction coefficient	-
Γ_x	adsorbate/adsorbent mass ratio	-
Γ_{max}	maximum adsorbate/adsorbent mass ratio	-

Abbreviations:

APV	water vapour pressure	kPa
CN	carbon number	
DN	donor number	
HCF	humidity correction factor	µm/kPa
HFRR	high-frequency-reciprocating-rig	
LCC	load carrying capacity	
MWSD	measured wear scar diameter	µm
PA	palmitic acid	
RH	relative humidity	%
SRV	German acronym for reciprocating, friction and wear	
$WS_{1.4}$	wear scar adjusted for humidity	µm

1. Introduction

Background

The lubricity of liquid fuels gained prominence with the introduction of environmental regulations concerned with the reduction of sulphur content. Sulphur content is reduced by means of hydrotreating, which also removes many of the natural polar molecules responsible for good fuel lubricity behaviour. The reduced lubricity led to catastrophic failure of fuel distribution systems. Liquid fuel lubricity standards had to be introduced which led to widespread research regarding fuel additization to enhance fuel lubricity. Additionally, increasingly more severe operating conditions are introduced in modern fuel injection technology to reduce both incomplete combustion and particulate matter. These changes places additional strain on the lubricity performance of liquid fuel (Lacey, Gunsel, De La Cruz & Whalen, 2001).

The accepted bench test standards for lubricity testing of liquid diesel fuels include either the High Frequency Reciprocating Rig (HFRR) as per (ASTM D 6079 & ISO/CD 12156-1) or the Scuffing Load Ball On Cylinder Lubricity Evaluator (SLBOCLE) as per ASTM D6078. The HFRR is known as a wear test, it evaluates the amount of wear that occurs under a constant oscillating normal load. The SLBOCLE is a seizure load test, that tests the ability of the fuel to prevent adhesive seizure in a heavily loaded oscillating contact. Seizure load tests are done at various normal loads to determine at what load seizure occurs. The maximum load attained is indicative of the fuel lubricity behaviour.

During the initial round robin testing of the HFRR it was noted that humidity affected the repeatability of results (Davenport, *sa*). A few studies have since been published by various research groups with some contradicting conclusions on the effects of humidity on fuel lubricity performance. According to (Shaver, Giannini, Lacey & Erwin, 1998) there exists no general trend with increasing humidity, whilst according to (Lapuerta, Sánchez-Valdepeñas & Sukjit, 2014) there is an increase in wear with increasing humidity.

Problems and Objectives

In order to accurately evaluate fuel lubricity it is important to obtain repeatable results. This requires understanding the effects of humidity, to be able to put measures in place to minimize its' effects. The main objectives of this study were therefore to:

- Determine what parameters affect water transfer from moist air to the fuel, through the fuel and onto the tribo-contact.
- Understand how the presence of water alters both the chemical and physical nature of the wear surface.
- Determine if the water molecules present interact with other surface active species.
- Determine how wear and seizure load testing differ in their response to soluble moisture content in the test fuel.
- Determine how significant the effect of soluble water content is at different lubricity levels on the lubricity performance.

Method, Scope and Limitations

The solubility of moisture, transferred from the surrounding air, in n-hexadecane was investigated to assess what parameters could influence transfer before and during lubricity testing. This study was limited to soluble water content only. Measurements were done with a 787 Karl Fischer Titrino volumetric titrator supplied by Metrohm. The values were compared to calculations using diffusion models and solubility data available in literature.

The effect of the dissolved water on fuel lubricity testing was investigated. Wear testing was performed on a HFRR lubricity evaluator supplied by PCS Instruments. Seizure load testing was performed on a SRV®4 lubricity evaluator supplied by Optimol Instruments. Lubricity of fuels on this equipment will be determined in the boundary lubrication regime or mixed lubrication regime at best. Lubricity performance in the boundary lubrication regime is strongly affected by surface active species present (Stachowiak & Batchelor, 2003: 357). Lubricity additisation was limited to 100, 250 and 2000 ppm of PA for the wear testing and 100, 500 and 2000 ppm of PA for seizure load testing. Surface analysis of oxides was done using Raman spectroscopy and was limited to small user selected areas since a mapping functionality was not available.

2. Literature

2.1 Friction

Friction is the resistance to movement between two bodies that are in contact. The direction of frictional force is parallel to that of the tangential component of an applied force (Gohar & Rahnejat, 2012: 57).

Surface roughness greatly affects friction. Surfaces on a macroscopic level might appear smooth but on a microscopic level consists of numerous asperity peaks. An example of this can be seen in Figure 2.1. When surfaces slide over each other it is the interaction between asperity peaks that determine friction behaviour rather than the apparent area of contact.

The friction coefficient (μ) is the ratio of the frictional force (F) to that of the normal force (W) caused by the load as can be seen in Equation 2.1.1. A higher friction coefficient results from higher frictional force needed to overcome a larger resistance to movement (Stachowiak & Batchelor, 2003: 357).

$$\mu = \frac{F}{W} \tag{2.1.1}$$

2.1.1 Laws of friction

The following “laws” for dry friction were confirmed by Amontons (1699) and Coulomb in the 18th century: (Gohar & Rahnejat 2012: 57-59)

- The friction force is independent of the apparent area of contact.
- The friction force is directly proportional to the applied normal load.
- Friction force is independent of the sliding speed (This relationship holds nearly true for dry contacts at moderate sliding speeds).
- For sliding contacts the relative velocity vector and total friction vector are in the same direction.

2.1.2 Friction contribution terms

The two largest contributions to dry friction are adhesion and deformation as can be seen in Equation 2.1.2.

$$F = F_a + F_d \tag{2.1.2}$$

When a normal load is applied on two surfaces in contact, localized asperity contact occurs. At these contacts asperities can adhere to one another by a process of cold-welding. This can be seen in Figure 2.1. When one surface is then moved parallel to the other (sliding) the surface will experience a tangential force F_a due to adhesion. When considering Figure 2.1 (right hand side) it can be see that if the top surface is to slide horizontally deformation of the asperity tip will occur. This is the deformation component F_d. This component generally is a combination of asperity ploughing and deformation. Note that a component of F_a is also present at this contact due to contact adhesion of the point (Gohar & Rahnejat, 2012: 60-61).

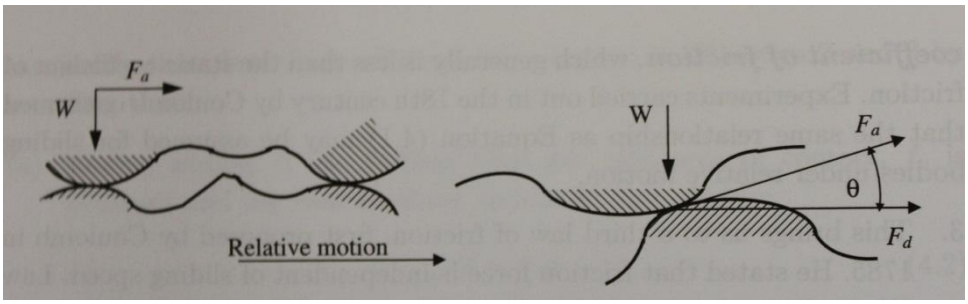

Figure 2.1: Adhesive (left) and deformation (right) components of friction.

(Gohar & Rahnejat, 2012: 60)

The adhesive component is generally much larger than the deformation components in contaminant free environments. However the role of deformation components becomes more important when contaminants are present due to reduced adhesion.

Adhesive component

When a load is applied contact is only made between the largest asperities. The harder material will plastically deform the softer material if the yield point of the softer

material is exceeded. Increasing loads will allow more asperities to make contact as well as increase the contact area of asperities that are plastically deformed. The true area of contact will increase until the pressure drops to the point of metal elasticity. Cold welding occurs between these plastically deformed asperities and is favoured in metals due to delocalized electrons from the metal. The adhesive component of friction is the force needed to shear welded junctions.

Recall Equation 2.1.1, the friction coefficient

$$\mu = \frac{F}{W} \tag{2.1.1}$$

Equation 2.1.3 and Equation 2.1.4 are expressions for the friction force and the normal load based on the true area of contact A_t. Note that τ is the effective shear stress of the material and p_y is the plastic flow stress of the material.

$$F = A_t\tau \tag{2.1.3}$$

$$W = A_t p_y \tag{2.1.4}$$

Substitution of Equations 2.1.3 and 2.1.4 into Equation 2.1.1 leads to Equation 2.1.5 (Stachowiak & Batchelor, 2003: 357).

$$\mu = \frac{\tau}{p_y} \tag{2.1.5}$$

This gives an estimation of the adhesive friction coefficient based on material properties. However experimental studies done in clean environments resulted in larger friction coefficients than predicted. This was attributed to a phenomenon known as junction growth. Junction growth is the increase in true area of contact due to the application of shear force, resulting in decreased normal pressure (Stachowiak & Batchelor, 2003: 539-540).

The effects of contaminants are generally to reduce asperity junction adhesion. A lower shear strength interface is introduced. This lowers the adhesive component of friction. These ‘contaminants’ can include metal oxide layers, debris, oils, lubricating additives or other formed layers (Gohar & Rahnejat, 2012: 61-66). Attention to this will be given in other sections of this study.

Deformation component

The relative hardness of the two surfaces in contact influences the type of deformation. The asperity of the harder material will plough through/penetrate that of a softer material rather than just deforming it, when one surface is slid against the other. This will create grooves in the softer material. In most contacts the deformation component is a combination of these two mechanisms. The presence of wear particles will greatly damage the softer surface (Gohar & Rahnejat, 2012: 66).

2.2. Wear

Wear is the loss of material in use and results in a decrease in material integrity. This has large monetary implications globally. Numerous types of wear occur between contacting bodies. There usually exists a dominating mechanism of wear. The most common mechanisms are listed in Table 2.2.1 Severe wear usually occurs in the absence of a lubricating film and mild wear in the presence of a lubricating film. Examples of some of the more common types of wear are shown in Figure 2.2.1

Table 2.2.1: Different types of wear (Stachowiak & Batchelor, 2003: 2-3,5).

Wear type	**Group**	**Cause**
<u>Severe</u>		
Adhesive	-	Adhesion between contacting surfaces.
Scuffing	-	Heavy loaded contacts.
<u>Mild</u>		
Abrasive	Particle-Solid	Particles or fluid flow.
Erosive	Particle-Solid	Impacting particles.
Corrosive	Chemical	Chemical attack.
Oxidative	Chemical	Oxygen acts as corroding agent.
Fatigue	-	Repetitive stresses on the surface.
<u>Minor</u>		
Fretting	-	Destructive trapped film material.
Impact	-	Surface impact.
Melting	-	Surfaces melt due to high speeds and loads.
Diffusive	-	High interface temperatures.

Optimizing against one type of wear can lead to vulnerability towards another type of wear. It is important to consider the application.

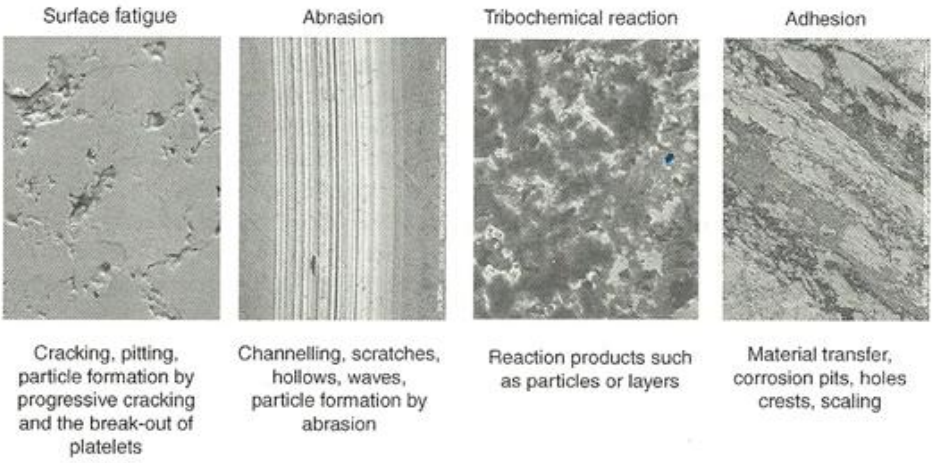

Figure 2.2.1: Some of the more common wear types. Adapted from (Mang, Bozin &Bartels, 2011: 39).

2.2.1. Adhesive wear

Adhesion of sliding metal contacts can result in excessive wear. Adhesive wear results in high wear rates and is characterized by unstable friction coefficients. Destruction of the surface can occur and in some cases cause total seizure. When adhesion is strong metal transfer of the weaker metal to the stronger metal is common. Metal surfaces that are not sufficiently lubricated are prone to this form of wear. Adhesion in metals is strong due to the easy transfer of free electrons between metals (Stachowiak & Batchelor, 2003: 533-536).

The formation of a transfer particle: After initial adhesion between two surfaces a shear band forms. Upon reaching a limit in size a crack will start to form and initiate the formation of a new shear band below the first. This process will continue and the crack will continue to grow until the particle can eventually detach. These particles are generally harder than the original surface due to work hardening and can result in ploughing of the surface. These particles can be removed from the adhesion surface forming a wear particle. Alternatively they can remain on the surface and are continuously flattened to form a transfer film. These films and transfer particles then carry most of the load and can lead to seizure.

Increases in surface roughness, hardness and surface energy reduce adhesive wear. Lower chemical reactivity and more densely packed crystal structures are known to experience less adhesion. Adhesion between two metals is hindered by the presence of contaminant layers. Metal surfaces rapidly form an oxide layer of approximately 5 nm when exposed to an oxidizing atmosphere. These films prevent adhesion. Upon removal, these oxide films are rapidly regrown but if removal rate exceeds growth rate adhesion will occur. The main purpose of lubricants is to prevent adhesive wear (Stachowiak & Batchelor, 2003: 542-550).

2.2.2 Scuffing wear

Scuffing is a severe and sudden form of wear that takes place in heavily loaded contacts. The contact would seem well lubricated but then have sudden film failure. It is suggested that scuffing is due to the large amount of frictional heat being released. This heat results in thermally induced film collapse and possible equipment seizure. The temperature at which this occurs is called the critical temperature. It has been suggested that this temperature is related to desorption temperatures but this has been found to be a crude estimation. Since various lubrication mechanisms can be at play, the exact mechanism of film failure can be complex. There is much uncertainty surrounding the failure mechanisms of scuffing (Stachowiak & Batchelor, 2003: 374-375);

The presence of nascent metal surfaces can further induce scuffing by acting as a catalytic decomposer. It can decompose the base fuel or lubrication additive to lower molecular mass species. These new species not only use lubricant species as reagents but also hinder movement of fresh species to the surface. This can be significant if enough nascent metal surface is exposed by wear. Measures to prevent scuffing include extreme pressure additives and conservative mechanical designs (Stachowiak & Batchelor, 2003: 378-379).

2.2.3. Abrasive wear (rapid, severe)

Abrasive wear occurs when tribo-elements have different hardness values. The harder materials penetrates the surface of the softer material resulting in furrows previously shown in Figure 2.2.1.

The mechanisms involved in abrasive wear are indicated in Figure 2.2.2 below. All these mechanisms can contribute simultaneously to abrasive wear on a body. The extent of each mechanism is determined by the hardness, geometries and contact angle of the particles. The characteristics of the surface also influences which mechanisms dominate. In Figure 2.2.3 the effect of the angle of attack on the dominating mechanism is shown. The mechanisms include:

- **Micro-ploughing:** Significant plastic deformation occurs. Abrasion is reduced by material build up as can be seen in Figure 2.2.2.
- **Micro-cutting:** Abrasive particles cut into the surface resulting in shaving debris. Can be caused by hard peaks from roughness
- **Micro-fatigue:** Repeated micro-ploughing can cause localized metal fatigue.
- **Micro-fracture:** When a brittle material is loaded above a critical load, cracks can form and grow. Cracks can result in the release of significant amounts of material (Mang, Bozin & Bartels, 2011: 41).

Also shown in Figure 2.2.2 is the f_{ab} value which indicates whether micro-ploughing or micro-cutting is the more dominating mechanism. This is done by comparing what fraction of the material removed from the furrow ended being separated from the surface. Ai denotes cross-sectional areas.

Two modes of abrasive wear are known:

- **Two-body abrasive wear**: Wear particles are held rigid and can only slide over the surface. Material is removed in a series of scratches.
- **Three-body abrasive wear**: Wear particles can both roll freely and slide over the surface. This mode is slower than two body adhesive wear due to other mechanisms affecting it. Material is removed in a gradual and random arrangement (Stachowiak & Batchelor, 2003: 486 - 487).

The moisture content of air is found to affect abrasive wear. The results however vary. The moisture content can either result in more cutting edges being produced from a slightly weakened grit or result in grit disintegration to nonabrasive particles. Two-body abrasive wear is found to increase with higher moisture content whereas three-body abrasive wear can increase or decrease (Stachowiak & Batchelor, 2003: 496, 507).

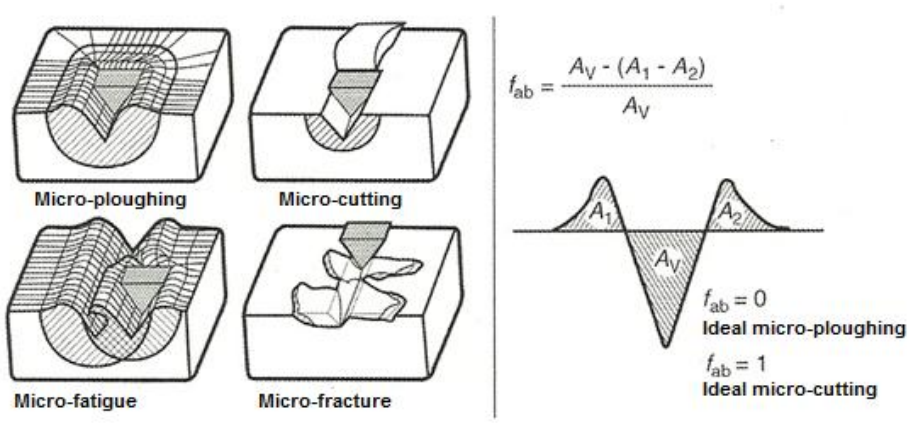

Figure 2.2.2: Mechanisms of abrasive wear. Adapted from (Mang, Bozin &Bartels, 2011: 41).

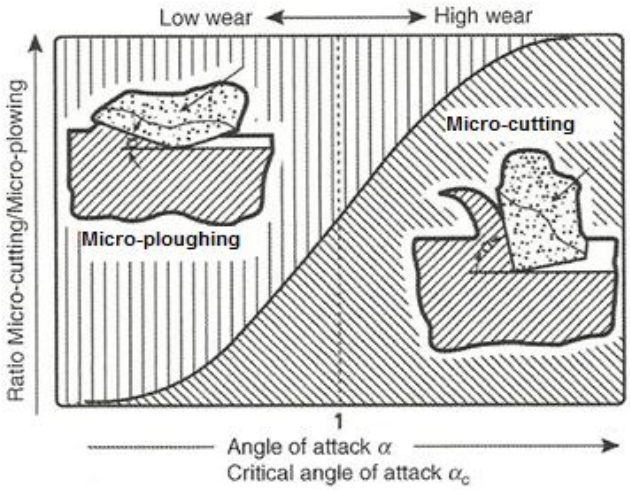

Figure 2.2.3: The influence of the angle of attack on the dominating abrasive mechanisms (Mang, Bozin & Bartels, 2011: 42).

2.2.4 Erosive wear (rapid, severe)

Erosive wear is the impact of liquid or solid particles against a surface. The mechanism of erosive wear is controlled by the particle size, particle material, impact velocity and impact angle. A low angle favours a process similar to abrasion whereas a high angle causes fatigue typical of erosion. If the speed of impact is low then only fatigue effects are possible but at higher velocity plastic deformation or brittle fracture is also possible depending on particle geometry. Blunt particles favour plastic deformation whereas sharp particles favour cutting and brittle fracture. At high speeds melting can occur. Damage to the crystal lattice is also possible. (Stachowiak & Batchelor, 2003: 515-521).

2.2.5 Corrosive wear

Corrosive wear is any wear that is due to chemical processes. The corrosive reagent is normally some species associated with the lubricant medium or surrounding atmosphere. When a film is produced from corroded metal and placed under a sliding contact one of the following processes is likely to occur:

- A thin durable film may be formed that continuously protects against both wear and corrosion.
- The film may be weak or brittle. It is continuously destroyed and regrown in a sacrificial manner. This will likely lead to high wear. This mechanism is very common.
- A galvanic coupling may form due to a damaged film resulting in rapid corrosion of the damaged area. This is more likely with strong corroding agents. A combination of independent wear and corrosive processes. This however is unlikely since heat and mechanical agitation from the wear process will promote corrosion (Stachowiak & Batchelor, 2003: 553).

Most corrosive films only grow to a certain thickness; therefore the continual removal of the film is what causes high wear rates. Corrosive and oxidative wear are distinguished from other types of wear in that a fast wear rate is associated with a low friction coefficient. This is due to the formation of a lower shear strength surface layer.

Water content is important for corrosive wear for to occur for a number of species. Both acids and alcohols are reported to cause increased wear at higher concentrations of water. Higher temperatures increase the extent of corrosive wear significantly (Stachowiak & Batchelor, 2003: 554-555).

As can be seen in Figure 2.2.4 there is an optimum lubricant activity for most lubricating species. If the activity is too high corrosive wear will be high. If the reactivity is too low the lubricating species will be ineffective in maintaining any protective film or layer. This will result in a sharp increase in wear due to adhesion.

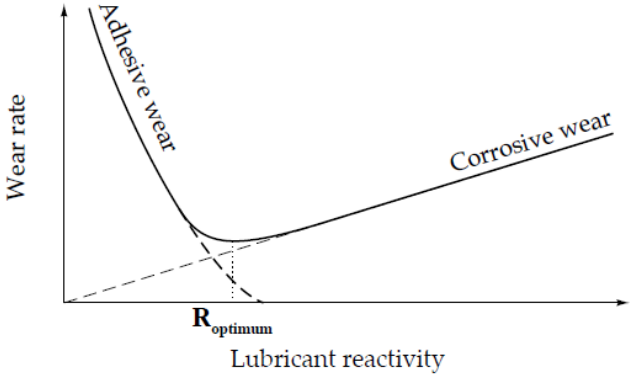

Figure 2.2.4: Balance between adhesive and corrosive wear (Stachowiak & Batchelor, 2003: 557).

The optimum lubricant reactivity shown in Figure 2.2.4 is dependent of the applied load and temperature. At higher loads a higher reactivity is required since more asperity contact will occur. Therefore optimum values are normally application specific and determined experimentally.

2.2.6 Oxidative wear

Oxidative wear is caused by atmospheric oxygen in mainly unlubricated contacts. Oxide films form on metal surfaces exposed to oxygen. These films grow up to a limited thickness which is thicker at higher temperatures. At temperatures above 500 ºC almost unlimited oxidation occurs for most metals which result in thick oxide layers (1-10 µm). This phenomenon can be seen in Figure 2.2.5.The large difference in thickness is due to the increased solid state diffusion of metal ions or oxygen across the film at elevated temperatures.

At lower temperatures a different wear mechanism takes place. Metal ions and oxygen atoms exchange places across the oxide film crystal lattice to enable oxide growth. This is why oxide thickness is limited to a few atomic layers at lower temperatures. Oxidative wear will persist even at very low temperatures (Stachowiak & Batchelor, 2003: 560- 562).

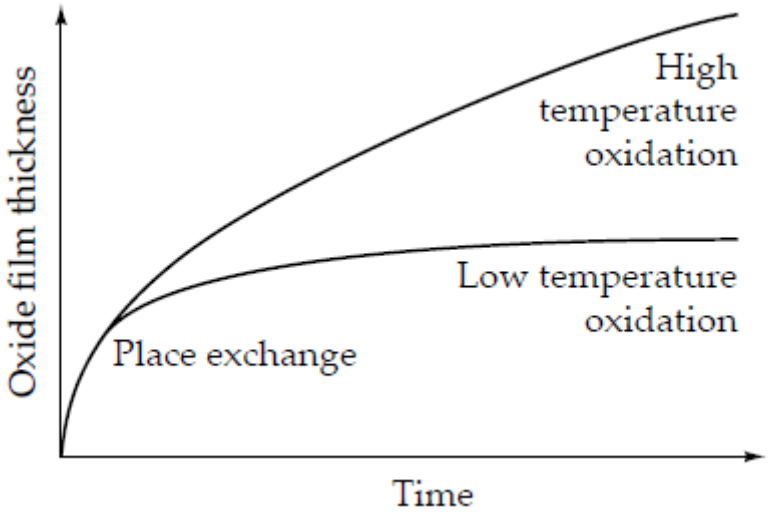

Figure 2.2.5: The effect of temperature on oxidation of metals (Stachowiak & Batchelor, 2003: 561).

Work done by (Möller, 2012) revealed that oxidation can be beneficial if it is not severe for a wet contact. Samples of n-hexadecane additized with 2000 ppm PA was used. Wear and seizure load testing were compared at different atmospheric oxygen concentrations. Samples were aerated before testing and the chamber was thereafter maintained at the same atmosphere that was used to aerate the sample. A SRV 4 was used to carry out both wear and seizure load testing. This machine has an oscillating point contact (Optimol Instruments, 2008):

- Wear testing: At high concentrations of atmospheric oxygen oxide layers grew faster. These layers became unstable above a critical thickness. Therefore if the growth rate is too fast excess unstable oxide is formed increasing wear. Abrasion was found to increase with increasing oxygen concentration whereas measured wear scar diameters were less affected. This is likely because of the more oxide debris that are harder than the metal surface.

- Seizure load testing: At high oxygen atmospheric concentration, oxidation was excessive and this prevented re-adhesion of surface cracks promoting wear particle formation. At very low oxygen concentration oxide growth was slower. Since the load is increased in constant intervals the contact is constantly driven to the adhesive wear regime. When oxygen concentrations were low, the oxide layer growth was too slow to cover the surface fast enough resulting in adhesion. Intermediate concentrations gave the highest seizure loads.

Whether or not an oxide film is coherent is dependent on the Pilling-Bedworth ratio. This is the ratio of the volume of oxide formed to the volume of metal corroded. The higher the ratio, the more stress is experienced on the oxide. Iron normally has a ratio of 2,1:1. Under stress growth might not be completely parabolic, but rather quasi linear or logarithmic. Cracks can form under this combination leading to sudden structural failure. Crevice attack occurs at geometrical discontinuities due to differences in reactant availability. A similar selective corrosion occurs at grain boundaries (Cornell & Schwertmann, 2007: 496).

(Lacey, Gunsel, De La Cruz, & Whalen, 2001) found that wear rate is strongly influenced by both temperature and pressure for fuels that have poor lubricity. They constructed a High-Pressure-High-Frequency-Reciprocating-Rig (HPHFRR). This unit could do tests at higher temperatures and pressures more realistic of fuel injection systems. Higher pressure also allowed them to test more volatile fuels.

It was found that the effects of pressure only became significant if the atmosphere contains oxygen. At higher oxygen partial pressure, more oxygen is dissolved into solution resulting in increased oxidative wear. This effect becomes less significant as fuel lubricity is increased. (Lacey, *et al*, 2001). Work done by (Möller, 2012) would suggest that this is due to the competing nature of chemical species for reaction/interaction with the surface of the metal. A higher concentration of lubricating molecules would interfere with surface oxidation.

Lubricated contacts experience wear depending on the lubrication regime (see Section 2.3). In the hydrodynamic and elastohydrodynamic regime very limited surface oxidation occurs. However in the boundary lubrication regime, asperity contact does often occur resulting in higher temperatures. It has been shown that oxide layers are necessary for lubricant films to operate effectively. Increased wear has been shown to occur at reduced oxygen concentration (Stachowiak & Batchelor, 2003: 567)

The oxide surface, which acts as an adsorbent in the adsorption process, will be covered more extensively in Section 2.5 concerned with adsorption.

2.2.7 Fatigue wear

Only sliding contacts will be considered due to the nature of the tribological experimental techniques performed. When a crack forms in a surface it can spread progressively due to periodic osscilation of the applied load. This can lead to the release of a wear particle. Surface fatigue was previously shown in Figure 2.2.1.

The original grain structure of most metals can be broken down into dislocation cells due to repeated induced strain. Surface defects act as stress concentrators. When a crack forms at a defect point on or near the surface it can propagate along the cell boundary or a slip plane resulting in a wear particle being released. These wear particles can be laminar due to orientation effects from plastic deformation. Another indication of fatigue on a surface is the formation of bands of deformed material on the surface (Stachowiak & Batchelor, 2003: 571- 577,589).

Higher oxygen concentrations have been shown to increase the rate of fatigue wear. It has been suggested that this is due to crack surface oxidation that prevents re-adhesion of crack surfaces. This phenomenon only occurs for surfaces that form oxide layers substantiating the theory. Crack initiation is very dependent on the material itself. Any inclusion or impurity can act as a point of crack initiation. Lubrication lowers the coefficient of friction resulting in lower propagation of cracks (Stachowiak & Batchelor, 2003: 577- 578).

2.2.8 Diffusive wear

This type of wear occurs at very high interface temperatures and when there is true contact between atoms. Chemical elements can then diffuse from one body to the other. This can lead to a loss in structural integrity in alloys as one species is selectively soluble in another body. This type of wear is only important when the bodies are of different composition (Stachowiak & Batchelor, 2003: 612-613).

2.3. Lubrication

The motion of one surface against another can be made easier by means of a low shear layer between moving surfaces. This layer can be a solid, liquid or a gas depending on the application. These layers reduce wear by separating the surfaces, this is known as lubrication (Stachowiak & Batchelor, 2003: 2-3).

In Figure 2.3.1 it can be seen that as the Stribeck number is reduced (moving from right to left) the hydrodynamic film thickness decreases (blocks at the top of the figure) until the asperities of the surfaces come into contact. This leads to an increase in the friction coefficient which can have numerous values depending on the film. U is the sliding speed and η is the viscosity. W is the normal load and μ is the friction coefficient.

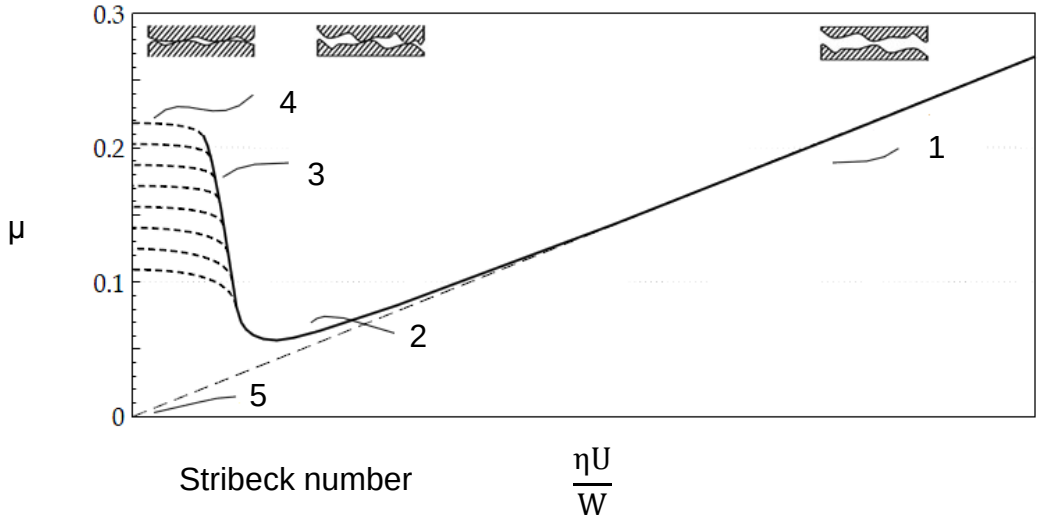

Figure 2.3.1: Changes in friction coefficient with decreasing Stribeck number. Adapted from (Stachowiak & Batchelor, 2003: 183) and (PCS Instruments)

Different lubrication regimes are indicated on Figure 2.3.1 and annotated below:

1: Hydrodynamic lubrication regime.
2: Elastohydrodynamic lubrication.
3: Mixed lubrication. The Increasing coefficient of friction is caused by partial contact.
4: Boundary or extreme pressure lubrication. Friction coefficient depends on non-hydrodynamic characteristics.
5: Zero friction coefficient at zero sliding speed.

2.3.1 Hydrodynamic lubrication

In this regime, surfaces are separated by a generated pressure that can support a certain load. Theoretically no wear will occur if surfaces are completely separated and operation can continue indefinitely. The following requirements need to be satisfied for hydrodynamic lubrication to occur:

- Sufficient velocity is needed to sustain a load carrying lubricating film.
- A pressure field needs to be formed by some mechanism. This is usually done by having the surfaces inclined towards each other or stepped if parallel. This ensures entry and exit of the lubricating medium.

Damage to equipment during starting and stopping occurs due to the non-zero sliding speed of the first requirement (Stachowiak & Batchelor, 2003: 102,197).

2.3.2 Elastohydrodynamic lubrication

This regime is similar to the hydrodynamic lubrication regime in that a hydrodynamic film needs to be generated that separates the surfaces. The difference is that elastic deformation of contacting bodies also occurs due to the different geometry resulting in a higher contact pressure.

The generation of an elastohydrodynamic film is caused by the following effects acting simultaneously:

- Hydrodynamic film formation as discussed in Section 2.3.1.
- Modification of the film geometry via the elastic deformation of the surface.
- Changes of rheology and viscosity under extreme pressure. These extreme pressures are caused by load concentration due to non-conformal geometry of the contacting surface.

An increase in viscosity due to extreme pressure is required for effective operation. This means that the film material is mostly limited to oils that are piezo-viscous.

These oils are in an approximately ideal liquid state outside the contact allowing them to enter the contact by viscous drag. When the oil is between the contacting surfaces they show remarkable viscosity increases being able to sustain a contact stress within the contact (Stachowiak & Batchelor, 2003: 282,306-307,352).

2.3.3. Mixed lubrication

If direct contact occurs between some of the deformed asperities it is termed mixed lubrication. It is also called partial lubrication since the load is shared between both the film and the contacting asperities. The contact geometry of this regime changes during operation due to the occurrence of wear. This regime has some combination of hydrodynamic, elastohydrodynamic and boundary lubrication. There is a possibility of scuffing in this regime (Stachowiak & Batchelor, 2003: 323-324).

2.3.4 Boundary and extreme pressure lubrication

Most of the lubricating mechanisms in this regime operate by forming some low friction, protective layer on the wear surface since asperity contact is increased from mixed lubrication.

Recalling Equation 2.1.5 it can be seen that a low friction coefficient is obtained by having a low shear interface, but hard material. Since this combination of material properties is not likely the advantages of utilizing a low shear layer between surfaces can be seen.

$$\mu = \frac{\tau}{p_y} \tag{2.1.5}$$

This lubrication regime is complex and can best be explained if subdivided. The subdivision is based on the relative load capacity and limiting frictional temperature as shown in Table 2.3.1. This regime can include any of the lubricating mechanisms indicated in Table 2.3.1(Stachowiak & Batchelor, 2003: 357).

Table 2.3.1: Boundary and extreme pressure sub-regimes

(Stachowiak & Batchelor, 2003: 358)

Prevalent lubrication mechanism	**Temperature**	**Load**
Localized viscosity enhancement	Low	Low
Adsorption	Low100 – 150 °C	High(Up to 1GPa)
Amorphous layers and/or chain matching	High	Medium
Sacrificial films	High	High

2.3.4.1 Low temperature – Low load

At low temperature, low load and low speed, surface localized viscosity enhancement can occur. The polar ends of linear hydrocarbons are attracted to the metallic substrate. They then attach normally onto the metallic contact surface. The localized viscosity enhancement results in reduced occurrence of severe wear since these areas act as points of near hydrodynamic behaviour (Stachowiak & Batchelor, 2003: 359-360).

2.3.4.2 Low temperature – High load (adsorption regime)

At these conditions a mono-molecular layer is adsorbed on to worn surfaces. This layer is all separates the surfaces. These layers have a low shear strength at the layer-layer interface of two contacting surfaces, due to weak interaction between non-polar groups. These groups therefore act to reduce the friction coefficient. The layer-substrate and substrate-substrate bonding on each surface is significantly stronger than the layer-layer interface (Stachowiak & Batchelor, 2003: 360-361). Adsorption onto relevant tribological surfaces will be further discussed in Section 2.5.

2.3.4.3 High temperature – Medium load

At these conditions two mechanisms of lubrication have been found to be favourable.

- Chain matching – Better lubricating properties are obtained if the lubricant additive chain length and the base fuel chain length match. The formed layer is similar to the viscosity enhancement effect but operates at higher contact stresses (> 1 GPa) and higher temperatures (> 100 °C).
- The additive in the base fuel can react with the nascent metal surface to produce films of soapy or amorphous material. These films are in addition to adsorbed films and viscous surface layers. They are typically 100 -1000 nm thick and very viscous. They have an advantage over adsorption lubrication in that they avoid the limitations imposed by desorption (Stachowiak & Batchelor, 2003: 381).

2.3.4.4 High temperature – High load

If loads and speeds are high enough, then a transient friction temperature occurs that is able to cause desorption of lubricating species. An additional lubricating mechanism is then required to prevent seizure or scuffing at these conditions. This is done by the formation of a short lived sacrificial film more aptly called extreme pressure lubrication. A sacrificial film is one that is constantly being destroyed and reformed during the wear process.

During severely loaded contacts oxide films are partially removed. This exposes extremely reactive nascent metal surface. The presence of phosphorus, sulphur or chlorine (from additives) will lead to the formation of films containing these compounds. These films hinder nascent metal contact reducing possible adhesion. Higher sliding speeds hinder sacrificial film formation. Additives used for this application are termed extreme pressure additives. A high temperature is crucial to ensure rapid film regrowth and is why this mechanism is limited to these conditions. (Stachowiak & Batchelor, 2003: 388-390)

In Figure 2.3.2 the friction coefficient of a white oil with an extreme pressure and adsorption additive is shown over a range of temperatures. The rise in friction coefficient over the narrow range of temperatures is termed temperature distress.

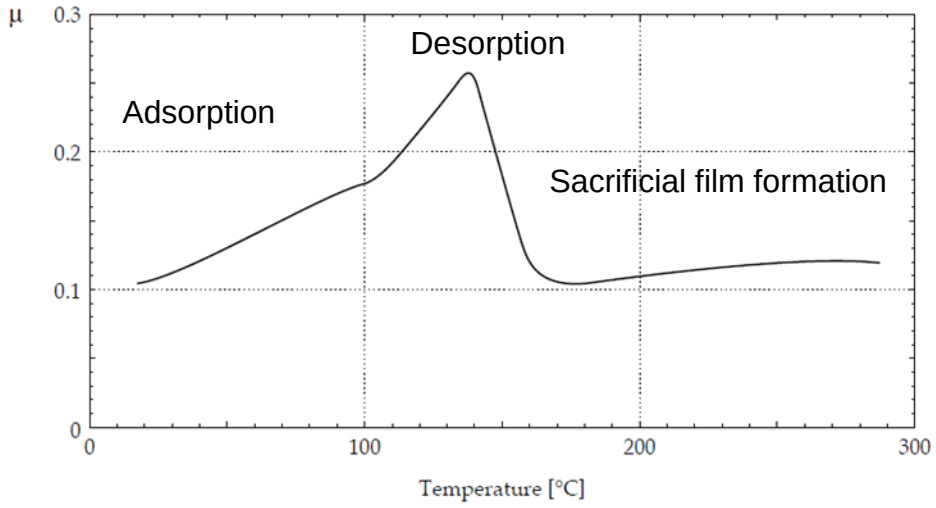

Figure 2.3.2: Temperature distress (Stachowiak & Batchelor, 2003: 402).

At low temperatures adsorption lubrication occurs. As the temperature increases the temperature for desorption is reached resulting in the increased friction coefficient. The subsequent drop in friction coefficient occurs as the minimum temperature for the occurrence of sacrificial films is reached. This clearly illustrates the transition between the two regimes. Practical formulations ensure that the temperature for desorption is higher than the minimum temperature for sacrificial films. Note that the sacrificial film can affect the heat of adsorption (Stachowiak & Batchelor, 2003: 401).

2.4 Water and Air: solubility and diffusion in liquid fuels

2.4.1. Transfer of water and air into a liquid fuel sample.

This section is limited to transfer via diffusion between a gas phase and a liquid (fuel) phase. Special attention is given to water and oxygen due to its known interactions with tribological surfaces. Where data is available on N_2 it will be presented.

Water

Due to the low solubility of water (a polar molecule) in alkane type fuels (non-polar), Henry's law is typically used to represent the equilibrium concentration of fuel in contact with moist air. Equation 2.4.1.a represents this equilibrium relation where y_i is the mole fraction of water in the gas phase and P_{tot} is the total gas phase pressure. H is the Henry's law constant and x_i is the liquid phase mole fraction (Yaws & Rahate 2009). Equation 2.4.1.a is rewritten into Equation 2.4.1.b to allow the calculation of mole fraction. P_i is the gas partial pressure.

$$y_i P_{tot} = H * x_i \quad (2.4.1.a)$$

$$x_i = \frac{Pi}{H} \quad (2.4.1.b)$$

It is noteworthy to mention at this stage that it could be confusing to compare mole fractions of water solubility in different alkanes which have different chain lengths. For example whilst mole fraction will be shown to decrease with increasing chain length the opposite trend will be true for mass fraction. The reason for this is that a increase in mole fraction is due to the fact that more atoms are incorporated into a larger molecule compared to a shorter n-alkane of the same mass. It therefore is prudent to note that solubility will throughout the whole of Section 2.4 be discussed using a mass basis even though some figures, like those for Henry's constant, refer to a mole basis.

When comparing the same alkane solvent under different temperatures the trends for mole- and mass based are the same, but the same format as mentioned in the previous paragraph will be used for uniformity.

The Henry's law constant, at 25 °C, is plotted for a number of straight chain alkanes and some cycloalkanes in Figure 2.4.1. Figure 2.4.1 was constructed using data from (Yaws & Rahate 2009) and (Yaws 2010) for air-alkane equilibrium systems. The Henry's law constant (on a mole basis) clearly decreases with increasing chain length. The same is true for the introduction of side branches. Cycloalkanes have lower values than their straight chain counterparts. **Therefore a higher water solubility (mass-based) could be expected for shorter chain length organic molecules with a linear shape rather than a bulky shape.**

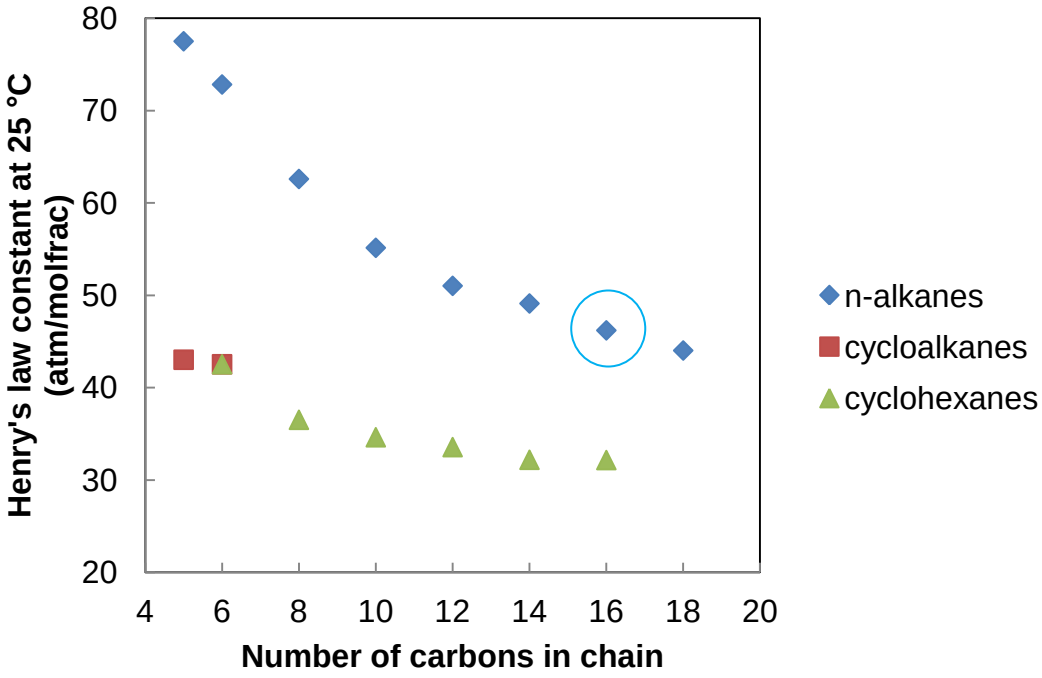

Figure 2.4.1: The Henry's law constant for alkanes at 25 °C. Note that the increase in the carbon number of cyclohexane is on a single straight branch. Other organic species are available in the source data. n-Hexadecane is indicated in the light blue circle due to its relevance to this study.

Oxygen

In Figure 2.4.2 The Henry's law constants for oxygen in various alkanes are presented at different temperatures. This data was taken from experimental work in a Masters thesis by (Manku, 1994).

Firstly it is noteworthy that these Henry's constant values are much higher than that of water in similar solvents and at similar temperatures. The Henry's constant of

oxygen should however not be directly compared to the Henry's constants of water when considering ambient systems since:

- The partial pressure of oxygen in air is significantly higher than that of water. Which affects the mole fraction (See Equation 2.4.1.b).
- Water and oxygen have different molecular weights affecting the mass fraction calculation.

Therefore the solubility limits at ambient conditions and the Henry's constant should not be used interchangeably without care.

Although the data in Figure 2.4.2 do not show a completely consistent trend, it would seem to be safe to remark that the Henry's constant decreases with increasing carbon chain length. Therefore it would seem from this data source that oxygen shows the same increased solubility in alkanes with smaller molecules as water did. This could still make sense even though oxygen is not polar like water, since oxygen is still a smaller molecule than most of these alkanes and would be more soluble in similar sized molecules.

It would again be incorrect to say that mass solubility decreases (increased Henry's constant) with increasing temperature. The reason being that the total pressure of the system also increases with temperature. Therefore the actual solubility response of a system to temperature depends on whether the pressure or the Henry's constant increases more. This is based on the assumption that the Henry's constant increases with increasing temperature.

Henry's constant is known to generally increases with increasing temperature for most systems. This continues to a maximum value whereupon it starts to decrease as the temperature increases further. The temperature at which the maximum value occurs is dependent on the solute-solvent combination (Smith & Harvey, 2007).

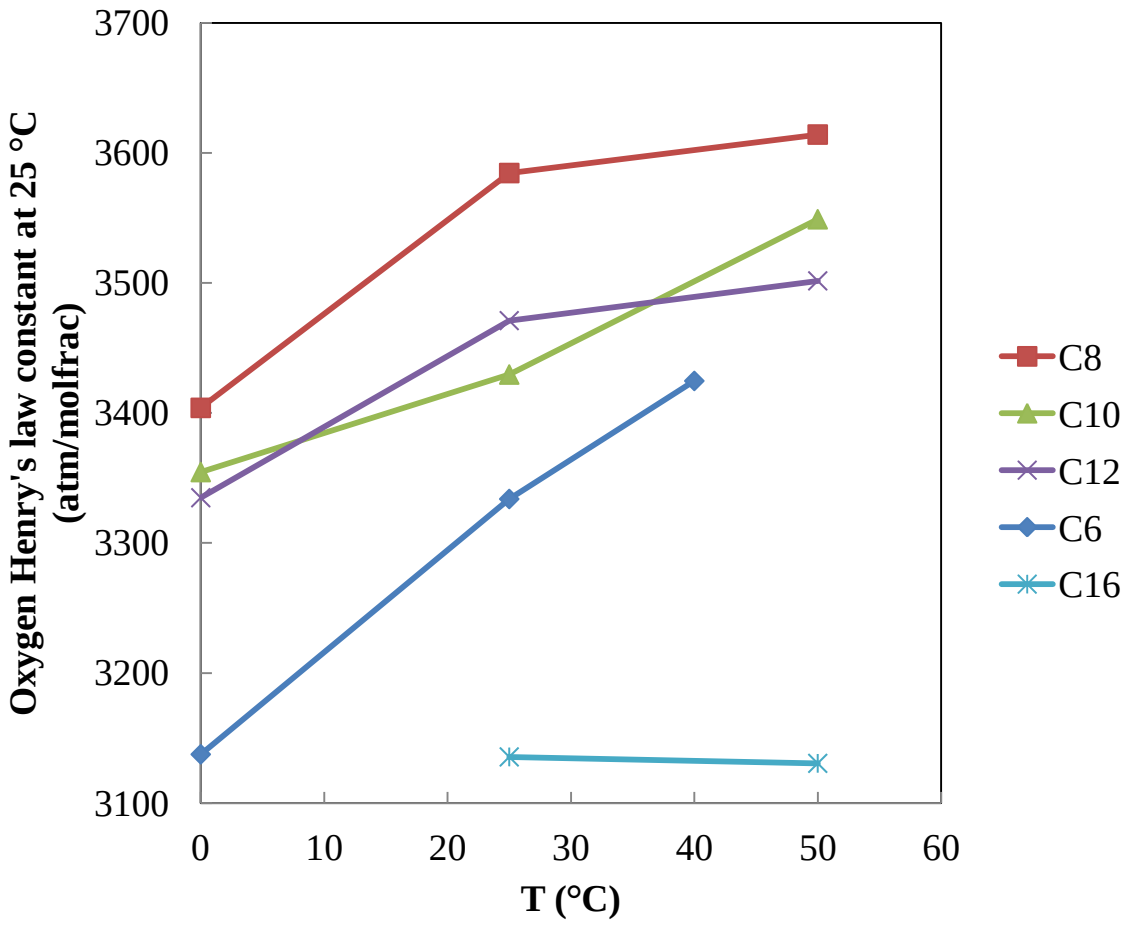

Figure 2.4.2: Experimental Henry's law constants for oxygen in n-alkanes. Data points obtained from (Manku, 1994). Note n-hexadecane is indicated in light blue.

2.4.2. Solubility limits of water and air in liquid fuels and the effect of temperature.

Water

In Figure 2.4.3 below the solubility limit of water in various n-alkane solvents is illustrated. There is a clear decrease in water mass content with increasing chain length (Schatzberg, 1963). Light blue lines indicate values for n-hexadecane.

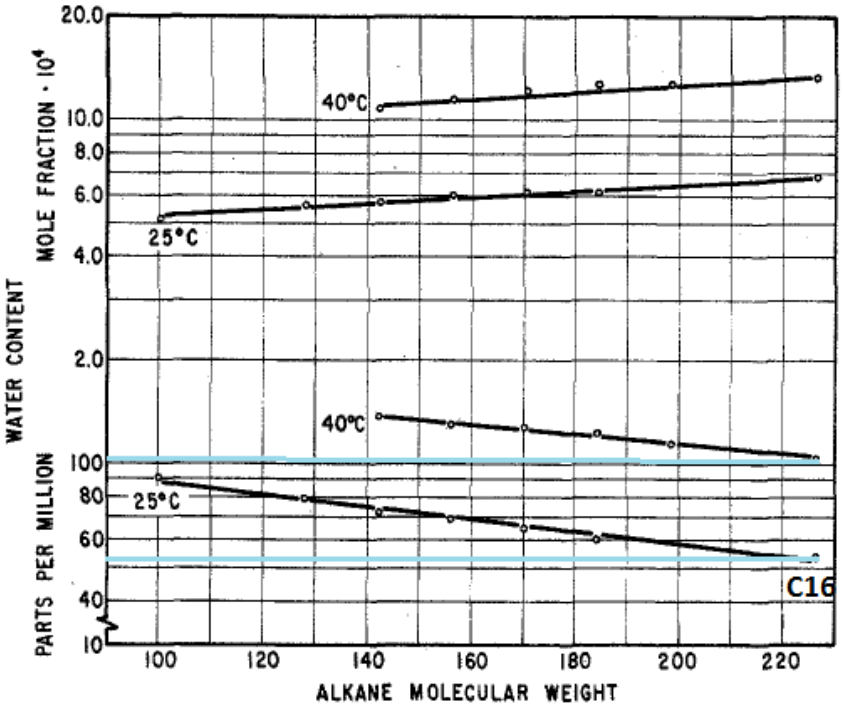

Figure 2.4.3: The effect of chain length of n-alkanes on its water solubility. Adapted from (Schatzberg, 1963).

In Equation 2.4.2 (Yaws & Rahate, 2009) fitted the solubility limit, S in units of ppm at 25 °C, of various alkanes to the boiling temperature, T_B in Kelvin, of the alkane. The boiling point is an indication of the alkane size and shape. The equation is limited to boiling temperatures between 280 – 590 K. A and B are constants listed in Table 2.4.1. The value obtained for n-hexadecane is 53.97 ppm which compares well with the value obtained in Figure 2.4.1.

$$\log_{10}(S)=A + B*T_B \qquad (2.4.2)$$

Table 2.4.1: Constants for alkane solubility Equation 2.4.2.

	A	B	Reference
n-alkanes	2.2740	$-9.7*10^{-4}$	(Yaws & Rahate, 2009)
cycloalkanes	2.7470	$-1.5*10^{-3}$	(Yaws, 2010)

In Figure 2.4.4 a monogram of water in various organic solvents is presented. Only n-hexadecane will be considered due to its use in this study but others can easily be found in the reference. Solubility limit values of interest are indicated. The solubility limit of water in n-hexadecane clearly increases with temperature.

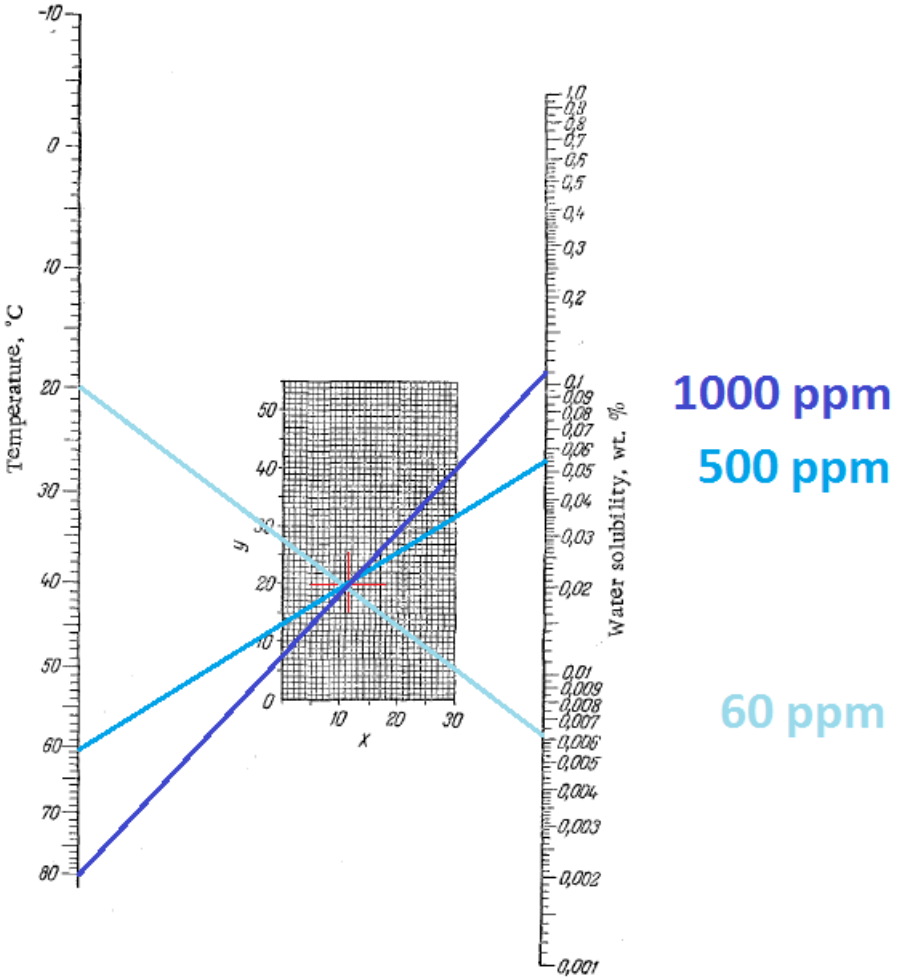

Figure 2.4.4: Solubility of water in various organic solvents. Adapted from (Chernyshev, 1970).

Equation 2.4.3 was developed by (Yaws & Rane, 2010) via regression of various sources of experimental data. The solubility limit, in ppm, of various alkanes can be determined as a function of the temperature, T (298 - 475K). The constants A,B & C are unique to each alkane and can be found in the referenced material. This relation is presented in Figure 2.4.5 for some n-alkanes. Water solubility increases to a larger extent for short chain alkanes than for long chain alkanes. Some constants are presented in Table 2.4.2.

$$\log_{10}(S)=A+\frac{B}{T}+C*\log_{10}(T) \qquad (2.4.3$$

Table 2.4.2: Constants for use with Equation 2.4.3 (Yaws & Rane, 2010).

Alkane		**A**	**B**	**C**
n-hexane	n-C_6H_{14}	-20,3272	-423,8698	9,5791
n-octane	n-C_8H_{18}	-5,3659	-1199,9296	4,5618
n-hexadecane	n-$C_{16}H_{34}$	-32,9113	260,0994	13,6480
n-octadecane	n-$C_{18}H_{38}$	-32,7754	250,2903	13,5941

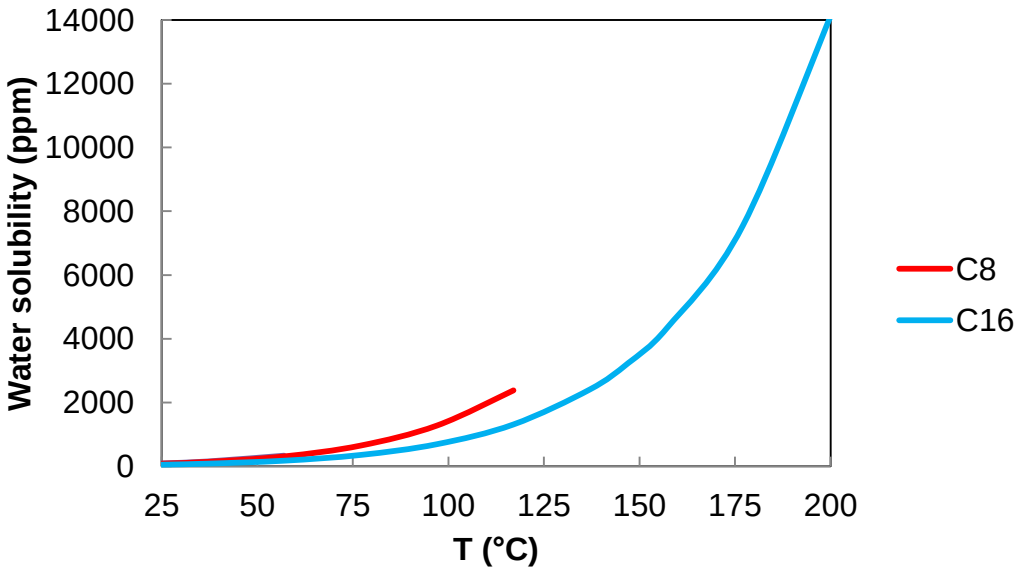

Figure 2.4.5: The effect of temperature on water solubility of some n-alkanes.

All of these sources show similar trends, but not the exact same values. The important observations to make here are that the water mass based solubility limit is higher for shorter chain alkanes. Furthermore water solubility increases with temperature.

Oxygen

In Figure 2.4.6 the mole fraction solubility limits of oxygen in n-alkanes are presented from a number of sources. Oxygen has a higher solubility in alkanes than water. There is disagreement between the two of the most comprehensive sources, 1 and 2 on the effect of chain length. Although values are order-wise similar, the trends are opposite. This disagreement was noted by (Manku, 1994) and also consequently investigated. The results of (Manku, 1994) is in agreement with source 2 and indicated in Figure 2.4.6 by the solid markers with error bars.

From Figure 2.4.6 it could be dangerous to say that oxygen solubility limit increases with temperature since the temperatures indicated are close to each other and also from three different studies. It was however noted by (Battino, Rettich & Tominaga, 1984b: 170) that soluble oxygen content was a very weak function of temperature.

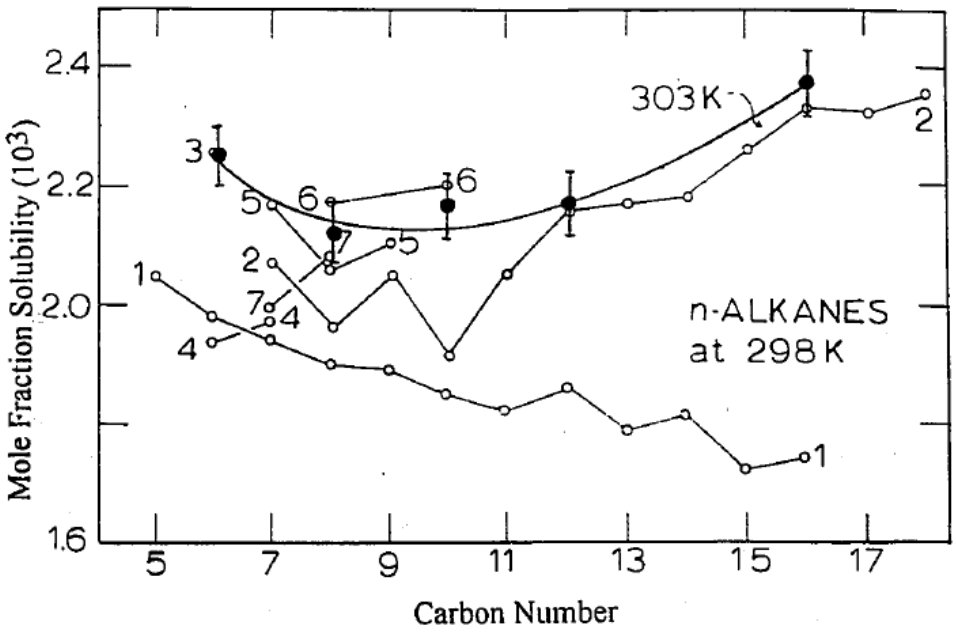

Figure 2.4.6: Oxygen mole fraction solubility in n-alkanes. This data is taken from (Manku, 1994) which plotted this data from 7 literature sources. There seems to be disagreement between study 1 and 2. The data generated by (Manku, 1994) is shown as the solid round markers.

Nitrogen

In Figure 2.4.7 the solubility of N_2, in various n-alkanes, is presented on a mole basis. There is therefore an increase of mass solubility with chain length opposite to the behaviour of water and oxygen. This is unexpected since one would expect oxygen and nitrogen to behave similar due to their similar size, shape and lack of polarity. It must therefore be noted again that sources on oxygen solubility differed in Figure 2.4.6.

There is a general increasing mass solubility with increasing temperature similar to water.

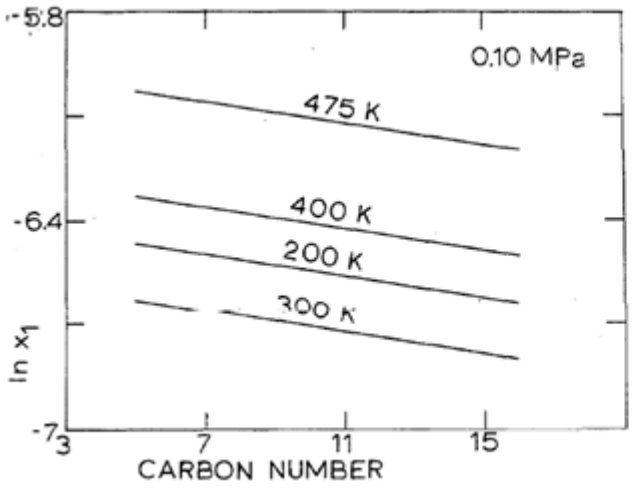

$$\ln x_1 = -15.393 + 11.827/\tau_t + 4.4606 \ln \tau_t - 0.015\,587\,CN$$

τ_t= T/100 (with T in K)

CN is the number of carbon atoms

The temperature range

C_{16} 298–475 K

Figure 2.4.7: The solubility of N_2 in n-alkanes at 101.325 kPa expressed as mole fraction (Battino, Rettich & Tominaga, 1984a). An equation is also fitted for N_2 mole fraction in n-hexadecane. The figure contains smoothed data.

2.4.3. Diffusivity of water and air in liquid fuels.

When a system contains more than one type of molecule, a natural tendency exists for mass transfer from regions of high concentration to regions of low concentration known as diffusion. Two modes of mass transfer exist: molecular mass transfer and convective mass transfer. These two modes often occur simultaneously depending on the system (Welty, Wicks, Wilson & Rorer, 2001: 421).

Liquid diffusion coefficients tend to be orders of magnitudes smaller than that of gases (Welty, Wicks, Wilson & Rorer, 2001: 438).

Equation 2.4.4 represents the Stokes-Einstein equation which is used to estimate the diffusion coefficient of a solute molecule in a solution.

- With K_b = Boltzman constant, T = temperature, μ = friction coefficient.
- Also C = 4 (slip) or C = 6 (stick) is a constant, η = solvent shear viscosity and R_{solute} = solute radius.

$$D = \frac{K_b T}{\mu} = \frac{K_b T}{C\pi\eta R_{solute}} \quad (2.4.4)$$

From this relation it can be seen that diffusion is inversely proportional to the solvent's shear viscosity (Cussler, 1997). Longer molecules of the same homologous series have higher viscosities and therefore lower diffusion coefficients as will be shown in Figure 2.4.8 and 2.4.9 (Su, Duncan, Momaya, Jutila, Needham, 2010).

2.4.3.1 Deviations from the Stokes-Einstein Equation – Solute size

Solute diffusivities tend to be larger than predicted by Stokes-Einstein equation for solute molecules that are smaller than the solvent molecules. This is likely because the continuum assumption for the Stokes drag equation no longer holds. Experimental observations have shown that in these cases the diffusivity is now inversely proportional to a fractional power of viscosity as can be seen in Equation 2.4.5. Both A and p are constants. Values for p normally range between 0.67 to 1 (Su, Duncan, Momaya, Jutila, Needham, 2010).

$$D = \frac{AT}{\eta^p} \quad (2.4.5)$$

In Table 2.4.3 molecules from the surrounding atmosphere are listed along with their predicted bond lengths. The reported lengths are in the longest dimension of the molecule. From this size estimation it can be predicted that diffusivity will deviate from the Stokes-Einstein behaviour in order of $N_2 > O_2 > H_2O$. Therefore these molecules will have larger diffusivities than predicted.

Table 2.4.3. Longest effective bond length of relevant solute species.

(Kotz & Treichel, 2003)

Molecule	Longest effective bond length (pm)	Reference Page
H_2O	172	94
O_2	121	403
N_2	110	403

2.4.3.2 Deviations from the Stokes-Einstein Equation – Solute solvent interaction.

The Stokes-Einstein equation furthermore does not account for possible attractions between solute and solvent. These attractions are known to decrease the diffusivity through a sample. This is illustrated in Figure 2.4.8 when comparing the diffusion coefficients of water in n-alkanes and n-alcohols of the same chain length. Although these solvent molecules are similar in size and shape, they give very different diffusion coefficients. This is due to the hydrogen bonding occurring between water and the alcohol functional group which is not present for the alkanes.

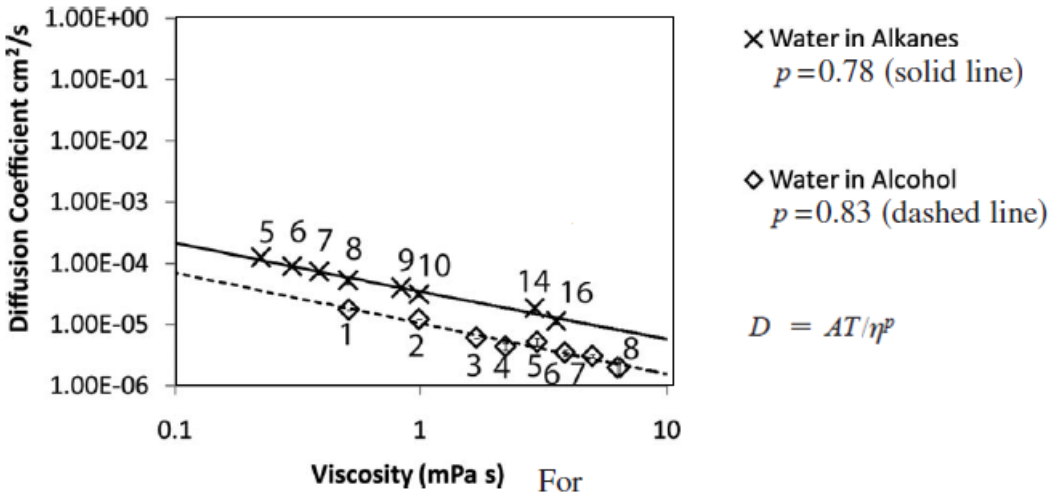

Figure 2.4.8: Diffusion of water in n-alkanes and n-alcohols. The numbers indicate the carbon chain length. T = 22 °C.

(Su, Duncan, Momaya, Jutila, Needham, 2010)

It was suspected that the possible formation of a solute-solvent complex could lead to an increased hydrodynamic solute radius. This would then be responsible for the decreased diffusivity. This however is not the case since the measured hydrodynamic radius did not increase for longer chained alcohol species in work done by (Su, Duncan, Momaya, Jutila, Needham, 2010). It is rather suggested that the hydrogen bonding leads to increased residence time for a solute. Changing conditions from slip (C = 6 for alkanes) to stick (C = 4 for interaction) tend to overestimate the effect of polarity on diffusivity for certain combinations of interacting solute and solvents (Wakai & Nakahara, 1997).

2.4.3.3 Comparing diffusivities of solutes

The diffusivities of O_2 through a number of n-alkanes are fitted to Equation 2.4.5 and presented in Figure 2.4.9.

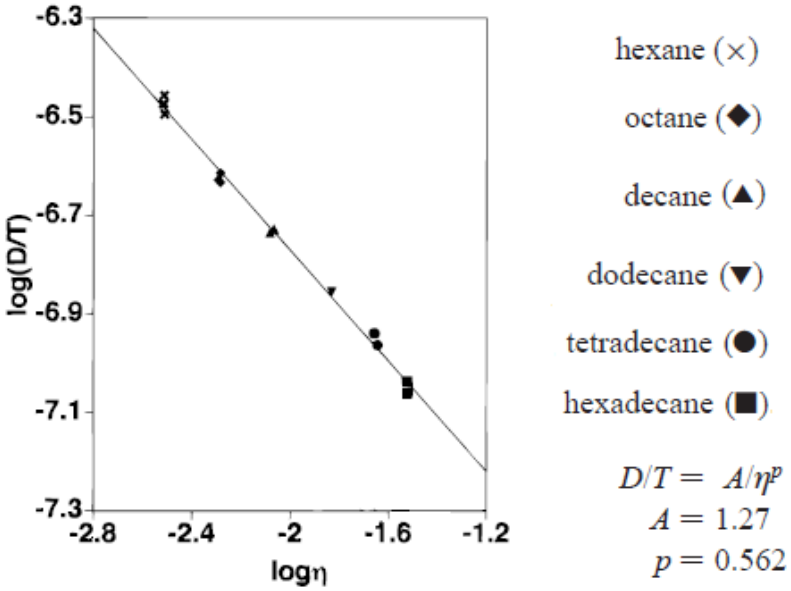

Figure 2.4.9: Diffusivity of O_2 in n-alkanes (Kowert & Dang 1998).

Experimental values of the diffusion coefficients of H_2O and O_2 in n-octane and n-hexadecane are presented in Table 2.4.4. Oxygen has a higher diffusivity in n-alkanes than H_2O. The difference in O_2 and H_2O diffusivity increases as the solvent chain length increases for the given data. Furthermore O_2 will not be affected by the presence of polar species since it is not a polar molecule.

Table 2.4.4: Measured diffusion coefficients of water and oxygen in various solvents

Solvent		**Solute diffusion coefficient (cm^2/s) × 10^5**		
		H_2O [a]	O_2 [b]	
n-octane	n-C_8H_{18}	5.38 ± 0.43 @ 22 °C	7.04	@ 25.05 °C
n-hexadecane	n-$C_{16}H_{34}$	1.15 ± 0.13 @ 22 °C	5.32	@ 25.55 °C

[a] (Su, Duncan, Momaya, Jutila, Needham, 2010)

[b] Averaged values (Kowert & Dang 1998)

Diffusivity values could not be obtained for N_2. This however is not of extreme importance since N_2 does not react with the surface as is the case with oxygen or significantly interact as is the case with water.

As a concluding remark it is noteworthy from what was presented in this section that oxygen has a higher solubility and diffusivity than water.

A diffusion model of water in n-hexadecane will be presented in the results section, since the effects of water is the focus of this study. Data presented here for oxygen is for comparative purposes.

2.5 Adsorption lubrication

The boundary lubrication regime affords protection of contacting surfaces through the adsorption of surface active species. Section 2.5 is limited to lubricating-, base fuel- and water adsorbates. Adsorbents are limited to iron, iron oxides and iron oxyhydroxides. These limitations are imposed to remain relevant to the experimental setup.

2.5.1 Adsorption

The molecule that adsorbs onto a surface, due to some surface affinity, is known as the adsorbate. The adsorbate is denoted by X and the surface by ≡ in adsorption Reaction 2.5.1. The site on a surface that is active to the adsorbate is known as the adsorbent.

$$\equiv Fe + X \leftrightarrow \equiv FeX \qquad [2.5.1]$$

Equation 2.5.1 allows the calculation of the equilibrium constant for this surface adsorption reaction.

$$K_{ads} = \frac{[\equiv FeX]}{[\equiv Fe][X]} e^{\frac{(-\Delta G_{ads})}{RT}} \qquad (2.5.1)$$

Adsorption data is most commonly presented as an isotherm. An isotherm is a plot of the quantity of the adsorbate, per unit adsorbent, as a function of the equilibrium solution concentration of absorbate. Other variables like temperature and pH are held constant (Cornell & Schwertmann, 2007: 253-254).

2.5.2 Absorption mechanisms

Adsorption is classified into two main mechanisms as shown in Table 2.5.1 Theoretically these two mechanisms differ mostly in that one is a physical bond that does not alter the adsorbate structure, whereas the other which forms a chemical

bond, does. It is however harder to distinguish reliably between these two mechanisms in practice. Chemisorption can furthermore be associative or dissociative. The magnitude of the heat of adsorption is often used for indication of mechanism as is shown in Figure 2.5.1. This method should however not be viewed as precise. Chemisorption analogies follow closely with the simple chemical bond which led to difficulty in early theoretical models, up to 1970. (Clark, 1970: 3,17,138,162).

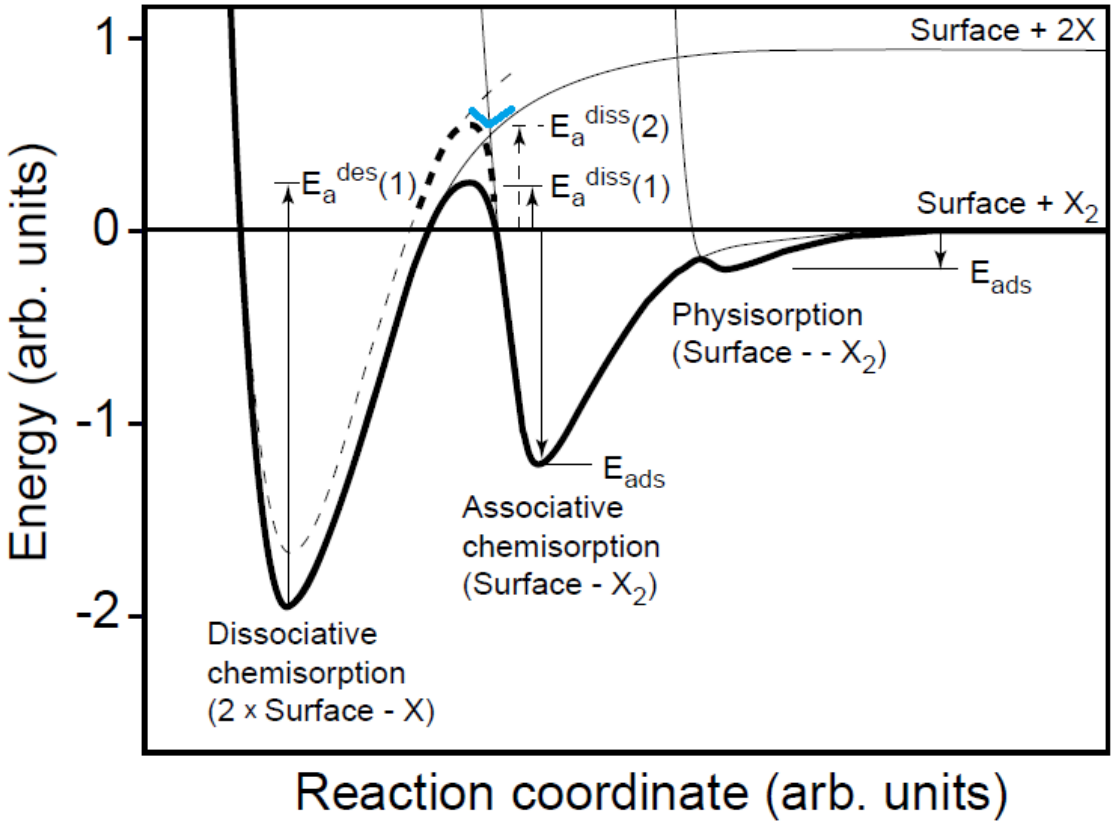

Figure 2.5.1: Potential energy diagram for a diatomic molecule as it approaches and interacts with a surface. Adsorption and desorption energies are indicated. Adopted from (Anderson, 2006: 14).

Table 2.5.1: Adsorption mechanisms (Stachowiak & Batchelor, 2003: 363-364) & (Clark, 1970: 137).

Physisorption (Physical)	Chemisorption (Chemical)
<u>Similar terms</u> • Non specific adsorption. • Outer sphere adsorption.	• Specific adsorption. • Inner sphere adsorption. • Ligand exchange.
<u>Adsorption</u> • Reversible. • Electrostatic contribution to free energy of adsorption dominating. • Influenced by ionic strength of system.	• Direct coordination to metal atom (no solvent molecule in between). • Free energy of adsorption. predominates. Can adsorb on to neutral or similar charged surface even. • Irreversible or semi-irreversible.
<u>Forces</u> • Van der Waals. • London dispersion forces. • Repulsive forces. • Low energy bonding mechanisms. • No electron transfer or sharing.	• Strong bonding – electron transfer or sharing. • Covalent character. • Modifies surface charge.
<u>Temperature</u> • Operates at lower temperatures than chemisorption. • Effective if temperature rise is not much above ambient, has an upper limit.	• Operates at higher temperatures than physisorption. • Reactivity of substrate material is temperature sensitive.
<u>Other</u> • Close packed with packing density near theoretical maximum. • Minor distortions.	• Normally maintains original molecule shape. • Drastic electron equilibrium redistributions.

In Figure 2.5.1, previously shown, the interaction of a diatomic molecule with a solid surface was presented. The approach is from the right hand side. Energy is released upon adsorption resulting in lowered surface energy. Only relative sizes are indicated between different modes of adsorption (Anderson, 2006: 14).

An energy barrier is indicated on Figure 2.5.1 in going from physisorption to associative chemisorption. This energy barrier is system-dependent and may even not exist if the molecule is directly associatively chemisorbed from the gas phase, as is indicated by the thinner line. It is important to note the larger energy barrier in going from associative chemisorption to dissociative chemisorption. If dissociative adsorption occurs directly from the gas phase it will not likely occur barrier less. This is highlighted with blue in Figure 2.5.1. This is mainly dependent on where the curve crossing occurs which is dependent on the adsorption strength of the two atoms of the diatomic molecule (Anderson, 2006: 15).

It is important to note that the barrier for dissociative chemisorption can be lower for a molecule already associatively adsorbed onto the surface compared to one from the gas phase. This is due to the already formed bonds to the surface possibly offering an energetically more favourable path (Anderson, 2006: 15).

The heat of adsorption on metals is known to decrease with increasing surface coverage for chemisorption. This could be due to adsorbate-adsorbate interaction, a change in the work function, surface non-uniformity or bonding alterations. (Clark, 1970:172)

Adsorbate surface difusion

Reports are made of diffusion of adsorbed water on magnetite(111) surfaces by rotational and translational movement (Cornell & Schwertmann, 2007: 293). Adsorbate diffusion on the adsorbent surface occurs when the energy barrier against lateral movement (surface diffusion) is overcome. This energy barrier is the difference in minimum potential of two points on a surface. This phenomenon therefore occurs mainly only for localized adsorption. Surface mobility can therefore occur if the thermal energy of the molecule is similar to or larger than the barrier against lateral movement. Surface diffusion is furthermore increased if the energy of adsorption is low. An intermediate exists between stationary and mobile molecules referred to as hopping molecules (Clark, 1970: 18,19).

Non-localized adsorption occurs when the energy barrier against lateral movement (surface diffusion) is very low for the bulk of the surface. This means the surface has a more uniform potential. This form of adsorption can therefore be seen as mobile, unless condensation occurs at high surface coverage for some unique cases. (Clark, 1970: 18,20).

The different **modes of coordination** can be seen in Figure 2.5.2. Protonation of these complexes are possible. Note that mononuclear bidentate means that the ligand binds to two hydroxyl sites on the edge of a single $Fe(OH)_6$ octahedron, denoted ^2E linkages. For binuclear bidentate the ligand binds to two corner hydroxyl groups from two adjacent $Fe(OH)_6$ octahedra, denoted ^2C linkages. The ratio of edge sites to corner sites differ for some iron oxyhydroxides.

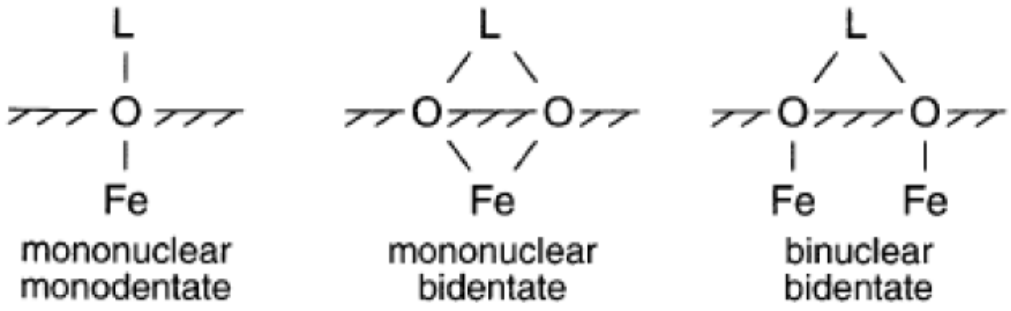

Figure 2.5.2: Different modes of complex coordination. The adsorbate is denoted by L (Cornell & Schwertmann, 2007: 265).

Anion adsorption having a Langmuirian type isotherm is believed to have a single type of adsorption site. On iron oxides this represents the singly coordinated surface hydroxyl group.

Chemisorption reactions of anionic ligands: The chemisorption or desorption of an anion which is a ligand (L) can be seen in Reaction 2.5.2 and 2.5.3 below. The surface is again denoted by ≡. The ligand replaces surface hydroxyl groups (Cornell & Schwertmann, 2007: 258).

$$\equiv FeOH + L^- \leftrightarrow \equiv FeL + OH^- \qquad [2.5.2]$$

$$\equiv (FeOH)_2 + L^- \leftrightarrow \equiv Fe_2L^+ + 2OH^- \qquad [2.5.3]$$

Desorption: An ordered film is needed for adequate lubrication. If the melting point of the layer is exceeded this order is lost and the layer will no longer give adequate protection. A subsequent rise in the friction coefficient is observed and this temperature is called the friction transition temperature. Increases up to 80 °C are known to increase surface coverage of fatty acids caused by both physisorption and chemisorption. Desorption temperature is very dependent on the substrate. It would seem that 150 °C is not yet at the transition temperature for stearic acid on iron oxide (Loehle, Matta, Minfray, Le Mogne, Martin, Iovine, Obara, Miura & Miyamoto 2014).

2.5.3 Adsorbates (Adsorbing species)

Organic polar molecules are known to have different chemical affinities at different sections of the molecule. The polarity of a molecule is typically expressed as the dipole moment (μ) and measured in debye. The dipole moment of some molecules related to the experimental work can be seen in Table 2.5.2.

Table 2.5.2: Dipole moment of some molecules (Yaws, 2012)

Molecule	Formula	Dipole moment (D) [a]
palmitic acid	$C_{16}H_{31}OOH$	1.739
n-hexadecane	$C_{16}H_{34}$	0
water	H_2O	1.85
oxygen	O_2	0
nitrogen	N_2	0

[a] 1 D = 3.34 x 10^{-30} C.m, with C = Coulomb

When polar molecules interact with metals they induce an attracting charge distribution in the metal. Non-polar molecules interact with ionic systems via electrostatic forces (Clark, 1970: 138, 153)

The dissociation constants for a number of chemical species are presented in Table 2.5.3. The dissociation constants can be used as a very rough estimate of the likeliness of a molecule to be more favourable towards chemisorption. This however is not completely true since the surface characteristics influences the type of adsorption. Lower values of pK_a favour higher dissociation.

The solvent to be used in the experimental is n-hexadecane which is a non-polar aprotic solvent. Disscociation constants are different in different solvents. The three standard solvents universally used are shown in Table 2.5.3. Water is a protic solvent than can form hydrogen bonds whereas DMSO and acetonitrile are aprotic meaning they are incapable of forming hydrogen bonds. Dissociation increases with higher relative permittivity (ε_r) and donor numbers (DN).

Although none of these solvents are non-polar to the extent of n-hexadecane, they still give a good indication of the behaviour. All dissociation constants decrease in going from protic water to aprotic solvent. Water dissociates to a lesser extent than palmitic acid in water. Dissociation decreases for carboxylic acids with increasing chain length, as is indicated.

It is interesting to note that from this data that the pK_a value roughly doubles for water going from water (protic) to DMSO (aprotic) whereas for acetic acid it almost triples.

Table 2.5.3: Dissociation constant of some molecules in various solvents

Molecule	Formula	pK_a in solvent		
		Water (Protic) $\varepsilon_r = 78$ DN = 18	DMSO[1] (Aprotic) $\varepsilon_r = 47$ DN = 30	Acetonitrile (Aprotic) $\varepsilon_r = 37$ DN = 14
Acetic acid	CH_3COOH	4.76[a]	12.3[b]	23.51[a]
palmitic acid	$C_{15}H_{31}COOH$	6.64[c]		
Alkanes	C_xH_{2x+2}	>=50[d]		
water	H_2O	15.7[b]	32[b]	
	H_3O^+	-1.7[b]		
oxygen	O_2			

[a] (Raamat, Kaupmees, Ovsjannikov, Trummal, Kütt, Saame, Koppel, Kaljurand, Lipping, Rodima, Pihl, Koppel & Leito, 2012) [b] (Ripin & Evans, 2005) [c](Solomons, 1992: 763) [d] (Gorzynski Smith 2008,60) [1]Dimethyl sulfoxide.

2.5.3.1 Water as adsorbate

Water is known to adsorb both physically and chemically. The following number of studies presented in Table 2.5.4 will summarize some of these:

Table 2.5.4: Studies of water adsorption on metal oxide

Surface	**Mode of adsorption**	**Bulk phase**	**Other detail**	**Analytical method**	**Reference**
Magnetite (111)	• Dissociatively chemisorbed (235 K) • Physisorbed monomeric (160 K) • Hydrogen bonded condensed ice(140 K)	Vapour	$p(H_2O) = 1x10^{-8}$	Photoelectron and thermal desorption spectroscopy	Joseph, Kuhrs, Ranke & Weiss, 1999)
Hematite (021)	Dissociative chemisorption			SIMS and programmed thermal desorption studies	(Cornell & Schwertmann, 2007: 293).
Wustite (111)	Physisorption				(Cornell & Schwertmann, 2007: 293)

In Figure 2.5.3 a relative comparison of bond energies is given for a water, hydroxyl and metal system. The absolute values are of course very dependent on the metal identity. Hydroxyls, possibly from dissociated water, adsorbed onto metal have significantly stronger bond energy than that of water molecules adsorbed onto metal surfaces.

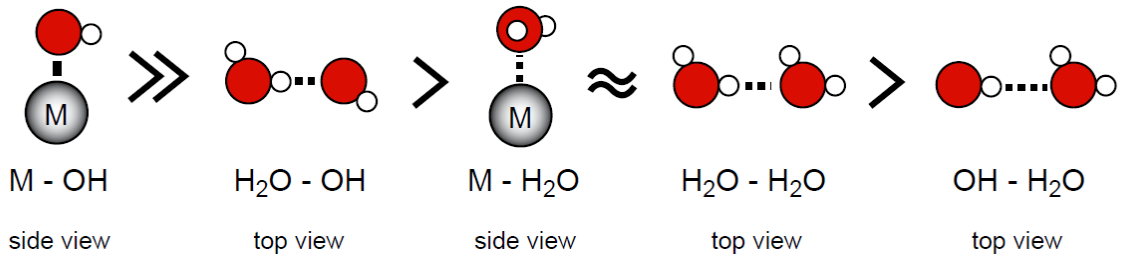

Figure 2.5.3: A relative comparison of bond energies for water, hydroxyls and metal (Anderson, 2006: 18).

It is very interesting to note that hydrogen bonding between water molecules and hydroxyl groups are very sensitive to the arrangement (2nd and 5th in ranking). This holds implications for adsorbed molecules since they tend to be geometrically orientated in specific directions. The reason for the difference lies in the fact that the hydrogen atom in the hydroxyl is less positively charged than the hydrogen molecule in water due to electron density spill over (Anderson, 2006: 18). Hydrogen bonding with other non bonded water molecules in solution is also possible.

2.5.3.1.1 Dissociative adsorption of water

Coordinatively unsaturated Fe atoms occur at iron oxide surfaces due to the termination of the oxide network. These atoms act as Lewis acids to accept electron pairs from Lewis bases. The high surface area to volume ratio of iron oxides increases the number of these available active sites.

Iron oxide can be hydroxylated within minutes to hours by water. The water molecule is dissociatively adsorbed onto the surface. The hydroxyl groups are coordinated with the underlying Fe atoms (Cornell & Schwertmann, 2007: 221 - 223). It is suggested by (Joseph, Kuhrs, Ranke & Weiss, 1999) that oxygen in the oxide structure act as anion sites and therefore act as proton acceptors for the surplus occurring from the dissociation of water into a hydroxyl and hydrogen ion.

It was found by (Kendelewicz, Liu, Doyle, Brown, Nelson & Chambers, 2000) that water vapour will dissociatively chemisorb onto magnetite surfaces (100 & 111), at 298 K, forming hydroxyl groups. The same observation was made for water vapour and hematite (0001) surfaces by (Liu, Kendelewicz, Brown, Nelson & Chambers, 1998).

Both these studies report that a critical water vapour pressure exists at which the adsorption increases extensively. Below this critical water vapour pressure adsorption is attributed to occur at only defect sites on the surface. Above the critical water vapour pressure adsorption coverage is more extensive. Prolonged exposure shows significant increases when above the critical water vapour pressure, but not below it. Results also indicated that magnetite is more reactive than hematite at higher water vapour pressures.

Geothite is considered to be the most common and stable iron oxyhydroxide. The reaction products of water adsorption on magnetite were found not to be goethite, limonite or hematite. This was done by comparing the O KVV Auger K-edge absorption spectra of the sample with the known spectra. These spectra are available in the source material. This was also evident from work done on an equilibrium thermodynamic model. This model predicted the critical water vapour pressure for $Mg(OH)_2$ as a reaction product from MgO as well as $Al(OH)_3$ as a reaction product from α-Al_2O_3 reasonably well, but over predicts the critical water vapour pressure at 8 Torr for goethite as a reaction product from magnetite and 10.6 Torr from hematite (Kendelewicz *et al*, 2000).

Observations based on chemical shifts could suggest that different bonding environments exist on the surface, with weaker bonds forming later in the process and are subsequently removed easier. One suggestion for hematite is that hydroxyl groups are associated with defect sites and that the hydroxyls on non-defect sites are similar to iron hydroxides (Kendelewicz *et al*, 2000).

Surface hydroxyl groups can be coordinated to either one, two or three underlying Fe atoms as shown in Figure 2.5.4. The charge indicated is based on a six fold Fe-O coordination system.

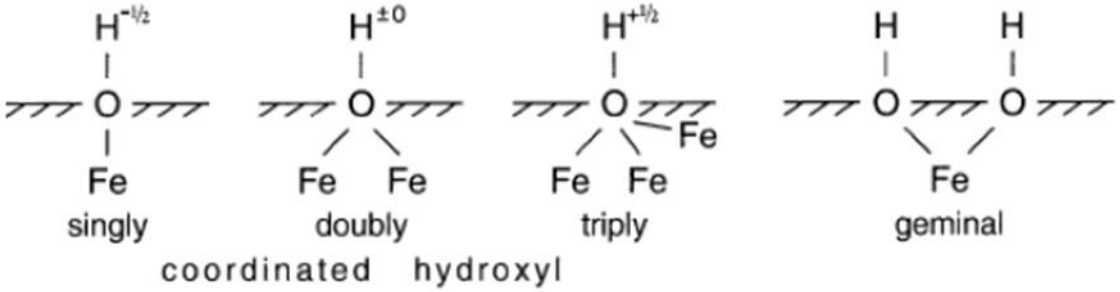

Figure 2.5.4: Hydroxyl surface coordination (Cornell & Schwertmann, 2007: 222).

Hydroxyl groups can occur as part of the oxide structure or as mentioned before from surface adsorption. They are reactive sites for both acids and bases due to the presence of a double electron pair as well as a dissociable hydrogen atom. Hydroxyl groups can be removed by heating the oxide until water condenses and desorbs (Cornell & Schwertmann, 2007: 221 - 222).

Crystal morphologies are known to influence the density of surface hydroxyl groups resulting in different values for different crystal faces.

2.5.3.1.2 Associative adsorption

Three popular proposed structural models for water adsorption on metals are shown in Figure 2.5.5. In these models water is adsorbed in hexagonal rings. The rings consist of two layers of molecules. The red spheres represent the lower layer which consists of water molecules. These water molecules have their lone pair of electrons directed towards the surface forming a weak surface bond. The two hydrogen atoms of these molecules lie nearly parallel to the surface. The models differ in the arrangement of the second layer of molecules which are denoted by blue spheres (Anderson, 2006):

- In the "H-up" model only half of the adsorbed water molecules bond directly to surface (red). The second layer water molecules (blue) have one hydrogen pointing upwards and the other hydrogen atom forming hydrogen bonds with the lower layer water molecules. Some experimental studies have found significantly smaller vertical displacements than proposed by this model.

- In the "H-down" model all molecules adsorb in an alternating metal-oxygen and metal-hydrogen bonds. This model has been proposed for the Pt (111)/water system.

- A mixed model that consists of a mixture of water molecules and dissociated water hydroxyls has been proposed for Ru (001)/water system. This model becomes more favourable if it is assumed that the produced hydrogens are displaced to uncovered Ru(001) surface (Anderson, 2006: 19-20). Hydroxyls

adsorbed on Pt(111) are believed to be stabilized by the binding of extra water molecules (Anderson, 2006: 20-21).

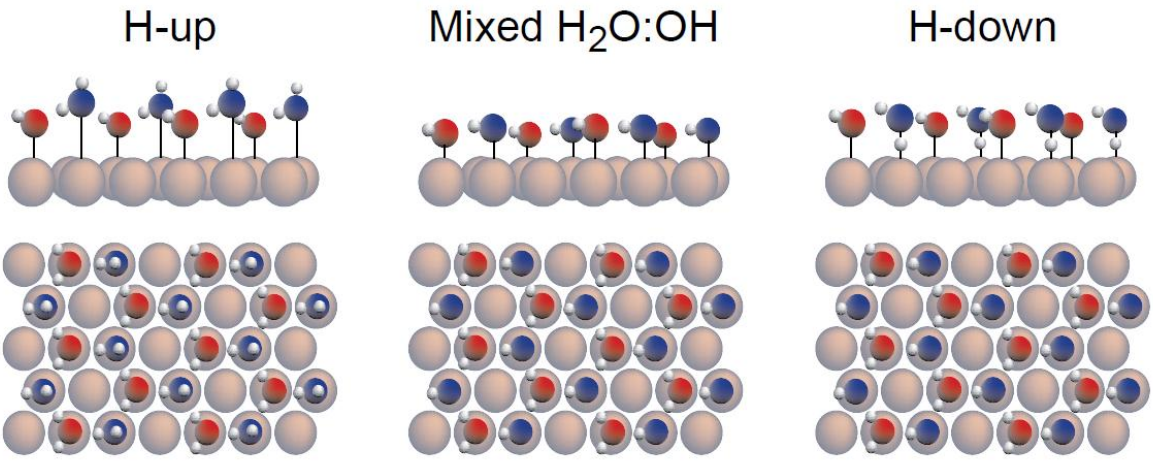

Figure 2.5.5: Proposed water adsorption structure models (Anderson, 2006: 19).

2.5.3.2 Lubricant adsorbates

Consider stearic acid which is a common lubricant additive, shown in Figure 2.5.6. The polar end is strongly attracted to a metal surface where it will adsorb. This is due to the free electron nature of the metal. The non-polar end will have a far lower affinity for the metal. It will however possibly form weak Van der Waals bonds with other neighbouring and contacting alkyl groups. These weak bonds ensure that a low shear interface is formed (ideal) whilst the strong adsorption ensures the presence of the species on the surface. This can be seen in Figure 2.5.7. A film is produced if the adsorption is strong enough to cover most available surface sites.
(Stachowiak & Batchelor , 2003:361-362)

Non-polar end
(Alkyl group)

Polar end
(carboxyl group)

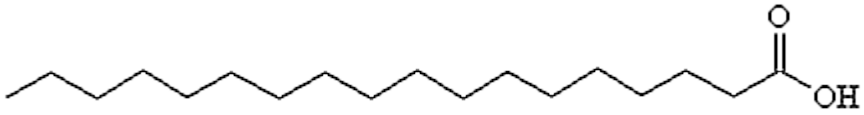

Figure 2.5.6: Stearic acid.

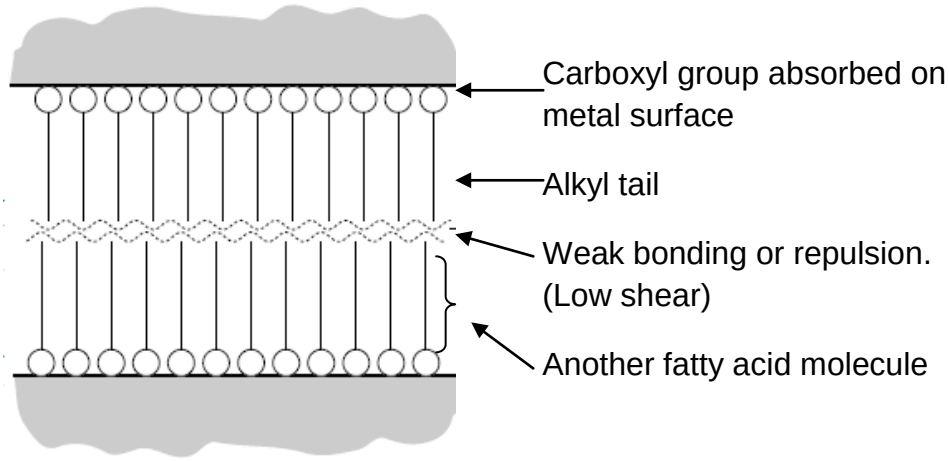

Figure 2.5.7: Mono-molecular layer adsorption lubrication.
(Stachowiak & Batchelor, 2003:362)

A closely packed monolayer is needed for effective lubrication. This limits the suitable molecular structure of the lubricant species to mainly linear type molecules. A marked reduction in lubrication is observed if isomers are used that are branched. Branched molecules will increase adjacent distances between molecules on the same surface resulting in weaker intra-molecular bonds and an irregular profile.

The size of these molecules greatly affect lubrication phenomena. If Figure 2.5.6 is considered again it will be noticed that stearic acid has an alkyl tail of 18 carbons. It has been observed that a minimum tail length of 9 carbons is needed for effective lubrication. This is due to the large number of weak bonding CH_2 groups needed on adjacent molecules, for monolayer durability. The longer the tail the higher the frictional transition temperature due to bonding and molecular size.
(Stachowiak & Batchelor, 2003: 365-367)

Organic compounds with sufficient polarity include fatty acids, alcohols, esters and amines. Silanes (compounds containing oxygen and silicon) have also been used and found to form mono layers with durability better than fatty acids.

In Figure 2.5.8: The different modes of fatty acid adsorption on iron oxide and hydroxides are presented. In (a) the initial surface is presented before adsorption. Note the different ways in which the surface is bound to oxygen and hydroxides. In (b) and (c) physisorption is indicated on the left and chemisorption on the right.

Rubbing contatcs tend to form via chemisorption as is indicated by (d) (Loehle, Matta, Minfray, Le Mogne, Martin, Iovine, Obara, Miura & Miyamoto 2014).

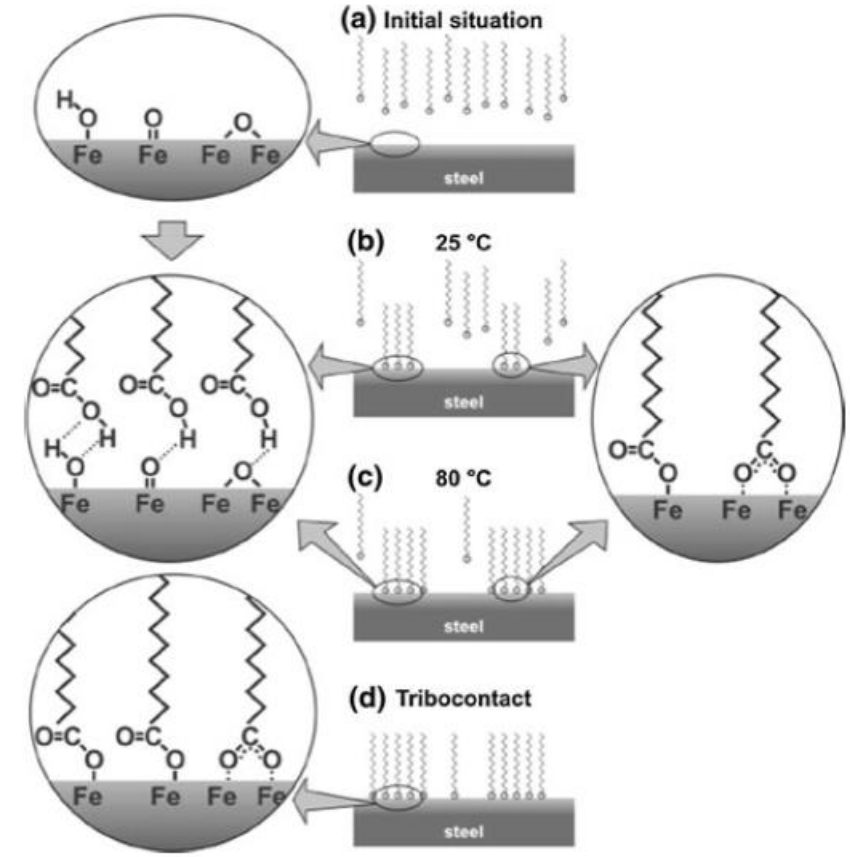

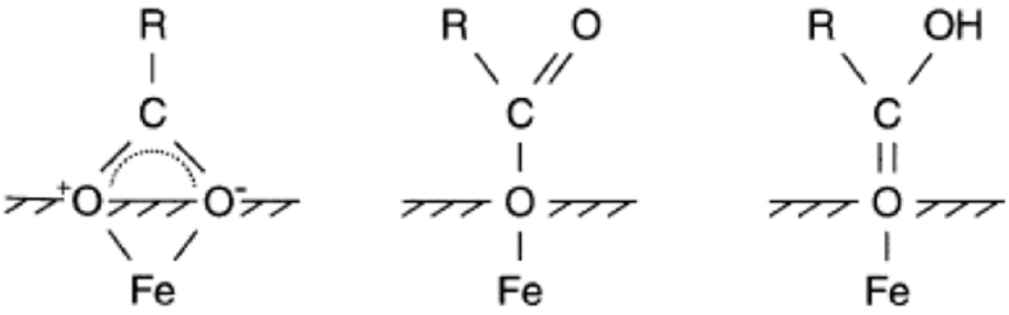

Figure 2.5.8: Different proposed modes of fatty acid adsorption on steel surfaces (Loehle, *et al*, 2014) & (Cornell & Schwertmann, 2007: 265).

Organic ligand adsorption on Iron oxides occurs mostly due to electrostatic effects. The occurrence of ligand exchange and hydrogen bonding may occur. This means that adsorption is more favourable for conditions that promote a positive surface. Chemisorption and hydrogen bonding does however also occur (Cornell & Schwertmann, 2007: 273).

2.5.3.2.1 The effects of unsaturation of the lubricating molecule

Work done by (Loehle, *et al*, 2014) suggested that unsaturated fatty acids will adsorb faster than their saturated counterparts of the same carbon length, on 52100 steel surfaces. They noted that although a simulated diffusion to the surface might occur faster due to the presence of the double bond, wear and friction was increased. This is because the packing efficiency decreases from the less linear shape of the tail of the unsaturated molecule. A poly-alpha-olefin base oil was used in this study.

It was observed that a C18 saturated fatty acid showed decreased friction and wear with increasing temperature (50→150 °C) indicating mainly chemisorption. The simulation also did not show changes in the Self-assembled-monolayer (SAM) formation in this temperature range, supporting this claim. The opposite trend was however observed for friction and wear of a mono unsaturated C18 fatty acid indicating that physisorption might be more prevalent than for the saturated fatty acid. This effect is however more likely linked with the poorer packing efficiency. The same could be said for a di unsaturated fatty acid which showed this same opposite trend in wear and friction, but to a greater extent. The simulation did however not show changes in the SAM formation in this temperature range for these two unsaturated fatty acids still indicating chemisorption (Loehle, *et al*, 2014).

In Figure 2.5.9 the adsorption of three unsaturated C18 fatty acids onto a steel is shown. They differ in that oleic acid , linoleic acid and linolenic acid has one, two and three double bonds in the carbon chain respectively. Clearly oleic acid adsorption reaches some saturation value in this concentration range whereas the less saturated molecules does not. It is proposed that oleic acid adsorbs horizontally, parallel to the surface leading to a lower plateau. Linoleic and linolenic acid are assumed to either adsorb vertically (allowing more molecules to adsorb) or form multi layers, either would explain the higher values (Lundgren, Persson, Mueller, Kronberg, Clarke, Chtaib and Claesson, 2007).

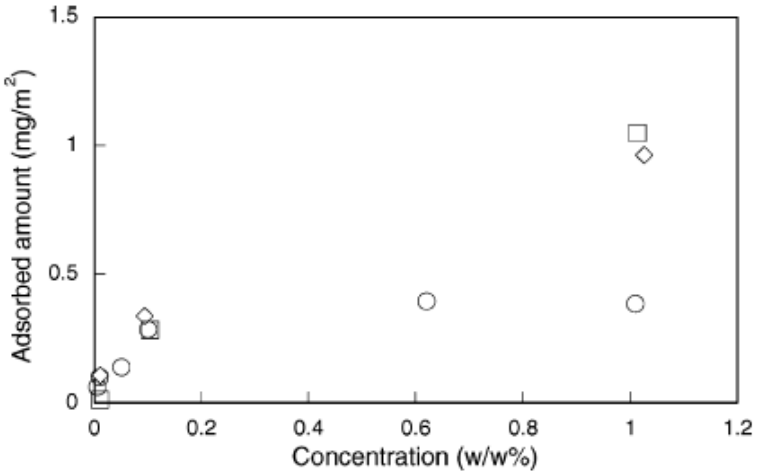

Figure 2.5.9: the adsorbed amount of oleic acid (O), linoleic acid (◊) and linolenic acid(□) from n-hexadecane onto steel (Lundgren, *et al*, 2007).

It is reported in a literature survey by (Lundgren, *et al*, 2007) that adsorption of fatty acids onto metal surfaces are much lower on oxide free surfaces than oxidized surfaces, they furthermore noted that mechanically activated surfaces show increased adsorption. Physisorption and chemisorption is possible on iron oxides. The number of chemisorption sites are independent of the fatty acid type based on static SIMS data of three different C18 unsaturated fatty acids. For physisorption the adsorbable amount is dependent on the type of fatty acid since this can induce steric hindrances both from size and the degree of saturation. It was found that physisorption increased with the degree of unsaturation (1 degree to 3) of C18 fatty acids.

2.5.3.2.2 Effect of solvent base fuel

It should be noted that in a study done by (Lapuerta, Sánchez-Valdepeñas & Sukjit, 2014) both alkanes and alcohols, unadditized, showed a trend wise decrease in wear with increasing chain length. The chain lengths of the alkanes and alcohols were small enough to still be relevant the boundary lubrication regime.

(Lundgren, *et al*, 2007) found similar adsorption results, using Quartz Crystal Microbalance, for three fatty acids adsorbed onto Fe_2O_3 from two isomerically different solvents: n-hexadecane and 2,2,4,4,6,8,8-

heptamethylnonane. It has been observed that the heat of adsorption and hence the friction transition temperature for a lubricating species is not a constant when using different base fuels.

Chain matching**:** When the lubrication additive and base fuel additive chain lengths match, then it has been observed that better lubrication characteristics are observed. It is suggested that a viscous layer forms on the surface when chain matching occurs similar to what was discussed in localized viscosity enhancement. It should however be noted that this does occur at higher contact stresses and temperatures than the localized viscosity enhancement effect (Stachowiak & Batchelor, 2003: 381).

2.5.3.2.3 Interaction of adsorption species with water

(Lundgren, *et al*, 2007) found, using static Secondary-Ion-Mass-Spectroscopy (SIMS) , that water inhibited linolenic acid binding onto steel surfaces from n-hexadecane. This lowered chemisorption can be caused by either adsorbed water on the surface or by carboxyl heads from the acids being directed towards water droplets.

2.5.3.2.4 Other noteworthy studies

(Loehle, *et al*, 2013) found with their simulation that a single stearic acid molecule will tend to adsorb horizontally onto a Fe_2O_3 surface at 50 °C rather than the packed vertical formation when more fatty acid molecules are present. A similar observation was noted by (Lundgren, *et al*, 2007) for the C18 unsaturated fatty acid, oleic acid. It was suggested that the molecule has a horizontal rather than vertical arrangement towards the surface. This was suggested since the concentration at which no further adsorption occurred matched that of a horizontal arrangement better than a vertical arrangement.

(Han, Healy & Fuerstenau, 1973) report that lauric and oleic acids adsorb to a lesser extent at high concentrations due to hydrophobic effects.

2.5.4. Adsorbents (Adsorbing surface)

Adsorption occurs at the site of minimum potential energy. Most adsorbent surfaces are highly irregular and therefore consist of a range of different adsorption energies. These sites can occur in patches of similar values or at random locations on the surface. If the site density is high a continuum can form rather than localized sites. (Clark, 1970: 3,127)

In Table 2.5.5 a number of reported interaction of fatty acids with surfaces are summarized. (Loehle, Minfray, Matta, Le Mogne, Martin, Iovine, Obara, Miura & Miyamoto 2013) utilized an ultra-accelerated quantum chemical molecular dynamics (UA-QCMD) simulator. They concluded that more oxidized iron is less chemically reactive to fatty acids, a claim also supported by (Ruby, Fusy, Alnot, Genin,& Ehrhardt 1997).

Furthermore (Ruby, *et al*, 1997) reported that transition metal surfaces tend to thermodynamically favour dissociation. This is not true for face specific elements from groups VIII and IB. Dissociation is reduced for more closely packed surfaces. They mention that some literature indicates that the presence of iron oxide layers does not favour dissociation of water and therefore nor the formation of oxyhydroxide groups.

Table 2.5.5: Surfaces to consider as adsorbates and some interaction.

Surface	**Adsorbate**	**Reported interaction**	**Reference**
Iron	Fatty acid	Catalytic decomposition	[a]
Iron oxides	Fatty acid	Chemisorption	[a]
	Fatty acid (C18)	Chemisorption / physisorption	[b]
Iron hydroxides	Fatty acid (C18)	Physisorption or not at all	[b]

[a](Stachowiak & Batchelor, 2003: 370), [b](Loehle, *et al*, 2013)

2.5.4.1 Iron oxides and oxyhydroxides

Oxygen and water react with chemically active metals. A metal oxide surface film is formed on reaction with oxygen. This oxide film can be hydrated by water. The oxide film allows lubricant adsorption by acting as a substrate. Removal of this oxide layer can result in lubrication failure but generally is rapidly reformed. If however the adsorbed lubricant prevents the nascent metal from reacting with oxygen, then adhesion could occur (Stachowiak & Batchelor, 2003: 370-371).

Reaction products of iron with oxygen and water are popularly collectively referred to as iron oxides. The correct classification distinguishes between:

- Iron oxides
- Iron hydroxides (See Appendix C)
- Iron oxyhydroxides

This collective group all have the same basic structural unit of either an octahedron displayed in Figure 2.5.10 or a tetrahedron. The Fe ion is surrounded by 6 locations being occupied by a combination of O atoms and OH ions depending on species. The iron oxides and iron oxyhydroxides differ in the arrangement of the Iron octahedrons into a bigger array (Schwertmann & Cornell, 1991: 6).

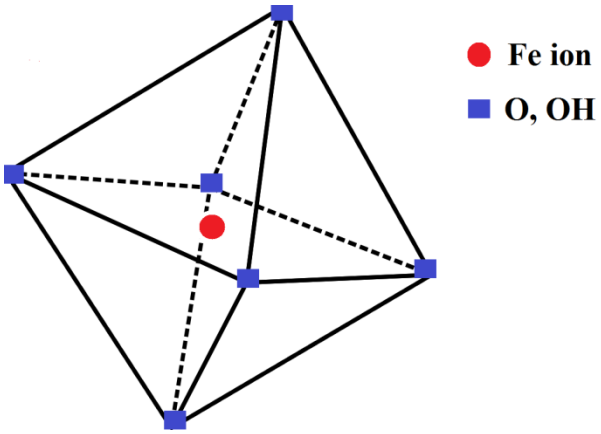

Figure 2.5.10: The octahedral structure of iron oxides, oxyhydroxides and hydroxides. In some instances tetraheral coordination can also occur.

Due to the required charge balance Fe^{3+} oxides will have more unfilled interstices than Fe^{2+} oxides. This means that the possible locations for Fe^{3+} cations are more for these oxides. It is these different possible locations that result in structural differences between some oxides.

Coordination is preferentially octahedral(6) for Fe^{2+} oxides. This is because crystal field stabilization energy is higher for the Fe^{2+} octahedral (6) match than for tetrahedral (4). Coordination for Fe^{3+} oxides can be either octahedral (6) or tetrahedral (4) since there is no crystal field stabilization energy for the unpaired d electrons of Fe^{3+}.

Hexagonal close-packed forms (hcp) are normally termed α phases (more stable), cubic close-packed (ccp) forms are termed γ phases. The Fe^{2+} and Fe^{3+} cations are larger than most interstices leading to a somewhat irregular close packing.

In Figure 2.5.11 the different ways in which octahedra can be linked is shown. Note the differences in Fe-Fe ion distances.

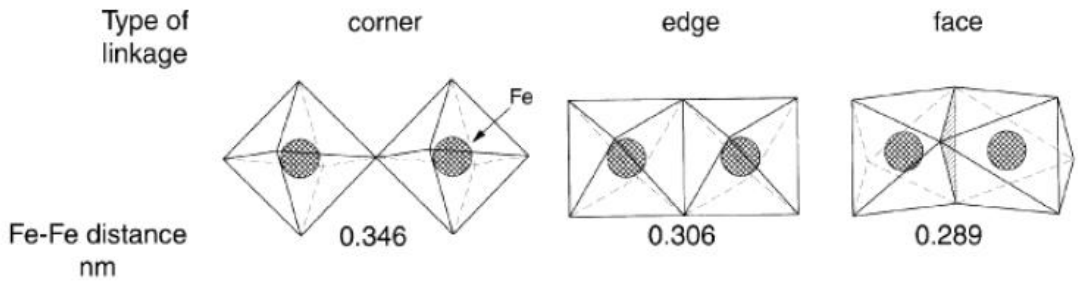

Figure 2.5.11: Types of octahedral linkages. Adapted from (Cornell & Schwertmann, 2007: 14).

In Figure 2.5.12 the colours of some common oxides and oxyhydroxides in powder form are presented. Focus here is to be placed on the reddish hematite and the dark magnetite. Other oxide colours are presented in Appendix C. Dense masses of oxides tend to be darker. There exist colour variations due to variations in crystal size, morphology or due to Fe substitutions by other similar sized metal cations. This however does not occur to the extent of yellow hematite nor red goethite

(Schwertmann & Cornell, 1991: 33-34) Hematite is reported to be blood-red if finely divided and black or sparkling grey if it is in a coarse crystalline state.

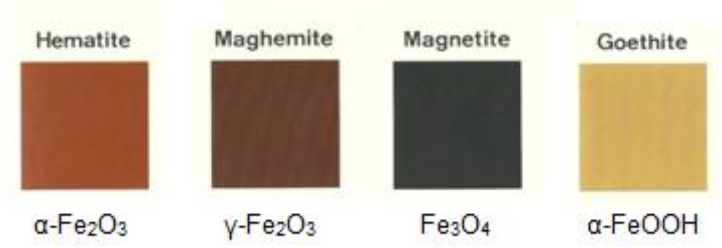

Figure 2.5.12: The typical colours of iron oxides. Adapted from (Schwertmann & Cornell 1991).

In Table 2.5.6 the expected formation of iron oxides and iron oxyhydroxides can be based on exposure to certain conditions. This list is limited to atmospheric and thermal conditions. The most prevelant oxides in corrosion studies are usually magnetite, maghemite, goethite, lepidocrocite, wustite and green rusts. (Schwertmann & Cornell, 1991: 1,14)

Table 2.5.6: Expected iron oxides in certain environments (Cornell & Schwertmann, 2007: 498).

.

Corrosion type	Environment	Oxides
Atmospheric	Temperate and Tropical	α-,γ-FeOOH & magnetite
	High SO_2 (accelerant)	α-FeOOH mostly
	High Cl^-	β-FeOOH
Thermal	Air, Ambient T	Magnetite, Maghemite
	Air, 250-550 °C	Magnetite (inner layer), hematite (outer layer)
	Air, 600 °C	Magnetite, hematite, wüstite

In Table 2.5.7 the properties of some iron oxides and hydroxides are presented, a more comprehensive list can be found in Appendix C which include iron hydroxides.

Table 2.5.7: Characteristics of iron oxides (Cornell & Schwertmann, 2007: 4 - 5).

		Mass % O	Crystallographic system	Formula unit cell	Octahedral occupancy	Anion packing	Density (g/cm3)	Hardness	
Oxides									
Wustite (FeO)	Iron(II)	22,27	Cubic	4		Ccp	5,9 – 5,99	5	Non- stoichiometric, oxygen deficient. Black.
Magenetite (Fe_3O_4)	Iron (II,III)	27,64	Cubic	8		ccp [111]	5,18	5,5	
Hematite (α-Fe_2O_3)	Iron (III)	30,06	hexagonal or Rhombohedral	6	2/3	Hcp [001]	5,26	6,5	Very stable
Maghemite (γ-Fe_2O_3)	Iron (III)		Cubic or Tetragonal	8		Ccp [111]	4,87	5	Cation deficient sites
Oxyhydroxides									
Goethite α-FeOOH			Orthorhombic	4	1/2 (2 rows filled 2 rows empty)	Hcp [001]	4,26	5 – 5,5	Thermodynamically stable at ambient T

2.5.4.2 Surface area and porosity of iron oxides and oxyhydroxides

The specific surface area of iron oxides influence many other properties thereof. Most noteworthy of these being the interaction with sorbents, dehyroxylation behaviour, phase transformations, and thermodynamic stability.

Surface area is inversely proportional to particle size. Therefore surface area is strongly dependent on the crystal growth conditions. Larger surface areas tend to occur at high growth rates and low temperatures since these crystals tend to be less ordered (Cornell & Schwertmann, 2007: 95).

Porosity can occur due to partial dehydroxylation or dissolution, aggregation of particles or simply exist between domains. During dehydroxylation slit-like micropores form in iron oxyhydroxides which can transform to mesopores at a higher temperature depending on the oxyhydroxide identity **(**Cornell & Schwertmann, 2007: 95-110).

In Appendix C some available data on the porosity and surface area of known iron oxides and oxyhydroxides is presented.

2.5.4.3 Electrical properties of iron oxides and oxyhydroxides.

Most iron oxides can be described as semiconductors, In Figure 2.5.13 the resistivity of 3 iron oxides and 1 iron oxyhyroxide are presented at various temperatures. Whilst the resistivity of goethite and hematite are similar in order that of magnetite is much lower (Guskos, Papadopoulos, Likodimos, Patapis, Yarmis, Przepiera, Przepiera, Majszczyk, Typek, Wabia, Aidinis & Drazek, 2002). Maghemite (001), which is metastable, is reported as the having the highest resistivity based on work done by (Hasegawaa, Yanagiharaa, Toyodaa, Kitaa & Rannob 2007). These oxides were synthetically prepared.

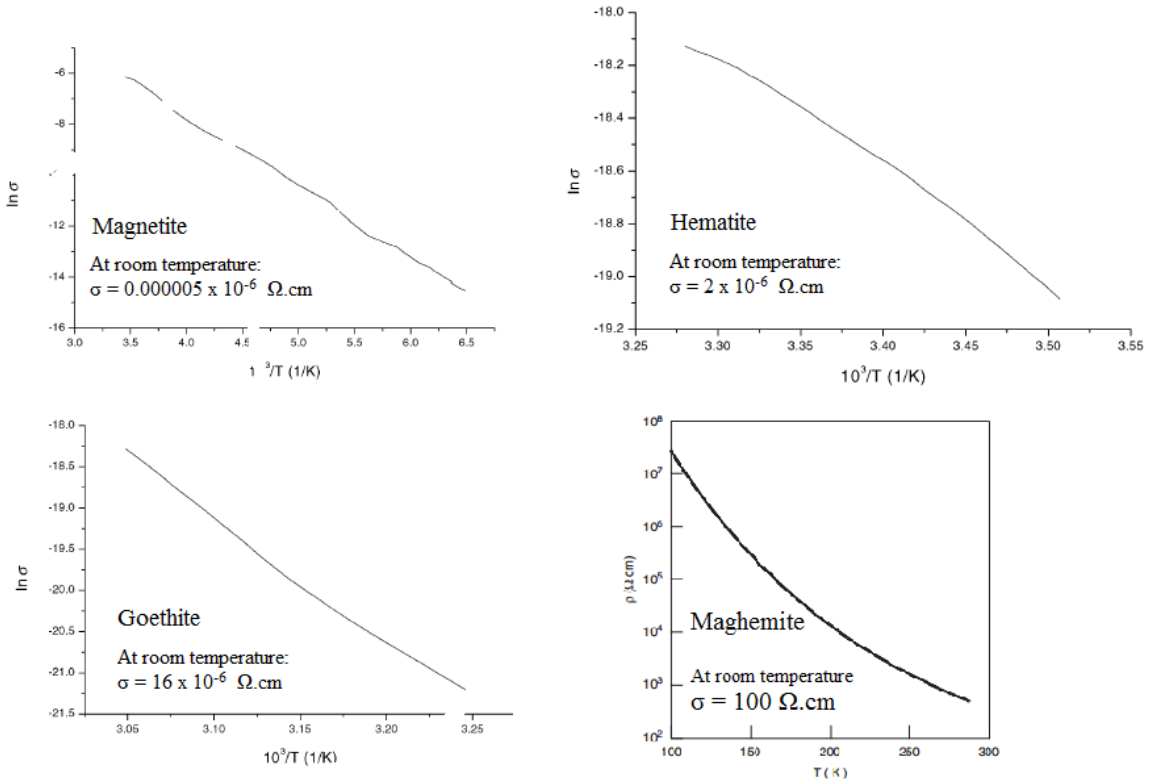

Figure 2.5.13: Resistivity of some iron oxides (Guskos, *et al*, 2002) & (Hasegawaa, Yanagiharaa, Toyodaa, Kitaa & Rannob 2007)

2.5.4.4 Stability of iron oxides and oxyhydroxides

In Figure 2.5.14 the formation and transformations of the common iron oxides are presented. Some reactions will be discussed in the text to follow. Reactions not indicated have not been observed in nature or under induced laboratory conditions. Some reactions are left out because they are very unlikely for the system in the experimental setup.

The reactions in Figure 2.5.14 can be of the following nature (Cornell & Schwertmann, 2007: 365):

- Isochemical (no change in chemical formula)
- Chemical modification
  - dehydration (loss of H_2O)
  - dehydroxylation (loss of OH)
  - oxidation/reduction (electron transfer)

Dehydration of FeOOH polymorphs and Ferrihydrtite into hematite result in the release of water. This can include both stoichiometrically bound (10.4 g/kg for FeOOH) water as well as adsorbed water. The amount therefore depends on the

surface area. This can occur between 150 - 500 °C depending on crystalinity and foreign inclusions. Above 600 °C sintering occurs.

Microporosity occurs at the onset (increasing surface area) followed by coalescence into mesopores at higher temperatures. Hydroxo-bonds are replaced with oxo-bonds. Protons diffuse towards the surface.The FeOOH does not have face-sharing octahedra, but hematite does. This means some Fe atom-movement is needed to create the denser structure. This movement is temperature dependent resulting in more ordered structures at higher temperatures.

Structural changes are described as the following:

- Topotactic - Solid state transformation. One crystal forms one new crystal.
- Pseudomorphic - Solid state transformation. One crystal does not form one new crystal.
- Reconstructive - Dissolution of original phase followed by precipitation of new phase. Dependent on dissolution rate and solubility. These type of transformations are not considered since solubility and precipitations are not likely in the experimental system.

Note that high temperatures are needed for solid state transformation to allow mobility. There tends to be some structural similarities between starting and end phases for solid state transformations (Cornell & Schwertmann, 2007: 365).

Thermodynamic considerations of these reactions are presented in Appendix C.

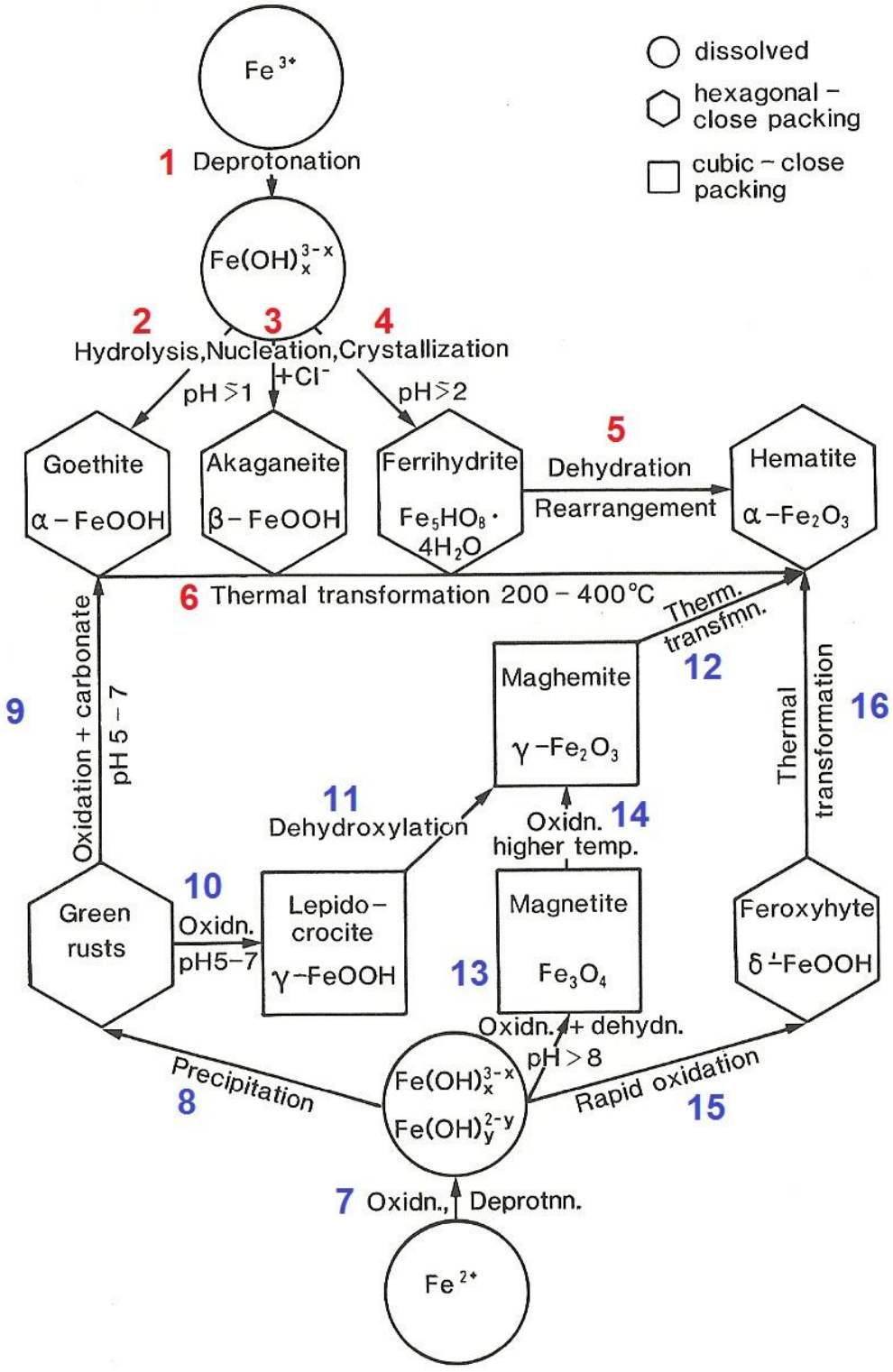

Figure 2.5.14: Iron oxide formation and transformation pathways. Reactions are indicated with numbers and discussed in text. Oxidation generally proceeds in an upward - right - handed manner. Adapted from (Cornell & Schwertmann, 2007: 346).

Table 2.5.8: Reactions from Figure 2.5.14 (Cornell & Schwertmann, 2007: 365-407):

Nr	Reaction	Temperature and activation energy (if available)	Compatible kinetics	Note
5	• ferrihydrite → hematite • A combination of thermal dehydration and dehyroxylation.	• At 227 °C 25% conversion after 9 hrs (2-line). • At 327 °C 100% conversion after 4 hrs (2-line). • At 400 °C 100% conversion after 1 hrs (6-line).	Diffusion controlled model	This transformation is gradual.
6	• 2α-FeOOH → α-Fe_2O_3 + H_2O • Thermal or mechanical dehydroxylation. • Pseudomorphic.	• T = 260 - 320 °C depending on crystalinity. • $\Delta H_{reaction}^0$ = 57.1 ± 3.5 kJ/mol (in presence of gaseous water). • Activation energy: 87.9 - 247 kJ/mol.	Random nucleation and 3D diffusion controlled process.	• There is uncertainty if there is an intermediate. Posibilitites are maghemite and β-hematite. • The anion structure mostly stays intact with cation movement and water loss.
11	• lepidocrocite → maghemite • Thermal dehydroxylation • Pseudomorphic	• T = 220 -280 °C in air, will form hematite since water vapour helps nucleation. • T = 120 °C in vacuum, will not form hematite. • Activation energy: 104-134 kJ/mol.	1st order random nucleation and diffusion controlled process	• Milling in a agate mortar with hexane or cyclohexane leads to a maghemite and hematite mixture, whereas milling without converts to only hematite. • An Anisotropic (directional dependency crystal shape occurs due to precursor (stacking faults). • Could contain some OH still in the structure.
12	• maghemite → hematite • Thermal conversion.	• Converts between 370 - 600 °C depending on what the precursor was and if foreign cation inclusions are present. • The high conversion temperatures are needed due to the rearrangement from ccp to hcp. • ΔH_f^0 @ 285 K: -15.6 ± 3.5 to -25.3 ± 0.6 kJ/mol.		The shape of hematite derived from magnetite with a lepidocrocite precursor maintains the lepidocrocite lath like particle shape different from other precursors.
14	• 4 Fe_3O_4 + O_2 → 6 Fe_2O_3 • Oxidation (air)	• At 220 °C an outer layer of maghemite forms which inhibits the reaction in the interior		• Isotropic crystal shape due to magnetite being the precursor.

		sections. • At 320 °C hematite nucleation starts in the outer layer. The inner sections disproportionates into a mixture of hematite and magnetite. • At 400 °C the last of the magnetite is transformed into hematite • Above 500 °C maghemite does not occur as an intermediate phase. • Activation energy: 83.6 – 137 kJ/mol		• Particles smaller than 300 nm transformed via a mixed phase to maghemite at 200-250 °C. • Particles larger than 300 nm show small hematite nucleus forming rather than maghemite, it is suspected that this occurs due to the larger diffusion lengths in the bigger crystals.
16	• feroxyhyte → hematite • Thermal deydroxylation	• Poorly crystalline δ-FeOOH converts directly to hematite at 150 °C (vacuum or air) dry grinding also facilitates this reaction. • Feroxyhyte (δ'-FeOOH) converts to hematite upon heating (240 °C). An N_2 atmosphere impedes the transformation.		• If high water vapour pressure is present during heating then a goethite like phase occurs as an intermediate before hematite. This phase does not completely fit the anion structure of goethite.
	Reactions not on the Figure 2.5.14			
17	• goethite or ferrihydrite or feroxyhyte → maghemite • Thermal dehydroxylation (air & organic).			• Occurs in natural soils after fires. • In absence of any organic phase it converts to hematite.
18	• ferrihydrite → maghemite • Thermal dehydration /dehyroxylation			
19	• FeO → magnetite + Fe • Disproportionation (Air)	• T < 570 °C		

Stability diagrams: These diagrams usually show the most likely or most stable compound under these conditions. Metastable phases can however also occur since the kinetics are not considered. Some of these metastable phases can exist for a long time. When different oxides have ΔG_f^0 values which differ by less than 8 kJ/mol it becomes impossible to predict which oxide forms based on this information alone.

In Figure 2.5.15 the stability diagram for the iron-oxygen system is shown as a function of oxygen content and temperature. Notice that wüstite only occurs above 570 °C.

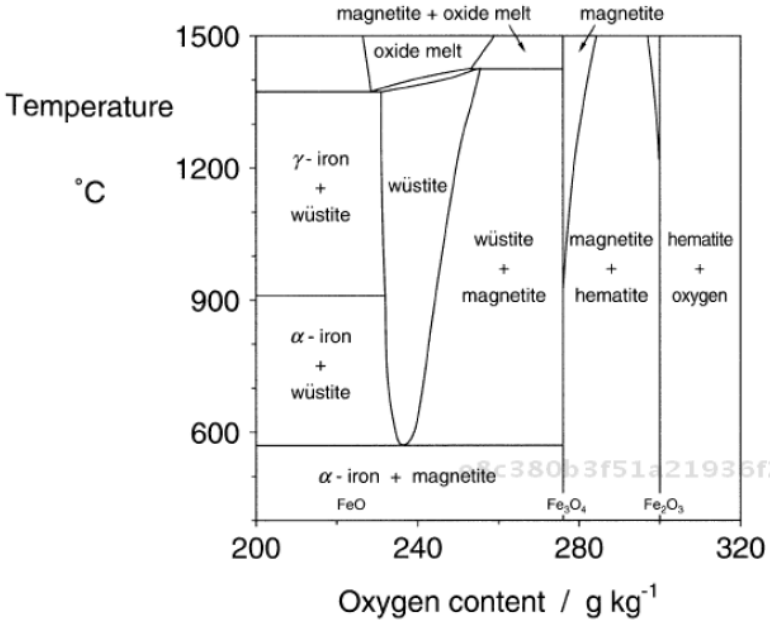

Figure 2.5.15: Oxygen-Temperature stability diagram form Iron and oxygen system **(**Cornell & Schwertmann, 2007: 196).

Thermodynamically hematite and goethite are the most stable Fe^{3+} oxides. This means that they tend to be the end products of transformation routes. The predominating phase of the two is dependent on conditions and crystal sizes (Cornell & Schwertmann, 2007: 197).

2.5.5 In summary

Various aspects have been shown to affect adsorption of chemical species onto surfaces. The most important of these included the adsorbate and adsorbent identities, temperature, adsorbent surface uniformity and the presence of multiple adsorbates.

2.6 Effects of water on diesel lubricity

2.6.1 The HFRR test: ASTM vs. ISO - the role of humidity

The High Frequency Reciprocating Rig (HFRR) is a tribo-tester used to do wear tests on fuels (See Section 3). It consists of a constant normal load being applied on a non-rotating steel ball-on-disk arrangement. The ball is oscillated by means of a vibrating arm that generates a wear scar to evaluate the diesel fuel's lubricity performance. The ASTM D6079 and ISO/CD 12156-1 test standards for a diesel fuel lubricity test on the HFRR have the same operating conditions. The difference is that the ISO standard makes an adjustment on the measured wear scar related to extent to which the humidity deviates from a set value, while the ASTM makes no correction. The ASTM does however state that a relative humidity (RH) > 30% is required without mention of a required ambient temperature.

With the initial development of the diesel lubricity test on the HFRR it was found that better differentiation between fuels was obtained at 60 °C than at 25 °C. It was discovered that this occurred due to differences in RH. By increasing the volume of the fuel to be tested from 1 to 2 mL the effects of humidity on wear testing results were reduced. Better correlation was obtained under moist conditions. At very dry conditions poor discrimination was observed. (Davenport, *sa*).

These new test parameters were implemented. The effects of RH were determined by testing 24 different fuels at both 60% RH (≈ 1.9 kPa) and 85% RH (≈ 2.7 kPa) at 25 °C ambient air temperature. A larger wear scar was obtained at 85% RH than at 60% RH for 22 of the fuels. Only 2 of the fuels gave slightly smaller wear scars at 85% RH compared to 60 %RH (Davenport, sa).

A round robin testing cycle was subsequently carried out on 12 low sulphur fuels to establish the effect of RH. The range tested was from (0,8 kPa to 2,2 Kpa):

- 2/12 fuels showed no response including the high lubricity reference.
- 10/12 fuels showed increased MWSD with increasing water vapour pressure.
- The average difference in MWSD per change in water vapour pressure was 60 µm/kPa for the 12 fuels tested.
- The high lubricity reference had a near flat response (3 µm/kPa)

This led to a correction of 60 µm/kPa being adopted by ISO and 1.4 kPa being selected as the standard. This 60 µm/kPa is referred to as the Humidity Correction Factor (HCF).This is illustrated in Equation 2.6.1 which makes a linear adjustment of the wear scar based on the deviation from the standard water vapour pressure of 1.4 kPa. The range of allowable water vapour pressures for Equation 2.6.1 was changed from (0,8 - 2.2Kpa) to (0,8 - 2 Kpa) . This is range is displayed in Figure 2.6.1. The standard water vapour pressure of 1.4 kPa was selected since this is the midpoint of the new proposed allowable range of water vapour pressure. (Davenport, *sa*).

$$WS_{1.4} = MWSD + 60(1.4 - AVP) \quad (2.6.1)$$

With $WS_{1.4}$ being the corrected wear scar, MSWD the averaged measured wear scar and APV the average water vapour pressure during the test. APV is related to RH by Equation 2.6.2.

$$RH = \frac{APV}{P_{sat}} * 100\ \% \quad (2.6.2)$$

With P_{sat} being the vapour pressure predicted by the Antoine equation at ambient temperature using Equation 2.6.3

$$Log_{10}(Psat) = A - \frac{B}{C + T} \quad (2.6.3)$$

A, B and C are constants for a specific compound. The constants are unit specific. The constants, for water, are given in Table 2.6.1. T is the ambient atmospheric temperature (ISO/CD 12156-1, 2003).

Table 2.6.1: Antoine constants for water, with T in °C and P_{sat} in mmHg (ISO/CD 12156-1, 2003).

A	B	C
8,017352	1705,984	231,864

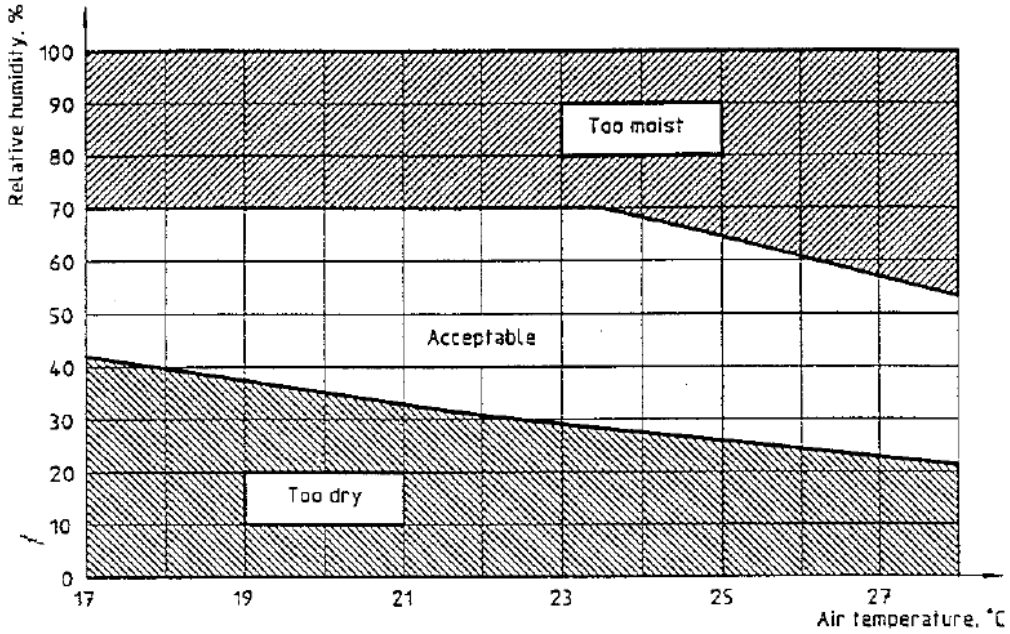

Figure 2.6.1: Allowable ambient test conditions for HFRR. The humidity adjustment of wear scar diameter is valid within the envelope (ISO/CD 12156-1, 2003).

2.6.2 Studies on lubricated contacts

Dissolved oxygen and water are present in all lubricants to some extent. Base fuel type and additive characteristics greatly influence water solubility. Water is a polar molecule and therefore will compete with other surface active species. Hydroxide can form from water's interaction with an oxide (Lancaster 1990). In Table 2.6.2 a summary of studies on the effect of water on lubricated tests is presented. A discussion will follow.

Table 2.6.2: A summary on studies on the effect of increasing humidity on lubricated contacts.

Metal	**Configuration**	**Inc %RH, effect on friction**	**Inc % RH, effect on wear/*SL***	**Additional detail**	**References**
Both: AISI E-52100	Ball on disk (Oscillating)	Not mentioned	Higher (1/6) Lower (2/6) Unclear (3/6)	• 0 – 100% RH • Continuous flow • Ref 2 • Isopar M • Jet fuel & Jet fuel with corrosion inhibitor • Gulf Coast F-76 • California diesel	(Shaver, Giannini, Lacey & Erwin, 1998)
Ball: AISI E-52100 *Cylinder: SAE 8720*	*Ball on cylinder* *(Rotating)*	*Not mentioned*	*SL:* *Unaffected (5/6)* *Increased (1/5)*		
Both: AISI E-52100	Ball on disk (Oscillating)	Not mentioned	Higher	• ≈ 0.8 – 2.4 kPa partial water vapour pressure for all, some RH ranges slightly bigger • Batch tests • Alkanes • Alcohols • Diesels & biodiesels etc.	(Lapuerta, Sánchez-Valdepeñas & Sukjit, 2014).

(Shaver, Giannini, Lacey & Erwin, 1998)

Work done by (Shaver, Giannini, Lacey & Erwin, 1998) suggested that no general correlation exists between water content of different fuels and lubricity behaviour. Six different fuels were tested using a HFRR and BOCLE for wear testing and a SLBOCLE for Scuffing Load (SL) testing. A continuous flow system was employed rather than batch testing specified by each standards. Air of different % RH was bubbled through a fuel holdup for 15 min before testing and during testing. The fuel would then enter the testing area and during testing air of the same RH would pass over the test bath. Only results relevant to % RH effects are reported in Figure 2.6.2 below.

Of the 6 fuels tested, 4 fuels showed a consistent trend of increasing water content with increased RH exposure, therefore only these results will be mentioned:

- Ref 2
- Jet A-1 + DCI 4A (20mg/L)
- Gulf Coast F-76
- California diesel

It is not stated why the other fuels do not show a consistent response in moisture content.

Very different responses are observed for wear testing of different fuels on the HFRR. No general trend was observed, however the following could be seen:

- Ref 2 showed an increase in wear with increased water content reaching a plateau at higher RH similar to its moisture content.
- Jet A1 + DCI 4A showed decreased wear with increasing water content. The wear values were however generally higher with the addition of the corrosion inhibitor.
- Gulf Coast F-76 and California didn't show any noticeable trends.

(Shaver, Giannini, Lacey & Erwin, 1998)

When comparing the wear testing on the HFRR and BOCLE it is clear that the BOCLE has a more limited ability to differentiate between diesel fuel lubricity of different fuels. The only significant response was for Jet A1 which showed a consistent increase in wear with increasing water content. Interestingly there was no response in wear for Jet A1 with the addition of a corrosion inhibitor (DCI 4A) with increasing water content. This is to be expected since the BOCLE is known to test

for corrosive wear (Shaver, Giannini, Lacey & Erwin, 1998). It would seem from this that water content becomes more important, in the absence of corrosion protection.

The SL test on the SLBOCLE did not show any significant response in the SL with changes in water content except for Gulf coast F-76 which showed decreased SL at lower % RH (Shaver, Giannini, Lacey & Erwin, 1998).

Fuel Type	Laboratory Reference	Sulfur† wt%	Viscosity cSt @ 40C	Aromatics*, Mass % Total	Di	Poly
Reference No. 2	AL-20573-F	0.42	3.02	27.8	10.5	1.3
Jet A-1	AL-20844-F	<0.01	1.07	11.0	0.8	0.1
Jet A-1 + DCI 4A	Blend	<0.02	1.07	11.0	0.8	0.1
ISOPAR-M	AL-20239-F	0.0	2.79	0.0	0.0	0.0
California Fuel	AL-23985-F	<0.01	3.84	<2	0.49	0.1
Gold Line	AL-24254-F	0.06	3.47	16.9	4.7	1.1

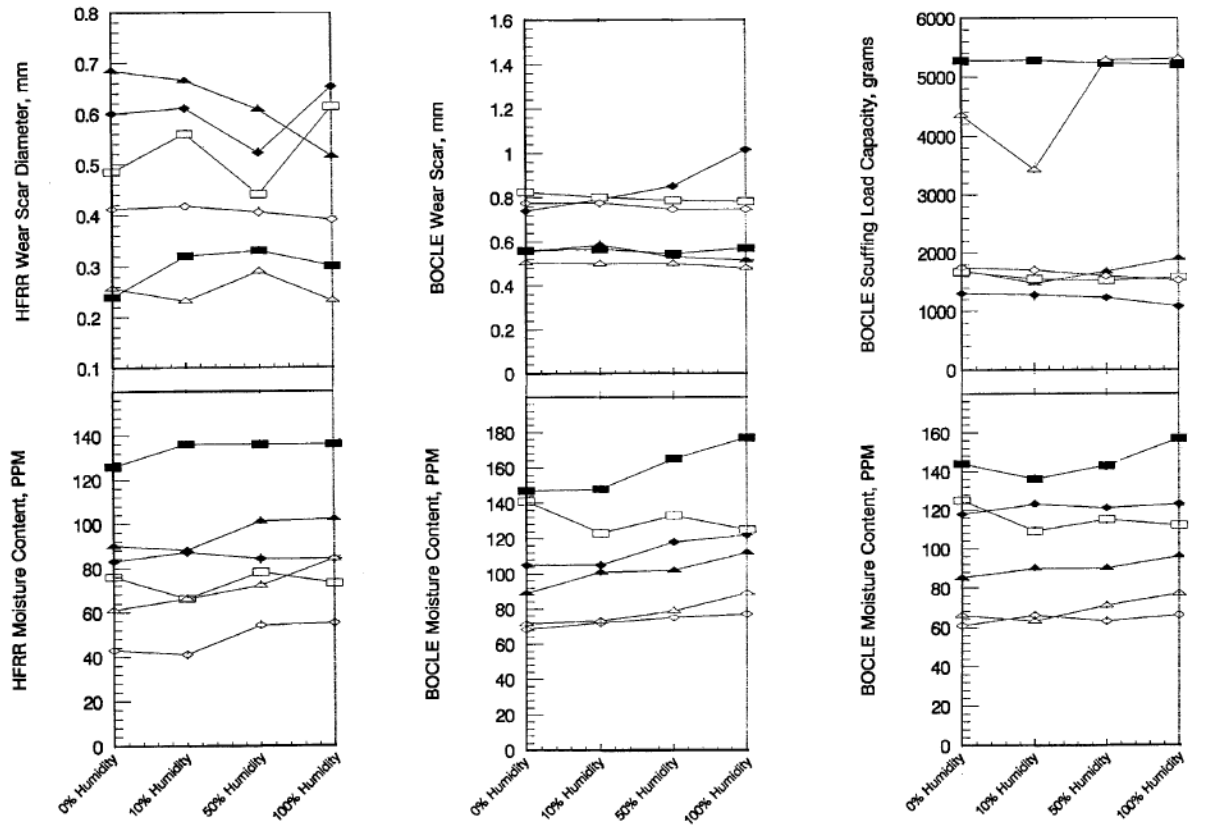

Figure 2.6.2: Effect of humidity pre-treatment on different fuels' water content and lubricity. Adapted from (Shaver, Giannini, Lacey & Erwin, 1998).

Clearly there is disagreement between this data and the ISO adjustment on the HFRR. It is stated why this would be. It should be noted that water content was not very repeatable between different tribo-testers as can be seen in Figure 2.6.2.

(Lapuerta, Sánchez-Valdepeñas & Sukjit, 2014)

An HFRR study by (Lapuerta, Sánchez-Valdepeñas & Sukjit, 2014) was done on a number of fuel fractions to try and identify Humidity Correction Factors (HCF) for each compound. Experimental HCF values for a number of components are presented in Figure 2.6.3. Interestingly enough the HCF value for most of the components are close to the averaged value suggested by ISO 12156 OF 60 µm/kPa. These were batch tests.

Recall that the HCF is the change in MWSD per change of unit water vapour pressure in the surrounding atmosphere. Biodiesel had higher HCF's, likely due to their higher water solubility. Alcohols had lower HCF's. It must be noted that some of these alcohols (ethanol and propanol) evaporated completely making the values for these alcohols irrelevant. No explanation is given for the low value for n-heptane. The hydrophilic nature of the fuel is reported to be less in the following order: bio-diesel & alcohol> paraffinic fuels > diesel fuels.

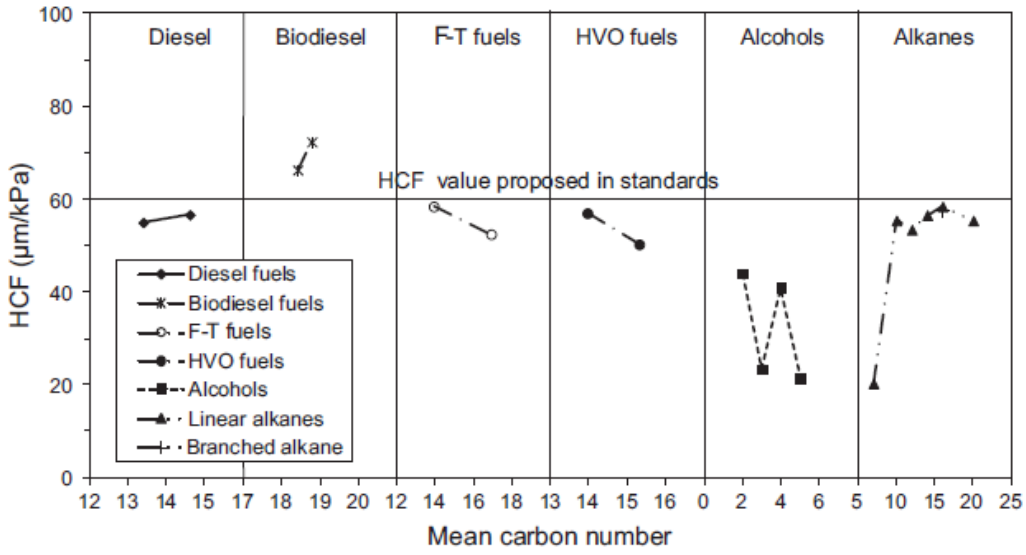

Figure 2.6.3: Humidity correction factors obtained for some fuels (Lapuerta, Sánchez-Valdepeñas & Sukjit, 2014). See source for compositional data of fuels.

In Figure 2.6.4 it can be seen that for all fuels tested, under ASTM test method, that there is a clear increase in MWSD with increasing RH. Bio-diesel performed best due to its fatty acid methyl ester content. Branched alkanes performed similar to their straight chain counterparts. Ethanol and butanol gave large MWSD due to the

contact running dry from evaporation. They therefore are not representative of base fuel lubricity. Increased molecular weight of alkanes resulted in better lubricity.

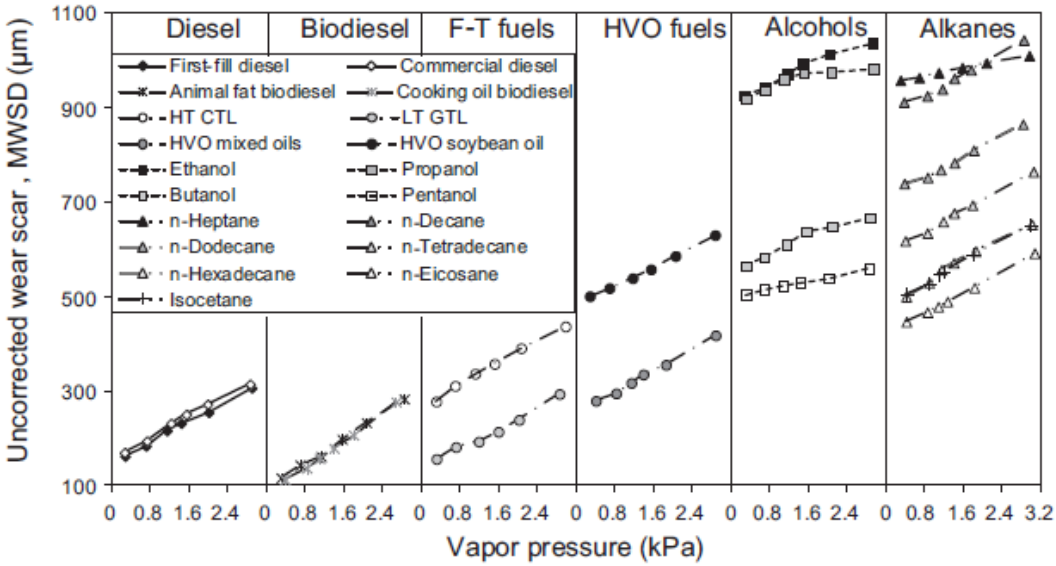

Figure 2.6.4: The effect of Vapour pressure on the lubricity of un-additized fuels (Lapuerta, Sánchez-Valdepeñas & Sukjit, 2014).

A correlation between the MWSD and the fuel's water content was made by (Lapuerta, Sánchez-Valdepeñas & Sukjit, 2014) for 6 fuels as can be seen in Figure 2.6.5. Linear increases of MWSD with water content was observed for al 6 fuels. It is suggested that the hygroscopy of the fuel is responsible for the different HCF values and effects rather than the fuels themselves (Lapuerta, Sánchez-Valdepeñas & Sukjit, 2014).

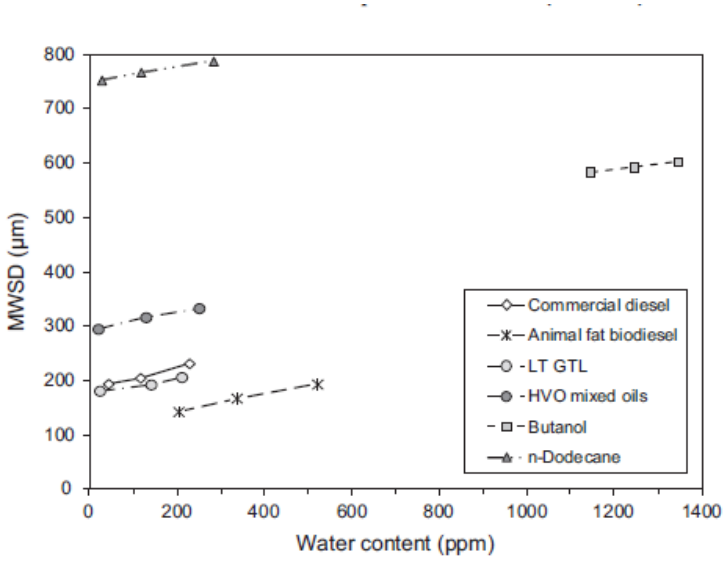

Figure 2.6.5: The effect of water content on fuel lubricity (Lapuerta, Sánchez-Valdepeñas & Sukjit, 2014).

2.6.3 Unlubricated contact

In Table 2.6.3 some relevant studies on the effect of humidity on dry contact wear testing is reported. The trend is opposite from the fuel lubricated contacts presented in Section 2.6.2 by (Lapuerta, Sánchez-Valdepeñas & Sukjit, 2014). This is not surprising since the lubrication protection offer by the lubricated contact is concerned with adsorption and that of the dry contact is concerned with oxide growth protection. Reports summarized by (Lancaster 1990) state that the effect of water on dry wear is mostly seen in the corrosive/oxidative, abrasive and fretting wear regime.

Table 2.6.3: Effect of humidity on unlubricated steel contacts.

Metal	**Configuration**	**Additional detail**	**Reference**
Both: AISI 52100	Ball on flat (Oscillating)	3 - 100 % RH	(Klaffke, 1995)
AISI 1020, 1041 & 1045	Pin on disk (Rotating)	35 - 70 % RH	(Oh, Yeon & Kim 1999)
Disk: AISI 304 Pin: AISI 52100	Pin on disk (Rotating)	20 - 80 % RH	Bregliozzi, *et al*, 2003)
Both: UIC860A steel	Pin on disk (Rotating)	28 – 80 % RH	(Liew, 2005)
Both: Mild steel	Pin on disk (Rotating)	60 - 80 % RH	(Chowdhury & Helali 2007)

The formation of oxidized wear particles was found in all tests. It is suggested that the presence of some of these particles in the contact is influenced by RH and is the reason for the decrease in wear. It is suggested that the wear on the disk is less than on the ball because the disk gets macroscopic exposure to the humid atmosphere (due to the oscillation process) while the ball does not. Many of the abovementioned studies had made reports of subsurface cracking.

2.7 The effects of temperature on lubricity testing of liquid fuel.

This section is not meant to cover every detail of the effects of temperature on every aspect of lubricity testing. The effect of temperature on some phenomena are better situated in previous sections related to that specific phenomena. This section will:

- Go into more detail on aspects not yet covered.
- Consider some experimental results combining these aspects.

2.7.1 Lubricity aspects affected by temperature

The following is a table (Table 2.7.1) of the phenomena affected by temperature and their locations within this document:

Table 2.7.1: Locations in document of major effects of temperature on lubricity behaviour.

	Section
Adsorption and desorption	2.5
Fuel oxidation	2.7 (current)
Solubility and diffusion of surface active species	2.4
Other fuel properties:	
• Viscosity	2.3 & 2.7 (current)
Air to fuel molecular mass transfer	2.4
Wear processes	2.2
Surface oxidation	2.5
Test specimen properties:	
• Mechanical	2.7 (current)
• Electrical (Resistance)	2.5

2.7.2 Flash temperatures

In Section 2.1 on friction it was stated that the true area of contact is much smaller than the apparent area of contact. Multiple asperity peaks make contact. The distance between contacting asperities on a surface is large compared to the true contact area. These points therefore experience very high pressures (Blok, 1937). This results in big temperature flashes that last in the millisecond range. The flashes are mainly confined to the area of contact. There have been reports of these

temperatures reaching 1000 °C (Archard, 1959). The magnitude of these flash temperatures makes their occurrence significant on processes like: lubricant chemistry, adsorption, desorption, surface oxidation, surface deformation, phase changes and wear mechanisms.

Raman spectroscopy was done by (Möller, 2012) on worn stainless steel surfaces from tests run at 60 and 110 °C. He was able to detect both hematite and magnetite on the surfaces. These oxides form only above 400 °C confirming the existence of flash temperatures.

2.7.3 The effect of bulk temperature on the mechanical properties of test specimens

The yield strength and elastic modulus of most metals and alloys decrease with increasing temperature. This decrease in strength leads to parts being more susceptible to deformation and abrasion damage at elevated temperatures. Fluctuating temperatures can affect oxide adhesion if the coefficient of thermal expansion of the oxide and metal differ in magnitude.

Alloy materials are susceptible to both segregation of metals and inward diffusion at elevated temperatures leading to embrittlement of materials. At elevated temperatures mixing of oxides, wear particles, deformed metal and other material on the surface into a glaze or tribo-layer occurs easier due to the softening effect on some substrates. These layers act as friction and wear reducers being reformed continuously (Blau, 2010).

2.7.4 Oxidation of liquid fuel

Oxidation of the liquid base fuel leads to increased viscosity and acidity which is detrimental to most systems. This is of course dependent on exposure time. Base fuel oxidation is affected by:

- Higher temperature leads to more oxidation.
- Type of metal in contact with fuel can either inhibit (e.g. copper) or accelerate oxidation (e.g. iron, iron oxide)
- Higher oxygen content increases oxidation.
- Base fuel type.
- Presence of ionizing radiation largely increases fuel oxidation.

Limited oxidation of the base fuel has however been found to be advantageous as can be seen in Figure 2.7.1 below. The oxidation results in some organic surface active species which improves friction (Stachowiak & Batchelor, 2003: 86,88).

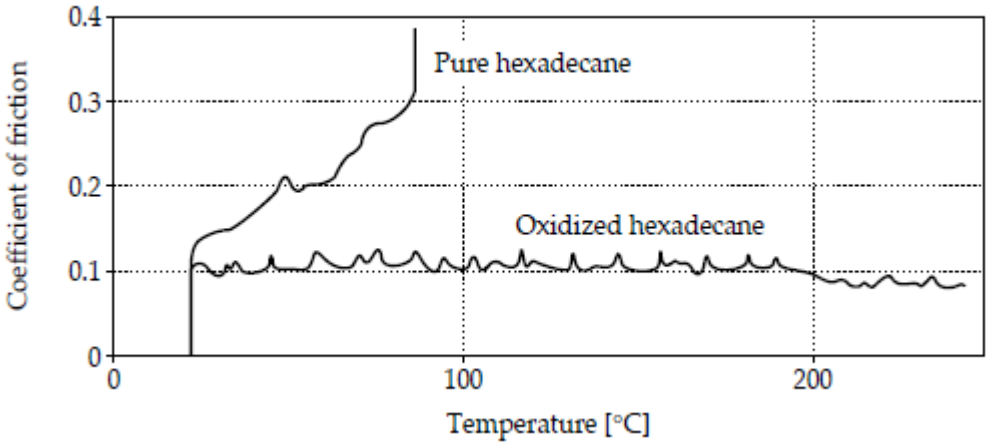

Figure 2.7.1: Friction characteristics of pure and oxidized hexadecane (Stachowiak & Batchelor, 2003: 89).

2.7.5 Effects of temperature on the fuel (liquid) physical properties

Viscosity: The viscosity of liquids decreases with increasing temperature (This trend is opposite to that of gases). Experimental data can be fitted to viscosity temperature equations available in literature (Gohar & Rahnejat, 2012: 85). It is noted however that viscosity plays a minor role in the boundary lubrication regime (See Section 3).

2.7.6 The effect of temperature on liquid fuel - examples

Work done by (Çavdar, 1997) consisting of wear testing using a cylinder on flat (Oscillating) tribo-tester tested a perfluoropolyalkylether. He found increased wear and roughness at 150 °C compared to 50 and 100 °C. Friction was reduced at the start of tests but increased towards the end of tests for 150 °C compared to 50 and 100 °C. The higher friction and wear is ascribed to the negative influence of high temperature on the organic adsorbate film formation.

(Lacey, Gunsel, De La Cruz, & Whalen, 2001) found that wear rate is strongly influenced by both temperature and pressure for fuels that have poor lubricity. They constructed a High-Pressure-High-Frequency-Reciprocating-Rig (HPHFRR). This unit could do tests at higher temperatures and pressures more realistic of fuel injection systems. Higher pressure also allowed them to test more volatile fuels.

A number of different fuels were tested at different temperatures as can be seen in Figure 2.7.2. The good lubricity fuels were insensitive to temperature over the temperature range tested. Low lubricity fuels however showed an increase in wear scar with increasing temperature up to 100 °C and a decrease in wear scar diameter at temperatures beyond this point. The use of higher concentrations of acidic type additives, biodiesel or corrosion inhibitors reduced this observed effect of temperature on wear.

The increase in wear up to 100 °C can be due to desorption of surface active species (Section 2.5.) or increased oxidative wear (Section 2.2.) The decrease in wear can be due to the formation of surface active species, frictional polymers (Section 2.5 & 2.7), evaporation of moisture or some unlisted mechanism. It should be noted that chemisorption operates at a higher temperature than physisorption.

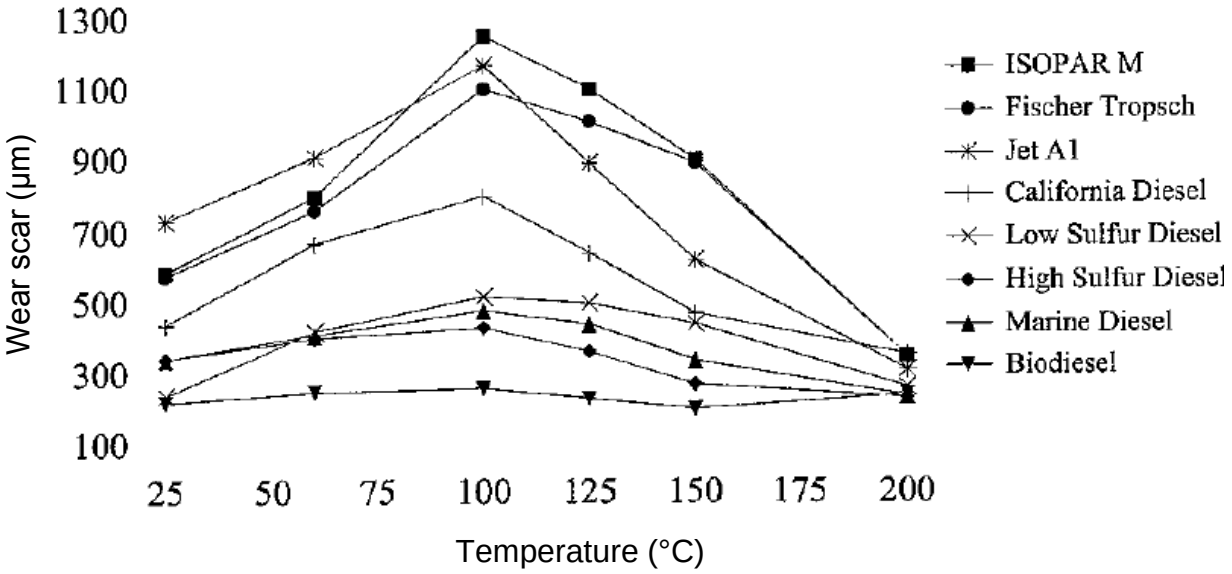

Figure 2.7.2. Wear tests on the HPHFRR at increased temperature for 8 different fuels (Lacey, *et al*, 2001).

2.8 Raman spectroscopy

Raman spectroscopy is an analysis method that utilizes the scattering of Infrared (IR) radiation rather than the absorption thereof. When light is absorbed in the IR region a bond is temporarily promoted to a higher vibrational energy state. The light is subsequently scattered with either the same frequency (Raleigh/elastic scattering) as the incident light or with a different frequency (Raman/inelastic scattering). The scattered light spectrum can be detected and quantified. The difference between these scattered light frequencies is known as the Raman shift and is unique to different bond vibrations. (Young & Lovell, 2011: 355-358)

In Figure 2.8.1 some useful considerations of Raman peaks are presented:

- Bandwidth increases with disorder at the bond scale.
- An asymmetrical peak occurs due to defects or grain boundaries.
- A shift in the band location can be due to temperature differences or grain size stress.

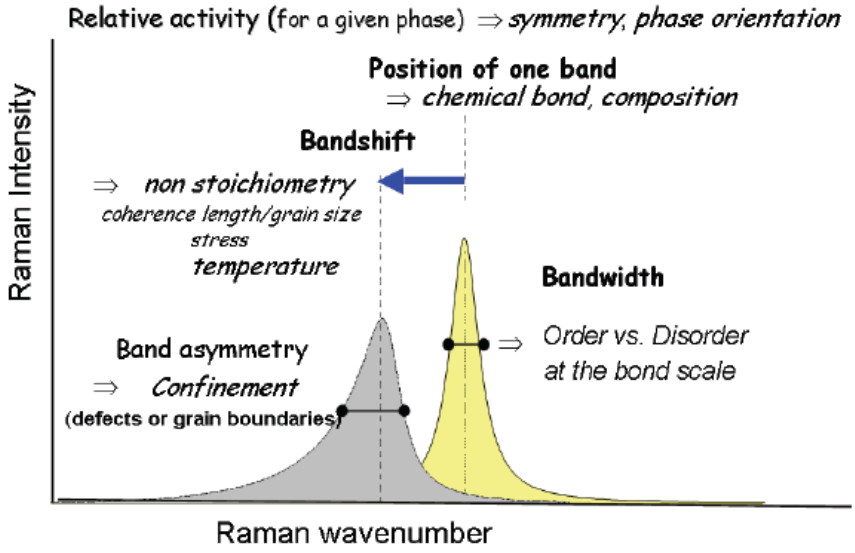

Figure 2.8.1: Raman peak information (Gouadec, *et al*, 2010)

Raman spectroscopy can be used to detect a number of species. The species most relevant to this study are shown in Figure 2.8.2 - 2.8.4. The organic bonds that can be detected using Raman spectroscopy are shown in Figure 2.8.2. Of special interest is amorphous carbon presented in Figure 2.8.3. It is however important to note that due to the detection limits of this method it might not detect organic monolayers.

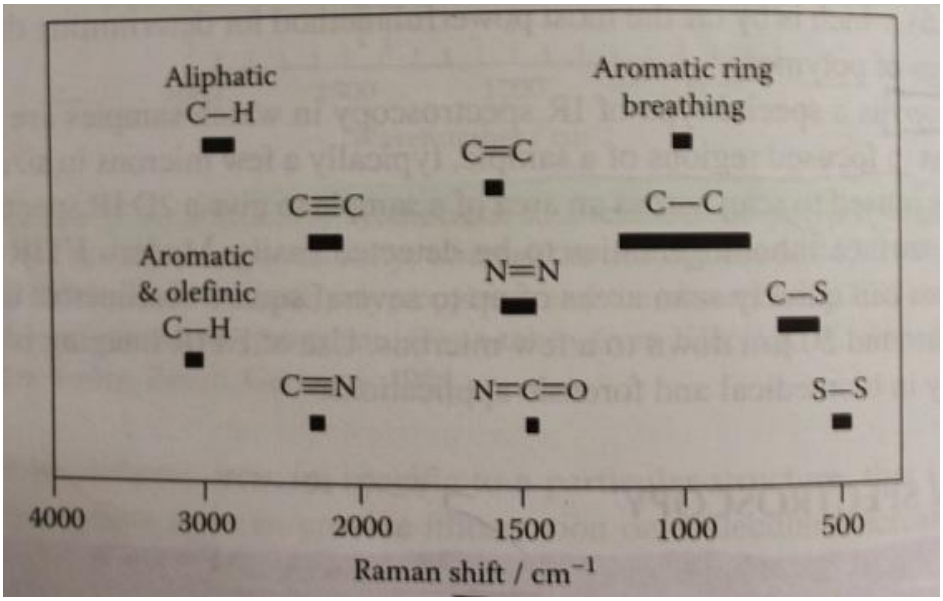

Figure 2.8.2: Raman shift regions for some organic bonds (Young & Lovell, 2011: 356).

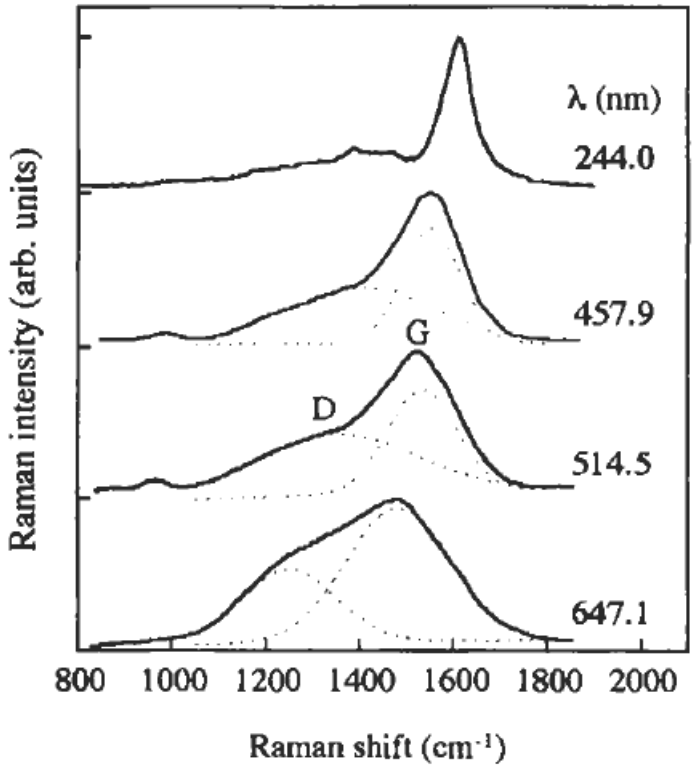

Figure 2.8.3: Raman spectra of amorphous carbon. Each spectrum was obtained with a different laser line as indicated (Yasuda, Inagaki, Kaneko, Endo, Oya & Tanabe, 2003).

In Figure 2.8.4 Raman spectra of common iron oxides and oxyhydroxides are presented since these compounds are most likely to form given the thermodynamic considerations. Typically, good Raman signatures are obtained up to 20 to 40 μm below the surface. (Colomban, 2011: 574).

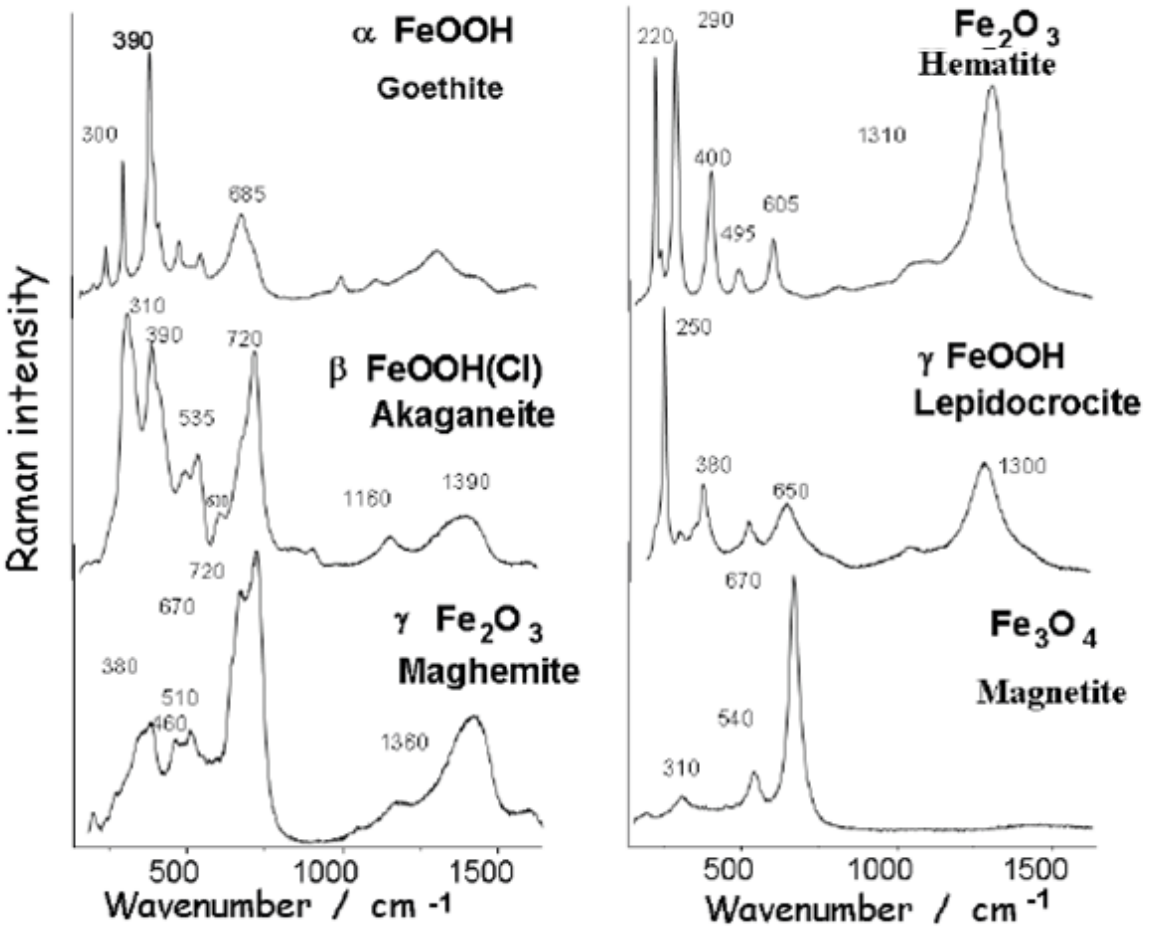

Figure 2.8.4: Raman spectra of the some of the more common iron oxides and oxyhydroxides. Adapted from (Colomban, 2011: 572).

Work done by (Olah, Szirmai &Resofszki, 2005) on the HFRR revealed that magnetite tends to form in poorly lubricated contacts whereas hematite tends to form in well lubricated contacts. This data can be seen in Figure 2.8.5.

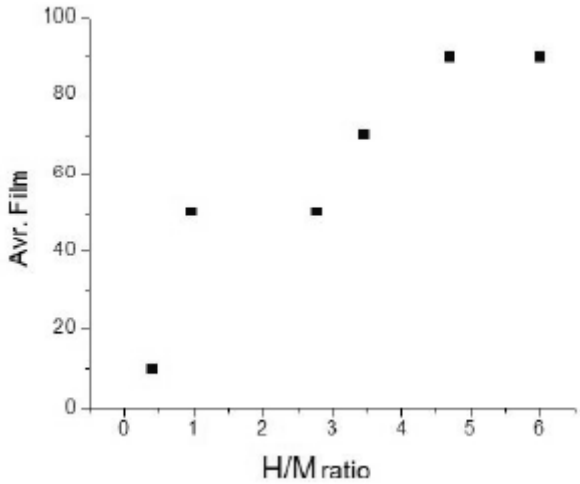

Figure 2.8.5: The ratio of hematite to magnetite as a function of the measured average film (Olah, Szirmai &Resofszki, 2005).

Iron oxides tend to transform into hematite under favourable conditions. According to (Colomban, 2011: 571) magnetite is easily transformed into hematite under a laser beam. Another source considers the conversion of goethite to other species under thermal conditions. In Figure 2.8.6 Raman spectra of a sample of goethite is shown, exposed to different temperatures. At 300° there was a clear conversion to hematite. The peaks indicated in the blue block do however not form part of the generally accepted hematite spectra as can be seen by comparing with Figure 2.8.4. This peak, at 657 cm^{-1} is identified as magnetite by some literature sources. This might seem a valid assumption since magnetite does not contain hydroxyls and has a similar peak at ≈670 cm^{-1}.This however is not magnetite since the peak ratio between magnetite and hematite would mean that there was 2.7 times more magnetite than hematite, This is not true since the material was too weakly magnetic. This peak can also occur from hematite weathering (de Faria & Lopes, 2007). According to (Gialanella, Girardi, Ischia , Lonardelli, Mattarelli & Montagna, 2010) this peak is due to defects that occur to a lesser extent at higher temperatures. It should be noted that it is due to more than one type of defect.

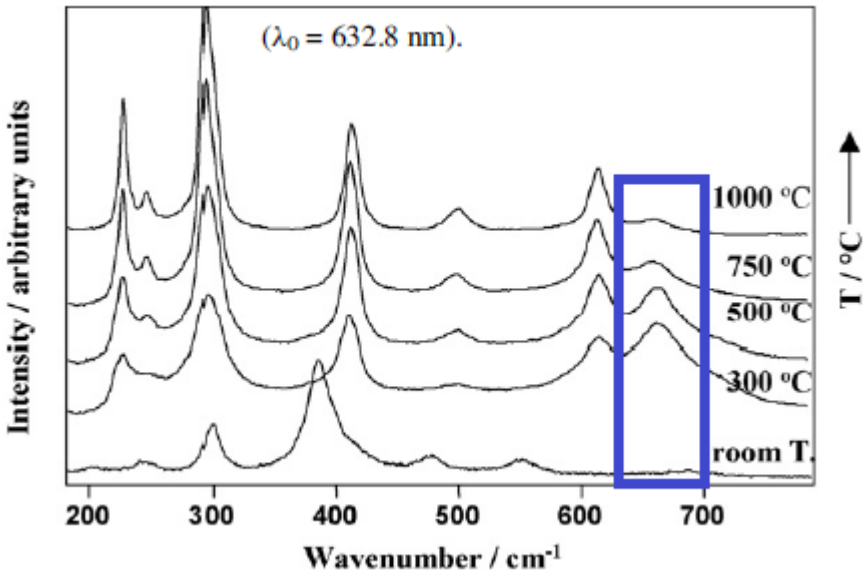

Figure 2.8.6: Raman spectra of a goethite sample transforming into hematite due to temperature. (de Faria & Lopes, 2007).

It was furthermore noted with a smaller temperature range that hematite starts to form between 250 - 300 °C from goethite.

Raman spectroscopy of mixtures of iron oxides and iron oxyhydroxides can be analyzed, but it should be noted that relative Raman intensity differs for these compounds as follows: lepidocrocite (1) > wustite, hematite, goethite, ferrihydrites, ferroxyhite (~1/3) > akaganeite (~1/4) >> magnetite, maghemite (~1/10). (Colomban, 2011: 571).

3. Experimental

Wear and seizure load testing will be limited to sliding contacts in the mixed to boundary lubrication regime. This limitation is imposed due to the in-field application requirements of the fuel. The lubrication requirements of fuels are mostly concerned with fuel distribution systems. An understanding of the effect of humidity on fuel lubricity testing is required for the mentioned regimes. An investigation into the following aspects will increase the understanding of the effect of water:

- Parameters that could affect water transfer from humid air into the fuel:
  - Fuel sample storage conditions.
  - Ambient exposure conditions.
  - The kinetics of water transfer into the fuel. Diffusion models and experimental studies will be utilized.
  - Temperature: Solubility limits in hydrocarbons are known to be affected by temperature. Furthermore the heating of a sample up to operating conditions is likely to change the water content of the fuel.
  - Lubricity additives are known to have polar functional groups in segments of the molecule. It could be that if the concentration of these species is high enough that they will enhance soluble water content.

- Wear testing of a fuel under the effects of soluble water content: Wear testing of fuel samples will be performed on the HFRR supplied by PCS Instruments utilizing different ambient RH conditions. Measurements to be utilized include:
  - Wear scar size and appearance.
  - Wear debris appearance. Great care will be taken not to disturb debris after a test.
  - Coefficient of friction.
  - Electrical contact resistance.

- Seizure load testing of a fuel under the effects of soluble water content: Seizure load testing will be performed on the SRV® 4 supplied by Optimol Instruments. Measurements to be utilized include:
  - Seizure load.
  - Coefficient of friction.
  - Height displacement measurement.
  - Stroke deviation.

- How significant the effect of soluble water content is on lubricity testing of fuel, at different lubricity additive concentration: Literature studied indicated that water

interferes with adsorption mechanisms. Therefore the effect of additive concentration on lubricity testing is likely to be influenced by the effects of water.

- How the presence of water alters both the chemical and physical nature of the wear surface: Surface analysis of iron reaction products in the tribo-contact will be done using Raman spectroscopy. The analysis is done to determine if detectable amounts of different iron reaction products formed in relation to test conditions.

3.1. Apparatus

Only the main apparatus will be listed here, less specific apparatus is presented in Appendix D.

3.1.1. Water content determination of fuel

The water content in the n-hexadecane fuel samples will be measured using a 787 Karl Fischer Titrino supplied by Metrohm. Relevant parameters are summarized in Table 3.1.1. LipoSolver CM will be used as a solvent due to the limited solvation of n-hexadecane in the standard Karl Fischer solvent (methanol). The ratio of solvent to sample is different depending on sample identity and is typically optimized to get repeatable results. Too much solvent is costly whilst not enough solvent will result in a fatty layer covering the detection probe. This layer leads to highly erroneous results. A ratio of 60 mL of solvent per 5 mL sample was found to be sufficient.

Table 3.1.1: Specifications of titrator utilized for water determination.

Type	Volumetric titrator
Detectable range	1-100 mg
Sample size	5 - 7 mL (depending on test type)
Titration vessel size	90 mL
Karl Fischer reagent	HYDRANAL®-Composite 5[a]
Solvent	HYDRANAL®-LipoSolver CM[b]
Standard used	ASTM D1744

[a] supplied by Sigma Aldrich lot # sSZBC2820V, [b] supplied by Sigma Aldrich lot # SZBD0630V & SZBD1510V.

3.1.2. Tribo-testers

The main purpose of an accelerated wear test is to measure a detectable amount of wear within a reasonable time. The method of wear detection typically employed involves surface inspection of some form. This limits the configuration of the wear specimens since the wear has to be locally concentrated to be detectable. Therefore wear is easier detectable on a surface that is continuously in contact compared to a surface that is periodically in contact (Zhang, Yamaguchi & Spikes, 2013). With all wear equipment used in this study, wear quantities are measured on a fixed oscillating ball specimen which is in continuous contact with a stationary disk specimen. The disk wear area is only periodically in contact with the ball due to the oscillation. Therefore wear measurements are made on the ball.

Although the localization of wear using a ball specimen allows the measurement of wear, it also results in a decrease in the pressure experienced on the contact. This is due to the continuous increase in surface area of the contact under a constant load. This means that the wear rate determined would be an average over the test period rather than a constant. The most significant changes in contact area occurs during the run-in period where after the wear rate reaches a more constant value (Zhang, Yamaguchi & Spikes, 2013).

The steady state wear volume is given by Equation 3.1.1 below and is known as the Archard wear equation. In this equation V is the wear volume, W is the normal load, H_s is the hardness of the softer surface, S is the total sliding distance and K_A is a constant (Williams, 1994). Equation 3.1.1 would suggest that the volume of wear is directly proportional to the sliding distance if the load and hardness remains constant. If the sliding speed therefore remains constant a linear increase in wear volume should be observed with sliding distance. Under these assumptions ($Ka\frac{w}{Hs}$) could be regarded as a wear constant. It is however uncertain how realistic the assumption is that the hardness remains a constant.

$$V = K_A \frac{W}{H_s} S_D \qquad (3.1.1)$$

Wear volume is not easily measured due to surface irregularities on the wear surfaces and surface angles. It is more general to measure the resulting area of wear since this is can be done with less effort, using a microscope. This is normal

practice for most test standards. Due to the geometry of the ball specimen the relationship between the wear scar and ball is however not linear as can be seen in Figure 3.1.1 which was constructed assuming perfectly flat wear scars.

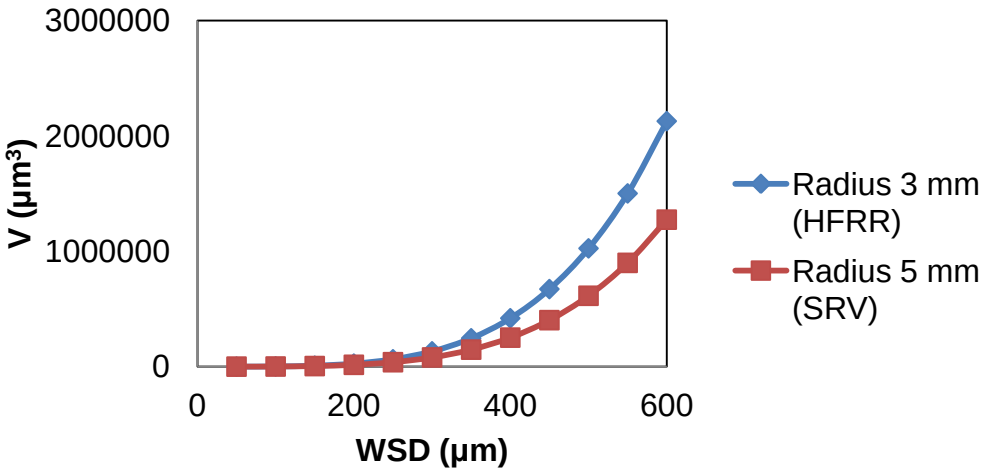

Figure 3.1.1. The relationship between wear scar and wear volume for a perfectly flat wear scar.

A correlation has however unexpectedly been obtained between the HFRR wear scar size (2D) and the failure of diesel distribution pumps as can be seen in Figure 3.1.2. This will be discussed in Section 4.2. of the results.

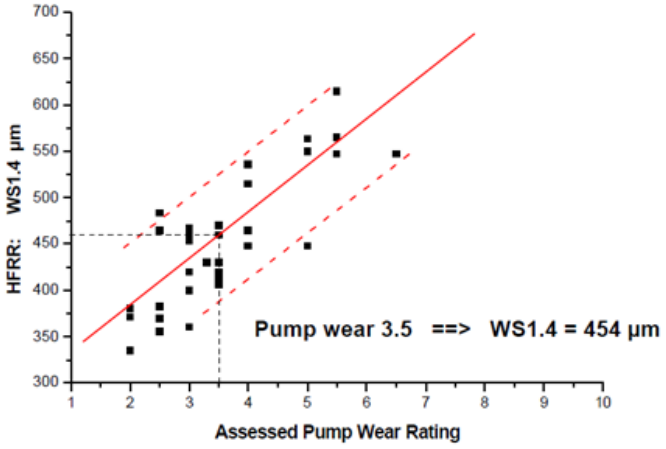

Figure 3.1.2: The correlation between pump wear rating and HFRR WSD1.4 (Meyer & Livingston, 2003) Do note that a pump rating of 3,5 was deemed acceptable and this led to a HFRR WSD1.4 of 460 µm becoming the maximum allowable size.

In seizure load testing the load on the tribo-contact is continuously increased until there is a sudden and significant rise in the friction coefficient. The test load, at the onset of the rise in friction coefficient, is known as the seizure load. This is a severe test that is likely to result in adhesion of the contact upon film breakthrough. Since different mediums will break through at different loads and therefore also sliding distances, it is of no purpose to compare wear volumes or scars as can be seen when reconsidering Equation 3.1.1.

The operating limits of the tribo-testers that will be used is summarised in Table 3.1.2. The composition of the test specimens utilized in this study are summarized in Table 3.1.3. A discussion of each test method is to follow.

Table 3.1.2: Fuel tribo-testers to be utilized (Sliding contact).

Unit	**HFRR**	**SRV**
Hardware		
Configuration	Ball on disk, Oscillation	Ball on disk, Oscillation
Model	HFRR	SRV ® 4
Ball	Ø 6 mm AISI E-52100	Ø 10 mm AISI -52100
Disk	Ø 10 mm AISI E-52100 3 mm thick	Ø 24 mm AISI -52100 7.8 mm thick
Tests		
Test type	Wear	Seizure load
ASTM/ISO	ISO/CD 12156-1, ASTM D6079	In-house
Test conditions		
Load applied	10 N	50 - 2000 N (50N/min) Starting at 50 N.
Stroke length	1 mm	1 mm
Frequency (speed)	50 Hz	50 Hz
Temperature	60 & 80 °C	80 °C
RH range[a]	15; 50 & 75 % RH @ 20 - 25 °C	15; 50 & 75 % RH @ 20 - 25 °C
Fuel volume	2 mL batch bath	Cont. flow: 1 drop/ 3 sec Residence time ≈ 120 sec
Test time	75 min	Until failure
	(PCS instruments, *sa*) (ISO, 2003)	(Optimol Instruments, 2008)

[a] The water content will be presented as water vapour pressure to allow a linear comparison since RH does not increase linearly with increasing water conent.

Table 3.1.3: Steel composition of test specimens.

Composition Species	**AISI E-52100 Mass %**
Fe	96.5 - 97.32
Cr	1.3 - 1.6
C	0.98 - 1.1
Mn	0.25 - 0.45
Si	0.15 - 0.3
S	0.025 max
P	0.025 max
Ni	
Mo	
Relevant physical properties	
Bulk modulus	140 GPa
Hardness (Rockwell)	62 – 66
Modulus of elasticity	210 GPa
Shear modulus	80 GPa
Thermal conductivity	46.6 W/mK
Heat Capacity	0.475 kJ/kgK (Kipp 2010)

3.1.2.1 Wear testing on the HFRR (High Frequency Reciprocating Rig)

In Figure 3.1.3 the basic operating principle of the HFRR is illustrated. A non-rotating test ball is oscillated under a constant load, at constant stroke and frequency, against a disk immersed in a 2 mL sample of fuel for 75 min. This is done using an electromagnetic vibrator. The disk is held stationary in a bath that contains the fuel. The test disk and ball form the tribo-contact which is fully submerged in the fuel sample. The bath temperature is controlled via a heating block.

Both the friction coefficient and temperature are recorded during the test. A contact resistance is also measured between the ball and contacting disk during the test and used as an indication of any film formation that would lead to an increase in the contact resistance. After the test is complete, the generated wear scar is measured under an optical microscope. The wear scar is used as the main indication of lubricity behaviour. Smaller wear scars diameters (WSD) result from better lubricity properties. Under ISO 12156 a WSD smaller than 460 µm is deemed acceptable whilst under ASTM D6079 a WSD smaller than 520 µm is acceptable.

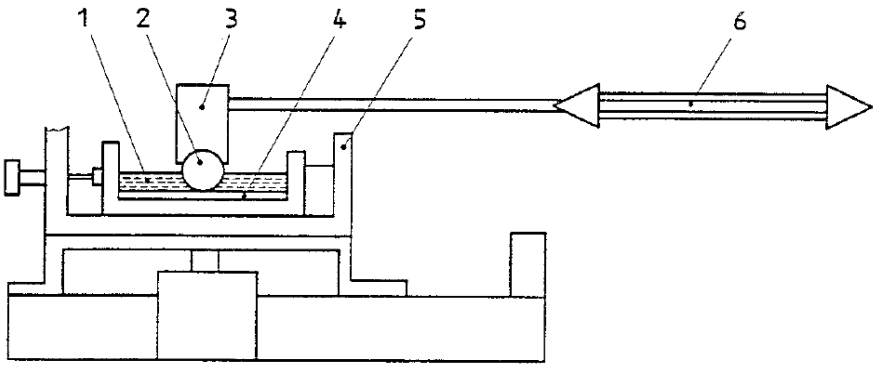

Key
1 Fuel bath (reservoir)
2 Test ball
3 Applied load
4 Test plate
5 Heating bath
6 Oscillating motion

Figure 3.1.3: The HFRR setup (ISO 12156).

Work done by (Marais, 2010) revealed the nature of wear testing on the HFRR. This was done by interrupting tests, using a model diesel fuel, and analyzing test specimens over the test period. It was summarized that the test evaluates the ability of the fuel to prevent oxidative wear under a constant load. The wear regimes observed in order:

- Mainly adhesive (initially).
- Milder abrasive and fatigue.
- Transitional between the above.

There were a number of reports where diesel fuels had a WSD smaller than that required by the ISO standard (460 µm), but still resulted in failure. It was noticed by (Olah, Szirmai &Resofszki, 2005) that the wear contact surface contained additional information that was not required by any test standards. It was observed that wear scar appearance on the HFRR could be classified between two extremely different appearances:

- A polishing of the surface which results in minimal material losses. Some indication of a rounded surface is maintained over the wear scar area.
- Material losses with grooves and clear edges that will lead to mechanical failure. The general surface is much less rounded over the wear scar.

A visual rating, also known as the complementary rating, was proposed by (Olah, *et al*, 2005) based on their findings as a guide on surface appearance. This rating is presented in Figure 3.1.4. Lower rating values are more favourable, whereas a high rating should receive further consideration since these ratings indicate severe wear. This rating system is obviously very subjective to the user. The method helps give a semi-quantative indication of the surface appearance when comparing several samples.

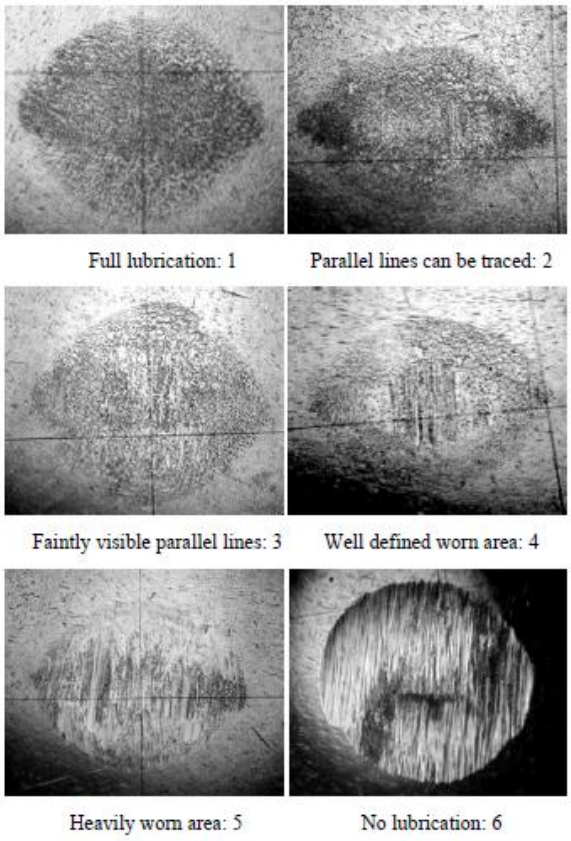

Figure 3.1.4: The visual rating scale proposed by (Olah, Szirmai &Resofszki, 2005).

3.1.2.2 Seizure load testing on the SRV®4

SRV is a German acronym for reciprocating, friction and wear. Although the SRV is a very versatile piece of equipment its application to diesel fuel lubricity testing is mainly limited to the seizure load testing method used at the University of Pretoria.

In Figure 3.1.5 the basic operating principle of the SRV is shown. A non-rotating ball is held in the triangular top specimen holder. The ball is oscillated, at a constant

frequency, against the disk held firmly in place by the lower specimen holder. In a seizure load test the test load is continuously increased until seizure of the contact occurs. Seizure is indicated by a sudden increase in the friction coefficient. The disk is secured by means of a slot and screw on the heating block, which is used to maintain the bulk temperature of the contact at the desired temperature.

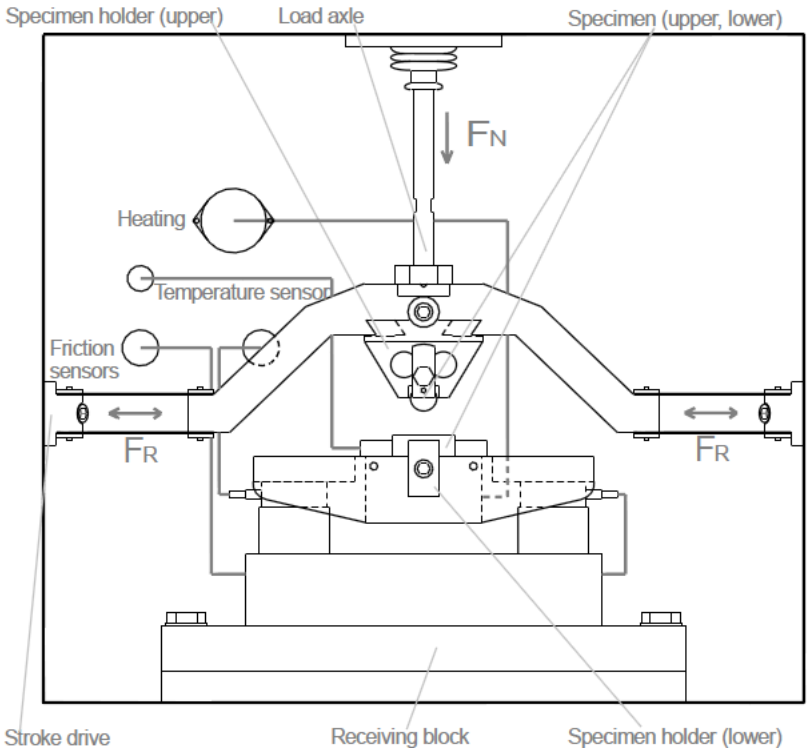

Figure 3.1.5: SRV Setup (Optimol Instruments, 2008 :45)

A fundamental study on the seizure load testing of a model diesel fuel was performed on the SRV by (Möller, 2012). The test was summarized as a test that evaluates the ability of the fuel to prevent adhesive wear at high normal loads by noting that the specimens are constantly driven to the adhesive wear regime. It was observed that upon test initiation to completion the wear regimes changed as follows:

- Upon test initiation
  - Adhesive wear (for a short time)
  - Transition to milder forms. (for a very short time)
- Bulk duration of tests
  - Mild oxidative-, fatigue- and abrasive wear.
- Towards completion
  - Adhesive wear, which leads to seizure.

The onset of failure occurs due to the desorption of the lubricity species at high flash temperatures due to the higher contact loads. This subsequently results in an increase in the rate of oxide removal which begins to exceed the rate of oxide growth. The oxide growth rate also increases due to the higher temperatures but not to a sufficient extent. As the oxide is removed from the two surfaces nascent metal of the two surfaces comes into contact resulting in adhesion (Bowman & Stachowiak, 1996).

3.1.3 Humidifier

In Figure 3.1.6.a the humidity-control-setup for the HFRR is illustrated. The purpose of this setup is to maintain a constant water content in fuel samples by manually controlling the humidity of the atmosphere in test chamber.

Compressed air is passed through a moisture trap and a particulate filter. This is to ensure that the air supply is clean. The air is then passed to two columns at 200 - 250 kPa. The air can be bubbled through a column of distilled water to increase the water content, or passed through a column of self-indicating SiO_2 drying medium to lower the water content. By controlling the ratio of air flow between the columns the required water content can be obtained. The conditioned air is then passed to the test chamber that is sealed off except for an outlet of similar size to the inlet. The chamber contains a humidity sensor.

A part of the conditioned air flow can be diverted to an aeration stone to pre-aerate samples to the desired water content. This is done prior to the test.

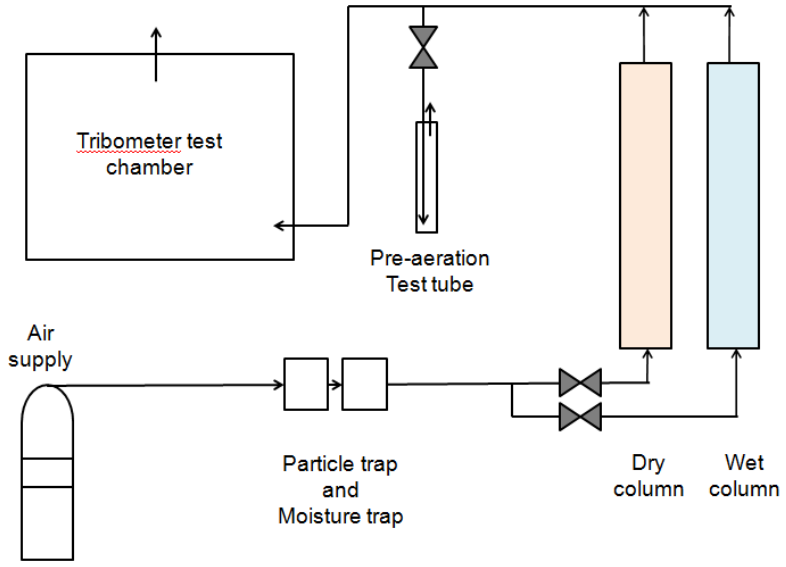

Figure 3.1.6.a: Humidity control of the HFRR test.

The SRV setup is different to the HFRR setup in that it uses a continuous flow of fuel to the contact unlike the batch test of the HFRR. The humidity-control-setup for the SRV is similar to that of the HFRR and illustrated in Figure 3.1.6.b. The fuel is still aerated before the test similar to the HFRR batch test. After pre-aeration it is manually passed into a fuel hold-up cell from where the flow of fuel (dotted line) is regulated to the tribo-contact.

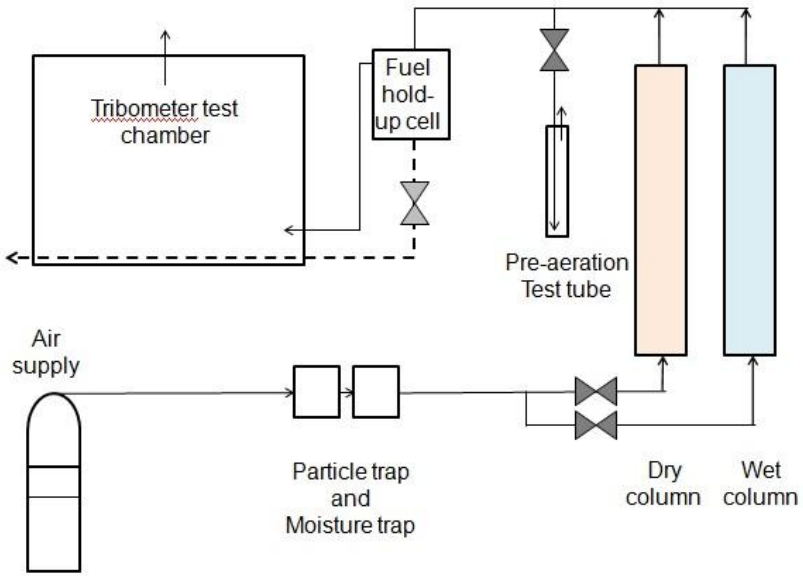

Figure 3.1.6.b: Humidity control of the seizure load (SRV) test.

The humidity control setup is altered only in that, before the conditioned air enters the test chamber, it is first passed into the fuel hold-up cell. The flow of air is directed above the fuel level within the hold-up cell to maintain the atmosphere at the same conditions that the fuel was aerated at. The air then passes from the fuel hold-up cell into the test chamber separately from the fuel supply line.

3.1.4 Raman microscope

Raman spectroscopy will be used to investigate if the amount of water present has any detectable effect on the bulk oxides formed during fuel lubricity testing on the HFRR and SRV. Wear areas exposed to the lowest and highest fuel water content, during lubricity testing, will be analyzed at all lubricity levels.

Top and bottom specimens will be very lightly rinsed with 0.2 mL hexane to remove the bulk of the additised n-hexadecane after wear and seizure load tests. Care will be taken not to disturb wear debris on the surface since debris consists of a lot of reaction products. The hexane evaporates within seconds after rinsing. The sample will then be placed in a desiccator and taken for Raman analysis. It is placed in the desiccator to prevent any further reaction of oxides or oxyhydroxides with moisture in the air. In Table 3.1.4 specific information of the Raman microscope utilized is provided.

Table 3.1.4: Raman microscope utilized.

Model:	T64000 micro-raman spectrometer.
Supplier	HORIBA Scientific, Jobin Yvon Technology (Villeneuve d'Ascq, France)
Laser System	Coherent Innova· 70C Series Ion Laser System.
Line	514.5 nm
Objective	50 x (Olympus optical microscope)
Spectrometer	- Integrated triple spectrometer. - Double subtractive mode (to reject Rayleigh scattering) - Light dispersed onto a liquid nitrogen cooled Symphony® charge coupled device (CCD) detector.
Calibration	Silicon phonon mode at 520 cm^{-1}

Note that more information on Raman spectoscopy was presented in Section 2.8.

3.2 Planning and Method

3.2.1 The effect of RH on water content - Determination

Water content determination is done to:

- To determine how fast changes occur in the water content of the fuel sample due to exposure to air with different RH.
- To determine how the lubricity testing temperature and lubricity additisation levels affect the water content of the test fuel.
- To determine how water content changes during lubricity testing.

Fuel samples will be exposed to the different conditions mentioned to determine the effects thereof. Samples will be placed in the HFRR bath and in a sealed chamber of which the humidity and/or temperature can be altered. Additionally samples will also

be aerated with an aeration stone to see what equilibrium water content is obtained under different temperatures using air of different RH.

Samples will be taken from a sealed source, of which the water content will be monitored daily to ensure that moisture content thereof is unchanged.

Mass transfer into a liquid sample occurs through the surface interface between the gas and liquid phase. It is important that if water content of samples, exposed to different conditions, are to be compared that:

- The interface surface area should be the same. A larger surface area will result in higher mass transfer of water.
- The volume of the samples should be the same. A larger volume with the same interface surface area will result in a lower concentration at the same humidity. The larger volume reduces the effect of mass transfer resulting in a lower average concentration.
- Temperature and pressure need to be fixed since these parameters directly affects mass transfer.
- If samples are agitated it should be in a similar way to ensure mass transfer conditions are consistent. The air flow rates through different samples needs to be the same.

3.2.2 Ensuring water transfer is from air only.

Because of the low solubility levels of soluble polar water in non-polar n-hexadecane, contamination with other sources of water can have large effects. It is very important that care must be taken in the handling of apparatus and utensils that come into direct contact with samples.

Addition of a water phase to an organic diesel phase has shown to actually decrease the water content of the organic phase in an extractive manner in work done by (Shaver, Giannini, Lacey & Erwin, 1998). It is therefore important to not expose samples to any form of bulk water. This will alter water content significantly.

Exposure to other solvents like hexane, heptane or acetone should be avoided. Water solubility in these solvents are significantly different from that in n-hexadecane and can therefore alter the water content of n-hexadecane easily:

- the cleaning of test specimens, screws, specimen holders, baths and retaining rings should be placed in an oven after the acetone cleaning step. In this study they will be placed in an oven at 60 °C for 25 min after cleaning and fixing of specimens into holders.
- Pipettes will be flushed 3 times directly after use with hexane. Pipettes used to transfer fuel samples should not contain residue hexane or heptane after cleaning. Pipettes were kept in an oven at 60 °C for 60 min after any bulk solvent was removed from the tip. The longer duration will be used since a pipette has a more confined shape compared to other items.

Since the SRV uses a continuous flow of fuel system, extra care is required. After a test, the fuel hold-up cell is rinsed 3 times with hexane. Complete drainage between tests is needed. The whole cell is not filled with hexane, but rather just rinsed on the inside walls. After this the cell is closed at the top and the humidifier turned on. The fuel line is left in the completely open position. The compressed conditioned air can now dry the fuel flow system for an hour whilst cleaning and preparing of ball and disk specimens occurs. Sample holders should be kept sealed between sampling.

3.2.3 Fuel matrix

The effect of humidity on the lubricity response of liquid fuel were investigated by and summarized by (Shaver, Giannini, Lacey & Erwin, 1998) and (Davenport, sa) respectively. In both these studies various fuels were tested. The severity, and in rarer cases even the effect, of water were shown to be unique to the fuel tested. No work or explanation was presented to clarify this issue. More uniform results were obtained by (Lapuerta, Sánchez-Valdepeñas & Sukjit, 2014) by using single organic compounds without additisation. It is for these reasons that this study is limited to a single base fuel with a single lubricity additive. Different levels of additive will be tested. This should reduce uncertainty in interpreting results.

In Figure 3.2.1 and 3.2.2 the effect of palmitic acid concentration , a lubricity additive, on wear (HFRR) and seizure load (SRV) testing is shown. The base fuel was n-hexadecane (Marais, 2010: 73) and (Möller, 2012: 114).

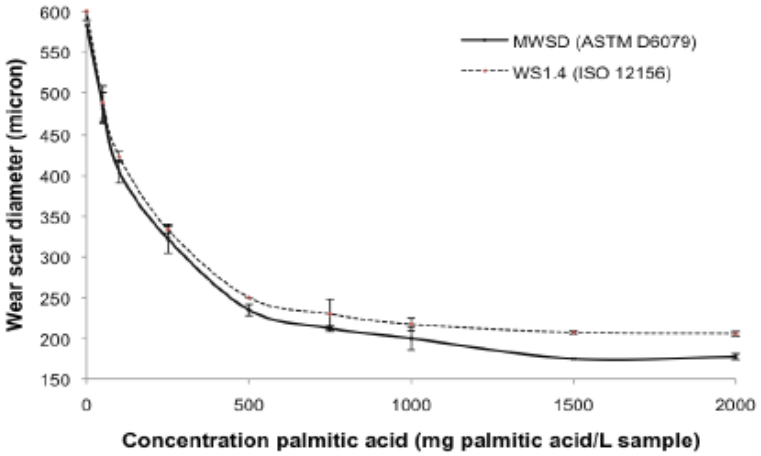

Figure 3.2.1: Effect of palmitic acid concentration on HFRR wear results at 60 °C (Marais, 2010: 73)

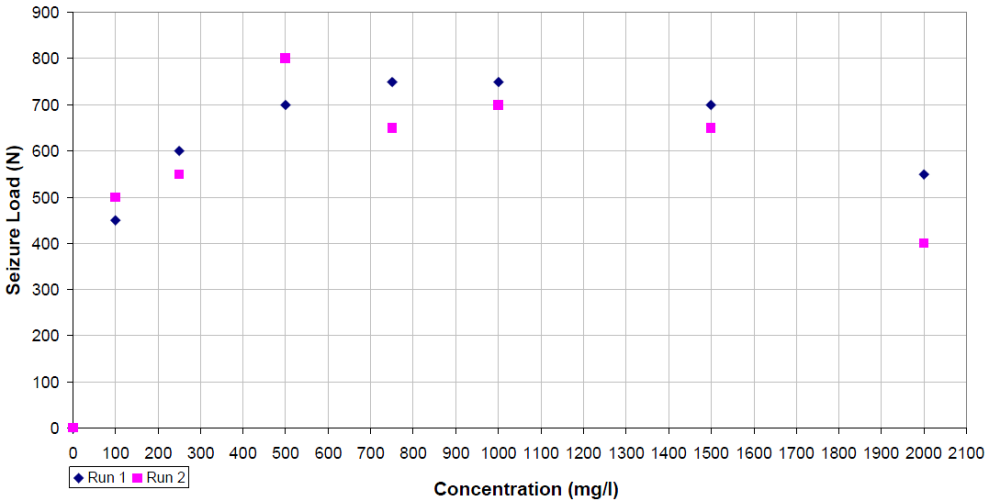

Figure 3.2.2: Effect of palmitic acid concentration on SRV LCC results at 110 °C (Möller, 2012: 114).

Since adsorption is very sensitive to the concentration of the adsorbing species, it is suspected that the effect of water on lubricity will be differently affected at different concentrations. In Figure 3.2.1 and 3.2.2. there appears to be 3 distinct wear regimes for both figures. For this study three levels of lubricity additive concentration will be tested. The concentrations were chosen to represent poor lubricity, good lubricity and over addisation. The details on the fuel matrix to be tested is presented in Table 3.2.1. The additive concentration levels differ for HFRR and SRV.

Table 3.2.1: Fuel matrix to be tested.

Base fuel	n-hexadecane (≥ 99%) [a]
Lubricity additive	Palmitic acid [b]
HFRR Additive levels	100, 250, 2000 ppm
SRV Additive levels	100, 500, 2000 ppm

[a] supplied by Sigma Aldrich, Lot # STB C8091, [b] supplied my Merck Lot/charge: S4963208007.

Lubricity testing should and will be from the same batch of fuel. This will be done, since small differences in palmitic acid (PA) concentration between different batches could possibly lead to erroneous data or inconsistent trends. This occurs because the effect of soluble water is known to be an order of magnitude smaller than that of lubricity additive concentration.

Great attention will be given to cleanliness of the whole system, especially in working between samples of different PA concentrations. Less than one drop of 2000 ppm PA is enough to alter lubricity behaviour of a 100 ppm sample significantly. The aeration stone should be cleaned with hexane between different concentrations and exposed to a similar sample at least once before the first aeration.

3.2.4 Choice of lubricity test conditions

Temperature

ASTM 6079 and ISO/CD 12156-1 requires that wear testing on the HFRR be done at 60 °C. It is however known that temperatures in a common-rail diesel injection system could exceeds this value (MAN Diesel & Turbo, *sa*). Tests will therefore be done at both 60 °C and 80 °C. The choice of 80 °C is to remain below the boiling point of water to eliminate vapour liquid equilibrium considerations at this point.

The in-house diesel seizure load test, at the University of Pretoria, is normally operated at 110 °C to simulate conditions in a diesel distribution system. To eliminate vapour-liquid equilibrium considerations at this point the tests will be operated at 80 °C. Seizure load tests will not be done at 60 °C since differentiation of fuel lubricity is smaller at this temperature due to reduced oxide growth.

Relative Humidity

A choice of three data points, between 0-100% RH at ambient temperature, is needed to confirm a trend:

- At values close to 100% RH condensation is likely if the temperature drops. The likelihood of this is increased due to the non-linearity of %RH with changes in water mole fraction. A conservatives value of 75% is therefore chosen to prevent condensation.
- A value of 50% RH at ambient temperature is chosen since this value is within the allowable humidity range to allow the ISO correction factor to be applied. This was discussed in Section 2.6. The value of 50% is close to typical conditions in the laboratory.
- A value of 15% RH at ambient temperature is selected. This is 5% above the built humidifier's lowest capability of 10%. This is chosen to still allow some form of control should the supply air fluctuate.

These values will be transformed to standard water vapour pressure to allow easier comparison.

3.2.5 Humidity control

HFRR

A 7 mL Sample will be pre-aerated at 3L/min for 20 min at the RH that the chamber will be maintained at during the test. This is to ensure that the test starts with a unique water content equilibrated to the exposed RH. This is based on preliminary experimental results from Section 4.1.

The airflow is adjusted beforehand to ensure the chamber is at the required RH. The top and bottom specimens are then fixed into the chamber, before fuel is aerated. Fixing the top and bottom specimens obviously changes RH since the chamber is opened to do this. As soon as Humidity is again within 5% of the desired value, aeration of fuel is started. After 20 min 2 mL of the fuel sample is transferred to the bath with a pipette through a small air outlet. The test is then started.

SRV

A 40 mL sample will be pre-aerated at 4 L/min for 30 min at the desired RH that the chamber will be maintained at. This is to ensure that the test starts with a unique water content equilibrated to the exposed %RH. As previously mention this volume of fuel is transferred to a fuel hold-up cell of which the space above the fuel is also maintained at the same RH. The fuel then runs to the contact using a drip system at 1 drop/ 3 sec. The same order of fixing specimens and maintaining Humidity is used as with the HFRR.

3.2.6 Cleaning of test specimens and preparation procedures

The test specimens are cleaned to remove any possible lubricity enhancing residue on the surface before fuel/lubricant testing. This procedure is shown in Table 3.2.2 Each ultrasonfication step will be done for 10 min even though only 7 min is required per standard.

Table 3.2.2: Cleaning procedures.

	HFRR & SRV (Per ASTM D6079)
Pre-clean	Wipe clean with paper cloth
Ultrasonification	Toluene[a]
Air dry	On paper cloth until dry
Ultrasonification	Acetone[b]
Air dry	On paper cloth until dry

[a] supplied by Merck charge/lot: 1039653, [b] supplied by Merck charge/lot:1042788

It should be noted that anything that comes into direct contact with the sample should be cleaned. For the HFRR this includes: test bath, screws and handling tweezers. For the SRV this includes the top specimen holder and copper retaining ring.

4. Results and Discussion

Results will be presented in four sub-sections:

- **Section 4.1:** Transfer of water from air into and through the test fuel sample.
- **Section 4.2:** The effect of RH on wear testing.
- **Section 4.3:** The effect of RH on seizure load testing.
- **Section 4.4:** Raman spectroscopy of wear and seizure load test surfaces.

4.1. Modelling and measuring water content in fuel.

4.1.1. Modelling diffusion of water in n-hexadecane

One dimensional diffusion of water, species A, into a sample of n-hexadecane, species B, is shown in Figure 4.1.1. The concentration of water, Ca, in the n-hexadecane is a function of both position, ƶ, and time, t. The concentration of water at the surface is denoted as Ca_s.

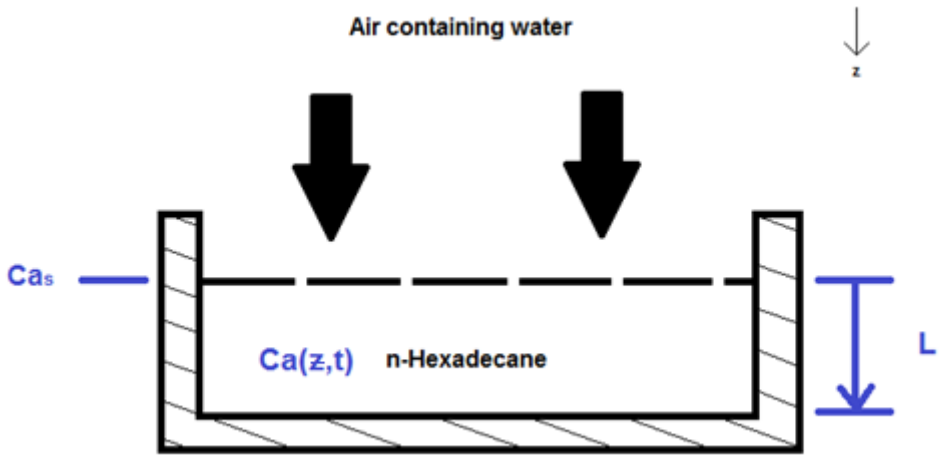

Figure 4.1.1: The diffusion of water into a sample of n-hexadecane.

Fick's second law of diffusion (Equation 4.1.1) for 1 dimensional diffusion is presented below. The concentration of a solute species diffusing through a medium is a function of position (ƶ) and time (t).

$$\frac{\partial Ca\,(t,z)}{\partial t} = D_{AB}\frac{\partial^2 Ca\,(t,z)}{\partial z^2} \qquad (4.1.1)$$

Equation 4.1.1 reduces to Equation 4.1.2. or Equation 4.1.3. under the different assumptions listed in Table 4.1.1 for each equation. These equations allow the determination of the water concentration in the sample, at any given location and any time. The derivation of Equation 4.1.2. and 4.1.3 is discussed in Section 4.1.1.1 and 4.1.1.2 respectively.

$$\frac{Ca - Ca_s}{Ca_0 - Ca_s} = 1 - \operatorname{erf}\left(\frac{z}{2\sqrt{D_{AB}t}}\right) \qquad (4.1.2)$$

$$Y = \frac{Ca-Ca_s}{Ca_0-Ca_s} = \sum_{n=1}^{\infty}\frac{4}{n\pi}\sin\left(\frac{n\pi}{2L}z\right) * e^{\left(-DAB\left(\frac{n\pi}{2L}\right)^2 t\right)} \qquad \text{for } n=1, 3, 5... \qquad (4.1.3)$$

Table 4.1.1: Methods and assumptions for diffusion models (Equation 4.1.2 and 4.1.3)

	Equation 4.1.2	Equation 4.1.3
Solution method	• Laplace transforms • Boundary value problem	• Separation of variables • Initial value & boundary value problem.
Assumptions	One dimensional mass transfer No fluid motion Non-reacting system Constant temperature Infinite diffusion length	One dimensional mass transfer No fluid motion Non-reacting system Constant temperature Finite diffusion length

In Figure 4.1.2 a visual representation of the solution to Fick's 2nd law is represented for both Equation 4.1.2. and 4.1.3. The constants used are presented in Table 4.1.2. The infinite diffusion length solution is presented as blue lines, whereas the finite diffusion length solution is presented as the red lines. Where the blue and red coincide a purple line results. Horizontal green lines indicate the initial and surface concentrations. The finite diffusion length assumption provide slightly higher predictions of concentration, at longer diffusion periods.

Table 4.1.2: Constants shown for the construction of Figure 4.1.2.

Constant	Infinite medium	Finite length	Units
Ca_0	20	20	Ppm
Ca_s	50	50	Ppm
D_{AB}	1.15[a]	1.15[a]	cm^2/s
L	∞	1	Cm

[a] at 22 °C from (Su, Duncan, Momaya, Jutila, Needham, 2010)

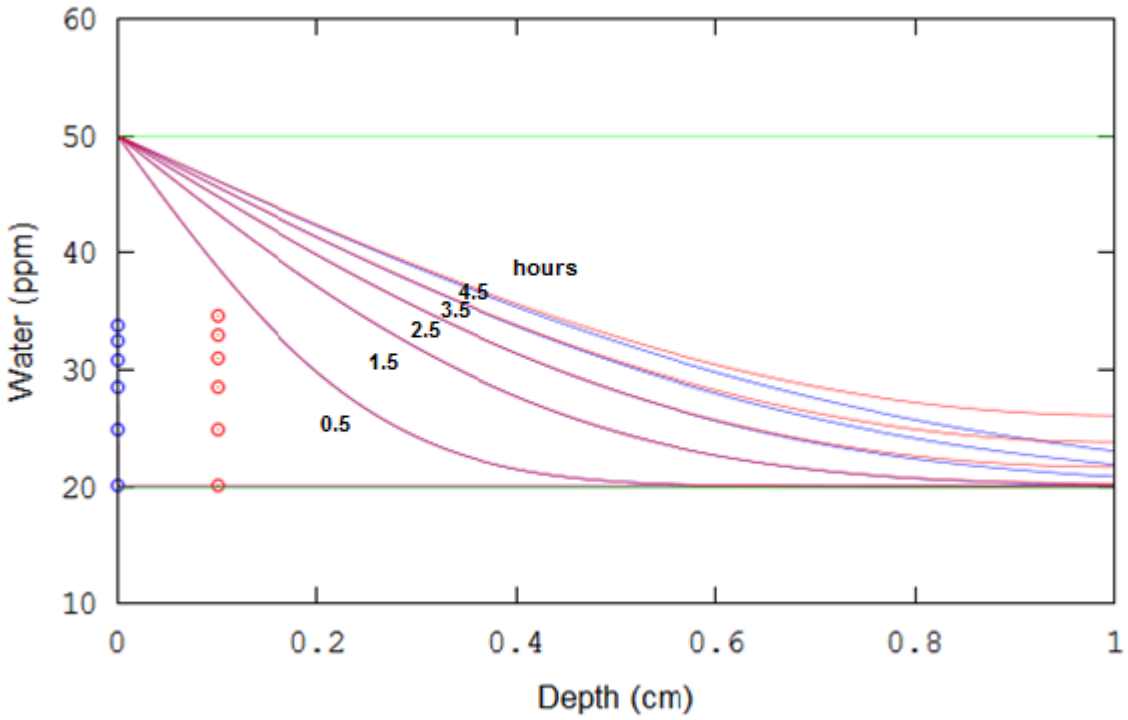

Figure 4.1.2: Solutions to Fick's second law of diffusion based on different assumptions.

The basic derivation of Equation 4.1.2 and 4.2.3 will now be separately presented.

4.1.1.1 Semi-infinite diffusion length

An infinite diffusion length does not correlate with the general HFRR system. The consideration thereof however allows a more complete picture and could be applicable to very deep fuel storage tanks exposed to moist air. For this reason the derivation will be considered very briefly.

Using the transformation presented in Equation 4.1.4 Fick's law can be rewritten as shown in Equation 4.1.5

$$\theta = Ca - Ca_0 \tag{4.1.4}$$

$$\frac{\partial \theta}{\partial t} = D_{AB} \frac{\partial^2 \theta}{\partial z^2} \tag{4.1.5}$$

The Laplace transform of Equation 4.1.5 can be rearranged into an ordinary differential equation with its general analytical solution shown in Equation 4.1.6.

$$\theta = a_1 e^{\left(\sqrt{\frac{s}{D_{AB}}} z\right)} + b_1 e^{\left(-\sqrt{\frac{s}{D_{AB}}} z\right)} \tag{4.1.6}$$

The following two boundary conditions can be used to obtain the two constants a_1 and b_1. The concentration at the surface is assumed to be the saturation concentration. This assumes negligible resistance to mass transfer of water from the gas to the liquid phase. The second boundary condition assumes that the concentration at infinity remains unaltered due to the distance of diffusion (Welty, Wicks, Wilson & Rorrer, 2008: 498-499):

- $Ca(0,t) = Ca_s$ at $z = 0$ for $t > 0$
- $Ca(\infty,t) = Ca_0$ at $z = \infty$ for $t \geq 0$

The inverse Laplace of Equation 4.1.6 is shown in Equation 4.1.2 after rearrangement and simplification.

$$\frac{Ca - Ca_s}{Ca_0 - Ca_s} = 1 - \text{erf}\left(\frac{z}{2\sqrt{D_{AB}t}}\right) \tag{4.1.2}$$

4.1.1.2 Finite diffusion length

To simplify the mathematics a normalized (dimensionless) concentration change is introduced as shown in Equation 4.1.7.

$$Y = \frac{Ca - Ca_s}{Ca_0 - Ca_s} \tag{4.1.7}$$

Fick's second law rewritten using Equation 4.1.7 is shown in Equation 4.1.8

$$\frac{\partial Y}{\partial t} = D_{AB} \frac{\partial^2 Y}{\partial^2 z} \tag{4.1.8}$$

Assuming that a general solution to Fick's second law of diffusion exists as is shown in Equation 4.1.9. With T only a function of time and Z only a function of position.

$$Y(z,t) = T(t)*Z(z) \tag{4.1.9}$$

The partial derivative of Equation 4.1.9 with respect to time and the second order partial derivative of Equation 4.1.9 with respect to position can be substituted into Equation 4.1.8. Upon rearrangement Equation 4.1.10 can be obtained in which the left-hand side is a function of only time and the right-hand side is only a function of position (Welty, *et al*, 2008: 501).

$$\frac{1}{D_{AB}} \frac{\partial T}{\partial t} = \frac{1}{Z} \frac{\partial^2 Z}{\partial^2 z} \tag{4.1.10}$$

A change in time can therefore not influence the right-hand side of Equation 4.1.10 and a change in position cannot influence the left-hand side. Both sides are therefore equal to an artibary constant $-\lambda^2$. An ordinary differential equation can therefore be written for each side with the general solution of each shown in Equation 4.1.11 and 4.1.12. The substitution of these equations into Equation 4.1.9 gives the solution shown in Equation 4.1.13. (Welty, *et al*, 2008: 501 - 502)

$$T(t) = c_1 e\text{^}(-D_{AB}\lambda^2 t) \tag{4.1.11}$$

$$Z(z) = c_2 \cos(\lambda z) + c_3 \sin(\lambda z) \tag{4.1.12}$$

$$Y = T(t)*Z(z) = \left[c_1' \cos(\lambda z) + c_2' \sin(\lambda z)\right]*[e\text{^}(-D_{AB}\lambda^2 t)] \tag{4.1.13}$$

The solution to Equation 4.1.13 was previously presented in Equation 4.1.3 for a specific HFRR system. The mathematical derivation of Equation 4.1.3 is presented in

Appendix A. The constants c_1', c_2' and λ can be solved using the boundary condition and initial conditions specific to the HFRR system.

For the HFRR system the following boundary and initial conditions were assumed to apply:

- $Ca = Ca_s$ at $z = 0$ for $t > 0$

  There is no significant resistance to mass transfer of water, from the gas phase to the liquid n-hexadecane phase. This means that the concentration at the surface will be at saturation concentration, instantaneously. The concentration will remain at that level as long as the air humidity remains constant. The surface concentration, Ca_s, can be obtained through knowledge of the humidity and the Henry's constant for water in n-hexadecane.

- $\frac{dCa}{dz}=0$ at $z = L$ for $t > 0$

  No diffusion occurs through the bottom of the bath surface. It is seen as a impermeable surface. No reaction with the surface is assumed to occur to simplify the model.

- $Ca = Ca_0$ at $t = 0$ for $0 \leq z \leq L$

  The concentration of water molecules in the sample is assumed to be uniform when initially exposed to the atmosphere. The sample was kept at some equilibrium value Ca_0 prior to exposure.

$$Y=\frac{Ca-Ca_s}{Ca_0-Ca_s}=\sum_{n=1}^{\infty}\frac{4}{n\pi}\sin\left(\frac{n\pi}{2L}z\right)*e^{(-DAB\left(\frac{n\pi}{2L}\right)^2 t)} \quad \text{for } n=1, 3, 5... \quad (4.1.3)$$

Equation 4.1.3 allows the calculation of the concentration in the n-hexadecane sample, Ca, at any location, z, and at any time, $t > 0$. A graphical representation of Equation 4.1.3 for this system was previously presented in Figure 4.1.2.

4.1.2. Experimental water determination

Air RH was controlled to be within 5% for all data presented.

4.1.2.1 The effects of air humidity on the water content of fuel under non-agitated conditions.

Samples of 3.5 mL each, were taken from the same sealed source and each exposed to air with different % RH in a HFRR bath. A bigger sample was used than is required by ASTM D 6078 and ISO/CD 12156-1 to increase the sensitivity of the Karl Fischer (KF) titrations. The temperature was at ambient levels of 20 °C ± 1 °C. The samples were placed in the HFRR bath to ensure that the exposed area, 6.38 cm^2, for mass transfer for each sample was the same. Samples from bulk storage contained 21 ppm water before any exposure.

From Figure 4.1.3 it can be seen that the water content of n-hexadecane was influenced by the RH of the air that the sample was exposed to. The higher RH tended to increase water content whereas lower RH tended to slightly decrease the water content of the samples as would be expected due to inter phase mass transfer. The kinetics are interesting indicating the sensitivity of fuel samples to changes in air RH. It should be noted that kinetics would be even faster for a 2 mL sample, as is required by the HFRR standards. The water content is likely to affect the lubricity characteristics of the fuel.

This figure highlights the importance of sealing of samples to the surrounding environment. If fuel samples were not to be sealed off, the water content thereof could fluctuate as the water content of the atmosphere changes. The kinetics of transfer will be affected by the size of the interface area of the liquid, in the container, in contact with air. The shape and size of the container opening will also affect kinetics.

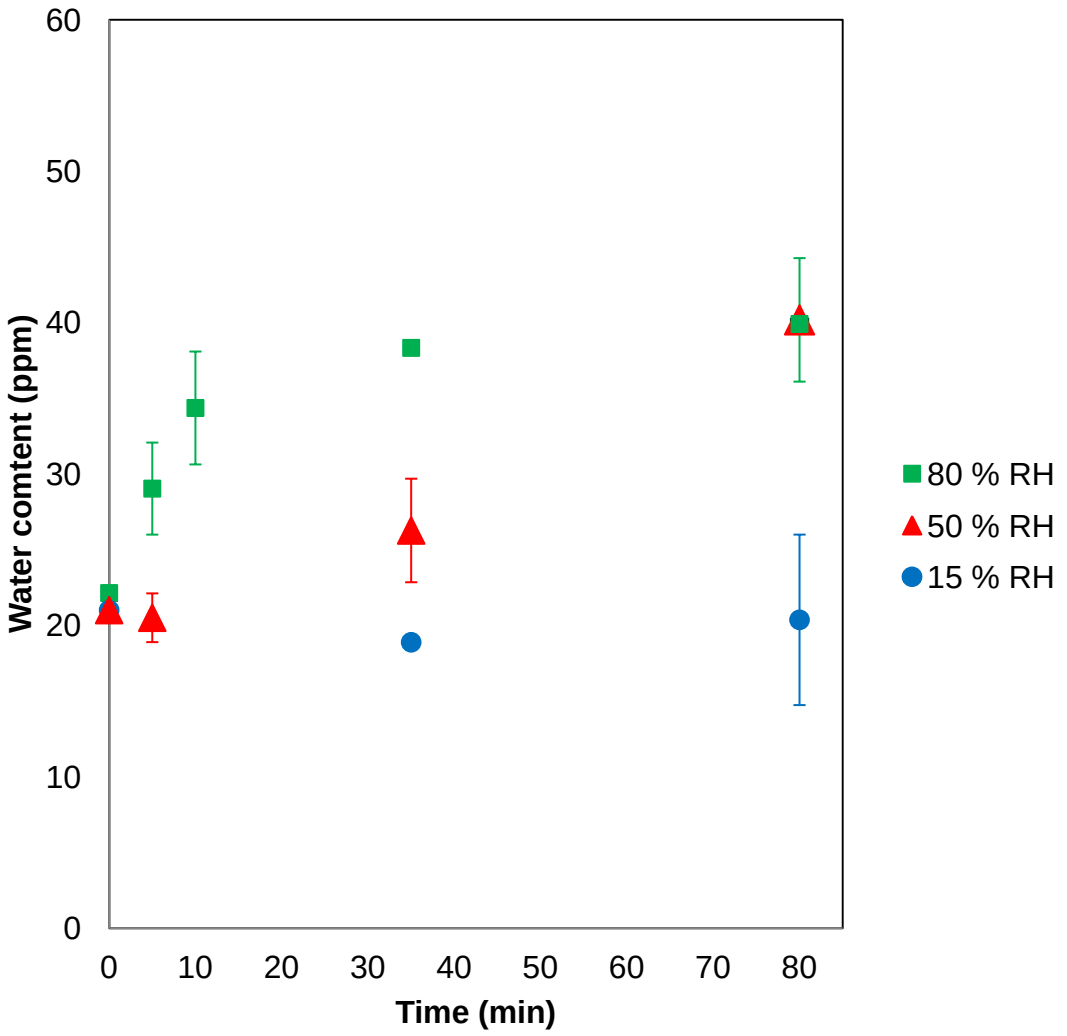

Figure 4.1.3: The influence of ambient RH at 20 °C on the water content of n-hexadecane.

4.1.2.2 The effects of air humidity on the water content of fuel under highly agitated conditions.

To enable the standardization of water content in n-hexadecane, it is suggested to bubble air of a certain humidity through a sample for a fixed period of time prior to lubricity testing. This enables more intimate mixing, allowing faster mass transfer of water to, or from, the fuel sample. All samples were taken from the same sealed source. The water content of this source is indicated by the green dashed lines in Figure 4.1.4. This water content was measured daily to ensure all samples started off with the same water content.

In Figure 4.1.4 air, of different RH, was bubbled through a 7 mL n-hexadecane sample in a sealed test tube. The test tube was fitted with two small tube openings at the top. An air flow rate of 3L/min for 20 min was used. Results indicated the following:

- Bubbling air with 20% RH and lower tended to strip water from the sample.
- Between 20 – 35% RH the water content was similar to that of the sample before aeration. This would suggest that at this RH, the saturation content of water in the air is in near equilibrium with the water content of the original sample.
- At 50% RH and higher, the saturation of water in n-hexadecane (at ambient temperatures) appeared to be reached. It should be noted however that at 50% RH data showed a higher standard deviation meaning that saturation would likely only occur at higher RH.

It can be assumed that equilibrium is reached within the 20 min of bubbling from data that will be presented later in Figure 4.1.5. A Henry's constant can be estimated since it would be equal to the slope of Figure 4.1.4 as is indicated. This will of course require a conversion to the correct units. Only the first four data points was used for the estimation. The value of 19 atm/molefrac at 20 °C is comparable order-wise with that of 46.2 atm/molefrac at 25 °C reported by (Yaws & Rahate, 2009).

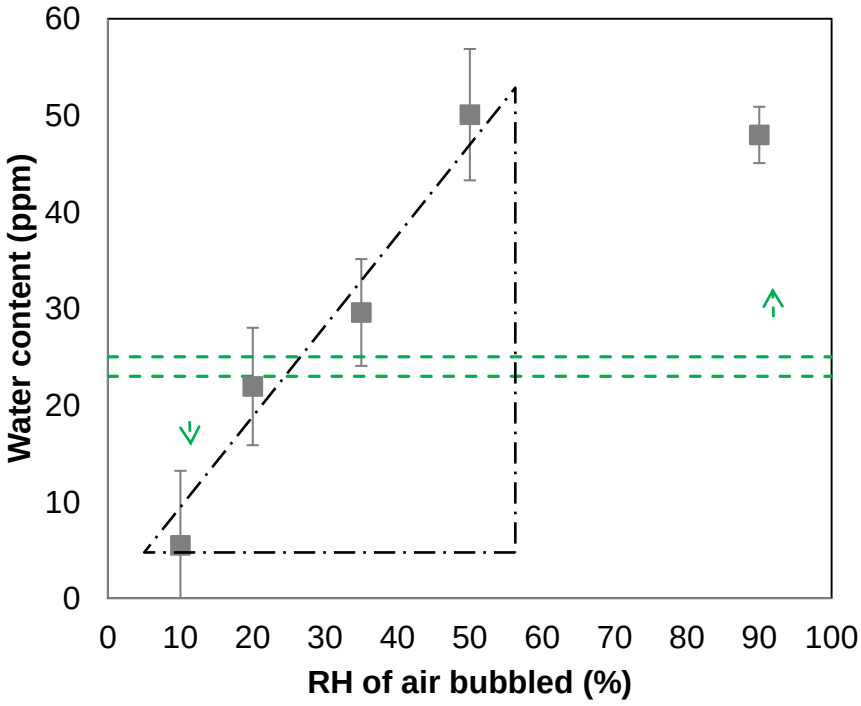

Figure 4.1.4: Water content of samples through which air is bubbled at different RH.

4.1.2.3 The effect of higher temperature on fuel sample water content

It is known from Section 2.4.2 that the solubility of water in n-hexadecane increases with increasing temperature. Since most lubricity tests are run at temperatures higher than ambient conditions it would initially be expected that water content will increase further upon initiating these tests. This however does not happen as is illustrated in Figure 4.1.5

Air of 90% RH (20 °C) was bubbled through a 7 mL n-hexadecane sample held at 60 °C at a 3L/min flow rate. This was to simulate the possible contact between ambient moist air and a sample at a higher temperature, but with intimate mixing. The solubility of water at 60 °C in n-hexadecane is >> 100 ppm (the exact value being different depending on source, see Section 2.4.2). Clearly this was not reached, not even after 2 hours of exposure. In fact, lower water content was obtained.

This can be explained by the increase of the air temperature from being bubbled through the hotter sample. The outlet temperature of the air was measured as 35 °C which is a significant increase from the 20 °C inlet. Since hotter air can contain more water, the relative humidity varied from (90% @ 20 °C) to ≈ 40% at 35°C. The ability of the n-hexadecane to contain more water increases with higher temperature, but the same is true for the gas.

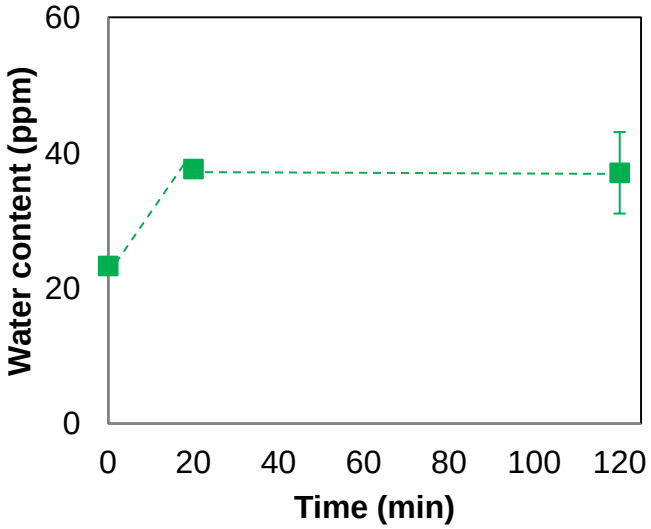

Figure 4.1.5: Bubbling (90% RH, 20 °C) air through n-hexadecane at 60 °C.

This prompted confirmation of the effect of temperature as is illustrated in Figure 4.1.6. Samples were bubbled similar to the procedure of Figure 4.1.5. There is a clear decrease in water content of the fuel (liquid) sample as the sample temperature increases. This effects seems to be more pronounced at higher RH. This could indicate that air's ability to retain water increases faster than that of n-hexadecane with increasing temperature.

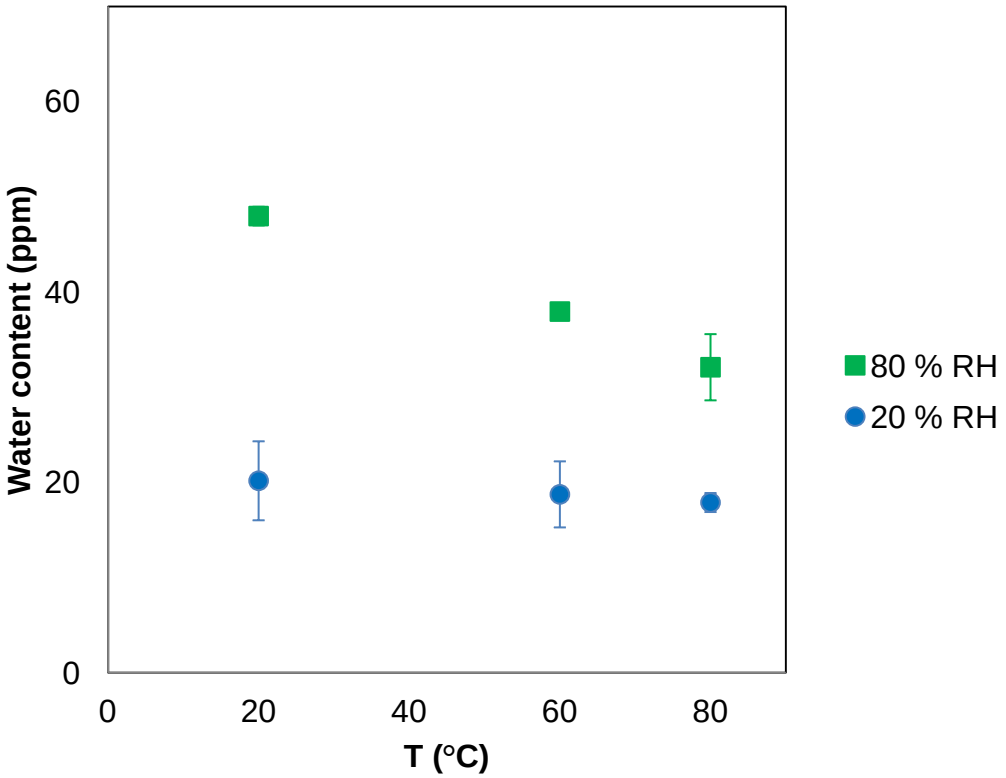

Figure 4.1.6 : The effect of bubbling air (at 20% RH and 80% RH) through n-hexadecane at different temperatures.

It is important to know how the water content of a sample changes during a typical HFRR test. No significant decrease was observed in water content when comparative tests were run with an active tribo-contact and those run without an active tribo-contact. Therefore no active tribo-contact was used in this assessment. This is probably due to the small area of contact compared to the spread of water molecules at the ppm scale.

Samples were first aerated at 20 °C for 20 min. The water content after aeration is reported at time = 0 in Figure 4.1.7. As the test is started the temperature increases to 60 °C which takes about 5 min. The test is then completed in 75 min. The water content clearly decreases due to the higher temperature, but on average different

water content was obtained. This would mean that the averaged water content is still unique at different air RH. From this results it would therefore be possible that lubricity could be differently affected at different values of RH.

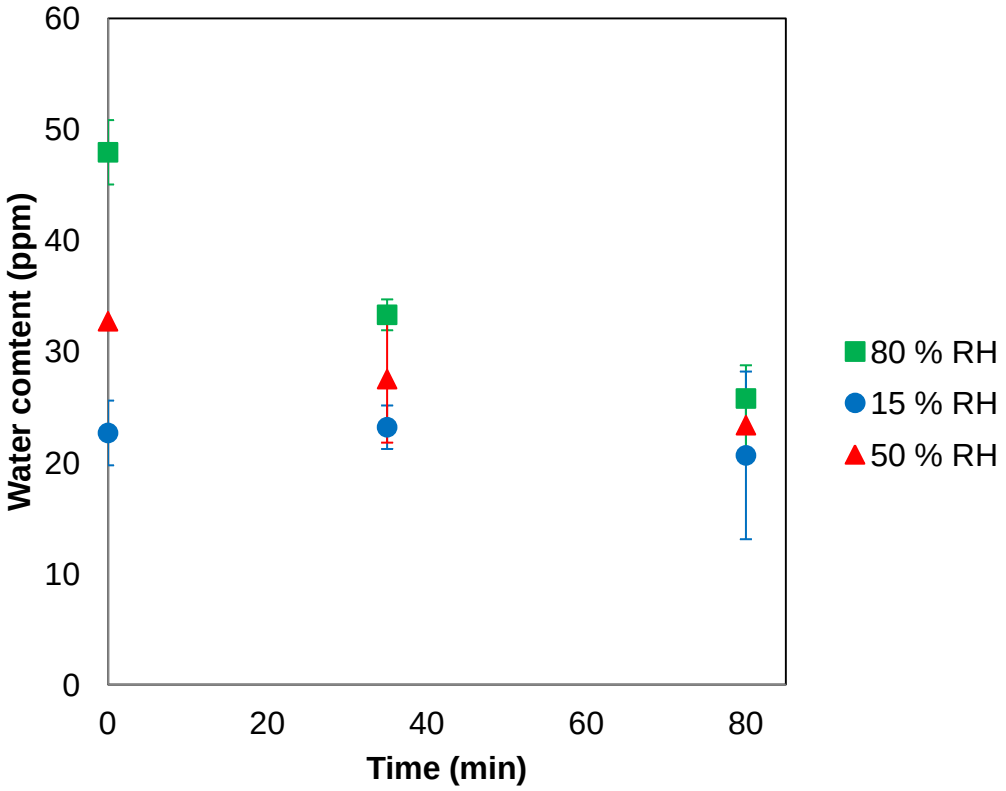

Figure 4.1.7: Water content of n-hexadecane during a typical HFRR test.

4.1.2.4 The effect of lubricity additives on water content of fuel samples

Since the fuel matrix to be tested in subsequent lubricity tests consist of 100, 250/500 and 2000 ppm PA in n-hexadecane it was prudent to see if these additization levels would affect moisture content of the fuel sample. This is possible since these molecules increase the average polar nature of the fuel sample. In Figure 4.1.8 it can be seen that when air of 90% RH was bubbled through both 0 & 2000 ppm fuel samples, there seemed to be no significant difference in water content. It should however be noted that a more polar mixture of fuels might have water content levels significantly higher. This is known to occur in biodiesel as was previously shown in Figure 2.6.3 in Section 2.6.

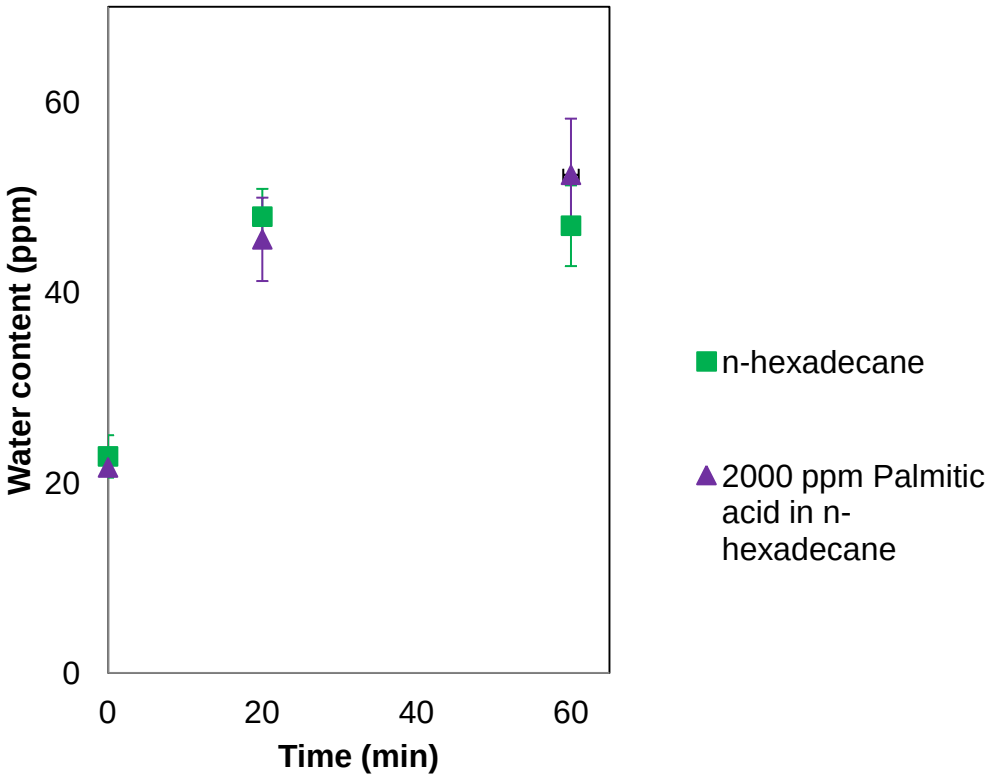

Figure 4.1.8: Water content of n-hexadecane and additized n-hexadecane.

It has been shown in this section that air RH influences the water content of the model base fuel n-hexadecane. It was shown that during lubricity testing the water content of test samples based in batch tests is likely to decrease due to changes in temperature. Different average water content was however still observed.

A continuous-fuel-flow-system would behave differently since the bulk of the fuel sample will not be exposed to the higher temperature in a fuel holdup cell continuously. Therefore the exposure during a test should be at a higher water content compared to a batch test. The water content will still decrease since the bath is still controlled to be at a set temperature. The kinetics will however limit the loss of water due to the small residence time of fuel in the heated bath.

In the next sections the effect of water on wear and seizure load testing will be investigated now that the presence of variable water levels has been confirmed.

4.2. Wear testing (HFRR): Effect of water in solution

The effect of humidity on the wear test behaviour of a model fuel was determined by comparing results at three different water vapour pressures. In the results that follow water content in the air is expressed as water vapour pressure rather than % RH. This is because of the non-linear change in % RH values as water content and temperature changes. At ambient temperature (around 20 - 22 °C) the water vapour pressures used corresponded to 15-20% RH, 45-55 %RH and 70-80 %RH depending on the ambient temperature.

n-Hexadecane with three different palmitic acid (PA) concentrations were tested. The concentrations were selected to give WSD representative of borderline acceptability (100 ppm), acceptable behaviour (250 ppm) and over additised fuel (2000 ppm). Tests were done at two temperatures (60 and 80 °C).

Each parameter which was measured will be considered separately to allow a better comparison between tests. This will be followed by an all inclusive summary of all measured parameters.

4.2.1. Friction coefficients

In Figure 4.2.1 to 4.2.3 the friction recordings of wear testing at 60 °C are presented. In Figure 4.2.4 to 4.2.6 the friction recordings of wear testing at 80 °C are presented. The effect of the three different water vapour pressures can be seen at each lubricity additive concentration.

Repeat runs of wear testing for both 60 °C and 80 °C can be found in Appendix B. A summary of the average friction coefficients for all wear runs will be presented in Figure 4.2.7.

When comparing the results in Figure 4.2.1 to 4.2.3 (60 °C) it can be seen that friction coefficients tended to be higher and more erratic at higher water vapour pressure (green > red > blue). This suggests that the polar water molecule interferes

with the adsorption mechanism of the polar PA segment onto the surface. This resulted in a reduced lubricating film and therefore increased friction.

The effect of water vapour pressure on friction becomes less apparent as the lubricity additive concentration increases from 100 to 250 ppm PA. At 2000 ppm PA there seems to be no significant difference except for the higher friction coefficient during the first few minutes of the test. It should be noted that the vertical scale for 2000 ppm is half of the scale of 100ppm and 250 ppm. Therefore the effects at 2000 ppm is much smaller than they would appear.

The same trends can be seen at 80 °C in Figure 4.2.4 to 4.2.6. What is interesting though, is the observation that at the higher temperature the difference in behaviour at different water vapour pressures is reduced when compared to the differences at 60 °C. This will be discussed later.

From Figure 4.2.1 to 4.2.3 and Figure 4.2.4 to 4.2.6 it would therefore seem that the effect of water content on friction becomes less significant with an increase in the polar surface-active PA concentration. This would suggest that the presence of more polar surface-active species inhibits the interaction of the water molecules with the surface.

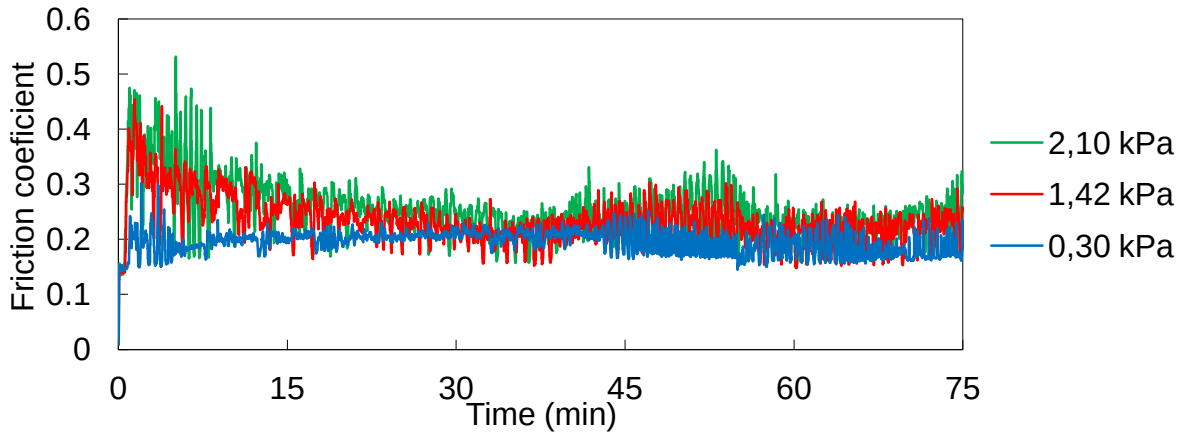

Figure 4.2.1: Effect of water vapour pressure on the friction coefficient of wear testing (60 °C, 100 ppm PA, run 1).

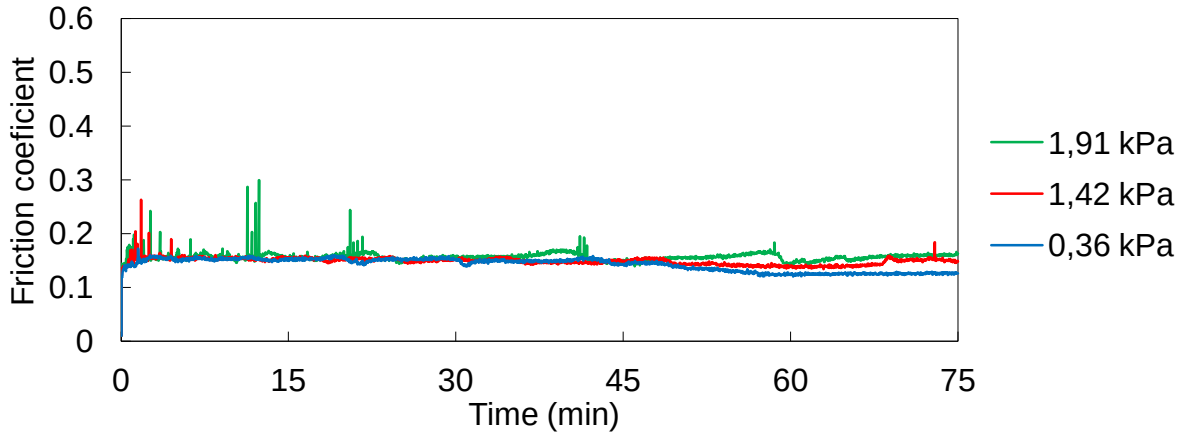

Figure 4.2.2: Effect of water vapour pressure on the friction coefficient of wear testing (60 °C, 250 ppm PA, run 1).

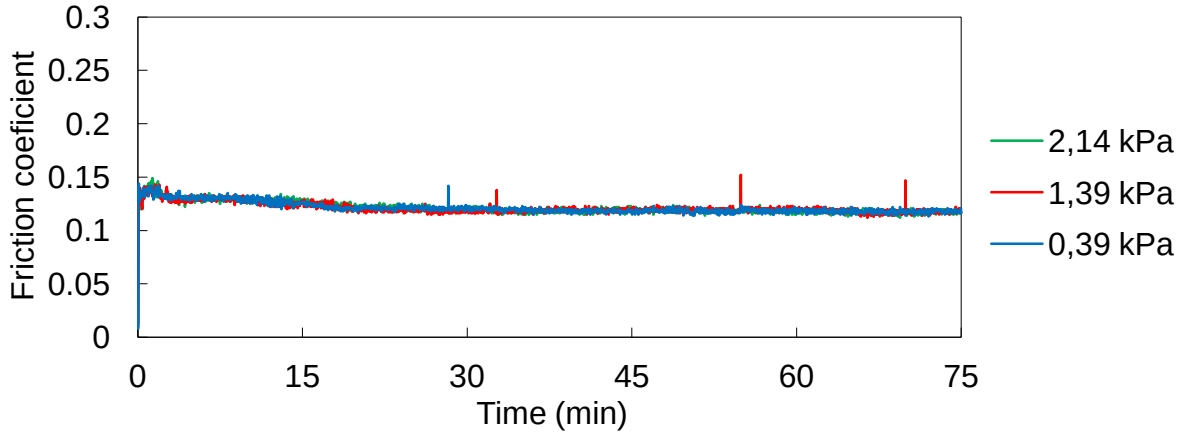

Figure 4.2.3: Effect of water vapour pressure on the friction coefficient of wear testing (60 °C, 2000 ppm PA, run 1).

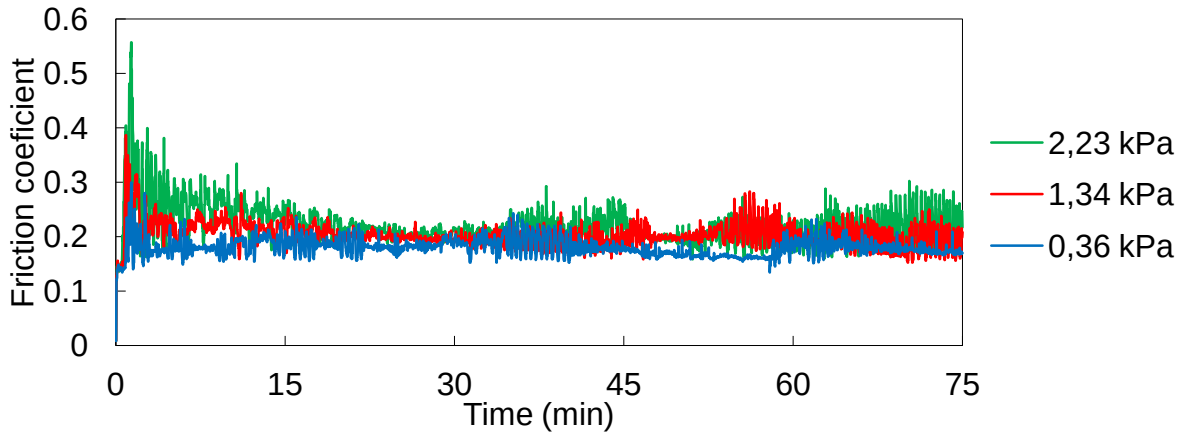

Figure 4.2.4: Effect of water vapour pressure on the friction coefficient of wear testing (80 °C, 100 ppm PA, run 1).

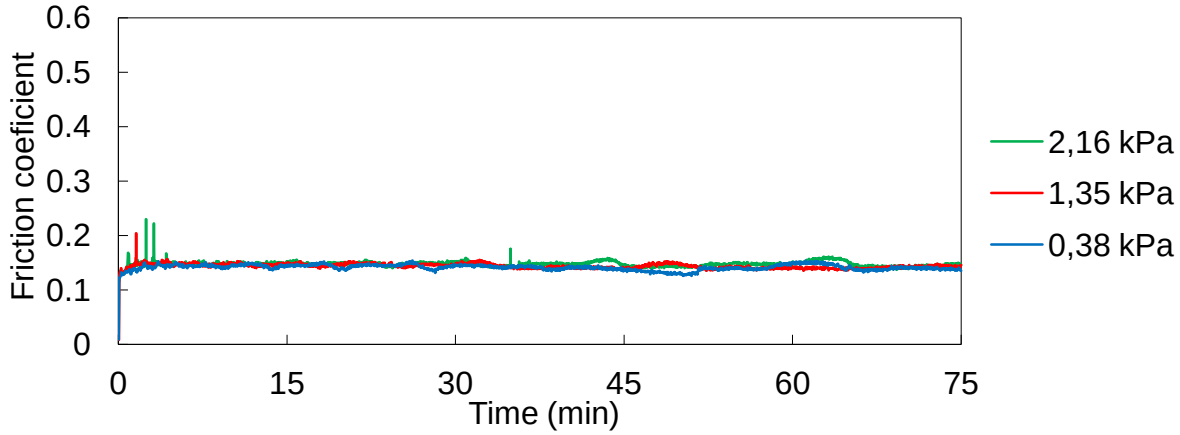

Figure 4.2.5: Effect of water vapour pressure on the friction coefficient of wear testing (80 °C, 250 ppm PA, run 1).

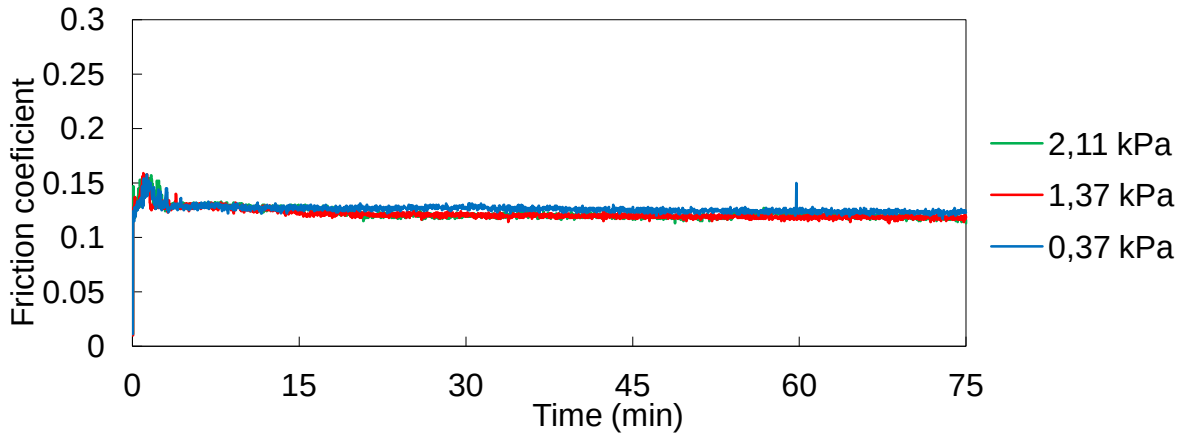

Figure 4.2.6: Effect of water vapour pressure on the friction coefficient of wear testing (80 °C, 2000 ppm PA, run 1).

In Figure 4.2.7 a summary is presented comparing the average friction coefficient and of all wear test runs, including repeat runs. The actual repeat test runs can be seen in Appendix B. In Figure 4.2.8 the standard deviations of all the wear test friction coefficients are presented.

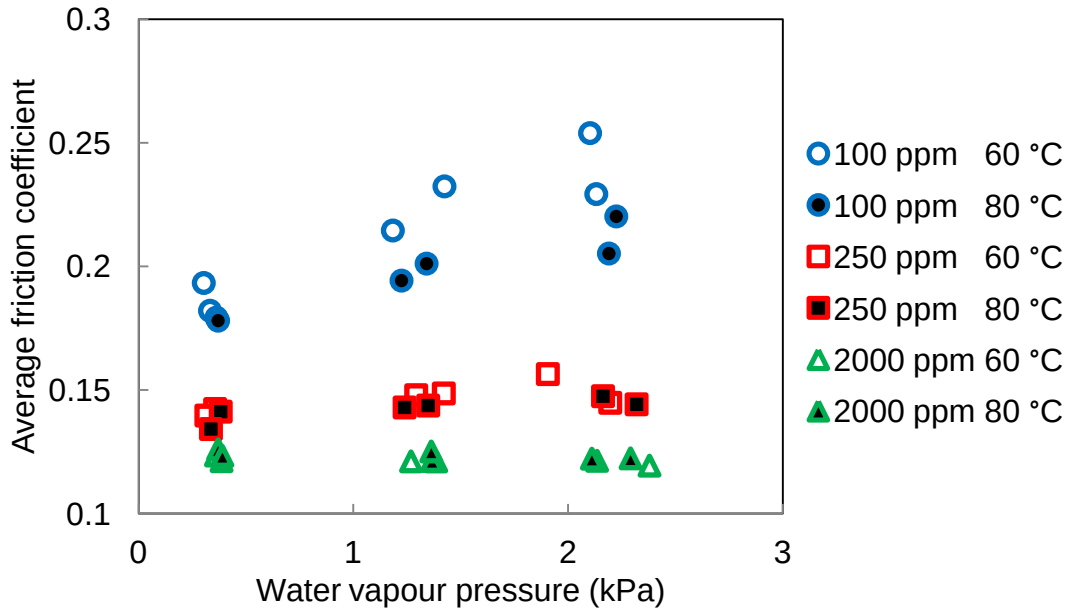

Figure 4.2.7: Summary of the effect of water vapour pressure on HFRR average friction coefficient (60 & 80 °C, 2 repeats).

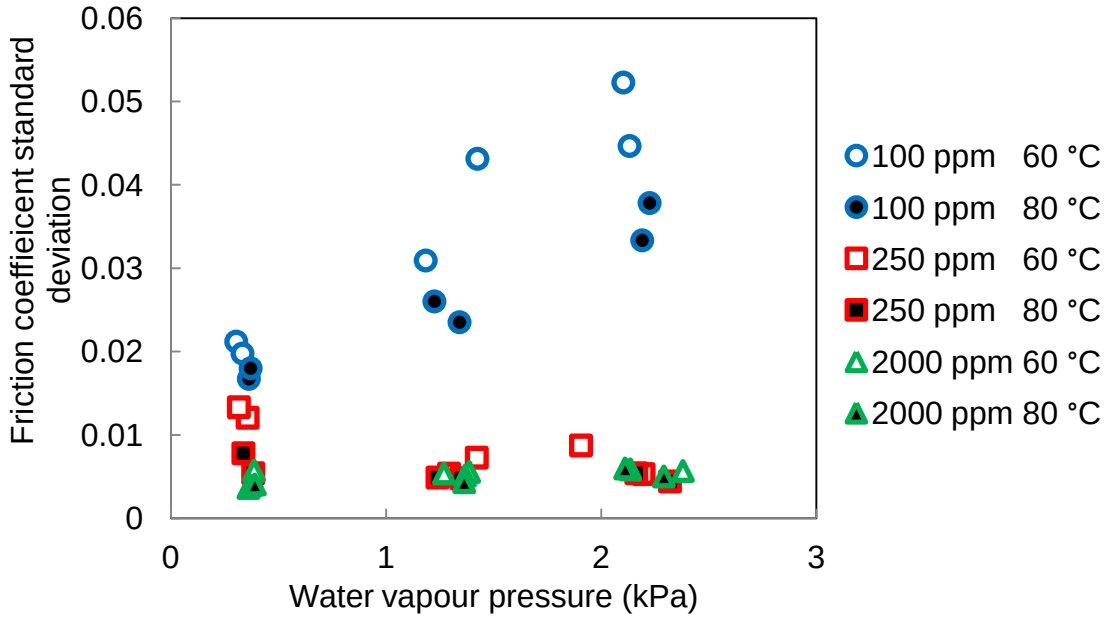

Figure 4.2.8: Summary of the effect of water vapour pressure on HFRR friction coefficient standard deviation (60 & 80 °C, 2 repeats).

The average friction coefficients displayed in Figure 4.2.7 allow easier comparison of the friction coefficients. It should however be noted that a lot of data can be lost or suppressed in doing this when differences are small or only occur for a limited period of time.

It can be seen that the average friction coefficient is higher at higher water vapour pressure with a drastically diminished effect at higher lubricity additive concentration. A similar observation can be made for Figure 4.2.8 in which the standard deviation of each friction response is presented, which is indicative of the erratic behaviour. The friction coefficient becomes more erratic at higher water vapour pressures for 100 ppm PA. This observation is not made at higher lubricity additive concentration. This is an instance where data was lost because of averaged values.

The average friction coefficient is lower and less erratic at higher temperatures. This could possibly be due to increased adsorption of PA at slightly higher temperatures.

The observations made here would suggest that the effect of water is a surface phenomenon since:

- Water molecules interfere with surface active behaviour of PA.
- Increased PA decreases the effect of the water molecules.

This illustrates the competitive nature of water molecules and PA for surface interaction.

4.2.2. ECR reading

In Figure 4.2.9 to 4.2.14 the ECR recordings are presented for the same friction responses displayed in Figure 4.2.1 to Figure 4.2.6 respectively. The water molecules have the effect of lowering the recorded ECR readings for low lubricity levels and delaying the build-up at higher lubricity levels. Since the ECR is a resistance measurement, it is indicative of the presence of film/material between the contact. This film could be due to the formation of oxides or the adsorption of PA layer. There also seems to be more erratic behaviour at higher water vapour pressure for 100 and 250 ppm PA.

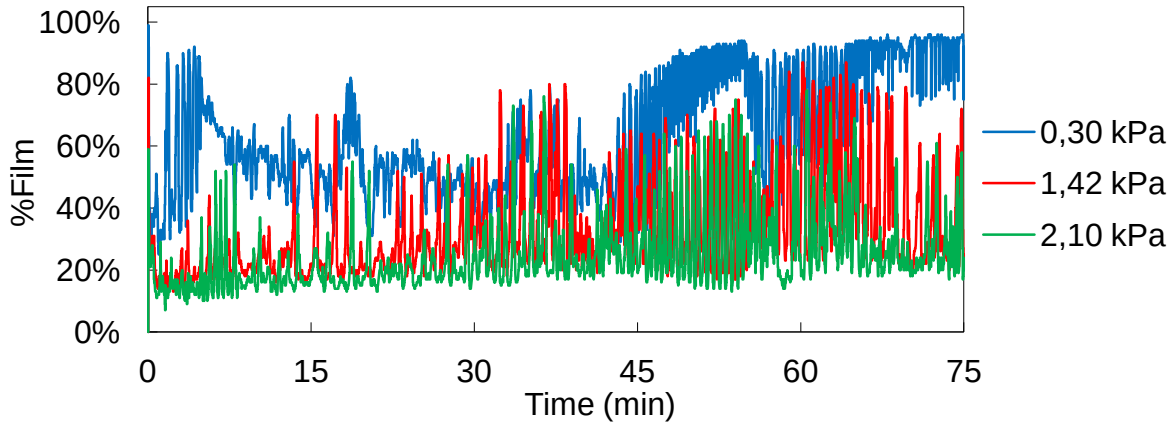

Figure 4.2.9: Effect of water vapour pressure on the ECR of wear testing (60 °C, 100 ppm PA, run 1).

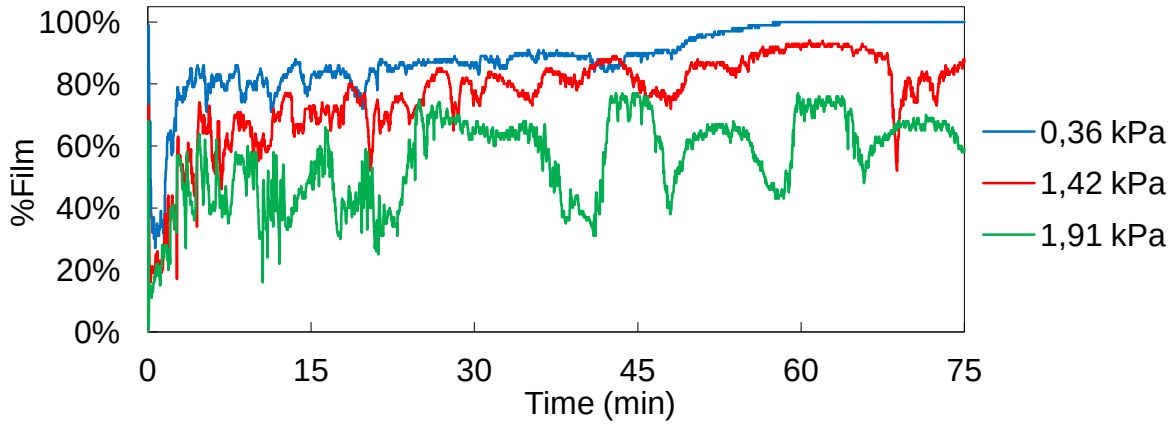

Figure 4.2.10: Effect of water vapour pressure on the ECR of wear testing (60 °C, 250 ppm PA, run 1).

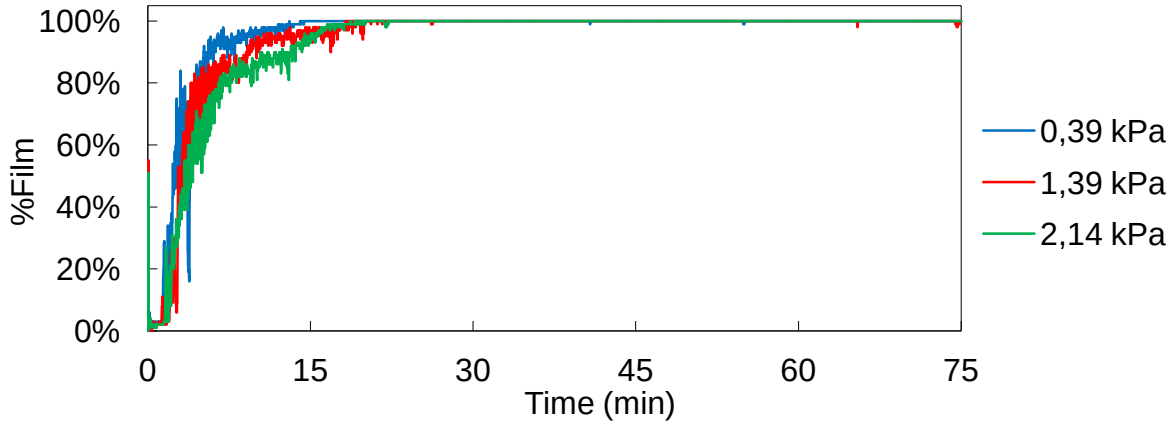

Figure 4.2.11: Effect of water vapour pressure on the ECR of wear testing (60 °C, 2000 ppm PA, run 1).

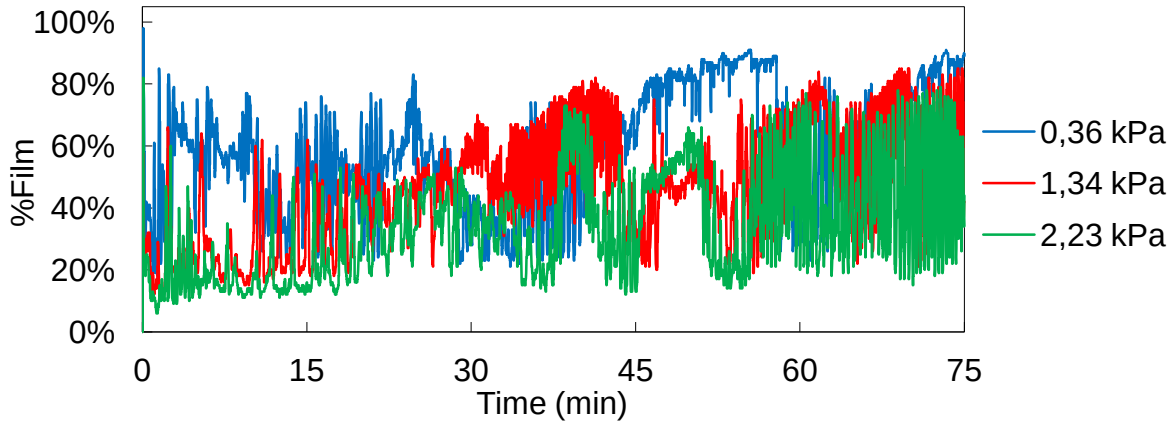

Figure 4.2.12: Effect of water vapour pressure on the ECR of wear testing (80 °C, 100 ppm PA, run 1).

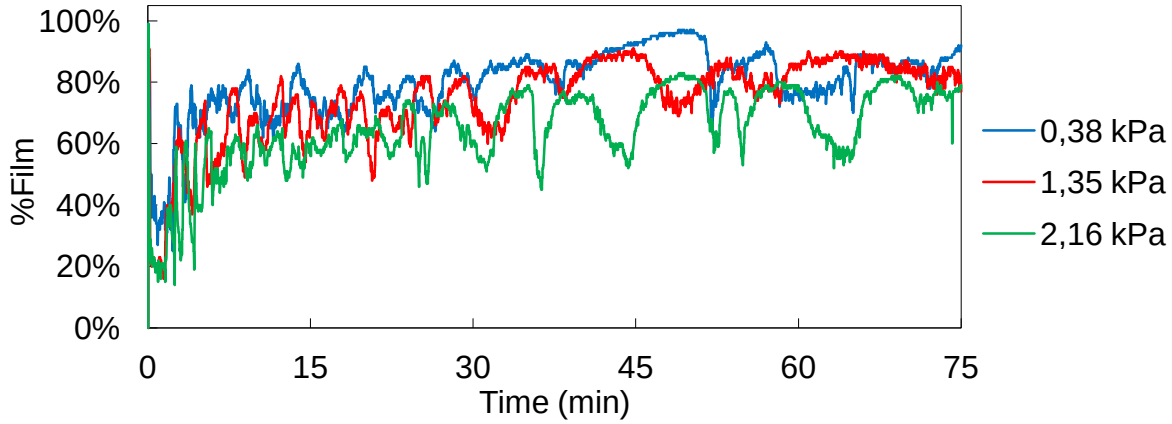

Figure 4.2.13: Effect of water vapour pressure on the ECR of wear testing (80 °C, 250 ppm PA, run 1).

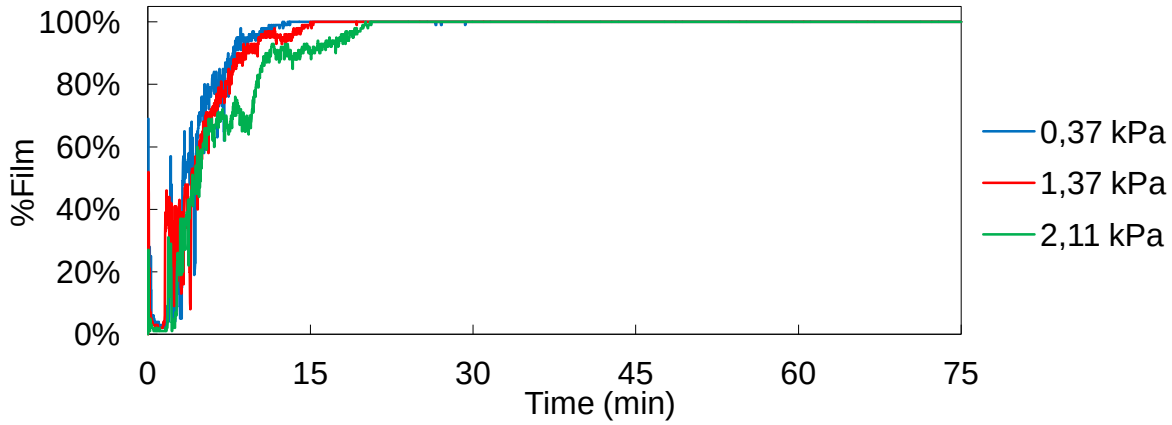

Figure 4.2.14: Effect of water vapour pressure on the ECR of wear testing (80 °C, 2000 ppm PA, run 1).

In Figure 4.2.15 a summary of the average ECR reading for all test runs is presented (60 & 80 °C, 2 repeats). Once again complete repeat ECR runs can be found in Appendix B which correspond with other run data presented in the appendix.

From Figure 4.2.15 it can be seen that more water resulted in lower average ECR readings with the effect becoming diminished at higher lubricity additive concentration. These results would suggest that water interferes with film build up either by retarding PA adsorption or by retarding the oxidation process of the nascent metal. The second possibility seems very unlikely from the known effects of a water phase on a metal surface.

The average ECR reading is higher for higher lubricity additive which is to be expected since the additive diminishes the removal rate of metal oxide. A good example of data being lost can be seen in comparing the complete ECR readings at 2000 ppm with the average values in Figure 4.2.15 since the differences are only observed initially during the test before the upper measurement range of the device is reached. It should however be noted that the differences are still significantly smaller in the range that was recorded before the limit was reached.

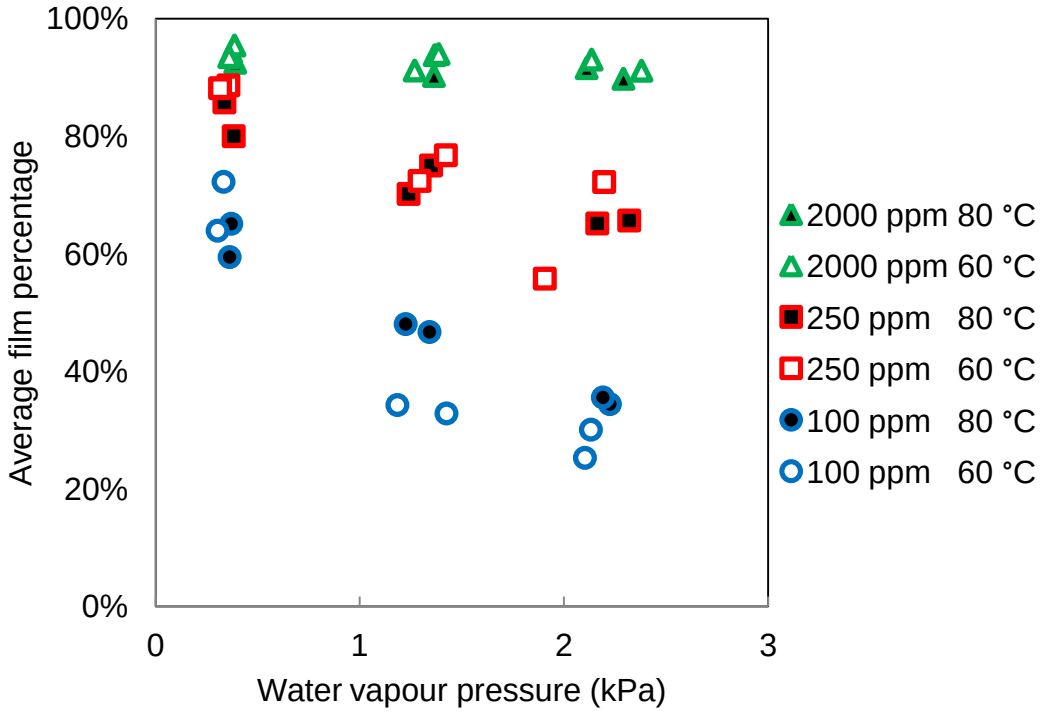

Figure 4.2.15: Effect of water vapour pressure on HFRR average ECR reading (60 & 80 °C, 2 repeats).

4.2.3. Wear scar dimensions

In Figure 4.2.16 the measured wear scar dimension (MWSD) is presented for tests done at both 60 °C and 80 °C. The figure includes repeat runs. It can be seen that larger MWSD are obtained at higher water vapour pressure. This trend is in agreement with the report on the ISO standard development by (Davenport, *sa*) and work done by (Lapuerta, Sánchez-Valdepeñas & Sukjit, 2014).

There is a clear decrease in the effect of water on the MWSD with increasing PA lubricity additive concentration. This is evident from the decrease in the slopes of the fitted trend lines.

Larger wear scars were obtained at higher temperatures indicating increased oxidative wear.

In Figure 4.2.17 Estimated wear volumes are shown. This is based on an assumption of a flat wear scar surface. Although this assumption is not good for all PA concentrations it is more likely to be true for low lubricity fuels than for high lubricity as revealed in work done by (Olah, *et al*, 2005). From Figure 4.2.17 it is clear that lower lubricity fuels will be significantly more sensitive to the effects of water than higher lubricity fuels.

If we were to furthermore assume that the surface approaches a rounder surface rather than a flat surface for better lubricity levels, the effects at 2000 ppm would be overestimated. This would make the difference between the response of high and low lubricity to water even more prominent supporting the observation even more.

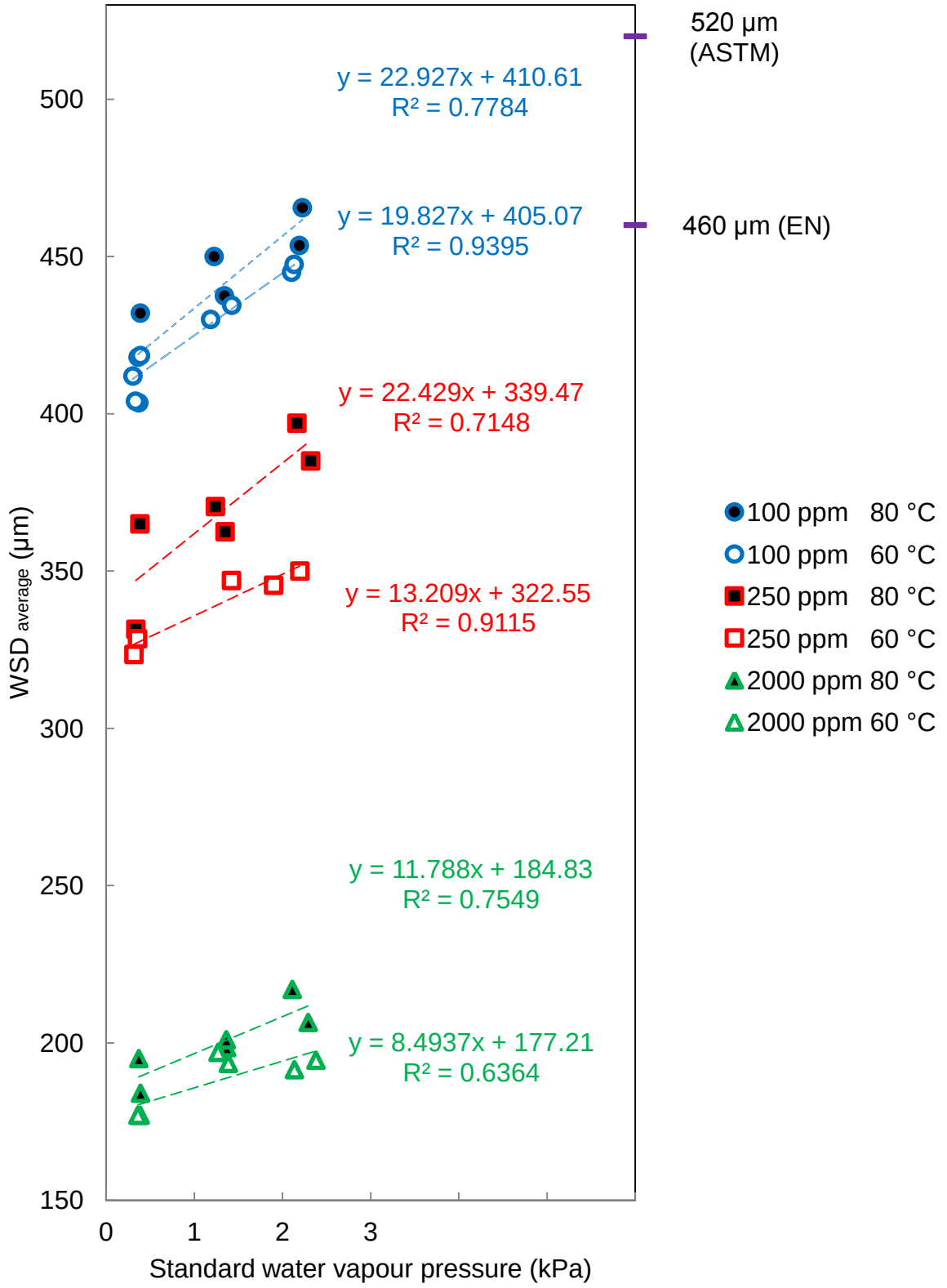

Figure 4.2.16: The effect of water vapour pressure on the ball WSD at 60 & 80 °C.

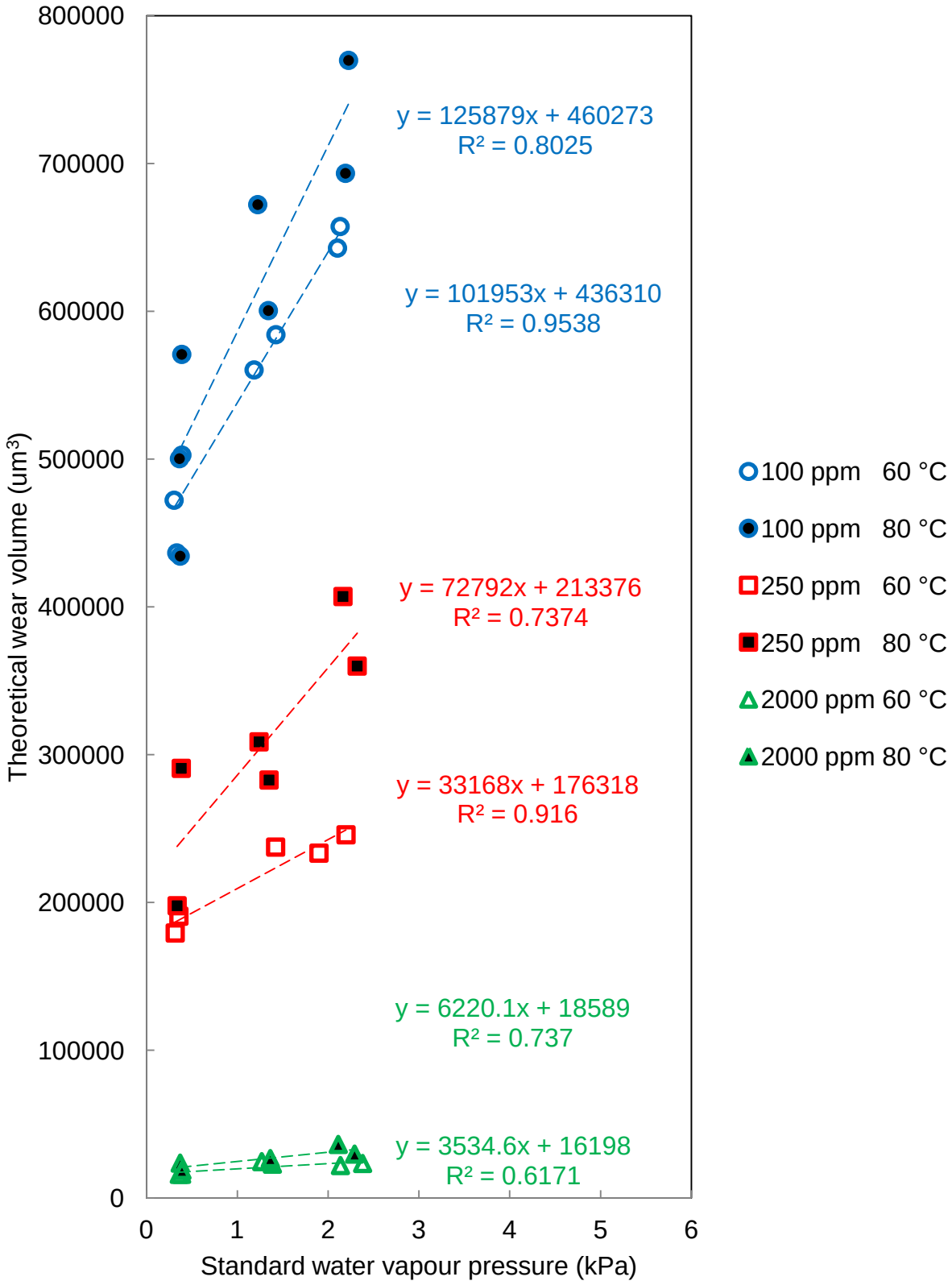

Figure 4.2.17: The effect of water vapour pressure on the estimated wear volumes.

It was previously observed in Section 3 that a good correlation between MWSD and pump failure was obtained even though the MWSD is a surface phenomenon and not volumetric.

This could perhaps make sense if we can assume that that the volumetric wear rate is constant. We may conclude that the incremental increase in wear volume gets spread over a larger and larger area with each time increment. The added wear volume therefore starts to approach a 2D rather than 3D shape as a test progresses w.r.t. time.

Furthermore protection against wear approaches 2D rather than 3D processes since:

- Adsorption is a surface phenomena.
- Surface oxidation a quasi-surface phenomena since the layer thickness limits further reaction with limited diffusion of reacting species across the layer.

4.2.4. Wear scar appearance

Each lubricity concentration level will be presented separately. This is done to limit confusion since different mechanisms might dominate at different PA concentrations. Although it is important to compare observations between different PA concentrations it should be noted that whilst one mechanism or parameter might be clear at one concentration, it might be completely indistinguishable at another concentration due to other mechanisms being promoted by the new conditions.

The specimens are first shown in a "as-removed" state where the wear debris is still clearly visible on the scars and tracks. Wear debris is inclined to be more highly concentrated around the track on the disk than around the ball. This is due to gravitational effects.

The specimens are then cleaned of any loose debris and wiped clean with n-hexane soaked tissue paper and shown again. This is to show which oxide particles are loose and which are adherent to the surface.

Although reference will be made to Raman spectroscopy results here, it will not be discussed in detail as this forms part of Section 4.4 which deals with Raman spectroscopy.

Note: The wear scar is located on the ball (top specimen) and the wear track is located on the disk (bottom specimen).

4.2.4.1. Surface appearance: 100 ppm

In Table 4.2.1 and 4.2.2 the wear scar and track appearance for 60 °C and 80 °C are presented respectively for 100 ppm PA.

There seems to be a very slight increase in wear debris around the track at higher water content. No visible difference is observed for debris around the ball. This is true for both temperatures. This could be indicative of higher wear rates if it could be assumed that wear particle sizes are similar at the different water concentrations.

At this low level of lubricity bright flat surfaces are easily formed on the wear scar. These are assumed to be nascent metal or very thin oxide layers since no oxides could be detected on these bright areas using Raman spectroscopy. The high reflective nature is typical of nascent metal. The reflective surfaces could result from inadequate lubricity protection. As the water vapour pressure increases there is a clear decrease in the size and occurrence of these regions with an increase of some layer being observed. Raman spectroscopy revealed these darker regions to be iron oxides.

When considering the disk track a significant unevenness is observed at lower water vapour pressures. This unevenness appears to be decreasing at higher water vapour pressures. It is suspected that these uneven areas act as stress concentrators resulting in the observed nascent metal formations on the disk wear scar. This could explain why it would appear that more oxides appear at higher water content. At higher water content loads are more evenly distributed on the surface and therefore the oxides are not selectively removed at points of stress concentration. Due to the unevenness of the track area it could be false to conclude

that oxide growth is enhanced, at higher water vapour pressure, simply by looking at the wear scar.

What is interesting however is that the wear scars seem to get bigger horizontally to a greater extent than vertically (direction of movement). This is due to the debris build up on the side of the track, along the length. The same does not occur along the track width due to the movement being perpendicular to that edge.

What exactly causes the unevenness is unknown at this point. Its occurrence however is associated with a combination of low lubricity, higher temperatures and water.

Table 4.2.1: The effect of water vapour pressure on the wear scar appearance (100 ppm, 60 °C, run 1)

	Wear scar	Wear scar - cleaned	Wear track	Wear track - cleaned
0,30 kPa	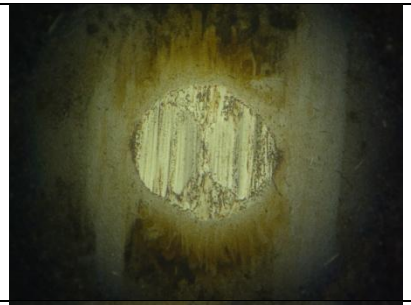		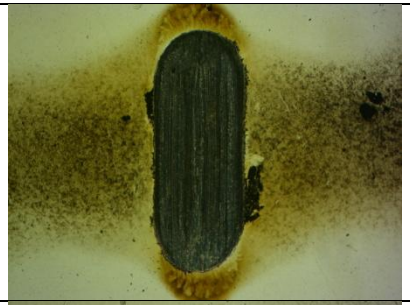	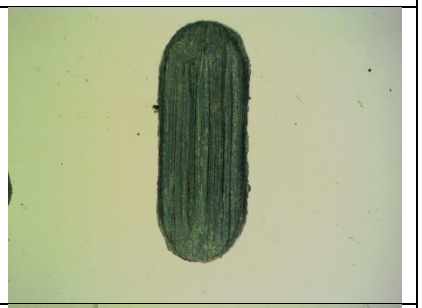
1,42 kPa			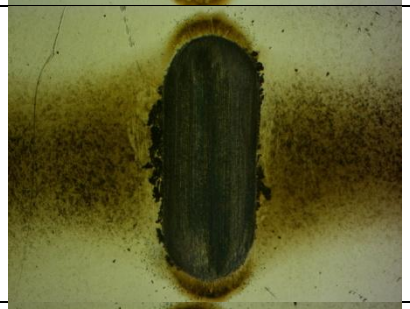	
2,10 kPa	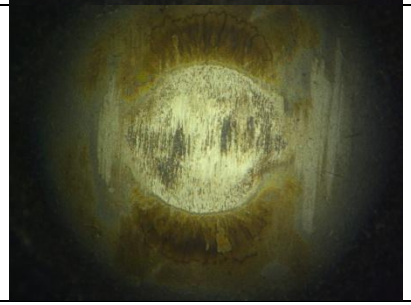	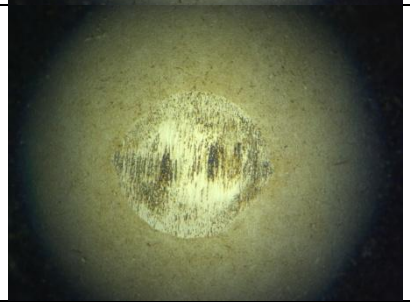	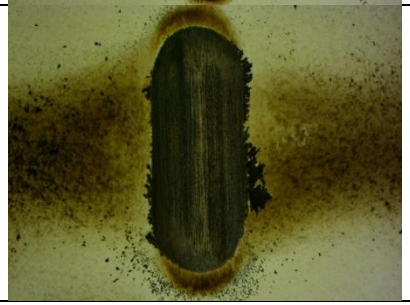	

Table 4.2.2: The effect of water vapour pressure on the wear scar appearance (100 ppm, 80 °C, run 1).

	Wear scar	Wear scar - cleaned	Wear track	Wear track - cleaned
0,36 kPa	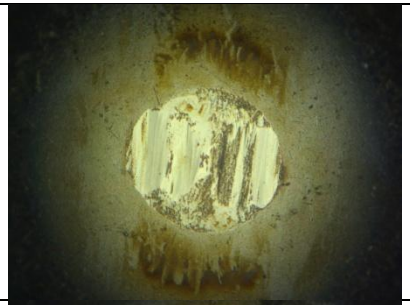			
1,34 kPa		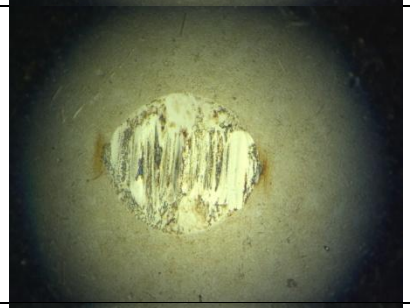	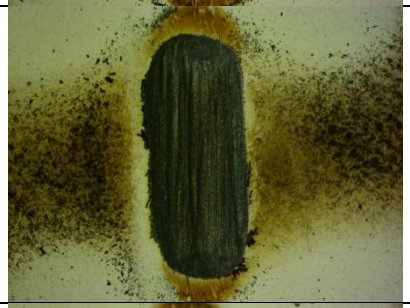	
2,22 kPa	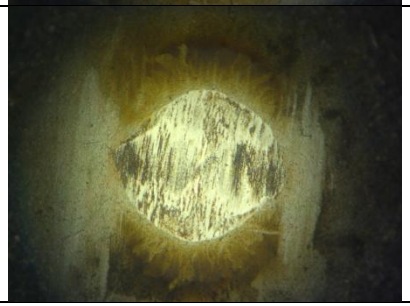	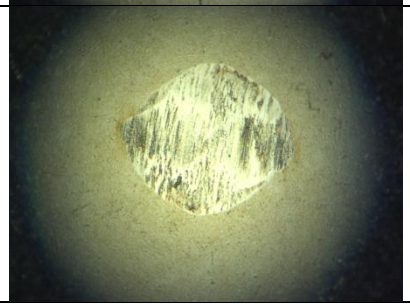	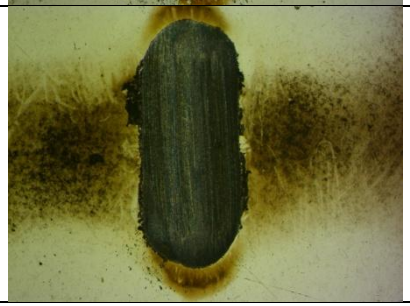	

4.2.4.2. Surface appearance: 250 ppm

In Table 4.2.3 and 4.2.4 the surface appearance for runs at 60 and 80 °C are presented respectively, at 250 ppm PA. No clear trend is observable in the amount of wear debris on the ball or the disk.

At both temperatures the wear scar surface shows the same change in surface area: The surface goes from (dark reddish → reddish/grey → grey) as the water content increases. Raman spectroscopy could not reveal any difference in the composition of these oxides. All were found to mostly consist of hematite. It therefore it is assumed that the colour differences are due to different oxide particle sizes and thicknesses:

- The change of darker red to lighter red oxide is likely indicative of less adherent hematite oxide. This is likely due to increased wear.
- Different colours of hematite, due to different particle sizes, are shown in Figure 4.2.18 below. This could possibly indicate that less of the smaller adherent oxide is present at higher water content. It would be easier to remove the smaller adherent particles than larger particles which would explain the change from red to grey at higher wear rates. This seems even more likely considering that smaller particles will form more towards the top of the oxides layers as these have grown for a shorter period of time. They would therefore be removed first. Do note that the red particles are adherent since they are not wiped from the surface.

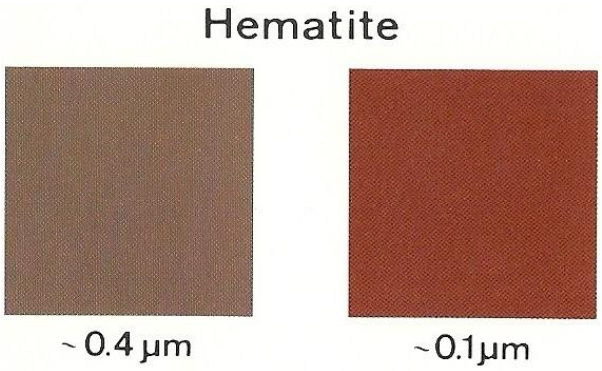

Figure 4.2.18: Changes in Hematite colour with different particle sizes (Schwertmann & Cornell, 1991: XIV).

The average oxide thickness is likely to be different for different PA concentrations since a unique equilibrium should exist. If water was to influence the effective PA concentration it could result in different oxide thicknesses.

Limited unevenness is observed on a few of the wear tracks at mid and low water content. The observed unevenness is to a far lesser extent than that observed for 100 ppm PA. The effect of this unevenness as stress concentrators is clearly observable on their wear scar counterparts.

Once again wear scars increased more significantly horizontally with increased water content than vertically.

Table 4.2.3: The effect of water vapour pressure on the wear scar appearance (250 ppm, 60 °C, run 1).

	Wear scar	Wear scar - cleaned	Wear track	Wear track - cleaned
0,36 kPa	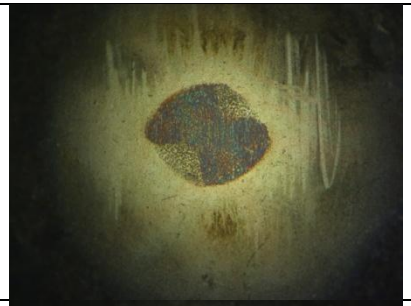	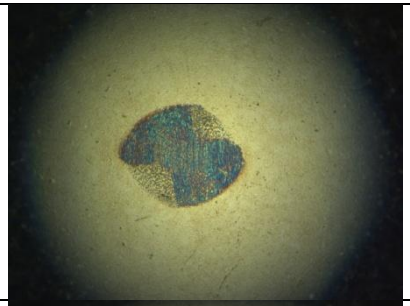		
1,42 kPa	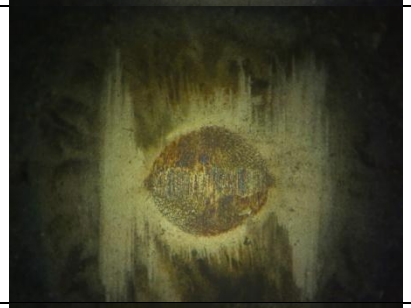	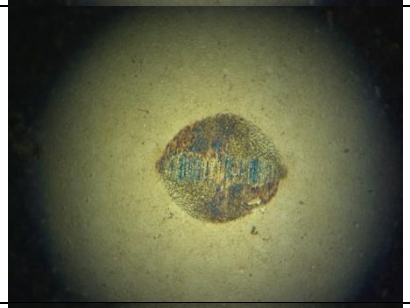	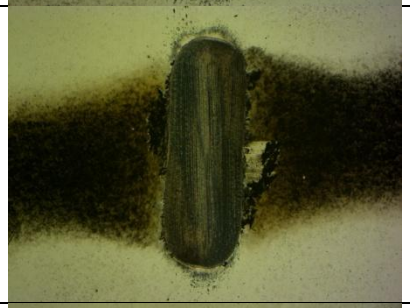	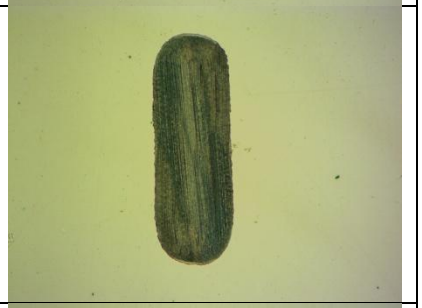
1,91 kPa	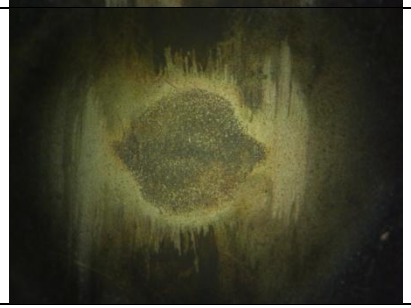		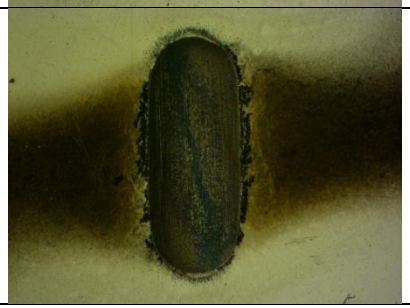	

Table 4.2.4: The effect of water vapour pressure on the wear scar appearance (250 ppm, 80 °C, run 1).

	Wear scar	Wear scar - cleaned	Wear track	Wear track - cleaned
0,38 kPa	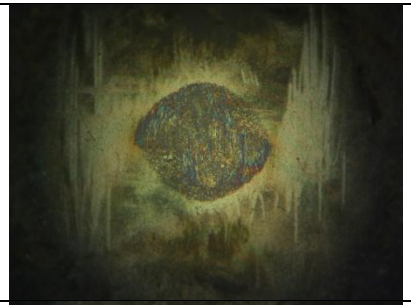	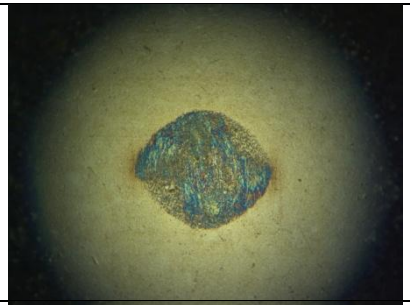		
1,35 kPa		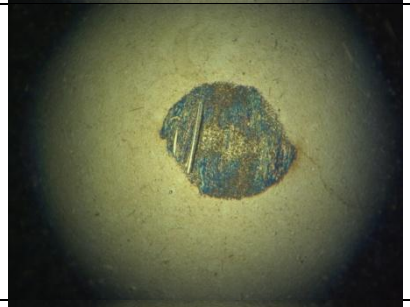		
2,16 kPa	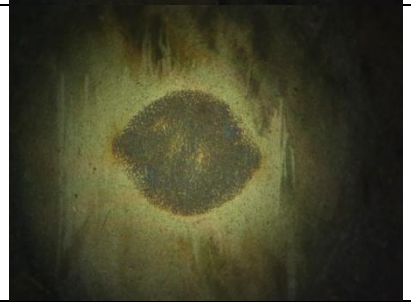	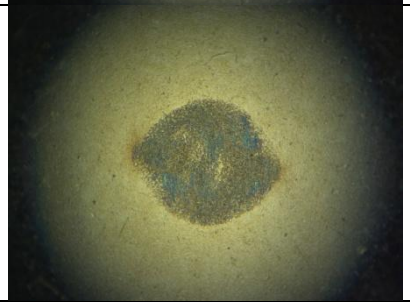		

4.2.4.3. Surface appearance: 2000 ppm

In Table 4.2.5 and 4.2.6 the appearance of wear scars at 60 and 80 °C are presented respectively, for 2000 ppm. At this high concentration of lubricity there is clearly an observable difference in the amount of wear debris around the disk track. There is more debris at higher water vapour concentration. The reason that the debris differences are clear at 2000 ppm PA and not at the lower PA concentrations is likely that at the lower PA concentrations so much debris is formed that the debris layers are too thick to differentiate optically.

What is very interesting is the increased presence of red debris on the wear scar itself at higher water content. This has not been seen at the lower PA concentrations. This is likely due to the decreased friction at higher PA concentrations not effectively removing the debris from the contact. This would then result in the debris being further reduced in size resulting in the more red like colour. There is a clear increase in the red debris with higher water content, likely due to increased wear. The red debris is easily wiped from the surface with a towel as can be seen. They are therefore not significantly adherent to the surface.

When considering the wear scar appearance there is a decolouration from dark to slightly dark red with increasing water vapour pressure. This again could be indicative of less iron oxide being present from increased wear.

The disk track however seems to be slightly darker at higher water vapour pressure possibly due to increased oxidative wear. This would however be contradicting to results thus far. The slight difference is attributed to differences of the illuminating source as can be seen by the differed in background colour.

Table 4.2.5: The effect of water vapour pressure on the wear scar appearance (2000 ppm, 60 °C, run 1).

	Wear scar	Wear scar - cleaned	Wear track	Wear track - cleaned
0,39 kPa	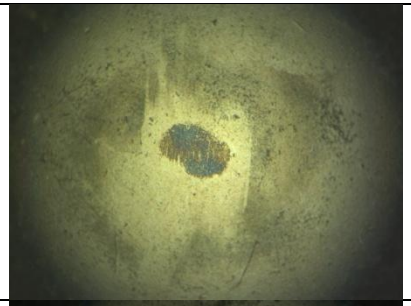	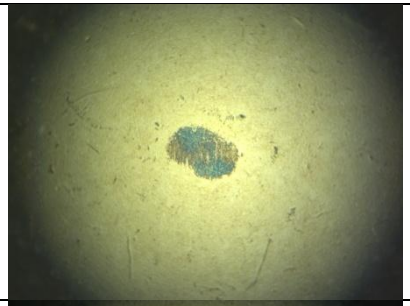	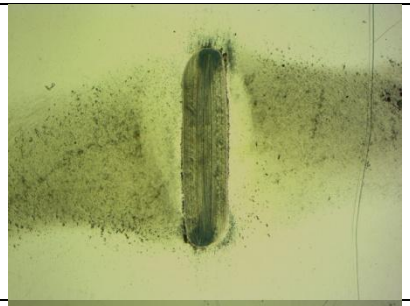	
1,39 kPa	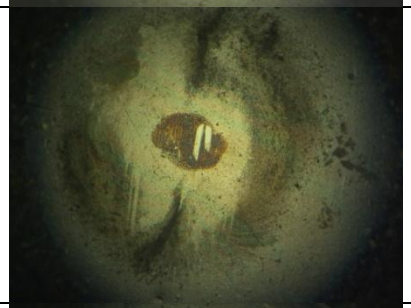	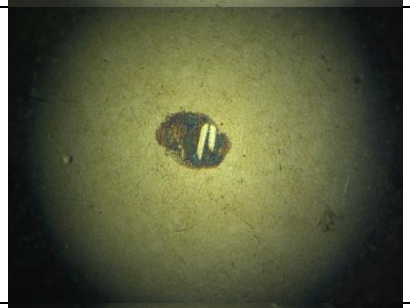		
2,14 kPa	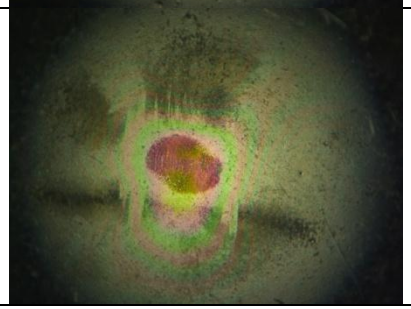	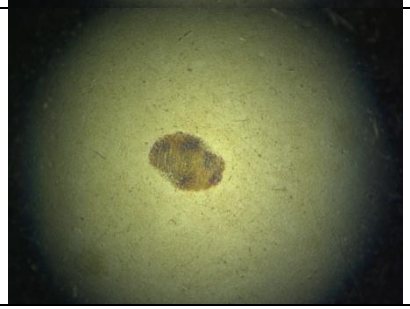		

Table 4.2.6: The effect of water vapour pressure on the wear scar appearance (2000 ppm, 80 °C, run 1).

	Wear scar	Wear scar - cleaned	Wear track	Wear track - cleaned
0,37 kPa		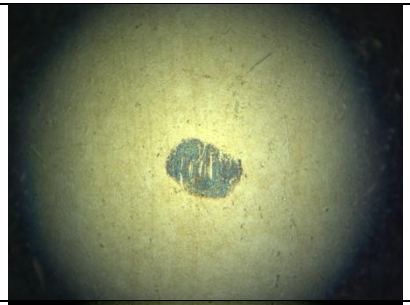	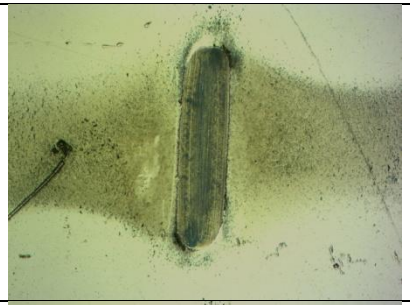	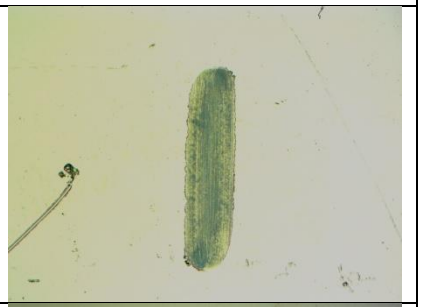
1,37 kPa		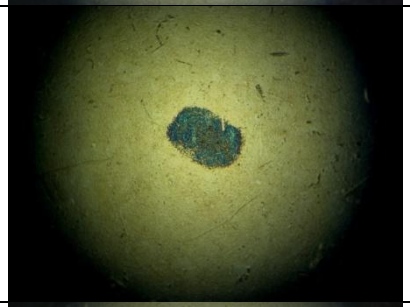	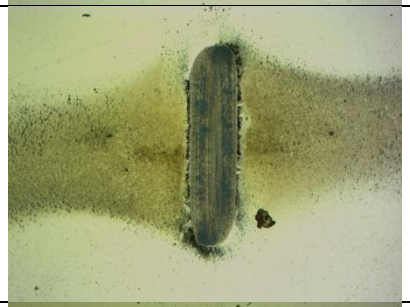	
2,11 kPa	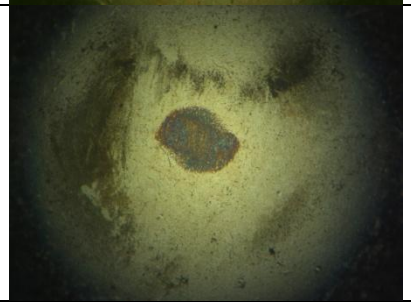	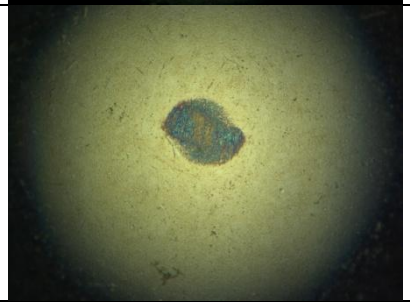		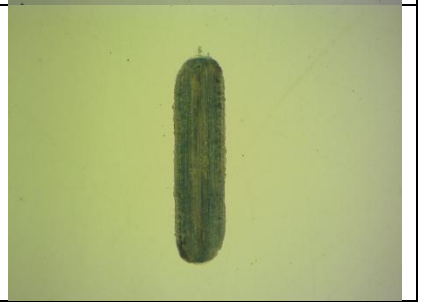

4.2.5 Summary of the effects of water content on wear testing

Considering all measured parameters it would appear that water molecules decrease the adsorption of PA on the contacting surfaces. This leads to increased wear with increasing water which is observable in:

- Higher friction coefficients resulted at higher water content, indicating more adherent contacting surfaces due to lowered functional lubricity.
- Lower ECR readings, indicating less lubricating protection from a formed layer.
- Larger MWSD indicative of higher surface wear rates.
- More wear debris on the track is observed at 2000 ppm PA with increasing water.
- A change in surface appearance at all lubricity levels:
    - At 100 ppm the observation of oxides is not clear due to the effects imposed by the unevenness of the wear track.
    - At 250 ppm less adherent oxide appears to be visible.
    - At 2000 ppm less adherent oxide appears to be visible.

If it can therefore be assumed that less adherent oxide is present, which could be due to:

- Water affecting oxide growth kinetics resulting in less adherent oxide scale from higher oxidative wear. No iron oxyhydroxides were however detected using Raman spectroscopy. This does not mean that they do not occur, only that if they occur, they do so to a far lesser extent than the iron oxides. This would therefore not seem likely to have a large influence.
- Water affects adsorption of PA, reducing the effective adsorption leading to higher removal rates of oxide.

It was previously noted in Section 2.5 that both water and PA can adsorb onto iron and iron like surfaces chemically and physically. Since the contacting surface has a limited area these two chemical species are competing for surface interaction.

If water is to adsorb dissociatively onto iron an OH ligand forms with the additional hydrogen molecule attaching to a neighbouring oxygen to form another OH ligand. These ligands are known to be active sites for ligand exchange which could enhance

adsorption. If water was to however adsorb physically it would likely act to block adsorption of PA, reducing the lubricity of a formed film.

The nature of the surface determines if a molecule is to adsorb chemically or physically. It has been noted by (Loehle, *et al*, 2013) that nascent surfaces tend to induce chemisorption of fatty acids whereas oxidized metal surfaces tend to induce physisorption. If the same is true for water molecules in the n-hexadecane medium it would explain the reduced lubricity behaviour with higher water content.

It is noteworthy at this point to mention that dry and wet lubrication seems to be oppositely affected by humidity as far as wear behaviour is concerned. This is because two different mechanisms of protection are likely to occur in each case. Water could increase oxide/oxyhydroxide formation in a dry contact which is the mechanism of protection. In a wet contact however bulk water moisture is physically excluded by a non-polar medium. The small amount that can dissolve interferes with adsorption to a greater extent than that it helps with oxidation. This leads to increased wear.

It should also be noted that the protection presented by lubricating species results in much less wear than that afforded by only oxide layers.

4.3. Seizure load testing (SRV): Effect of water in solution

A seizure load test is a test, in which a point contact is continuously loaded in an incremental manner. The loading regime continues until a sudden rise in the friction coefficient is observed. This is indicative of a transition of mild wear to severe seizure wear. The load at which seizure occurs is known as the seizure load.

Seizure load testing is dependent on oxides being present to prevent adhesion of surfaces. It is onto these oxides that the lubricity-enhancing molecules more readily adsorb. Oxide growth is kinetically favoured at higher temperatures. Therefore it becomes difficult to differentiate between fuels of different lubricity levels at low temperatures. A single temperature (80 °C) was therefore utilized and 60 °C was excluded from the test matrix.

In Section 4.2 repeat runs for wear testing were presented separately as Appendix B. In this section they will be presented alongside the original runs. The reason for this is that behaviour during seizure can be unpredictable and a direct comparison between repeat runs will be more beneficial to the discussion and interpretation. It is also for the same reason that repeat runs are presented on the same page as the corresponding initial run.

4.3.1. Frictional responses and load carrying capacity (LCC)

In Figure 4.3.1 to 4.3.6 the friction recordings at three different water vapour pressures are presented for each lubricity additive concentration. Friction coefficient values are on the left hand scale whereas the load applied can be noted on the right-hand side of each figure. Note that the sudden rise in friction coefficient is indicative of the start of seizure.

- 100 ppm PA (LCC < 50 N)

For 100 ppm PA (Figure 4.3.1 and 4.3.2) all tests failed upon initiation since the friction coefficient did not drop below 0,3 within 30 seconds. This is clear from the

drop in the friction coefficient to zero as the test automatically stops and immediately starts again (at 30 seconds). The additive concentration was therefore not sufficient to result in acceptable protection. It was however decided not to stop the test at this point to see what observations could be made from this point onwards unto a second seizure point.

It is very clear for both runs that the influence of water was to prolong the time it took for the coefficient of friction to drop during the run-in period. This is likely due to the water interfering with the lubricating action of the PA on the newly formed oxides.

Water content did not affect the LCC value obtained since all 6 test failed during run-in. A second LCC value however revealed significant differences. High water content resulted in a larger second LCC values. At first glance it would therefore appear that water facilitates lubricity. The opposite however can be seen upon closer investigation.

The differences in friction coefficient are quite substantial, which is likely to have led to rapid increases in wear surface area at the higher water content. A larger area would have resulted in a lower average Hertzian pressure at the contact point. This would explain why the higher water content resulted in larger LCC values since a higher load is needed to obtain similar pressure conditions.

Another observation is that after the run-in period and initial failure there is a higher average friction coefficient at higher water content. The friction coefficient was also less stable for the high water content as the 'second' seizure load is approached. All these observations could indicate that the molecules act in a manner to reduce the efficiency of the lubricating molecules in a severely loaded contact.

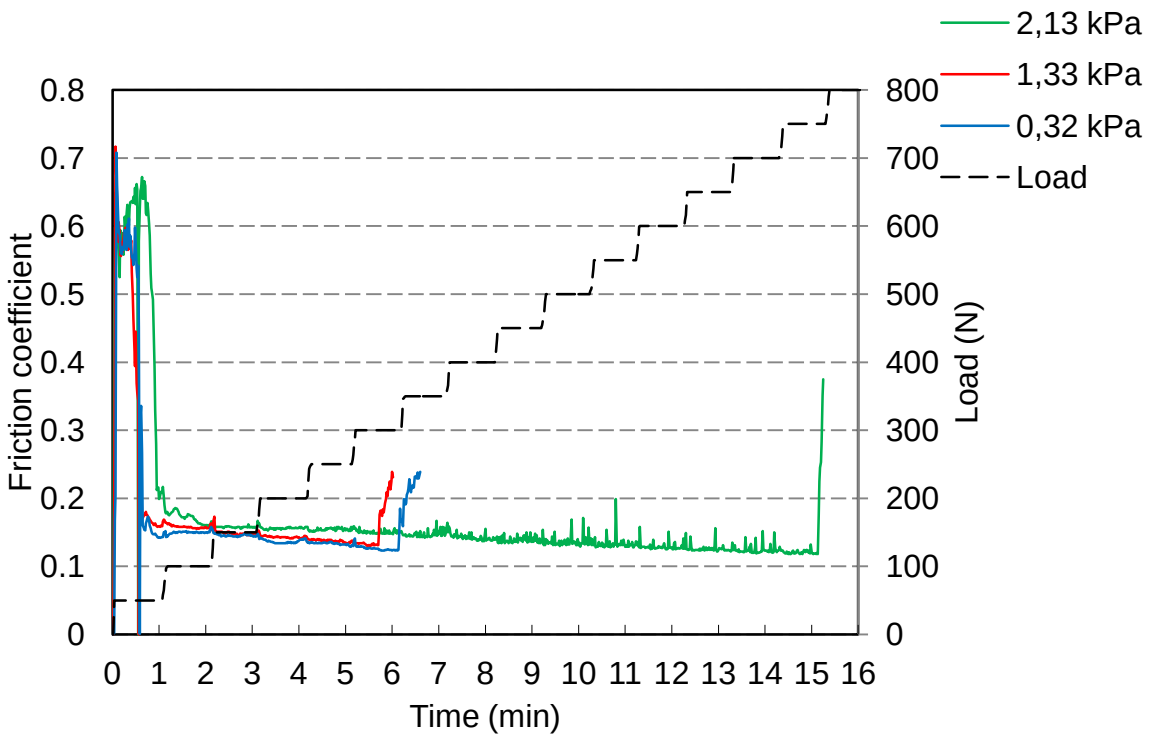

Figure 4.3.1: The effect of water content on the friction coefficient of a fuel seizure load test (100 ppm PA, 80 °C, run 1).

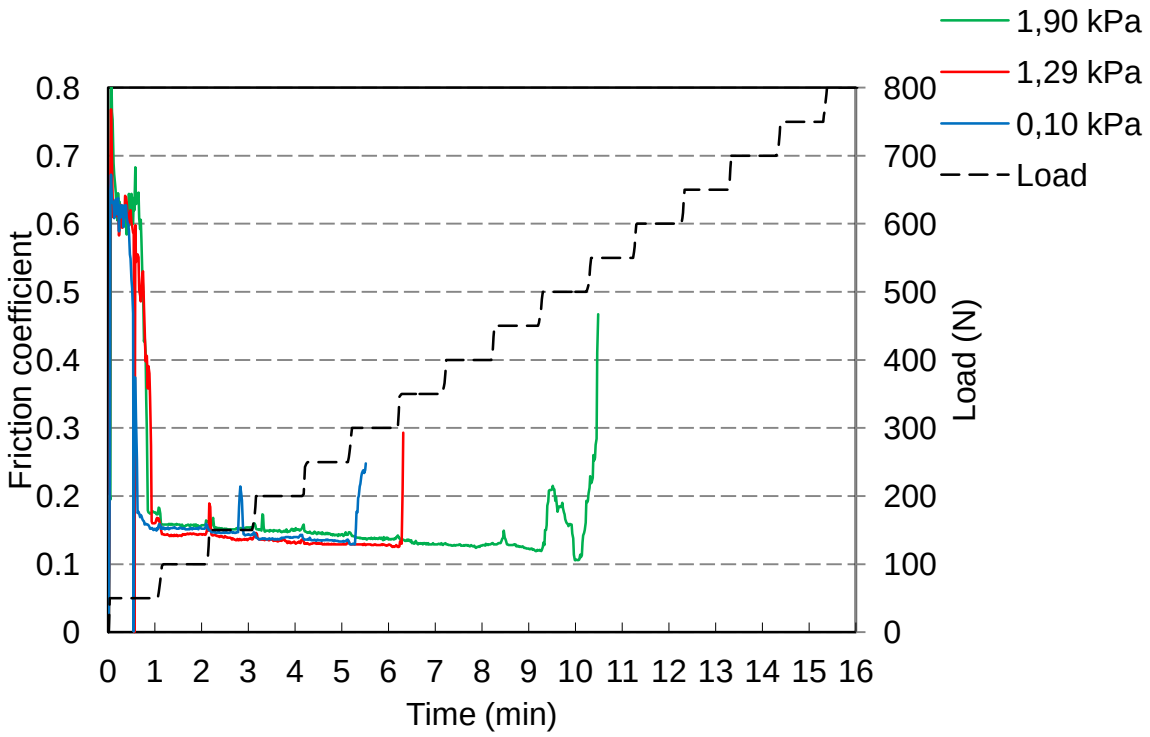

Figure 4.3.2: The effect of water content on the friction coefficient of a fuel seizure load test (100 ppm PA, 80 °C, run 2).

- 500 ppm PA (200 < LCC < 300)

In Figure 4.3.3 and 4.3.4 the friction coefficient at 500 ppm PA can be seen. These tests did not fail during the run-in period as can be seen. The tests would not seem very repeatable if the obtained LCC's are compared without carefully investigating the friction coefficient recordings.

Higher water content again resulted in high friction coefficients for prolonged durations during the run-in period. The differences at 500 ppm PA are however much less than what was previously observed at 100 ppm PA. This is true if one considers both the relative friction values and durations. The obtained LCC values would indicate that water reduces the lubricity performance of PA considering Figure 4.3.3. Although this might be true, Figure 4.3.3 is misleading if not considered in conjunction with the repeat runs in Figure 4.3.4.

In Figure 4.3.4 (run 2) the highest water content (green) fails at a similar load than it did in Figure 4.3.3 (run 1). The two lower water content (blue and red) samples however failed at a lower value than their run 1 counterparts, but at a similar LCC as the higher water content (green) samples. Upon re-evaluation of Figure 4.3.3 it can be seen that smaller peaks were observed at similar positions for the two lower water content (blue and red) samples in Figure 4.3.4. These observations could indicate the negative effects of water on lubricity. Water interferes with lubricity performance. It is postulated that the 500 ppm PA fuel inherently fails around 200-300N , but water affects the value as follows:

- In Figure 4.3.3 water acts to increase the severity of the seizure point. Therefore the high water content clearly causes failure at the mentioned load range. Lower levels of water can act to decrease the severity of seizure point. It could then appear to not have seized allowing the test to continue to a second seizure point.
- In Figure 4.3.4 it is however clear that higher and medium water content showed seizure faster that the lowest water content sample.

An interesting observation is that for the highest water content run 1 had a more severe run-in period and a more definitive seizure than run 2. This is likely due to the fact that the water content of run 1 was somewhat higher than that of run 2.

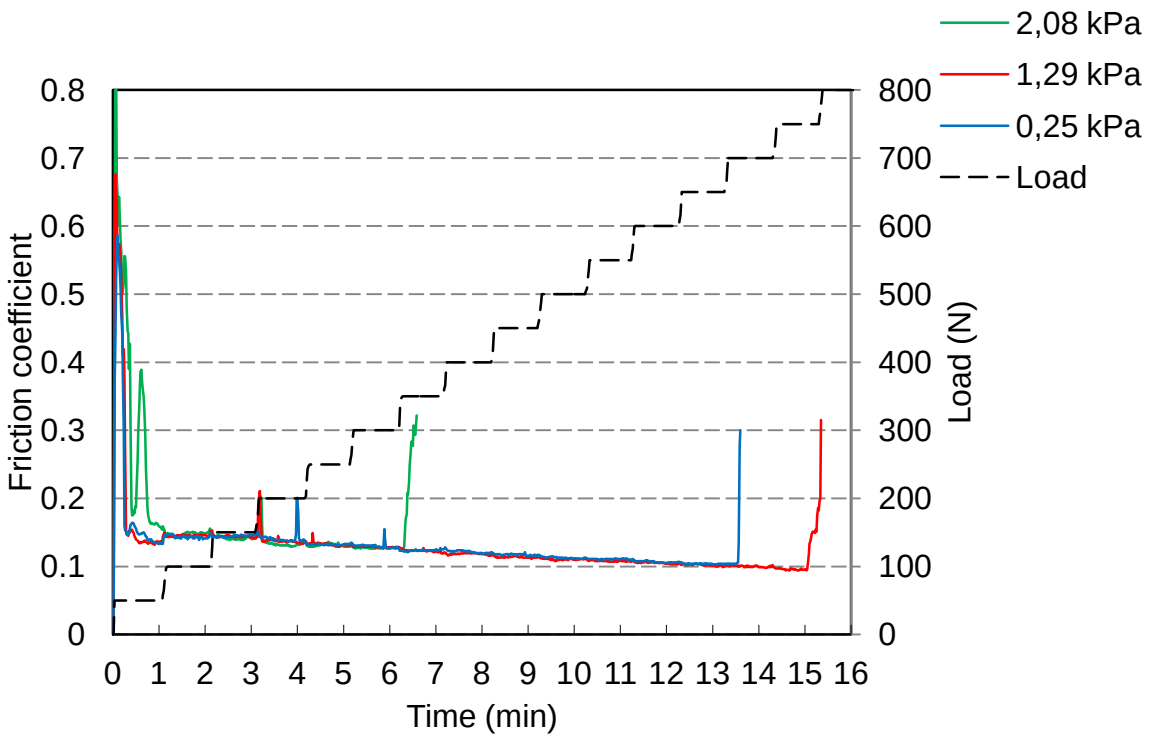

Figure 4.3.3: The effect of water content on the friction coefficient of a fuel seizure load test (500 ppm PA, 80 °C, run 1).

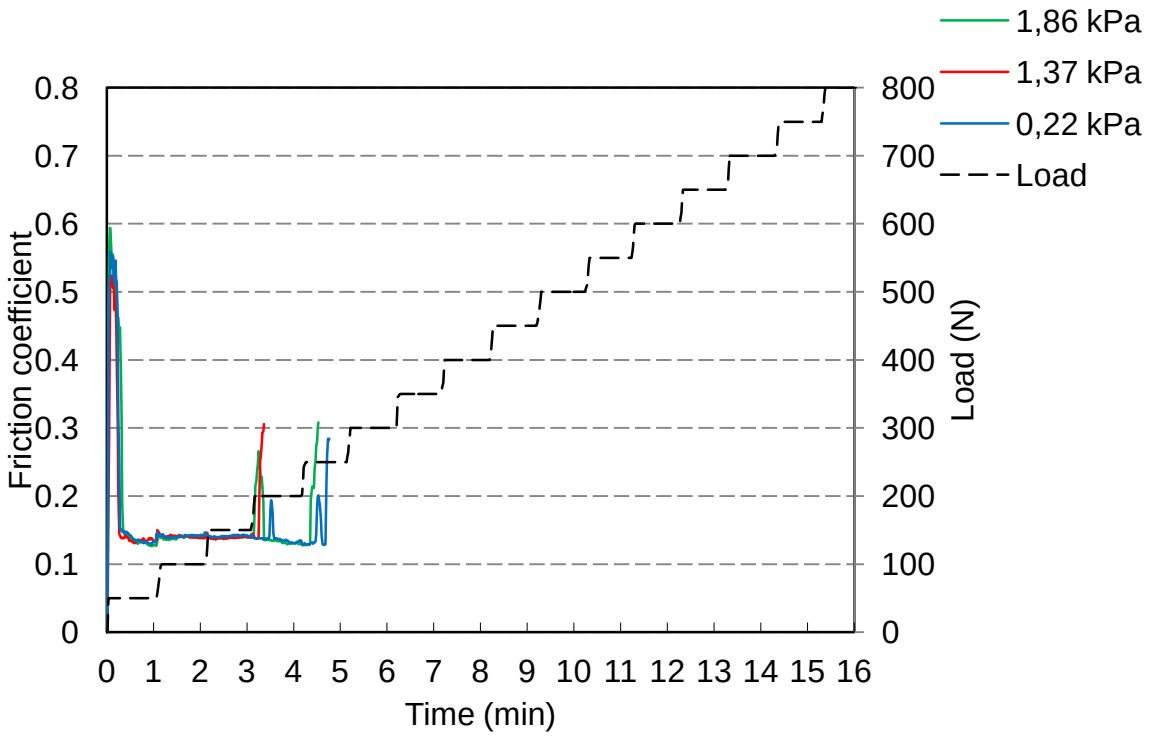

Figure 4.3.4: The effect of water content on the friction coefficient of a fuel seizure load test (500 ppm PA, 80 °C, run 2).

- 2000 ppm PA (400 < LCC < 600)

In Figure 4.3.5 and Figure 4.3.6 the friction coefficients are presented for tests conducted at 2000 ppm PA. **DO NOT** compare Figure 4.3.5 and 4.3.6 visually with Figure 4.3.1 - 4.3.4 since the vertical scaling on Figure 4.3.5 and 4.3.6 is half of that used for Figure 4.3.1 - 4.3.4. This is done to illustrate differences which are clearly much smaller at higher concentrations, hence the need for smaller scales. The general order can safely be compared.

The drop in friction coefficient during the run-in period doesn't show an observable difference for the samples as the water content varies. This indicates that higher lubricity additive concentration test fuels are affected to a lesser extent by water molecules than lower lubricity test fuels.

However water still appears to diminish the effectiveness of the PA to some extent. Higher water content resulted in a more frequent occurrence of small peaks (Figure 4.3.5 and 4.3.6) and even a slightly lower LCC (Figure 4.3.6). Again note that these peaks are significantly smaller than those in previous figures due to scaling. These small peaks should not therefore be regarded as seizure points. From Figure 4.3.5 and 4.3.6 it would seem that at 2000 ppm the reported LCC should be roughly between 400 - 600 N.

It would seem from the friction coefficient recordings presented that water does not always change the apparent LCC, but when it does it seems to do so in a trend-wise manner. It is recommended that seizure load tests of fuel should always be repeated with careful inspection of friction coefficient recordings and water content.

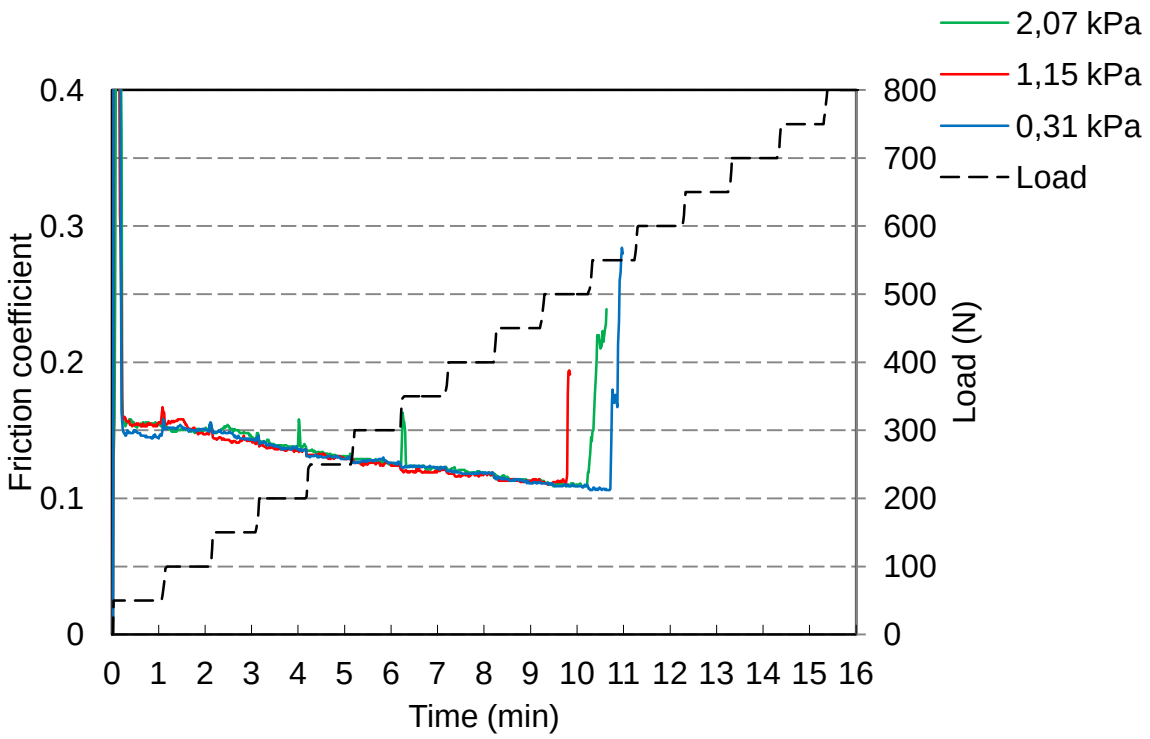

Figure 4.3.5: The effect of water content on the friction coefficient of a fuel seizure load test (2000 ppm PA, 80 °C, run 1).

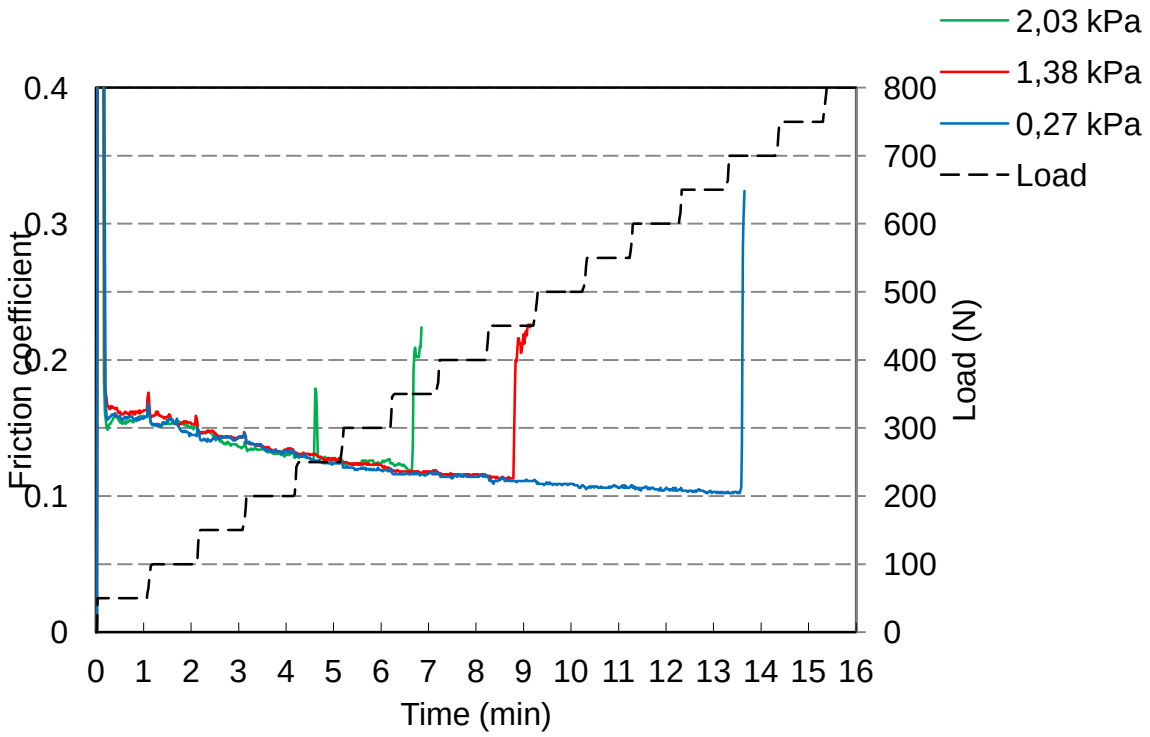

Figure 4.3.6: The effect of water content on the friction coefficient of a fuel seizure load test (2000 ppm PA, 80 °C, run 2).

4.3.2. Measured stroke

The measured stroke at three different water vapour pressures is presented in Figure 4.3.7 to 4.3.12 for each lubricity additive concentration. Measured stroke values are on the left hand scale whereas the load applied can be seen on the right-hand side of each figure. When the seizure point is reached the stroke will drop to zero, this continuous drop to zero is removed from the data to make graphs more readable and less cluttered. Any deviation up to that point can however still be observed in the data presented.

It will be observed that deviations tend to be negative from the set stroke of 1000 µm rather than positive. This is due to the nature of a forming seizure contact as the process is accompanied by progressive adhesion. Since more force is required to break these adhesive bonds compared to a normal stroke, there could be an excess of force if a weld point breaks unexpectedly leading to a positive deviation. This process will be referred to as stick-slip process in the remainder of this study.

For 100 ppm it will be recalled that tests failed during the run-in period. This is evident in Figure 4.3.7 and 4.3.8 again since the stroke falls to zero after 30 seconds. Allowing the test to run to a second seizure point revealed that there is a clear deviation, beyond normal, from the set stroke value at the highest water content. Deviation occurs more frequently as the second seizure point is reached.

Note that the amount of relatively larger positive deviations occur mostly at the highest water content (green).

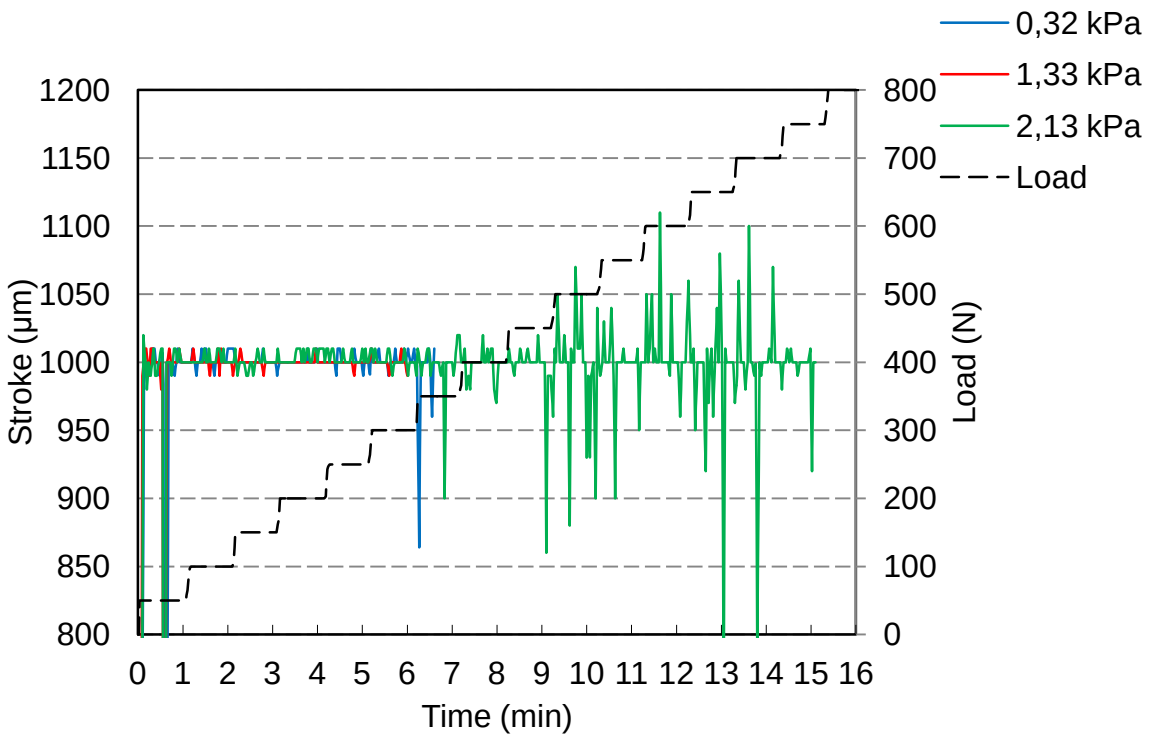

Figure 4.3.7: The effect of water content on the measured stroke of a fuel seizure load test (100 ppm PA, 80 °C, run 1).

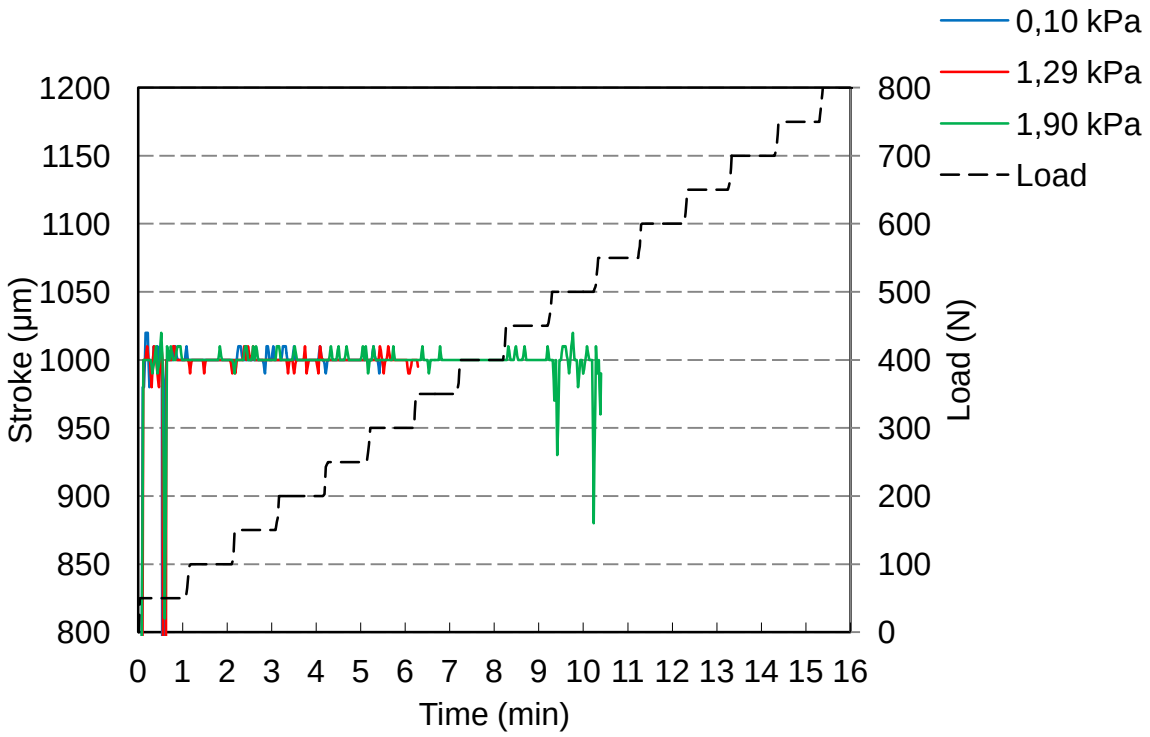

Figure 4.3.8: The effect of water content on the measured stroke of a fuel seizure load test (100 ppm PA, 80 °C, run 2).

In Figure 4.3.9 and 4.3.10 the measured stroke is shown at 500 ppm PA. Firstly it can be observed that large deviations occur to a much lesser extent than at 100 ppm PA. It furthermore will be noted in both figures that:

- At high water content (green) there are significant positive deviations beyond normal. Negative deviations are also observed in both figures, beyond normal.
- Medium water content (red) only showed a negative deviation in Figure 4.3.9, beyond normal.
- Low water content (blue) showed the least amount of negative deviation in Figure 4.3.9 but the most in Figure 4.3.10, beyond normal.

From these observations it would seem that the presence of water results in more deviation from the set stroke, beyond normal. This might be more observable if one considers that positive deviations only occurred at the highest (green) water content beyond normal, indicative of increased stick-slip conditions.

In Figure 4.3.11 and 4.3.12 the measured stroke is shown for 2000 ppm PA. Firstly it can be observed that large deviations occur to a lesser extent than at 500 ppm PA. It will be noted in both figures that:

- At high water content (green) there is both positive (initially) and negative (later) deviation in Figure 4.3.11 and only negative deviation (later) in Figure 4.3.12. The deviations mentioned are beyond normal.
- Medium water content (red) showed only negative deviation in Figure 4.3.12, beyond normal.
- Low water content (blue) showed only negative deviation in Figure 4.3.11, beyond normal.

From these observations it would again seem that the presence of water results in more deviation from the set stroke, beyond normal. This might be more observable if one considers that positive deviations only occurred at the highest (green) water content indicative of increased stick-slip conditions.

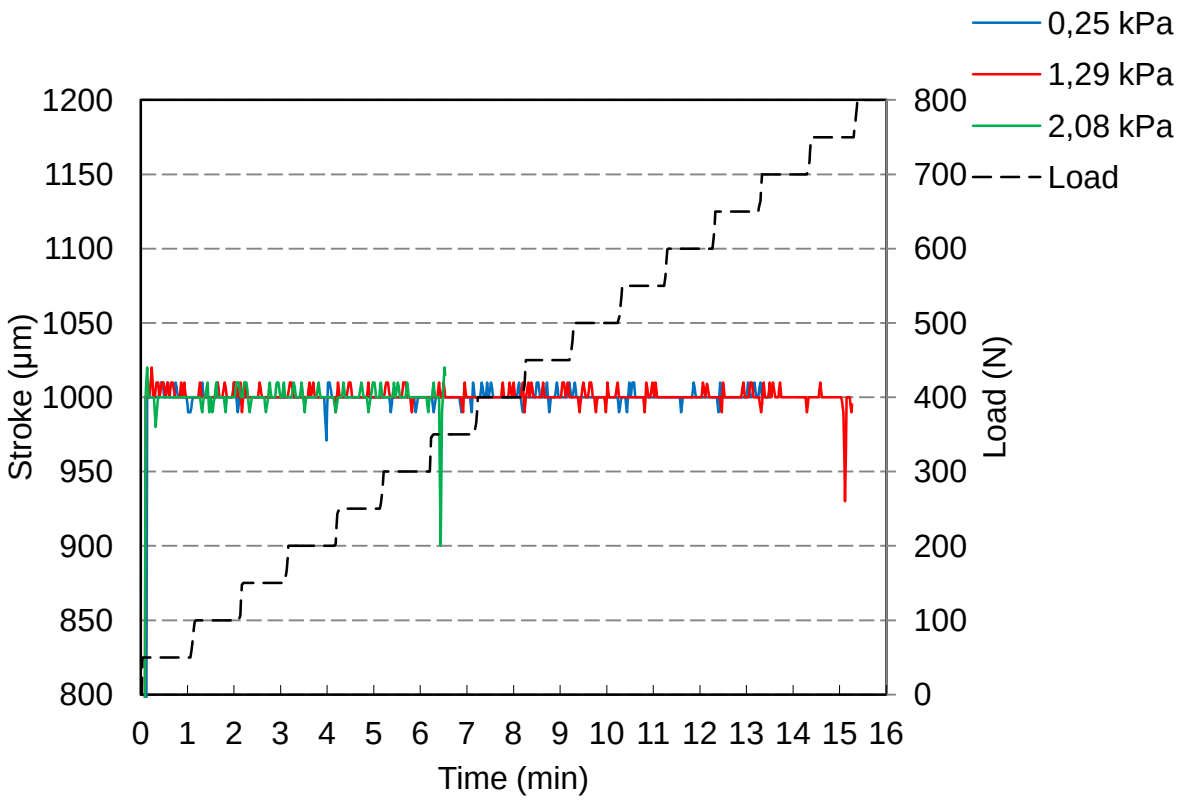

Figure 4.3.9: The effect of water content on the measured stroke of a fuel seizure load test (500 ppm PA, 80 °C, run 1).

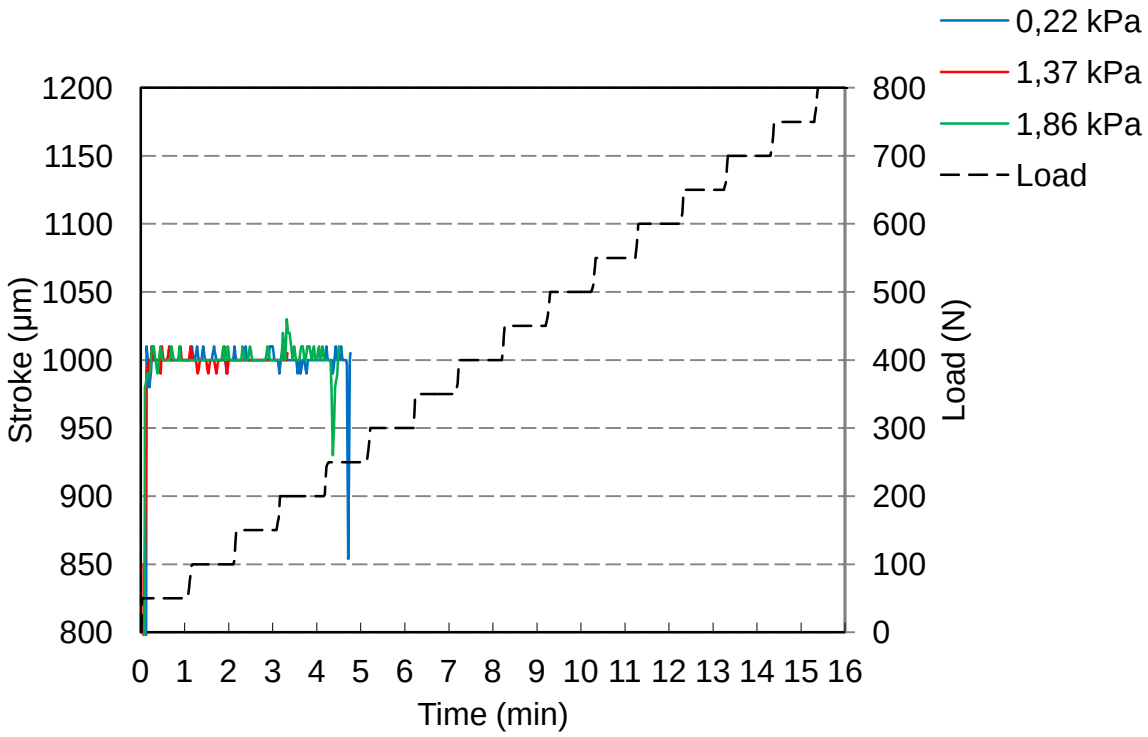

Figure 4.3.10: The effect of water content on the measured stroke of a fuel seizure load test (500 ppm PA, 80 °C, run 2).

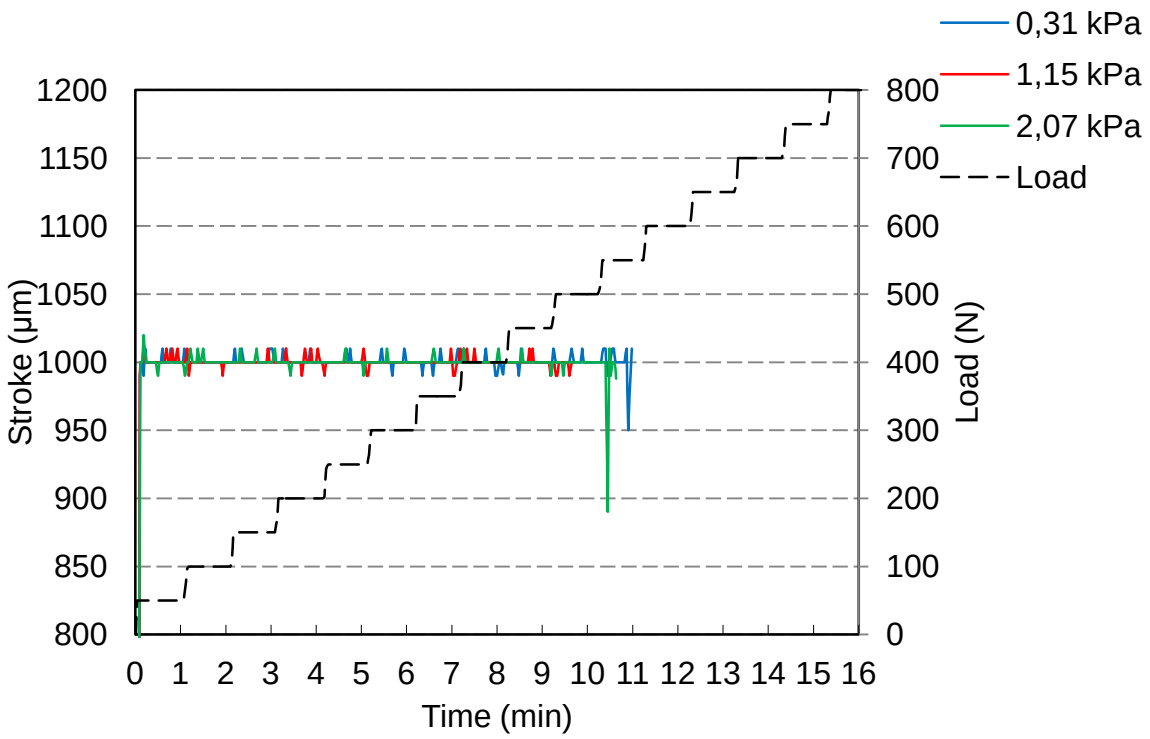

Figure 4.3.11: The effect of water content on the measured stroke of a fuel seizure load test (2000 ppm PA, 80 °C, run 1).

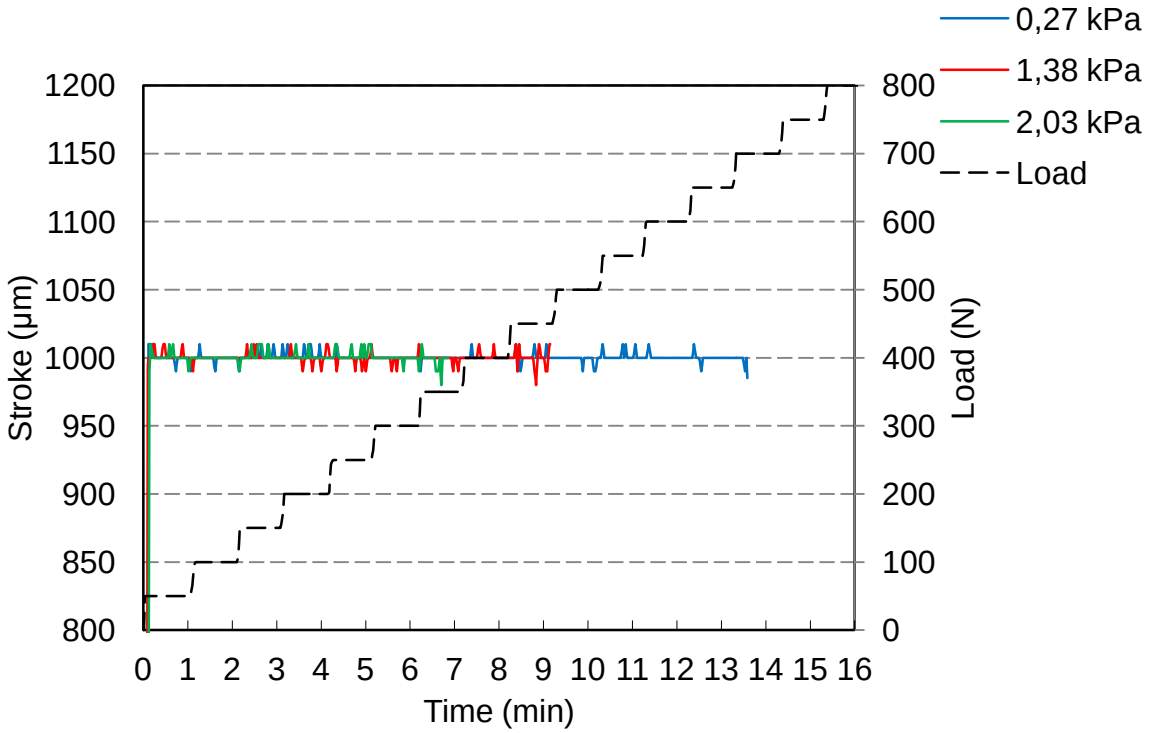

Figure 4.3.12: The effect of water content on the measured stroke of a fuel seizure load test (2000 ppm PA, 80 °C, run 2).

4.3.3. In-time height displacement (wear) measurement

The in-time height displacement at three different water vapour pressures is presented in Figures 4.3.13 to 4.3.18 for each lubricity additive concentration. Height displacement (wear) values are on the left hand scale whereas the load applied can be seen on the right-hand side of each figure. Note that each figure has a grey transparent section which indicates the area that data is allowed to be compared. Data outside this area can be misleading since not all tests run the same duration. Longer tests should generally result in higher end values which does not offer any new information. Relative positions within the transparent grey areas are of importance.

The wear measurement is based on a capacitive vertical displacement measurement, mounted near the top of the vertical loaded shaft of the SRV. Displacement is measured from the starting position of each test. Therefore the displacement is a sum of both the wear on the top (ball) and bottom (disk) specimen during the test. The resolution is 0,12 µm vertically.

One concern with this method is the thermal expansion of metal. If temperature control is poor it could lead to decreased wear measurements in heavier loaded or poor lubricity contacts compared to that of lower loaded or high lubricity contacts. In all figures in this section the reader will note that the controlled block temperature (thick horizontal) traces are plotted along with the measured wear (thin steps) with the corresponding colour. No significant deviations of block temperature were observed for any test as can be seen in Figure 4.3.13 to 4.3.18. This does not however mean that the contact itself was at exactly the same temperature. This is not measurable.

What can however be said is that up to this point all research in this complete investigation indicates that water should increase wear and this will be shown using the mentioned method. If the effects of the contact temperature were to be significant a decreased "false" wear measurement with increased water should have been observed. This however was not the case, reducing the stated concern that the method could be a poor indicator of actual wear.

In Figure 4.3.13 and 4.2.14 the in-time wear measurement at 100 ppm PA is presented. It can be seen in the two figures that low water content (blue) resulted in the lowest measured wear, whereas medium (red) and high water content (green) resulted in higher wear.

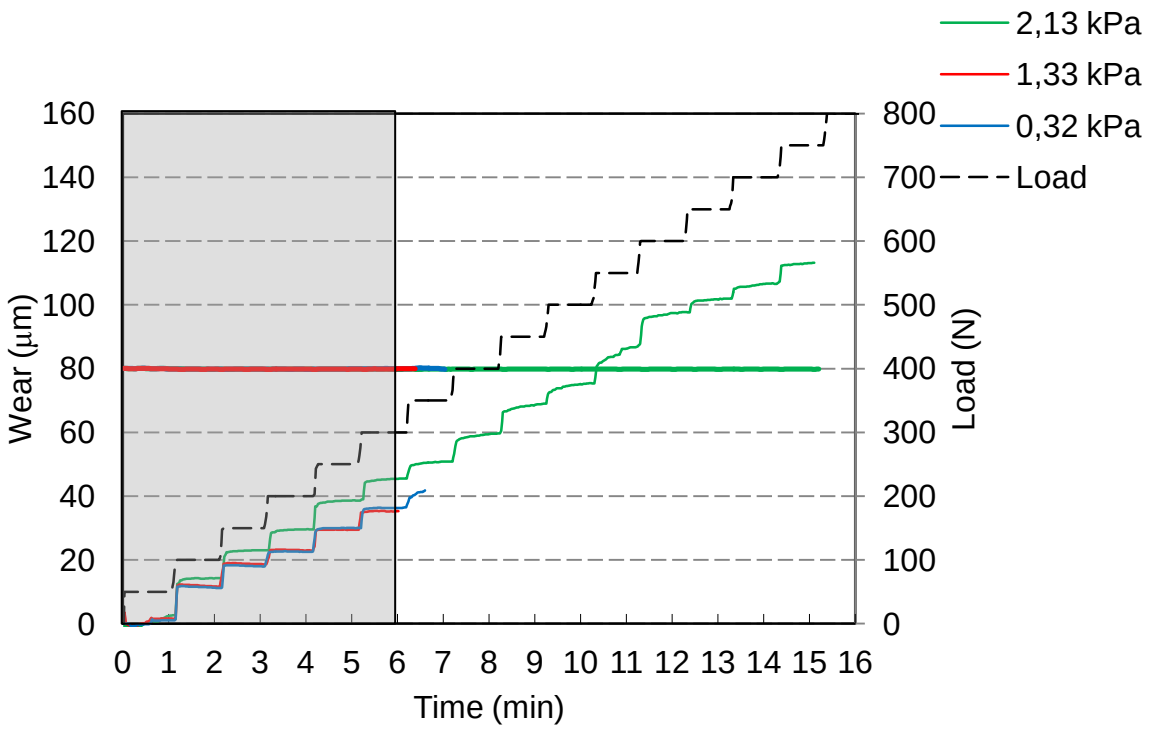

Figure 4.3.13: The effect of water content on the "In-time wear measurement" of a fuel seizure load test (100 ppm PA, 80 °C, run 1).

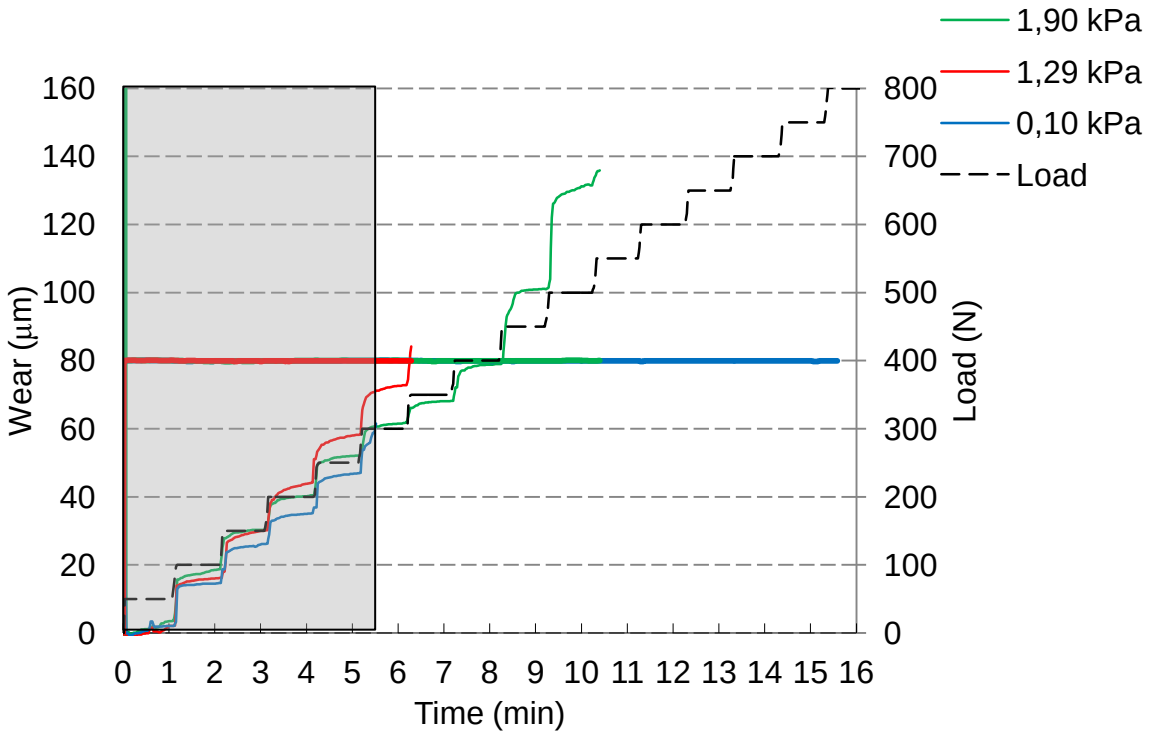

Figure 4.3.14: The effect of water content on the "In-time wear measurement" of a fuel seizure load test (100 ppm PA, 80 °C, run 2).

In Figure 4.3.15 and 4.3.16 the in-time wear measurement at 500 ppm PA is presented. For both figures it can clearly be seen that the measured wear increases with increasing water content (blue < red < green).

The same observation can be made for the in-time wear measurement at 2000 ppm PA presented in Figure 4.3.17 and 4.3.18. Measured wear can again be seen to increase with increasing water content.

It can therefore summarized that the effect of increased water content, on all tested concentrations was to increase the vertical displacement measurement which is indicative of increased wear.

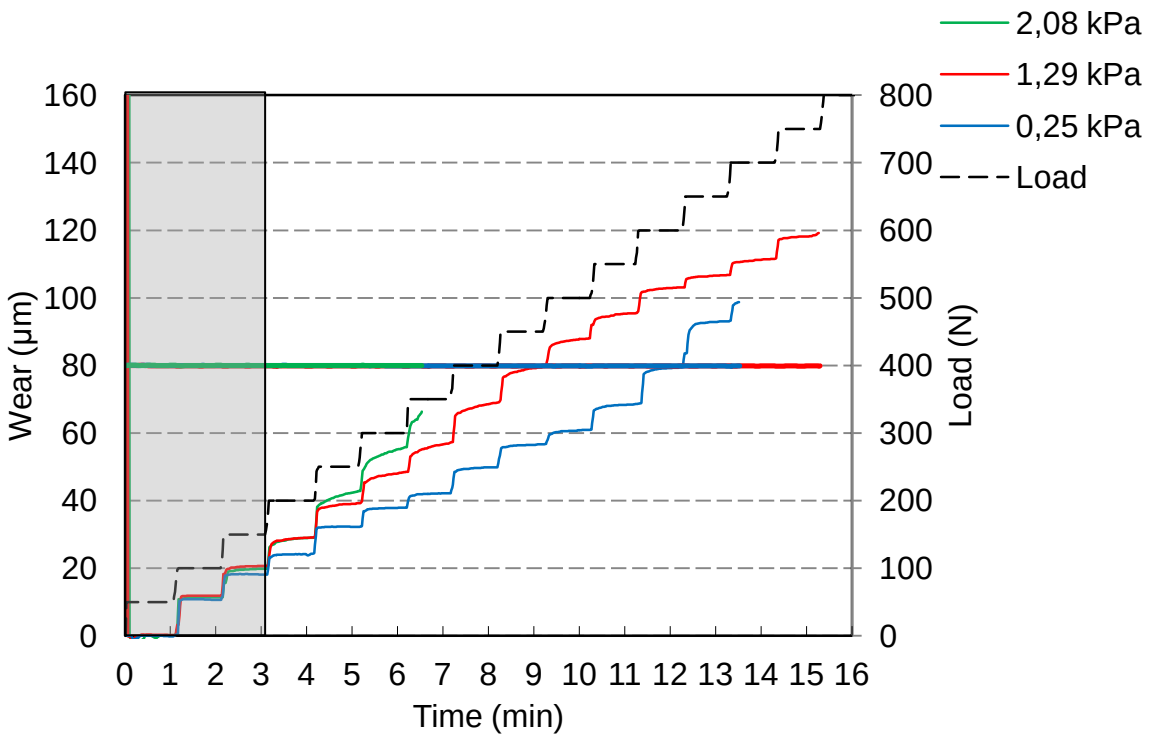

Figure 4.3.15: The effect of water content on the "In-time wear measurement" of a fuel seizure load test (500 ppm PA, 80 °C, run 1).

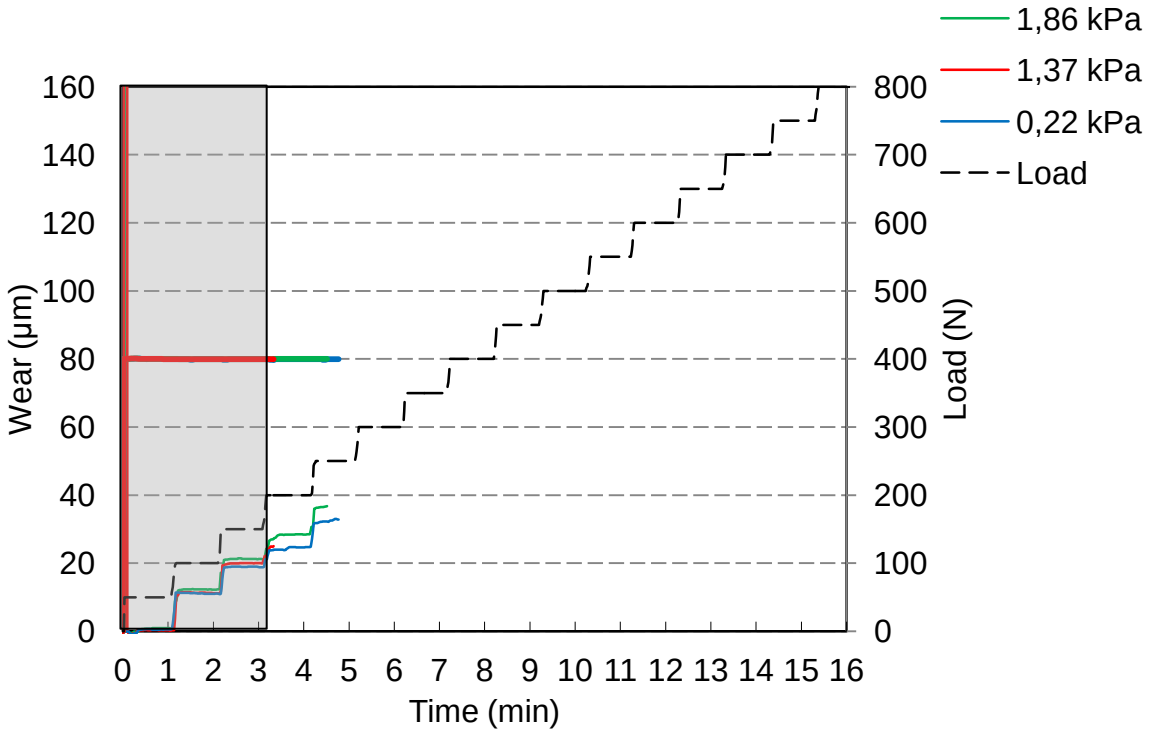

Figure 4.3.16: The effect of water content on the "In-time wear measurement" of a fuel seizure load test (500 ppm PA, 80 °C, run 2).

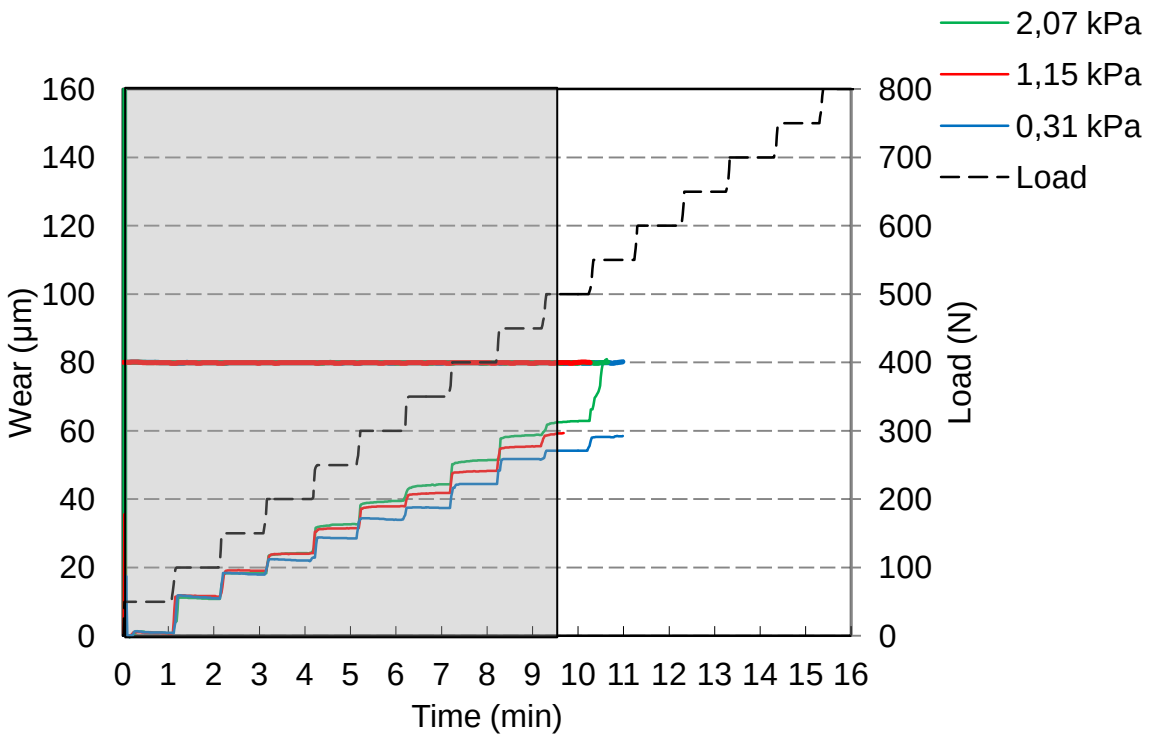

Figure 4.3.17: The effect of water content on the "In-time wear measurement" of a fuel seizure load test (2000 ppm PA, 80 °C, run 1).

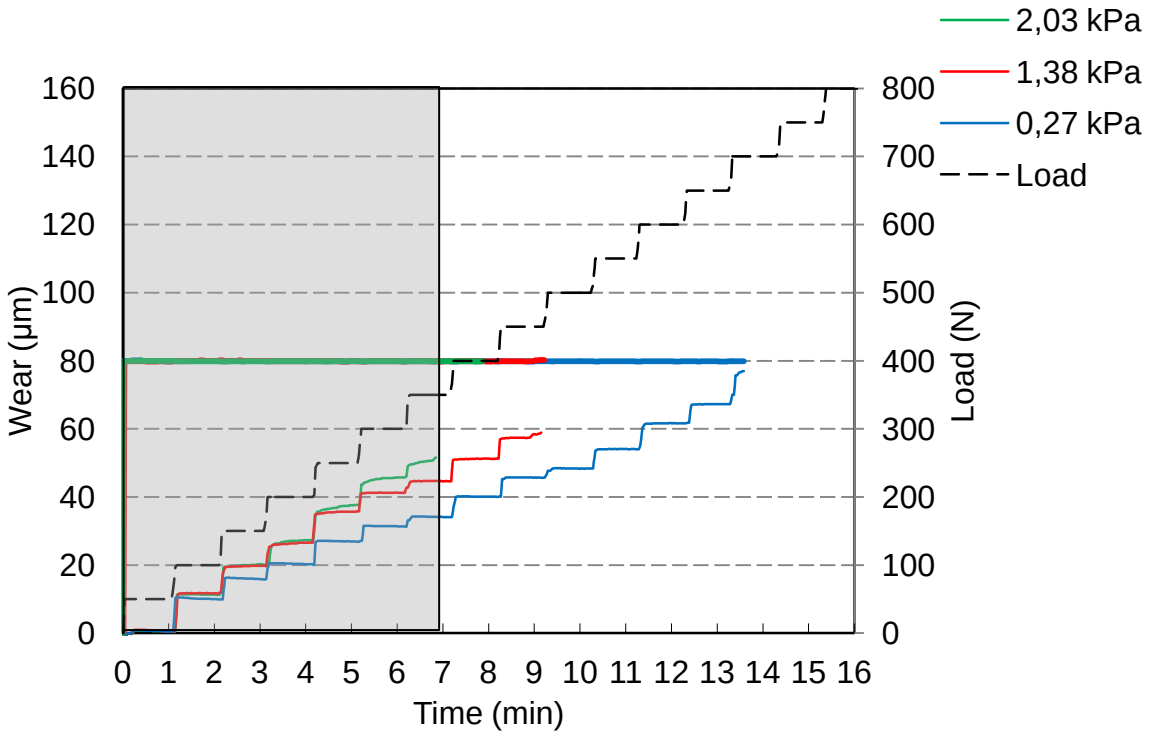

Figure 4.3.18: The effect of water content on the "In-time wear measurement" of a fuel seizure load test (2000 ppm PA, 80 °C, run 2).

4.3.4. Summary: the effects of soluble water content on seizure load testing

There is a clear effect of water on the seizure load testing of the test fuel. The following observations were made:

- There is an prolonged duration of higher friction during the run-in period at higher water content. If this period is significantly larger it will lead to over-evaluation of the seizure load due to the resulting larger surface area. The larger surface area requires a larger load for similar pressure conditions.
- There is an increased deviation of stroke at higher water content. This again is more significant for poor lubricity levels.
- The vertical displacement measurement is higher at higher water content which is indicative of increased wear.
- The effects of water on test parameters appears to be diminished at higher PA concentration.

In essence it appears that water disrupts the adsorption process of the PA onto contacting oxide surfaces. This leads to reduced lubricity performance which can affect the "observed" seizure load in two opposite ways:

- At extremely poor lubricity water could lead to over-evaluating the seizure load. This occurs if the run-in period occurs at a higher friction coefficient for a significantly longer period.
- At moderate and higher lubricity water could lead to under-evaluating the seizure load. This occurs because the water molecules act to reduce the adsorption of the PA lubricity molecules.

4.4 Raman spectroscopy of tribo-contact surfaces

Raman spectroscopy was done on the metal test specimens, after lubricity testing, to determine if any oxyhydroxides and oxides could be detected in the tribo-contact. Not all specimens were analysed:

- Analysis was only done on surfaces that formed during exposure to the highest and the lowest water content.
- Analysis was done for both wear tests (4.4.1) and seizure load tests (4.4.2).
- All palmitic acid (PA) concentrations were tested.
- Analysis was done on the wear scar (ball) and wear track (disk) of test specimens.

In the figures in this section (4.4) blue will be used to denote spectra of surfaces (wear scars or tracks). Warmer colours like red, yellow and brown will be used for spectra of debris (Loosely held surface particles). Green spectra will be used to illustrate the validity of the method. Each spectrum has a small accompanying picture with the analysed area being a small area in the centre of the picture. A description is also added. Spectra from literature can be found in Section 2.8, identification of species are based on these spectra.

Consider that the presence of a compound can be confirmed, while the absence thereof cannot, since the whole wear area is not analyzed. If a compound is however not observed in a large number of test it will be assumed unlikely to have been present in any of the regions.

4.4.1 Raman spectroscopy of wear tests

In Figures 4.4.1 and 4.4.2 Raman spectra are shown for wear tests at 100 ppm PA. The two figures are for 15% RH and 75% RH respectively.

Hematite could be identified for both high and low water content as is indicated. This is observed on both the surfaces and the debris. The four signature peaks at 220; 290; 400 along with the peak at 1310 cm^{-1} can easily be observed. In some instances two smaller peaks at 495 and 605 cm^{-1} can be observed. These smaller peaks only appear when the signature peaks are relatively large, compared to when they do not appear. This confirms their identity.

Magnetite could possibly be identified by the peak around 660-670 cm^{-1}. This is observed on both the surfaces and the debris. If it is magnetite, the peak should be around 670 cm^{-1}, but if it is due to some disorder it should be at 657 cm^{-1}. Therefore it is not clear if this is indeed magnetite since the smaller magnetite peaks cannot be identified. It could likely be a combination of magnetite and disorder.

Maghemite could be identified in the debris of 75%RH with the peak at 720 cm^{-1}. The other maghemite peak at 670 cm^{-1} coincides with the possible magnetite peak. This is clear since the peak at around 670 cm^{-1} appears slightly larger compared to the case when the other maghemite peak (720 cm^{-1}) cannot be clearly identified. Maghemite is an intermediate between a transformation of magnetite to hematite. This could confirm the presence of magnetite at low lubricity levels.

Carbon was identified in the debris of both tests but not on wear scars or tracks. These broad peaks occur around 1350 and 1500-1600 cm^{-1}. The broad peak at 1350 cm^{-1} coincides somewhat with the peak of hematite at 1310 cm^{-1}. One way of knowing that carbon is indeed still present is to observe an asymmetrical peak shape around 1350 along with a rise to the second peak at 1500-1600 cm^{-1}. Carbon can be present due to either residual petroleum products or more likely due to carbon from the metal specimen.

As mentioned previously in Section 2.5.4. iron oxides can be identified by colour. The colour of any object is however subject to the source of the light and should be kept in mind since this could possibly lead to discrepancies between different microscopes. Since multiple species are identified together a colour cannot easily be identified to be due to a single species. When a single or dominant species is however detected the colour observed is reported:

- Scars - Dark areas were confirmed to contain oxides whereas in light areas no oxides were detected. This confirms that light areas are likely visible due to the reflective nature of metal. It does not mean the areas are nascent, only that if an oxide layer is present it is much thinner than those generated during lubricity testing.
- Debris - A combination of brown, red, grey and black were observed. All these however contained a combination of species. Green and blue colours are likely due to the presence of residual petroleum products.

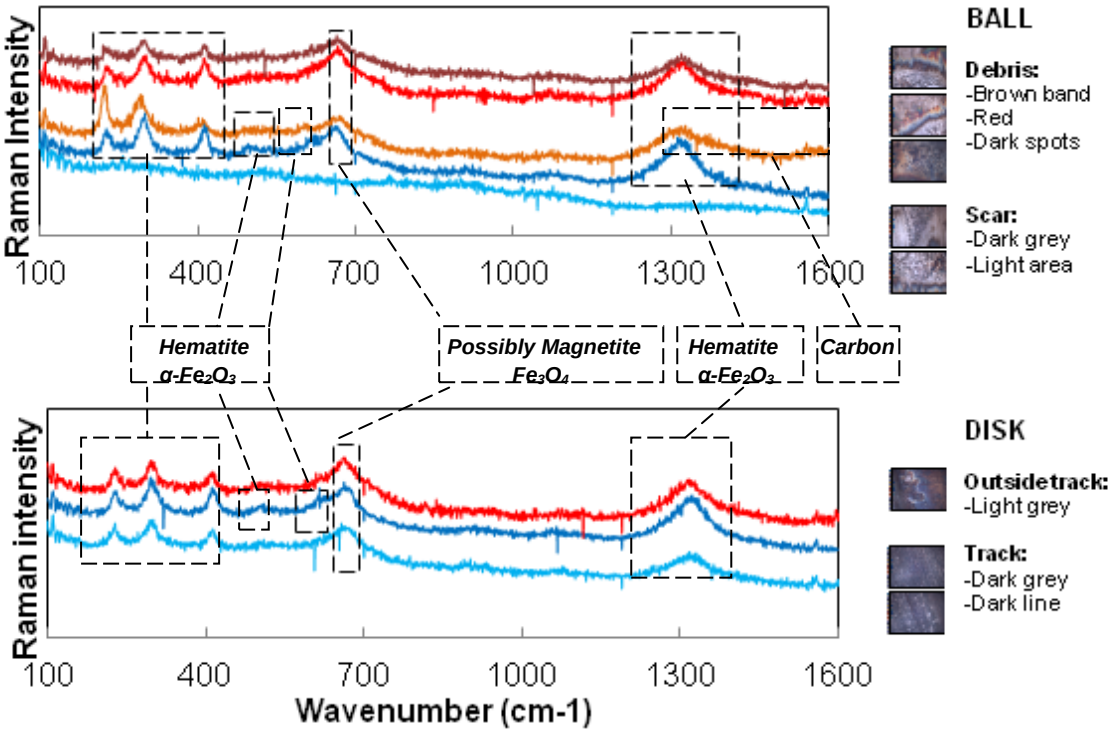

Figure 4.4.1: Raman analysis for a wear test, 100 ppm PA, 15% RH.

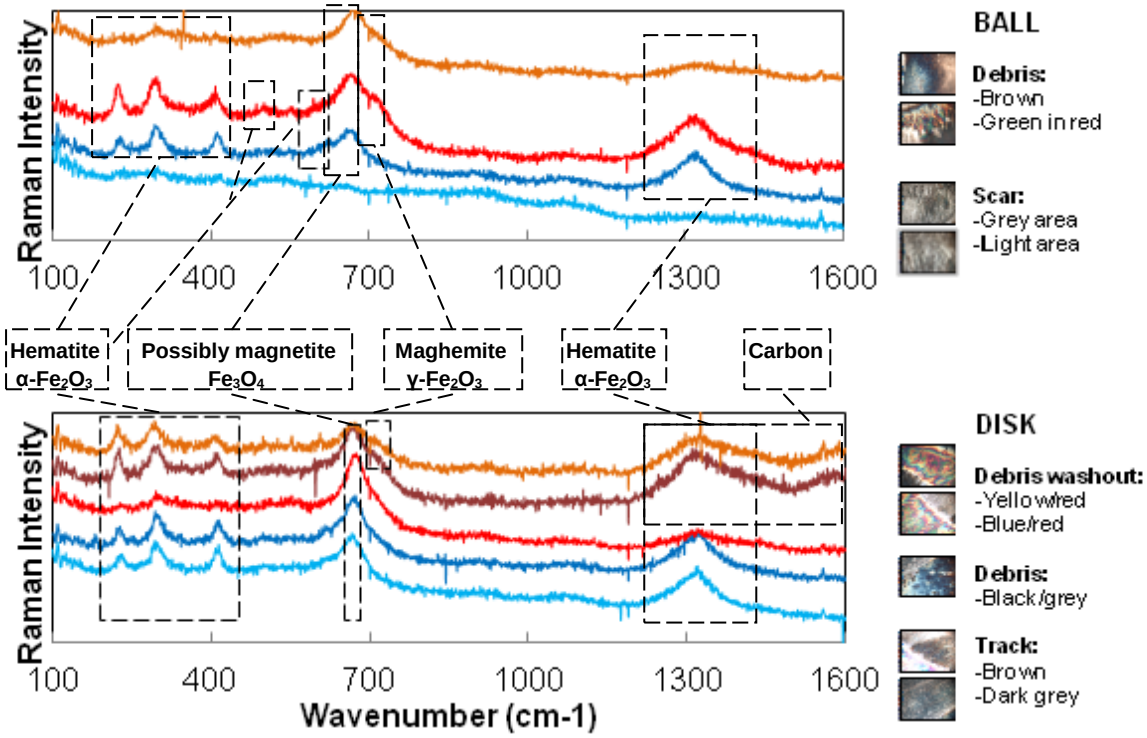

Figure 4.4.2: Raman analysis for a wear test, 100 ppm PA, 75% RH.

In Figures 4.4.3 and 4.4.4 Raman spectra are shown for wear tests at 250 ppm PA. The figures are for 15% RH and 75% RH respectively. The spectra in Figure 4.4.3 contain more noise due to light interference on the day of analysis. The noise around 1000 cm^{-1} is therefore of no significance.

- Hematite could be identified at both high and low water content as is indicated. This is observed on both the surfaces and the debris. The first hematite peak is larger than expected for some of the debris, but not on any of the adherent surfaces.
- Magnetite could possibly be identified by the peak around 660-670 cm^{-1}.
- No Maghemite could be identified.
- Carbon was identified in the disk debris of both tests but not on wear scars or tracks.

In Figures 4.4.5 and 4.4.6 Raman spectra are shown for wear tests at 2000 ppm PA. The figures are for 15% RH and 75% RH respectively:

- Hematite could be identified at both high and low water content as is indicated. This was observed on both the surfaces and the debris. The first hematite peak is larger than expected for some debris, but not for any of the adherent surfaces.
- Magnetite could possibly be identified by the peak around 660-670 cm^{-1}.
- No Maghemite could be identified.
- Carbon was not detected. There might be carbon in Figure 4.4.5 but this is not considered to be to any clear extent. If it is in fact carbon, the amount is much lower than for previous figures. This could be very significant as will be discussed later.

Although analysis presented up to this point was at a laser intensity of 150 mW, this was not initially the selected power. It was feared that the power could decompose oxyhydroxides into hematite or even convert metal into metal oxide. The first tests were done at 10 mW and two spectra are presented in Figure 4.4.5 and 4.4.6 in green. These spectra along with other did not indicate detectable levels of any oxyhydroxides. The low power did however produce peaks that were much less clear. Therefore a higher laser power of 150 mW was used to produce the data shown. This power was tested on a free spot (data in next sub-section) to show that it did not burn an oxide on a surface that did not have a detectable visible oxide layer before.

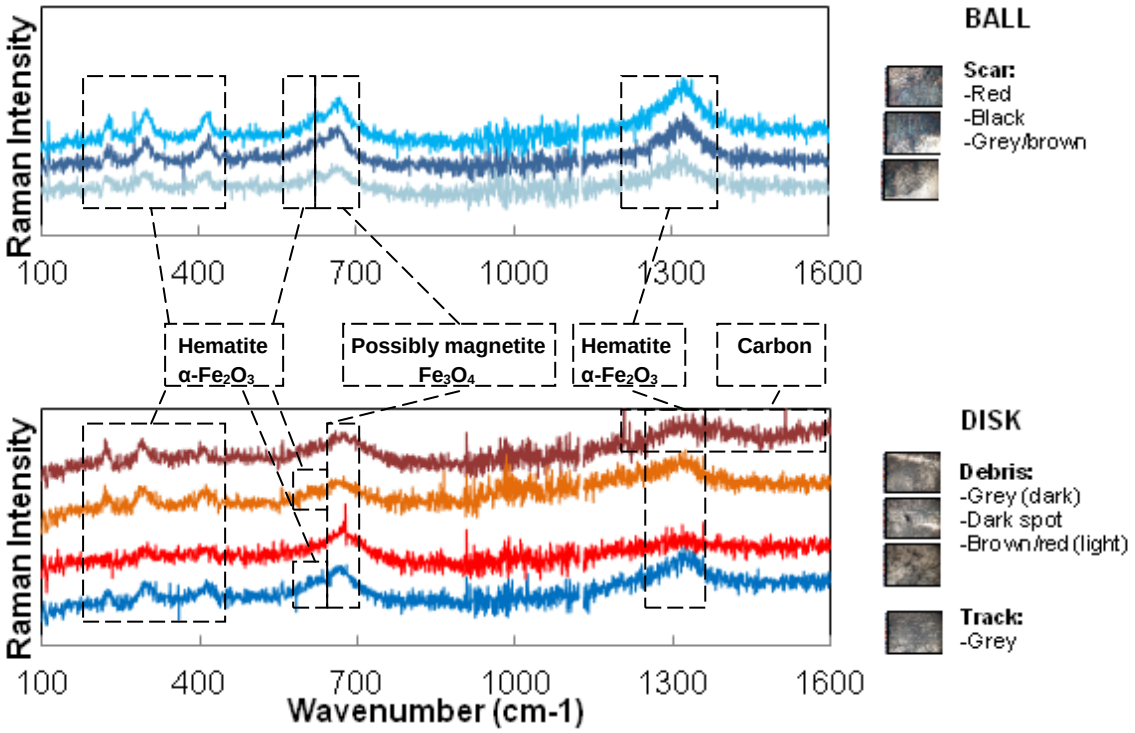

Figure 4.4.3: Raman analysis for a wear test, 250 ppm PA, 15% RH.

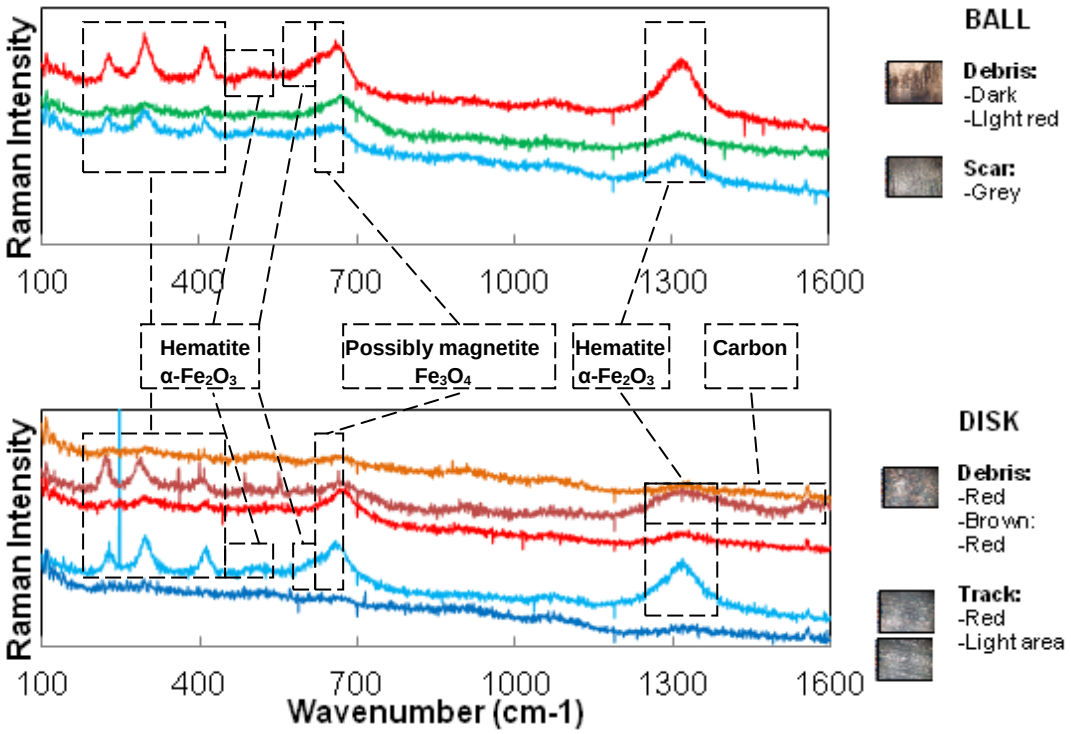

Figure 4.4.4: Raman analysis for a wear test, 250 ppm PA, 75% RH.

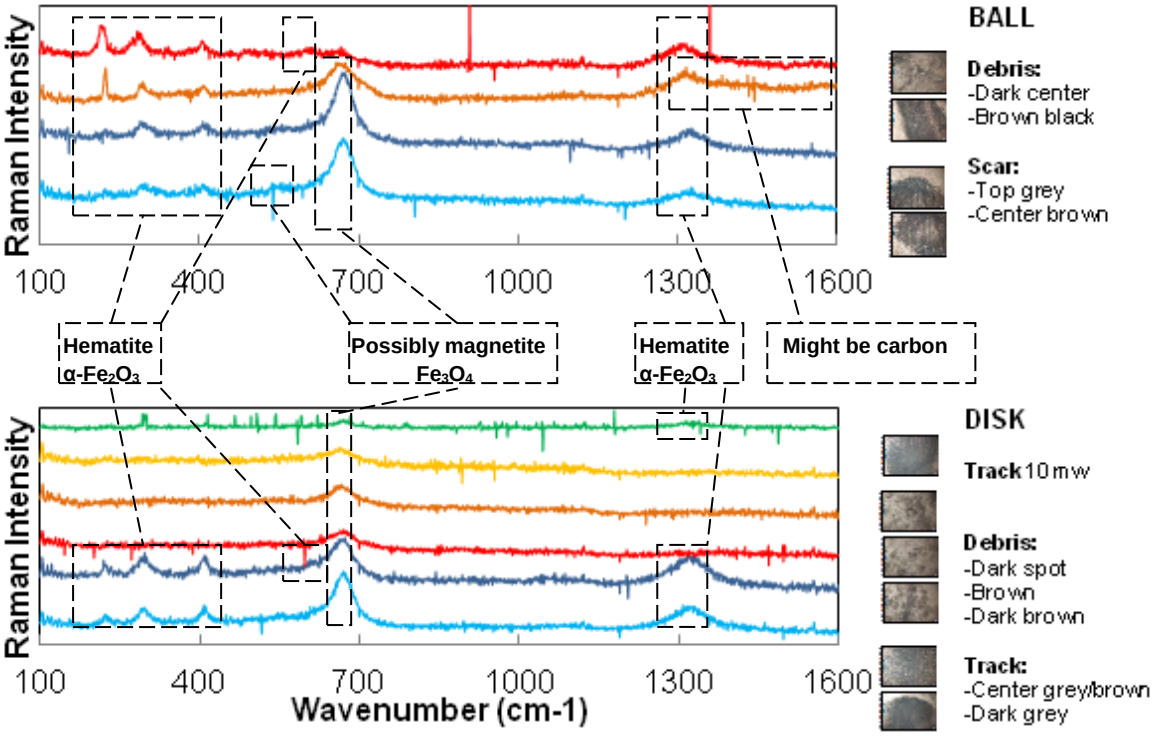

Figure 4.4.5: Raman analysis for a wear test, 2000 ppm PA, 15% RH.

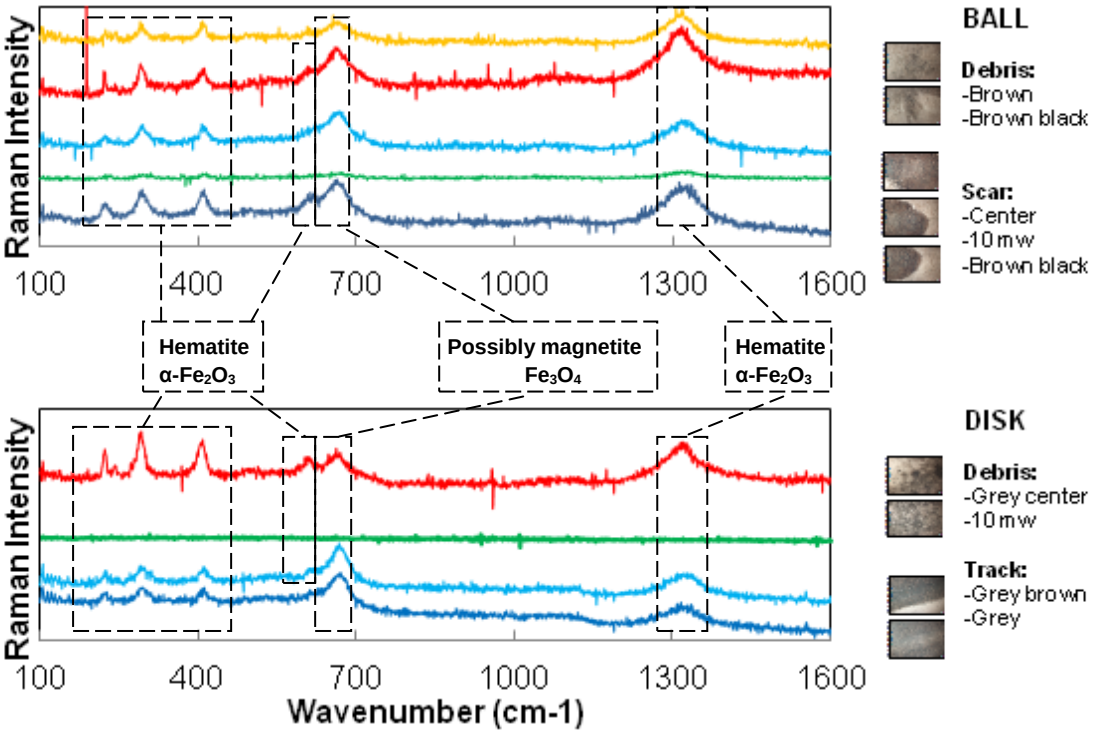

Figure 4.4.6: Raman analysis for a wear test, 2000 ppm PA, 75% RH.

4.4.2 Raman spectroscopy of seizure load tests

In Figure 4.4.7 to 4.4.12 Raman spectra are presented for seizure load tests. Only disks (Bottom specimen) were analyzed since the top specimen holder could not be used exclusively for this study.

Care must be taken when comparing Raman analysis of seizure load tests with that of wear tests. It must be remembered that a seizing contact will result in higher contact temperatures which in turn might affect the formation or diffusion of metal or other related species.

One should not directly compare Raman analysis of different seizure load tests. The reason is that not all seizure load tests run for the same period of time. This is likely to result in different amounts of debris and adherent material. This in turn could affect peak sizes. It is therefore safer to only compare indentified species when considering seizure load tests.

In Figures 4.4.7 and 4.4.8 the Raman spectra are presented for 100 ppm seizure load tests. The two figures are for 15% RH and 75% RH respectively:

- Hematite could be identified at high water content as is indicated. This is observed on both the surfaces and the debris. Note that the first hematite peak for the debris in Figure 4.4.8 is again, higher than expected.
- Magnetite could possibly be identified for both low and high water content.
- Maghemite could be identified in the both track and the debris at 15% RH, and also in the debris at 75%RH. This again is seen for low lubricity levels.
- Carbon was identified in the debris of both tests and on the track on 15% RH. The peaks for carbon are significantly larger for the seizure load tests compared to those obtained previously for the wear tests. This could be due to diffusion from within the metal to the surface under more severe seizure conditions.
- An unknown peak was observed at 345 cm^{-1} at 15%RH.

Concerning colours:

- A greyish colour of debris and adherent material was identified to consist of a combination of possibly magnetite, maghemite and carbon.
- When hematite was identified along with the above-mentioned species the colour of the debris was darker or brown.

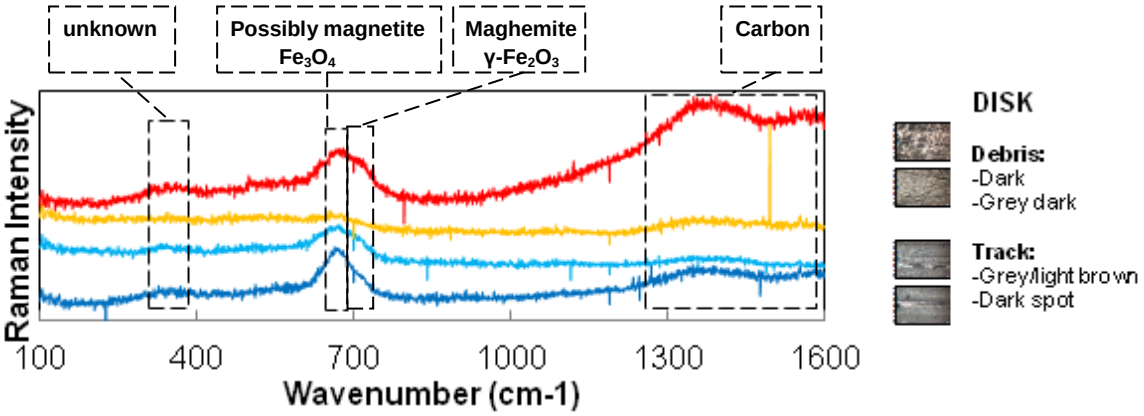

Figure 4.4.7: Raman analysis for a seizure load test, 100 ppm PA, 15% RH.

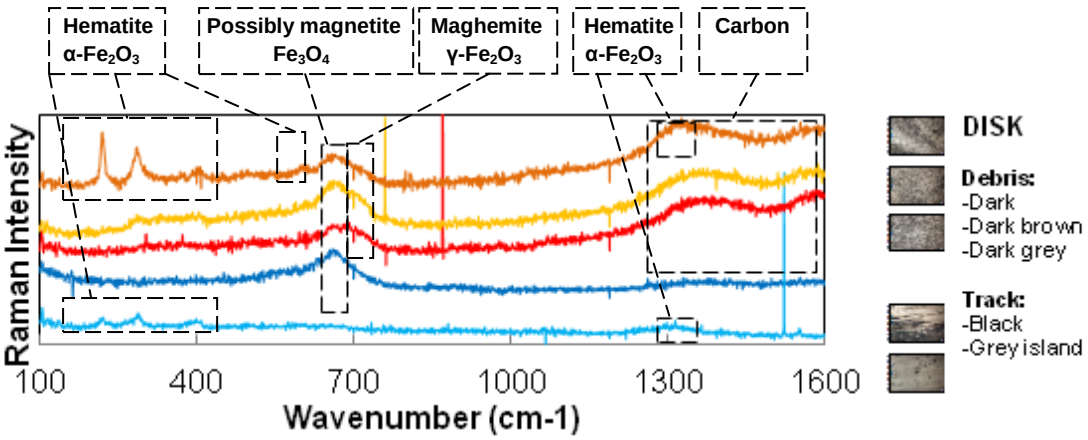

Figure 4.4.8: Raman analysis for a seizure load test, 100 ppm PA, 75% RH.

In Figures 4.4.9 and 4.4.10 Raman spectra are shown for seizure load tests at 500 ppm PA. The figures are for 15% RH and 75% RH respectively:

- Hematite could be identified for both high and low water as is indicated. This is observed on both the surfaces and the debris of 75% RH. The first hematite peak is larger than expected for certain debris but not for any adherent surfaces.
- Magnetite could possibly be identified by the peak around 660-670 cm^{-1}.
- No maghemite could be clearly identified.
- Carbon was detected only in the debris of 15% RH.
- Concerning colour: The presence of hematite again seems to be linked to dark brown debris.

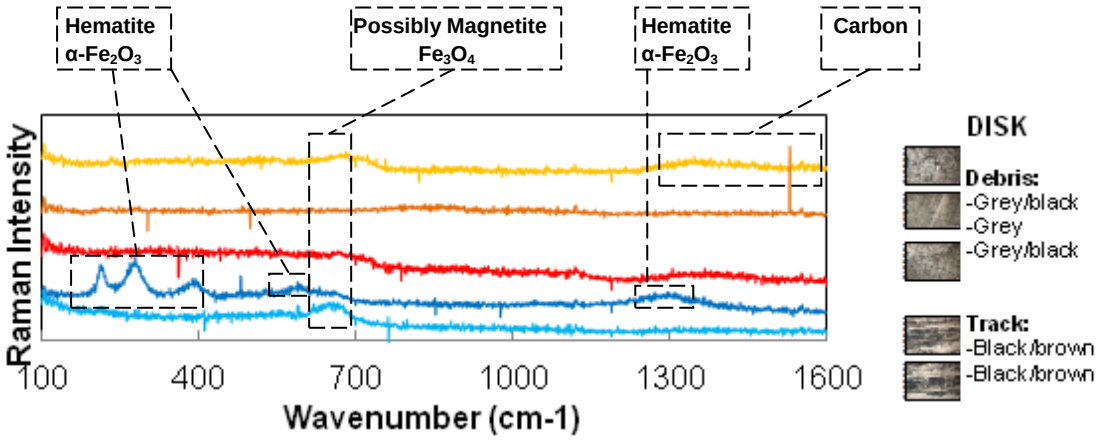

Figure 4.4.9: Raman analysis for a seizure load test, 500 ppm PA, 15% RH.

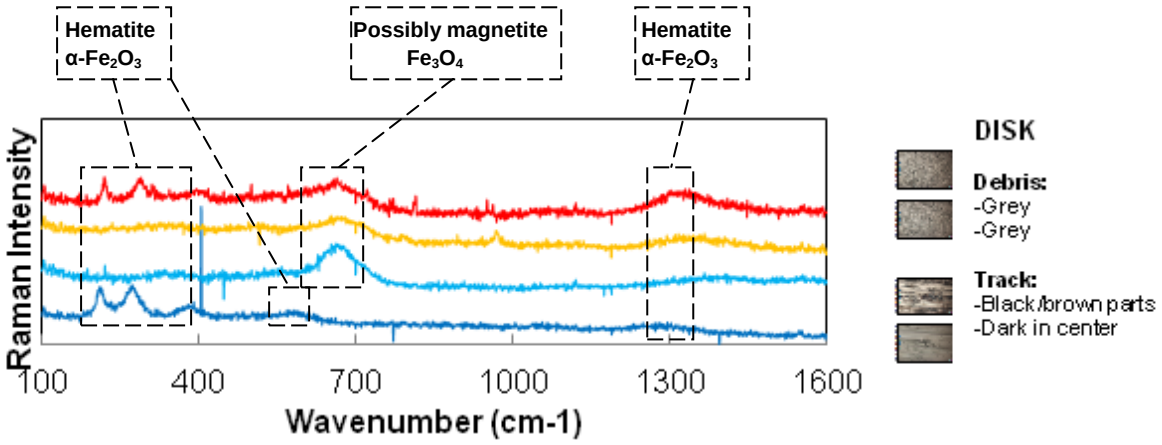

Figure 4.4.10: Raman analysis for a seizure load test, 500 ppm PA, 75% RH.

In Figures 4.4.11 and 4.4.12 Raman spectra are shown for seizure load tests at 2000 ppm PA. The figures are for 15% RH and 75% RH respectively:

- Hematite could be identified for high water content as is indicated. This is observed on the debris of 75% RH. The first Hematite peak is larger than expected for some of the debris.
- Magnetite could possibly be identified by the peak around 660-670 cm^{-1} for debris and adherent material at both high and low water content.
- No maghemite could be clearly identified.
- Carbon was detected only in the debris of both high and low water content.
- An unknown peak was observed at 220 cm^{-1}.

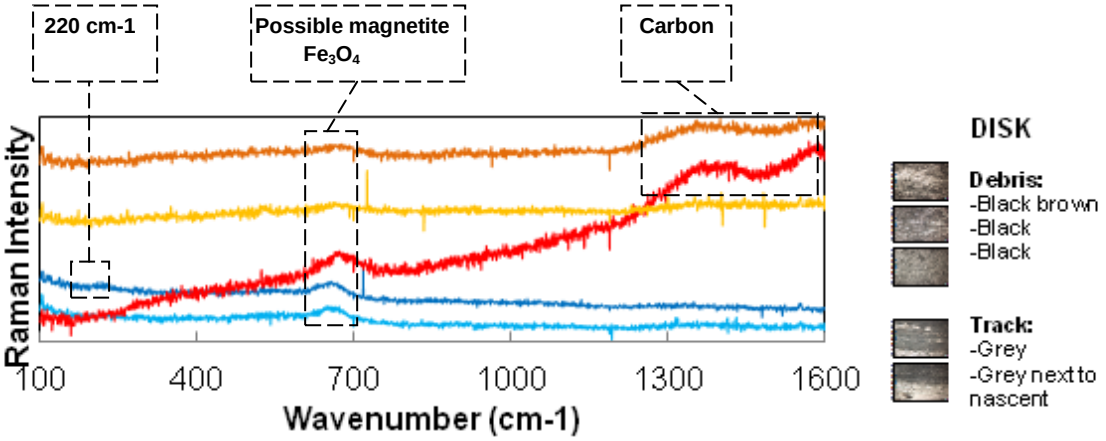

Figure 4.4.11: Raman analysis for a seizure load test, 2000 ppm PA, 15% RH.

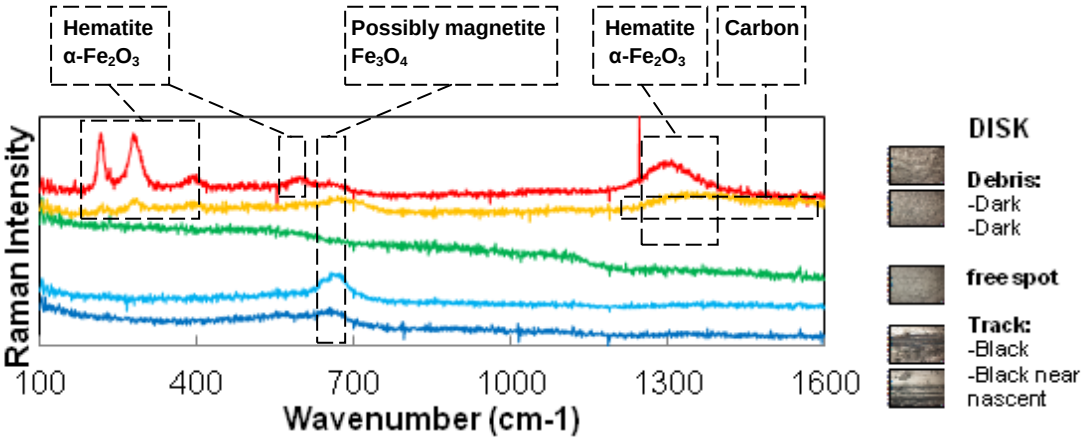

Figure 4.4.12: Raman analysis for a seizure load test, 2000 ppm PA, 75% RH

4.4.3 Discussion and summary - Raman spectroscopy

The following trends or observations could can be made:

- Neither hematite nor magnetite was found to form any observable trend.
- The first hematite peak was however observed to be larger than expected for some debris but not for any adherent surface. This could be indicative of an unkown species at 220 cm^{-1} which forms preferentially with debris material.
- Maghemite was formed at 100 ppm PA for both wear and seizure load tested, but was not detected at any other PA concentrations. This could be indicative of conditions being different to allow the formation of an Fe^{2+} rather than Fe^{3+} ions route to result in maghemite (see Figure 2.5.14). It is likely that maghemite occurs since it is an intermediate between the conversion of magnetite to hematite. Magnetite is known to form at higher temperatures. Since the contact temperatures are likely higher in the poorly lubricated contacts it would be more favourable for magnetite formation and subsequent conversion. If it were to be assumed that the possible magnetite peaks were magnetite it would still be sensible to observe maghemite at only the lowest lubricity level since the energetic conditions would favour conversion (see Figure 2.5.14).
- Carbon was detected predominantly in the debris. One spectrum for carbon was obtained in a seizure load track. The spectra for seizure load tests showed significantly higher carbon content. It is suspected that this is due to the outward diffusion of carbon from the metal due to the temperatures from seizing and pre-seizing contacts.
- It is interesting that no goethite was detected especially when one considers the fact that goethite peaks are 1,3 times more intense than magnetite peaks for the same amount of material. No significant difference was observed between low and high water content. This either means that no oxyhydroxides formed or that the amount formed is not detectable compared to the amount of oxides formed which is detectable. It is therefore suspected that the interaction of water, in the alkane medium, with the surface is localized and limited to the direct surface with little or no penetration.
- A peak at 220 cm^{-1} (2000 ppm PA) and 345 cm^{-1} (100 ppm PA) could not be identified on some of the seizure load tests. Interesting the peak at 220 cm^{-1} is at the same location as that which led to a larger and unexpected peak for hematite in the wear test debris.

5. Conclusions and Recommendations

It has been shown that water from the surrounding atmosphere can influence lubricity testing of a fuel sample. The concentration of water in the fuel depends on the water content of the atmosphere and temperature conditions of the system.

The ability of air to contain moisture is known to fluctuate as environmental conditions vary. This in turn can alter the moisture content within a contacting fuel sample. This was confirmed by modelling the transfer of water from air into a model diesel fuel sample. The extent of transfer under various conditions was investigated by exposing test fuel samples to different environmental conditions. The water content was measured before and after exposure conditions. The most important observations were:

- Water content of the fuel increased as the water content of the contacting air increased. The kinetics of transfer is affected by the contact conditions.
- The water content of samples decreased as the temperature of the system increased even though the capacity of the sample to hold water increased. This holds implications since the samples are typically heated from room temperature upon test initiation.
- 2000 ppm of polar PA in non-polar n-hexadecane did not significantly influence the water content of the sample.

The presence of water in the fuel sample was further shown to affect both wear and seizure load testing. Although the consequential effects of the water appears unique for the two tests, the primary effect of water on the molecular behaviour of the lubricity additive appear to be similar for both tests.

Lubricating molecules, functional in the boundary lubrication regime, are adsorbed onto metal surfaces due to their polar functional groups. Non-polar groups can also adsorb onto surfaces due to van der Waals interactions but these bonds tend to be much weaker. Adsorbed molecules introduce a lower shear surface between contacting surfaces, at the non-polar end of the molecule. This leads to reduced interaction between the contacting surfaces. It has been shown that the presence of soluble water reduces the lubricity properties of PA. Water is likely interfering with the adsorption process since it is known that water molecules can adsorb in different ways onto metal and metal oxide surfaces. It is very likely that adsorbed water

molecules adsorb in a manner as to prevent or reduce the adsorption capability of PA in the vicinity of the adsorbed water molecule.

Dissociated chemisorbed water molecules in the form of OH^- are known to be active towards ligand exchange. It is however unclear at this point if the kinetics of ligand exchange could be slower compared to "normal" adsorption of PA onto an oxide surface. At this point it is rather suspected that undissociated water physisorbs onto the surfaces.

The nature of the surface determines if a molecule is to adsorb chemically or physically. It has been noted by (Loehle, *et al*, 2013) that nascent surfaces tend to induce chemisorption of fatty acids whereas oxidized metal surfaces tend to induce physisorption. If the same is true for water molecules in a n-hexadecane medium it would explain the reduced lubricity behaviour at higher water content, since physisorbed water could be detrimental to PA adsorption.

As previously mentioned the primary effect of water leads to secondary "consequential" effects which might differ for wear and seizure load testing. In wear testing the reduced lubricity performance leads to increased wear and friction. This is quite easily observed since this is a static load test. In seizure load testing, water can increase or decrease the apparent/observed seizure load depending on the lubricity levels and water content. This occurs partly because this is a dynamic load test. The apparent seizure load might not represent the actual lubricity characteristics of the fuel and needs careful consideration.

The consequential effects due to increased water content (observed in this study) included the following.

For wear testing:

- Higher friction coefficients.
- Lower ECR readings.
- Larger MWSD.
- More wear debris on the track is observed for 2000 ppm PA.
- A change in surface appearance occur at all lubricity levels:
    - At 100 ppm the observation of oxides is not clear due to the effects imposed by the unevenness of the wear track.
    - At 250 ppm less adherent oxide appears to be visible.
    - At 2000 ppm less adherent oxide appears to be visible.

For seizure load testing:

- There is an prolonged duration of higher friction during the run-in period for higher water content. If this period is significantly larger it will lead to over-evaluation of the seizure load due to the resulting larger surface area. The larger surface area required a larger load for similar pressure conditions.
- There is an increased deviation of stroke at higher water content. This again is more significant for poor lubricity levels.
- The vertical displacement measurement is higher at higher water content which is indicative of increased wear.
- The effects of water on test parameters appears to be diminished at higher PA concentration.

In summary it appears that water disrupts the adsorption process of the PA. This leads to reduced lubricity performance which can affect the "observed seizure load" in two different ways:

- At poor lubricity water could lead to over-evaluating the seizure load. This occurs if the run-in period occurs at a higher friction coefficient for a significantly longer period.
- At moderate and higher lubricity, water could lead to under-evaluating the seizure load. This occurs because the water molecules act to reduce the adsorption of the PA lubricity additive molecules.

Raman analysis: Raman spectroscopy revealed the presence of a number of iron oxides and carbon but could not detect any iron oxyhydroxides. This means that the concentration of any oxyhydroxides are either extremely lower than that of the oxides or that water only adsorbed physically onto the surface.

Also note that:

- The first hematite peak was observed to be larger than expected for some debris but not for any adherent surfaces. This could be indicative of an unkown species at 220 cm^{-1}.
- Maghemite was formed at 100 ppm PA for both wear and seizure load tested, but was not detected at any other PA concentrations. This could be indicative

of more energetic conditions resulting in the conversion of magnetite into maghemite and/or hematite.

- Carbon was detected predominantly in the debris. One spectrum for carbon was obtained in a seizure load track. The spectra for seizure load tests showed significantly higher carbon contact. It is suspected that this is due to the outward diffusion of carbon from the metal from the seizing contact.
- A peak at 220 cm^{-1} (2000 ppm PA) and 345 cm^{-1} (100 ppm PA) has not yet been identified on some of the seizure load tests.

The results observed in this study shows that the effects of soluble water cannot simply be ignored. This was shown to be especially true for fuels with lower lubricity. It is postulated that this is because the water can then compete more favourably for surface interaction. Any lubricity testing of fuels done for research purposes should have a way of ensuring that the effects of water are kept constant. The systems employed in this study could be used, but this will require extreme cleanliness and preparation to ensure no cross contamination between samples. New alternatives should however always be considered if these methods could possibly result in better control of moisture content.

A closing remark would however be to always be aware of the composition of the fuel matrix to be tested. As the number of polar species increases the solubility of water should also increase. Although the effects of water at low water content might seem universal, extrapolation is always a risky practice. At significantly higher water content the formation of oxyhydroxides could have a more significant role, for example (Çavdar, 1997) did boundary lubrication wear testing on perfluoropolyalkylether oil as well as perfluoropolyalkylether with a fluorinated alcohol additive. He found a significant decrease in both wear and friction with increasing RH. It was observed that higher RH resulted in thicker film formation which is assumed to be the reason for the decreased wear and friction.

6. References

Archard, JF (1959) “The temperature of rubbing surfaces”, *Wear*, 2, 438 – 455.

American Society for Testing and Materials (ASTM) (1999) D 6078 Standard Test Method for Evaluating Lubricity of Diesel Fuels by the Scuffing Load Ball-on-Cylinder Lubricity Evaluator (SLBOCLE), ASTM, USA.

American Society for Testing and Materials (ASTM) (1999) D 6079 Standard Test Method for Evaluating Lubricity of Diesel Fuels by the High-Frequency Reciprocating Rig (HFFR), ASTM, USA.

Anderson, K (2006) "Structure, bonding and chemistry of water and hydroxyl on transition metal surfaces", Dissertation for doctorate degree, Stockholms university, Sweden.

Battino, R, Rettich, TR and Tominaga, T (1984a) “The solubility of nitrogen and air in liquids”, *Journal of physical chemistry*, Reference data, 13, 2, 563 – 600.

Battino, R, Rettich, TR and Tominaga, T (1984b) "The solubility of oxygen and ozone in liquids", *Journal of physical chemistry*, Reference data, 12, 2, 163 – 178.

Blau, PJ (2010) “Elevated-temperature tribology of metallic materials”, *Tribology international*, 43, 1203 - 1208.

Blok, H (1937) “Theoretical study of temperature rise at surface of actual contact under oiliness lubricating conditions*”, Gen. Disn. Lubn. Instn. Mech Eng*., 2, 222 – 235.

Bowman WF and Stachowiak GW (1996) “A review of scuffing models”, *Tribology Letters*, 2,113-131.

Bregliozzi, G, Di Schino, A, Kenny, JM and Haefke, H (2003) “The influence of atmospheric humidity and grain size on the friction and wear of AISI 304 austenitic stainless steel”, *Materials letters*, 57, 4505 - 4508.

Çavdar, B (1997) “Effect of temperature, substrate type, additive, and humidity on the boundary lubrication in a linear perfluoropolyalkylether fluid”, *Wear*, 206, 15 - 23.

Chowdhury, MA and Helali, MM (2007) “The effect of frequency of vibration and humidity on the wear rate”, *Wear*, 262, 198 – 203.

Chernyshev, AK (1970) “Determination of the solubility of water in hydrocarbons”, *Khimiya i Tekhnologiya Topliv i Masel*, No. 4, pp. 57-58.

Clark, A (1970) *The theory of adsorption and catalysis,* Academic press, New York and London.

Colomban, P (2011) "Potential and Drawbacks of Raman (Micro)spectrometry for the Understanding of Iron and Steel Corrosion, New Trends and Developments in Automotive System Engineering", InTech.

Cornell, RM and Schwertmann, U (2007) *The iron oxides, Structure, Properties, Reactions, Occurrences and Uses, Second edition,* Wiley-VCH GmbH & Co. KGaA, International.

Cussler, EL (1997) *Diffusion: Mass Transfer in Fluids Systems*, second edition, Cambridge University Press, Cambridge.

Davenport, JN (*sa*) “Development and verification of the HFRR test for automative diesel fuels”, Shell Research Ltd., Chester, UK.

de Faria, DLA and Lopes, FN (2007) "Heated goethite and natural hematite: Can Raman spectroscopy be used to differentiate them?", *Vibrational Spectroscopy*, 45, 117–121.

Gialanella, S, Girardi, F, Ischia, G, Lonardelli, I, Mattarelli, M and Montagna, M (2010) "On the goethite to hematite phase transformation", *J Therm Anal Calorim*, 102,867–873.

Gohar, R and Rahnejat, H (2012) *Fundementals of tribology, 2nd edition*, Imperial college press, United Kingdom.

Gorzynski Smith J (2008) *Organic chemistry, second edition*, Mcgraw-Hill, International.

Guskos, N, Papadopoulos, GJ, Likodimos, V, Patapis, S, Yarmis, D Przepiera, A, Przepiera, K, Majszczyk, J, Typek, J, Wabia, M, Aidinis, K and Drazek, Z (2002) "Photoacoustic, EPR, and electrical conductivity investigations of three synthetic mineral pigments: hematite, goethite and magentite" *Material research bulletin*, 37, 1051 - 1061.

Gouadec, G, Bellot-Gurlet, L, Baron, D and Colomban Ph (2010) *Raman mapping for the investigation of nanophased materials*, ch. 4, *Raman Imaging* , *A. Zoubir Ed.*, Springer.

Han, KN, Healy, TW and Fuerstenau, DW (1973) "The mechanism of adsorption of fatty acids and other surfactants at the oxide-water interface", *Journal of colloid and interface science*, 44 (3), 407 - 414.

Hasegawaa, M, Yanagiharaa, H, Toyodaa, Y, Kitaa, E and Rannob, R (2007) "Electrical and magnetic properties of γ-Fe2O3 epitaxial films", *Journal of Magnetism and Magnetic Materials*, 310, 2283–2285.

International Organization for Standards, ISO, (2003) ISO/CD 12156-1 Diesel fuel – Assessment of lubricity using high-frequency reciprocating rig (HFRR) Part 1, Test method, ISO, International.

Joseph, Y, Kuhrs, C, Ranke, W and Weiss, W (1999) "Adsorption of Water on Fe3O4(111) Studied by Photoelectron and Thermal Desorption Spectroscopy", *Surf. Sci.*, 433, 114-118.

Kendelewicz , T, Liu, P, Doyle, CS, Brown Jr, GE, Nelson, EJ and Chambers, SA (2000) "Reaction of water with the (100) and (111) surfaces of Fe_3O_4",*Surface Science,* 453, 32–46.

Kipp, DO (2010) *Metal material data sheets*, MatWeb – Division of Automatic Creation, Inc., Online, Knovel.

Klaffke, D (1995) “On the repeatability of friction and wear results and on the influence of humidity in oscillating sliding tests of steel-steel pairings”, *Wear*, 189, 117 – 121.

Kotz, JC and Treichel Jr, PM (2003) *Chemistry & chemical reactivity*, *fifth edition*, Thomson Brooks/Cole, International.

Kowert, BA and Dang, NC (1998) "Diffusion of Dioxygen in n-alkanes", *The journal of physical chemistry A*, 103, 7.

Lacey, P, Gunsel, S, De La Cruz, J, and Whalen, M (2001) "Effects of High Temperature and Pressure on Fuel Lubricated Wear," *SAE Technical Paper*, 2001-01-3523, 1-10.

Lancaster, JK (1990) “A review of the influence of environmental humidity and water on friction, lubrication and wear”, *Tribology International*, Vol 23, No 6, 371 – 389.

Lapuerta, M, Sánchez-Valdepeñas, J and Sukjit, E (2014) "Effect of ambient humidity and hygroscopy on the lubricity of diesel fuels", *Wear*, 309, 200 – 207.

Liew, WYH (2005) “Effect of relative humidity on the unlubricated wear of metals”, *Wear*, 260, 720 – 727.

Liu, P, Kendelewicz T, Brown, GE, Nelson EJ and Chambers, SA (1998) "Reaction of water vapor with α-Al_2O_3(0001) and α-Fe_2O_3(0001) surfaces: synchrotron X-ray photoemission studies and thermodynamic calculations", *Surface Science*, 417, 53–65.

Loehle, S, Minfray, C, Matta, C, Le Mogne, T, Martin, JM, Iovine, R, Obara, Y, Miura, R and Miyamoto, A (2013) "Effects of iron oxide layers on adsorption mechanism of C18 fatty acid: A computational study", 40th Leeds-Lyon Symposium on Tribology &TribochemistryForum 2013, September 4-6, 2013, Lyon, France, poster.

Loehle, S, Matta, C, Minfray, C, Le Mogne, T, Martin, JM, Iovine, R, Obara, Y, Miura, R and Miyamoto, A (2014) "Mixed Lubrication with C18 Fatty Acids: Effect of Unsaturation", *Tribology letters*, 53, 319-328.

Lundgren, SM, Persson, K, Mueller, G, Kronberg, B, Clarke, J, Chtaib, M and Claesson, PM (2007) "Unsaturated Fatty Acids in Alkane Solution: Adsorption to Steel Surfaces", *Langmuir*, 23, 10598-10602.

MAN Diesel & Turbo (*sa*) "Common Rail Design and maturity", http://www.mandieselturbo.com/files/news/filesof15326/TP_CommonRail_DRUCKDATEN.pdf, [2014 29 November].

Mang, T, Bozin, K and Bartels, T (2011) Industrial Tribology: tribosystems, friction, wear and surface engineering, lubrication, Wiley-VCH Verlag GmbH & Co. KGaA, Weinheim.

Manku, G (1994) "Solubilities of oxygen in selected alkane solvents and in aqueous copper electrorefining solutions", Master's dissertation, University of Ottawa, Ottawa.

Marais, G (2010*)* "An investigation into the role of compounds affecting friction, wear and lubricity", Master's dissertation, University of Pretoria, Pretoria.

Meyer, K and Livingston, TC (2003) "Diesel Fuel Lubricity, Requirements for Light Duty Fuel Injection Equipment CARB Fuels Workshop", Robert Bosch GmbH, Sacramento, CA.

Moller, VP (2012) "Exploring fundamental differences between wear and seizure load testing", Master's dissertation, University of Pretoria, Pretoria.

Oh, HK, Yeon, KH and Kim, HY (1999) "The influence of atmospheric humidity on the friction and wear of carbon steels", *Journal of materials processing technology*, 95, 10 - 16.

Oláh, ZS, Szirmai, L and Resofszki, G (2005) "Micro and Nano Analysis of Wear Scar Surfaces – A Complementary Rating Method to the Evaluation of HFRR Test Results", 5th International colloquium of fuels, Technische Akademie Esslington, 12 - 13 January 2005.

Optimol Instruments (2008) SRV ® 4 test system: Operating manual, Optimol instruments, Germany.

PCS Instruments (sa) "HFRR High frequency reciprocating rig", online brochure, http://www.pcs-instruments.com/pdf/hfr/HFRR_Brochure_ENGLISH.pdf [30 June 2014].

Raamat, E, Kaupmees, K, Ovsjannikov, G, Trummal, A, Kütt, A, Saame, J, Koppel, I, Kaljurand, I, Lipping, L, Rodima, T, Pihl, V, Koppel, IA and Leito I (2012) “Acidities of strong neutral Brønsted acids in different media”, *Journal of physical organic chemistry,* 26, 162-170.

Ripin, DH and Evans, DA (2005) Evans pKa table, Online, http://www2.lsdiv.harvard.edu/labs/evans/pdf/evans_pKa_table.pdf.

Ruby, C, Fusy, J, Alnot, M, Genin, JM and Ehrhardt JJ (1997) Structural properties and water adsorption behaviour of iron films grown on Cu (111), *Thin solid films*, 311, 44-50.

Schatzberg, P (1963) "Solubilities of water in several normal alkanes from C7 to C16",*Journal of physical chemistry*, 67, 776-779.

Schaumberg, H (1994) "Keramik", 5, BG Teubner Stuttgart, Germany.

Schwertmann, U and Cornell, RM (1991) *Iron oxides in the laboratory: preparation and characterization*, VCH Publishers Inc., New York, USA.

Shaver, BD, Giannini, RM, Lacey, PI and Erwin, J (1998) “Effects of water on distillate fuel lubricity”, *SAE Inc.,* 982568, 1480 – 1495.

Smith, FL and Harvey, AH (2007) "Avoid common pitfalls when using Henry's law", *CEP magazine: September 2007*, American institute of chemical engineers.

Solomons, RWG (1992) *Organic chemistry, 5th edition,* Wiley, New York.

Stachowiak, GW and Batchelor, AW (2003) *Engineering tribology,2nd Edition*, Butterworth-Heinemann, International.

Su, JT, Duncan PB, Momaya, A, Jutila, A and Needham, D (2010) “The effect of hydrogen bonding on the diffusion of water in n-alkanes and n-alcohols measured with a novel single microdroplet method”, *The Journal of Chemical Physics*, 132, 044506.

Wakai, C and Nakahara, M (1997) “Attractive potential effect on the self-diffusion coefficients of a solitary water molecule in organic solvents”, *Journal of Chemical Physics*, 106, 7512.

Welty, JR, Wicks, CE, Wilson, RE and Rorer, GL (2001) *Fundamentals of momentum, heat and mass transfer, 4th edition*, John Wiley & Sons, Inc, USA.

Williams, JA (1994), *Engineering Tribology*, Oxford University Press, Oxford.

Yasuda, E, Inagaki, M, Kaneko, K, Endo, M, Oya, A and Tanabe, Y (2003) *Carbon alloys: Novel concepts to develop carbon science and technology*, Gulf Professional Publishing.

Yaws, CL (2010) “Calculating H_2O solubility, Henry's Law constant for cycloalkanes in crude”, *Oil & Gas Journal*, 108, 4, 54-58.

Yaws, CL (2012). Yaws' Critical Property Data for Chemical Engineers and Chemists. Knovel, Online.

Yaws, CL and Rahate, M (2009) “Table, correlation give water solubility, Henry’s law constant for alkanes in crude”, *Oil & Gas Journal*, 107, 9, 52 – 55.

Yaws, CL and Rane, PM (2010) “How temp. affects H2O solubility in alkanes”, *Oil & Gas Journal*, 108, 46, 130 – 133.

Young, RJ and Lovell, PA (2011) *Introduction to polymers*, third edition, CRC Press, USA.

Zhang, J, Yamaguchi, E and Spikes, H (2013) "Comparison of three laboratory tests to quantify mild wear rate", *Tribology transactions*, 56, 919 - 928.

Appendix A

Obtaining the equation for a finite diffusion length (Equation 4.1.3) from the boundary and initial values.

Recall Equation 4.1.8 with the general solution Equation 4.1.13.

$$\frac{\partial Y}{\partial t} = D_{AB} \frac{\partial^2 Y}{\partial^2 z} \tag{4.1.8}$$

$$Y(t,z)=T(t)*Z(z)=\left[c_1' \cos(\lambda z) + c_2' \sin(\lambda z)\right]*\left[e^{(-D_{AB}\lambda^2 t)}\right] \tag{4.1.13}$$

The boundary conditions previously shown are rewritten in terms of:

$$Y = \frac{Ca - Ca_s}{Ca_0 - Ca_s} \tag{4.1.7}$$

- <u>Boundary condition 1</u>

  Y = 0 at z = 0 for t > 0

  $Y(0,t) = 0 = [c_1'\cos(0) + c_2'\sin(0)]*[e^{(-D_{AB}\lambda^2 t)}]$

  $0 = c_1'*e^{(-\lambda^2 t)}$

  The only way this can be true is if $c_1' = 0$.

- <u>Boundary condition 2</u>

  $\frac{\partial Y}{\partial Z} = 0$ at z = L for t > 0

  Since $c_1' = 0$ (resulting from boundary condition 1)

  $Y = [c_2'\sin(\lambda z)]*[e^{\wedge(-D_{AB}\lambda^2 t)}]$

$\frac{\partial Y}{\partial z}(L, t) = 0 = c_2' * \lambda * e^{(-D_{AB}\lambda^2 t)} * \cos(\lambda L)$

This condition requires that either $c_2' = 0$, or $\cos(\lambda L) = 0$.
$c_2' = 0$ cannot be since this would result in a trivial solution.
$\cos(\lambda L) = 0$ when $\lambda = \frac{n\pi}{2L}$ for n = 1, 3, 5...

- Initial condition

$Y = Y_0$ at $t = 0$ for $0 \leq z \leq L$

$Y(L,0) = Y_0 = c_2' \sin(\frac{n\pi}{2L} z)$ for n = 1, 3, 5...

Using the principle of orthogonality:

$c_2' = \frac{1}{L} \int_{-L}^{L} [f(z) \sin(\frac{n\pi}{2L} z)]\, dz$ for n = 1, 3, 5...

$c_2' = \frac{2Y_0}{L} \int_0^L \sin\left(\frac{n\pi}{2L} z\right) dz$ for n = 1, 3, 5...

$c_2' = -\frac{4Y_0}{n\pi}\left[\cos\left(\frac{n\pi}{2}\right) - 1\right]$ for n = 1, 3, 5...

$c_2' = \frac{4Y_0}{n\pi}$ (This is true for n = 1, 3, 5...)

Since $Y_0 = \frac{Ca_0 - Ca_s}{Ca_0 - Ca_s} = 1$

$c_2' = \frac{4}{n\pi}$

The solution to Fick's 2nd law with these boundary and initial conditions can be seen in Equation 4.1.3.

$$Y = \frac{Ca - Ca_s}{Ca_0 - Ca_s} = \sum_{n=1}^{\infty} \frac{4}{n\pi} \sin\left(\frac{n\pi}{2L} z\right) * e^{\left(-DAB\left(\frac{n\pi}{2L}\right)^2 t\right)} \quad \text{for } n=1, 3, 5... \qquad (4.1.3)$$

Appendix B

Wear testing repeat runs

In Figure B.1.1 to B.1.6 the friction responses of wear tests not presented in text can be found:

- B.1.1 – B.1.3 Friction coefficient for wear testing 60 °C, run 2
  (First run was previously presented in Section 4.2).
- B.1.4 – B.1.6 Friction coefficient for Wear testing 80 °C, run 2.

In Figure B.2.1 to B.2.6 the ECR recordings of wear tests not presented in text can be found:

- B.2.1 – B.2.3 ECR recordings for wear testing 60 °C, run 2
  (First run was previously presented in Section 4.2).
- B.2.4 – B.2.6 ECR recordings for wear testing 80 °C, run 2.

In Table B.1 to B.6 the wear scars at 60 °C and 80 °C for repeat runs of wear testing can be found:

B1: Friction coefficients

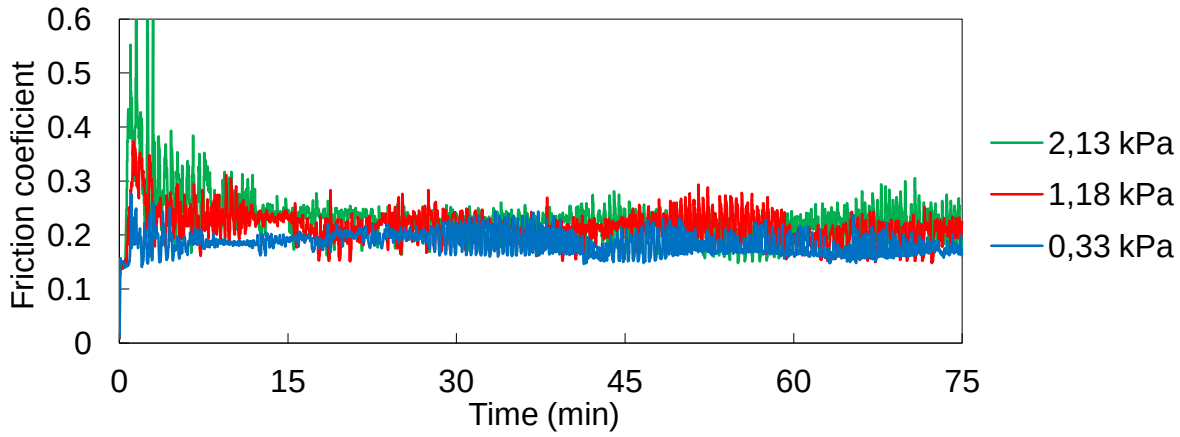

Figure B.1.1 : Friction coefficient for wear testing, 60°C, 100 ppm PA, run 2.

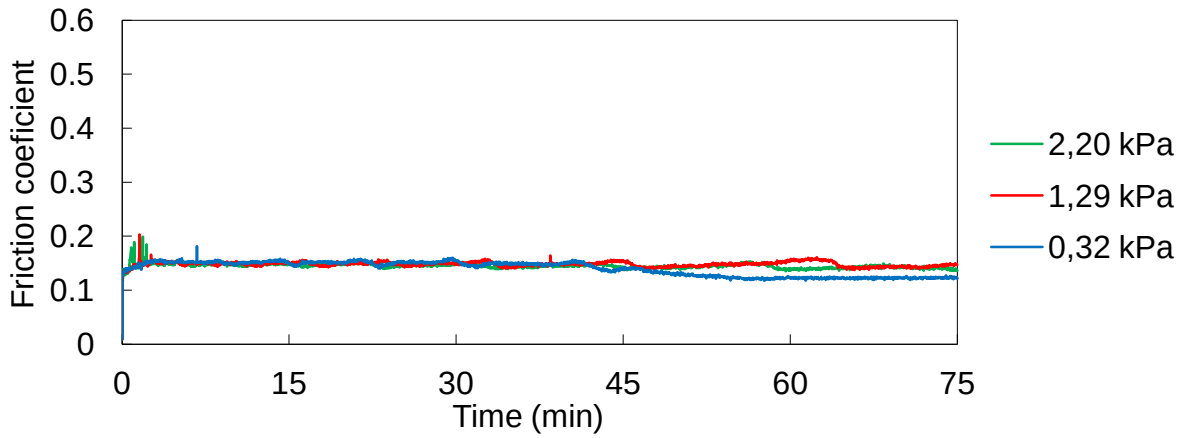

Figure B.1.2 : Friction coefficient for wear testing, 60°C, 250 ppm PA, run 2.

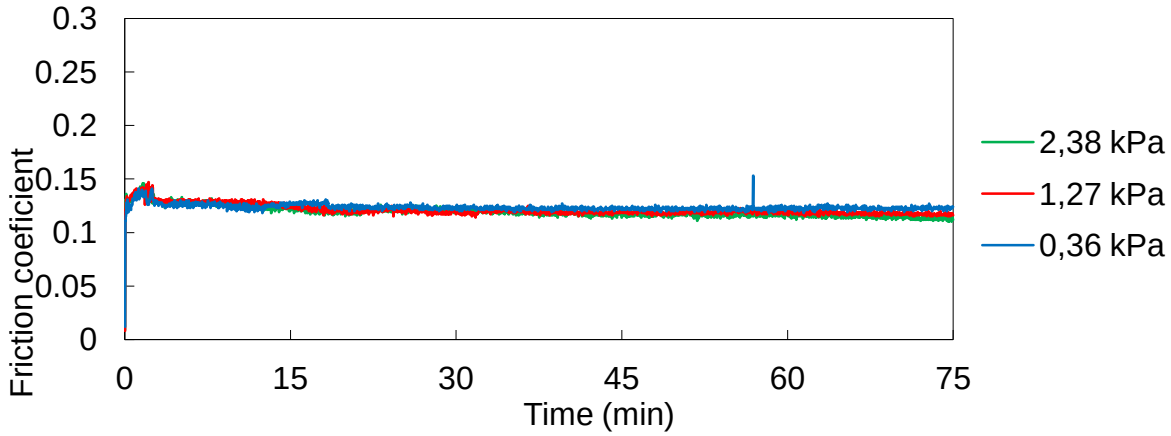

Figure B.1.3 : Friction coefficient for wear testing, 60°C, 2000 ppm PA, run 2.

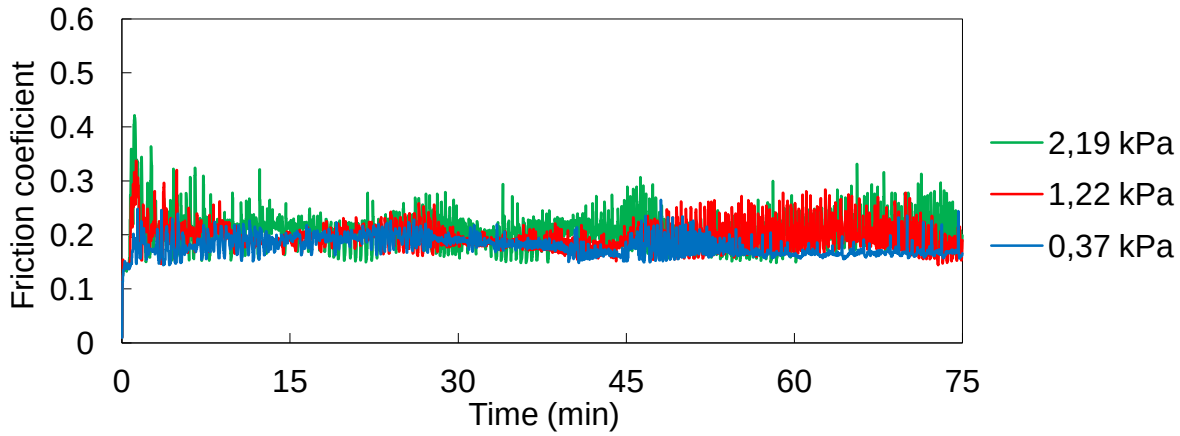

Figure B.1.4 : Friction coefficient for wear testing, 80°C, 100 ppm PA, run 2.

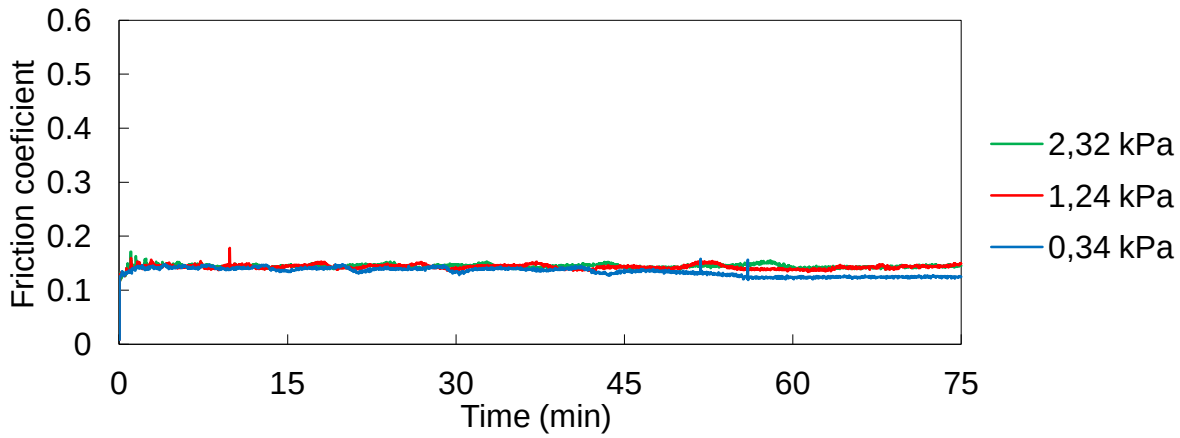

Figure B.1.5 : Friction coefficient for wear testing, 80°C, 250 ppm PA, run 2.

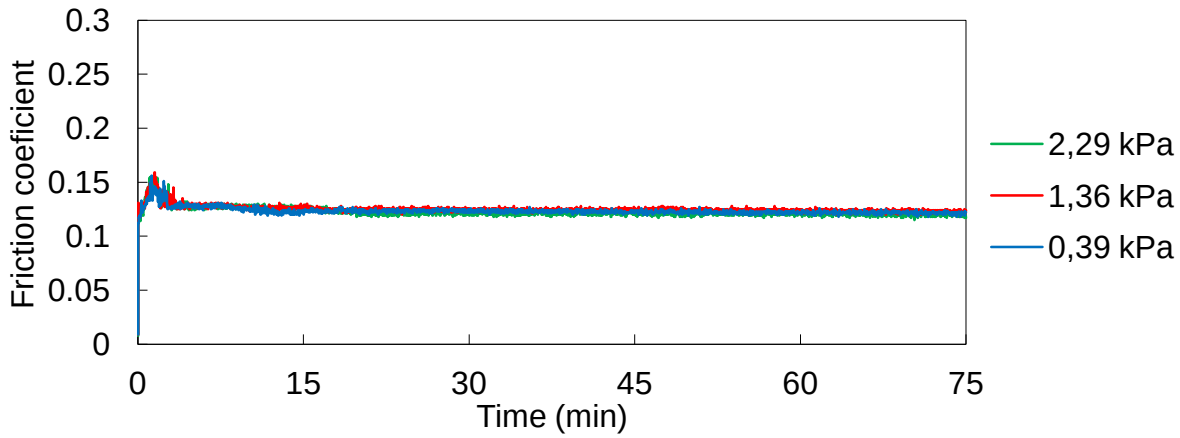

Figure B.1.6 : Friction coefficient for wear testing, 80°C, 2000 ppm PA, run 2.

B.2: ECR readings

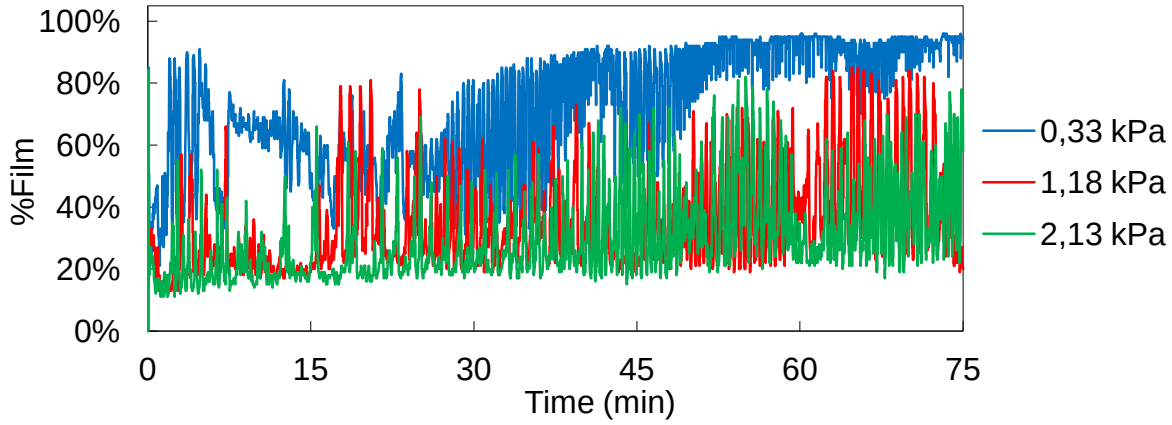

B.2.1: ECR recordings for wear testing 60 °C, 100 ppm PA, run 2.

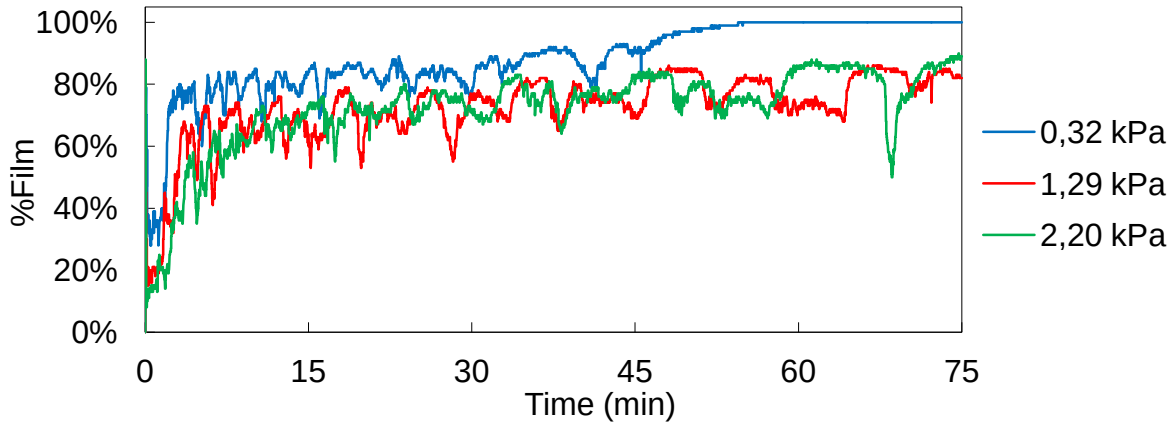

B.2.2: ECR recordings for wear testing 60 °C, 250 ppm PA, run 2.

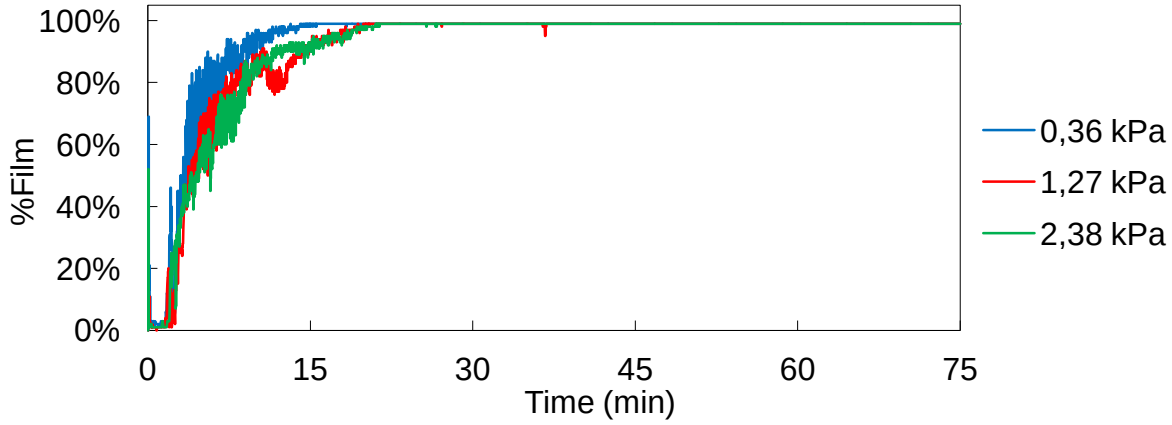

B.2.3: ECR recordings for wear testing 60 °C, 2000 ppm PA, run 2.

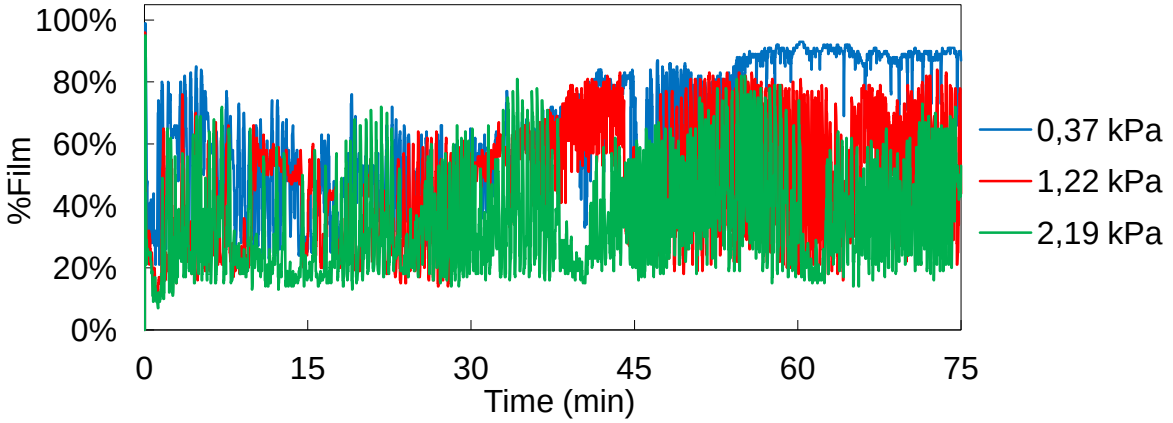

B.2.4: ECR recordings for Wear testing 80 °C, 100 ppm PA, run 2.

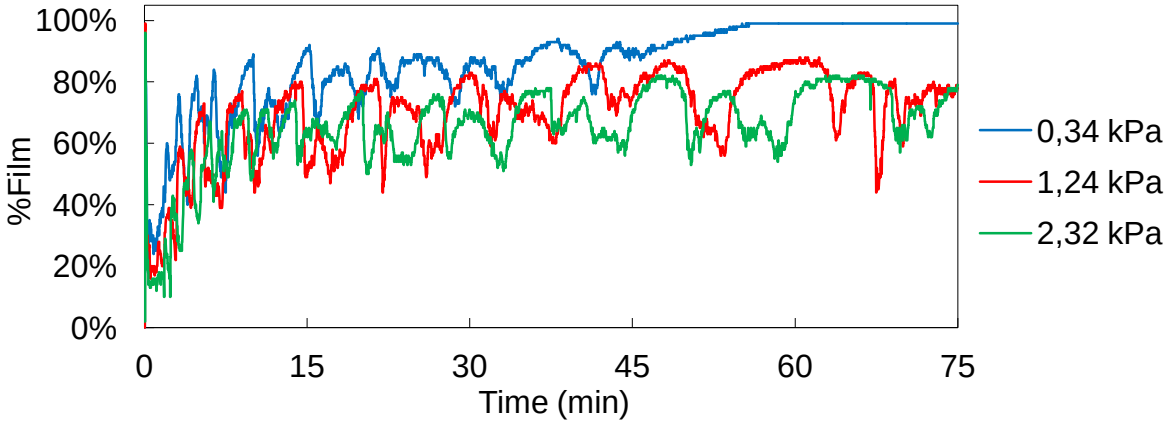

B.2.5: ECR recordings for Wear testing 80 °C, 250 ppm PA, run 2.

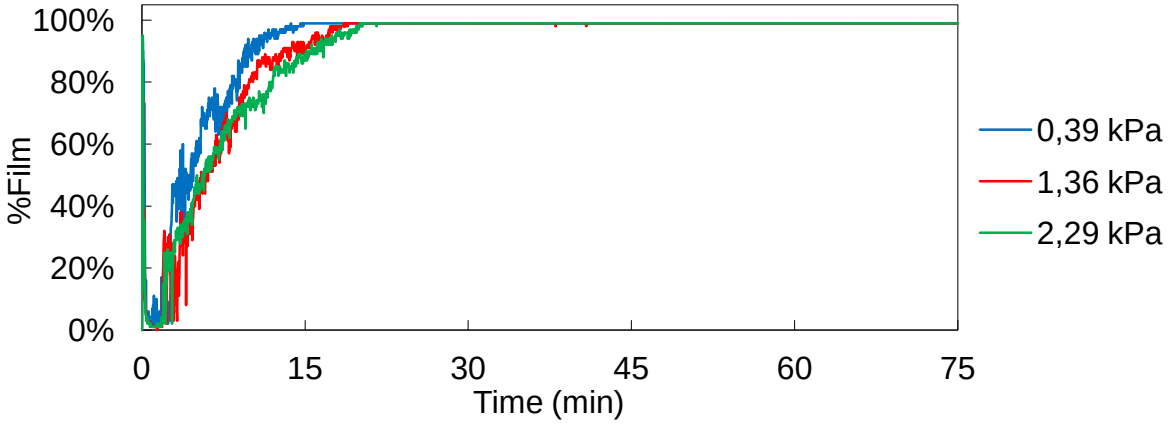

B.2.6: ECR recordings for Wear testing 80 °C, 2000 ppm PA, run 2.

Table B.1: The effect of water vapour pressure on the wear scar appearance (100 ppm, 60 °C, run 2).

	Wear scar	Wear scar - cleaned	Wear track
0,33 kPa	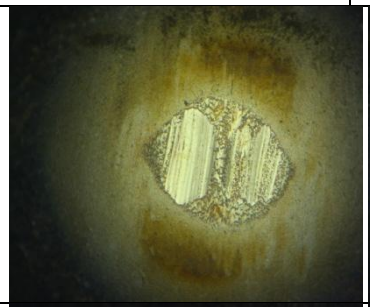		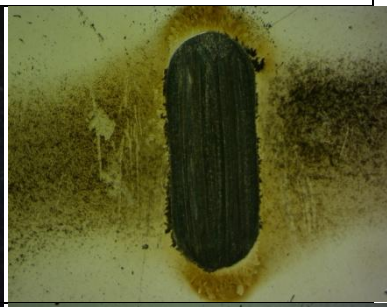
1,18 kPa		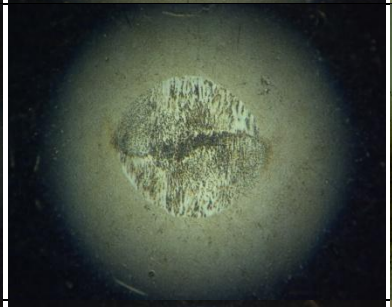	
2,13 kPa	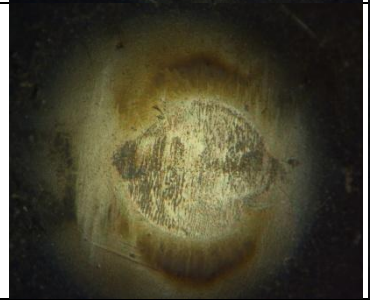		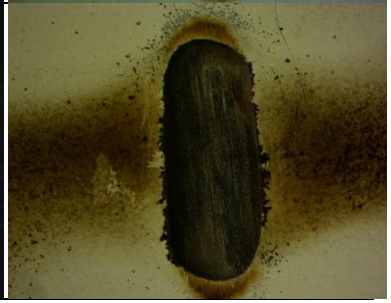

Table B.2: The effect of water vapour pressure on the wear scar appearance (100 ppm, 80 °C, run 2).

	Wear scar	Wear scar - cleaned	Wear track
0,37 kPa	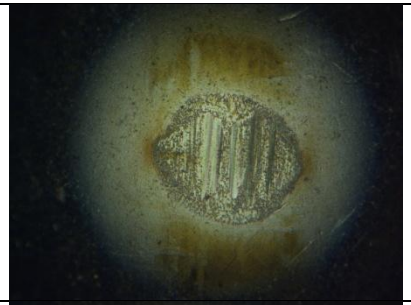		
1,22 kPa	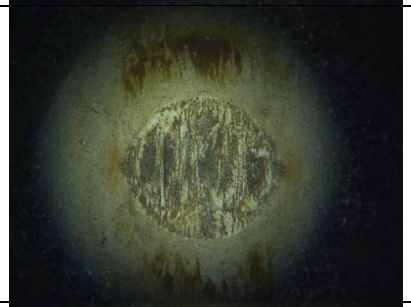	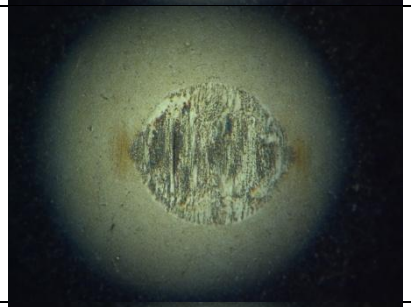	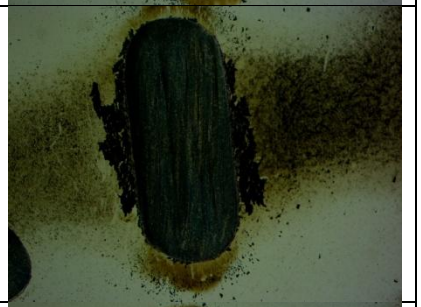
2,19 kPa	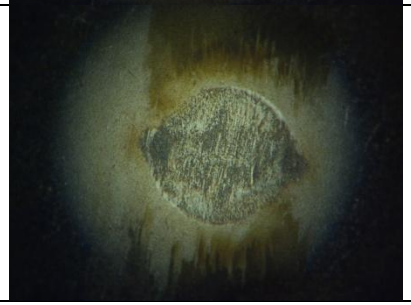	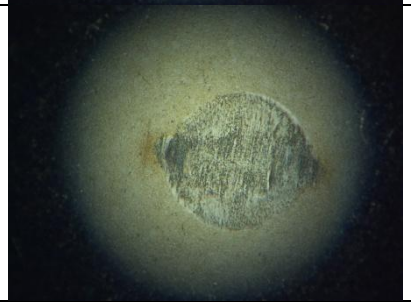	

Table B.3: The effect of water vapour pressure on the wear scar appearance (250 ppm, 60 °C, run 2).

	Wear scar	Wear scar - cleaned	Wear track
0,32 kPa	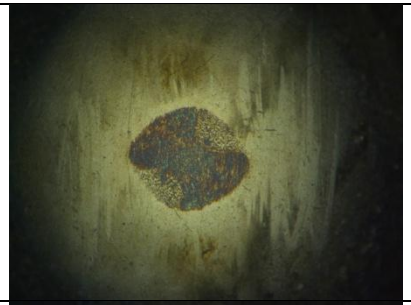	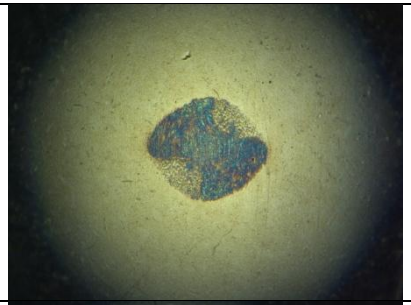	
1,29 kPa		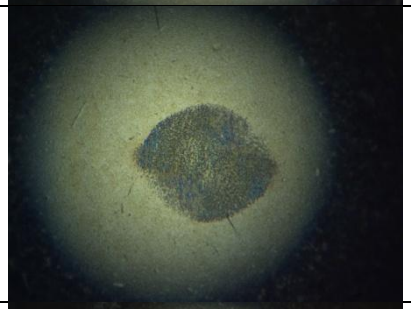	
2,20 kPa	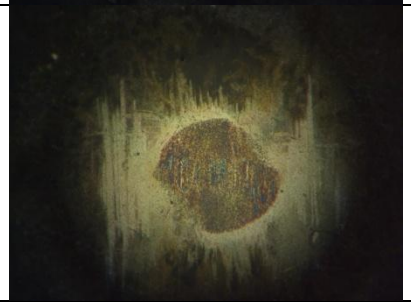	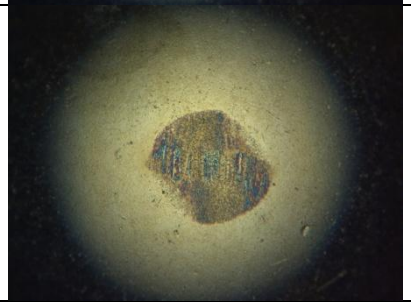	

Table B.4: The effect of water vapour pressure on the wear scar appearance (250 ppm, 80 °C, run 2).

	Wear scar	Wear scar - cleaned	Wear track
0,34 kPa	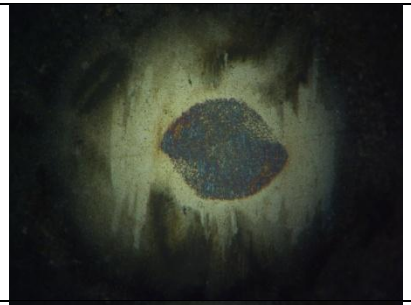	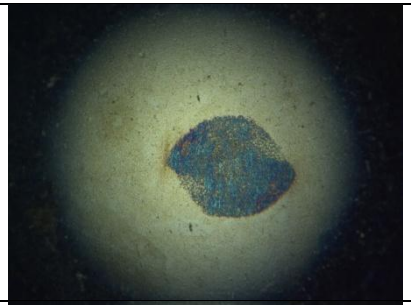	
1,24 kPa	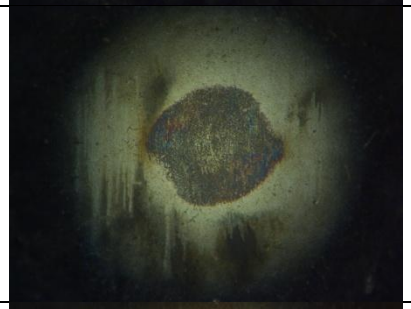	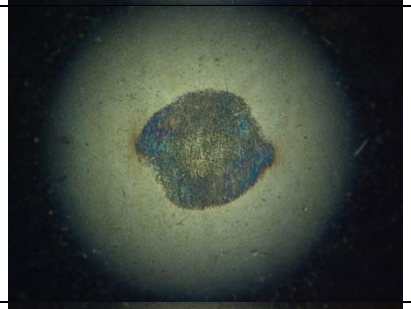	
2,32 kPa	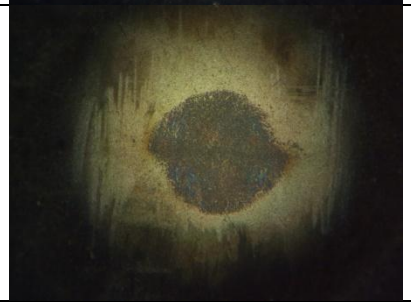	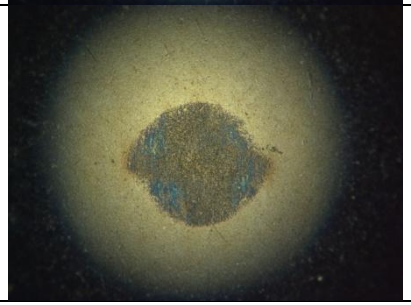	

Table B.5: The effect of water vapour pressure on the wear scar appearance (2000 ppm, 60 °C, run 2).

	Wear scar	Wear scar - cleaned	Wear track
0,36 kPa	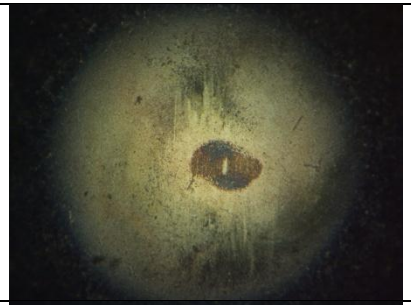	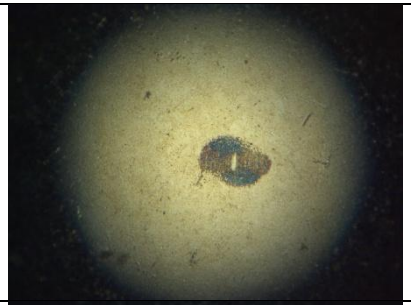	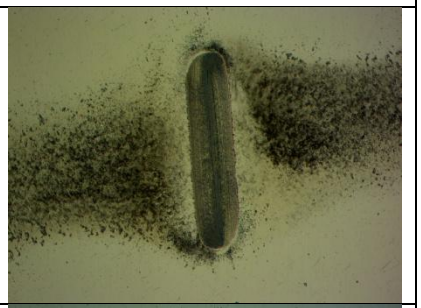
1,27 kPa		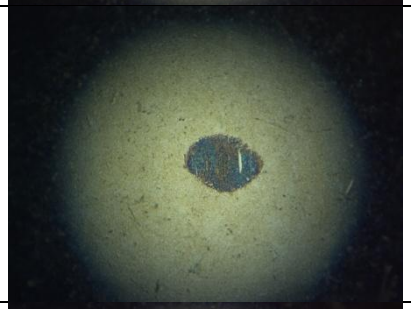	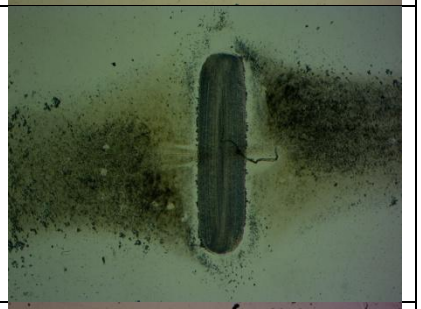
2,38 kPa	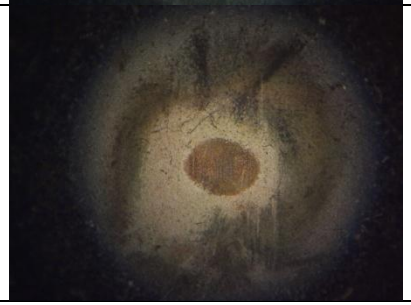	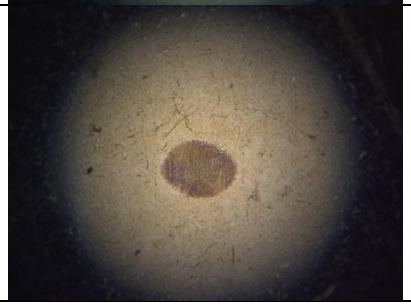	

Table B.6: The effect of water vapour pressure on the wear scar appearance (2000 ppm, 80 °C, run 2).

	Wear scar	Wear scar - cleaned	Wear track
0,39 kPa	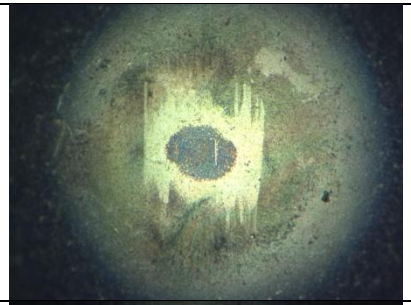	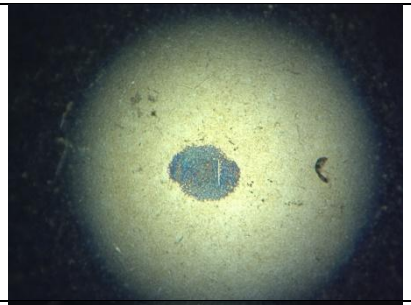	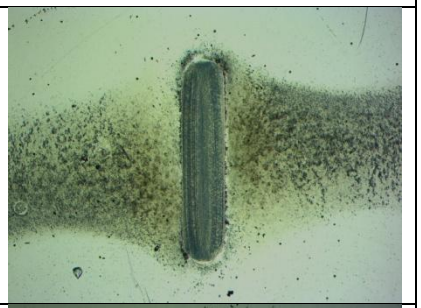
1,36 kPa	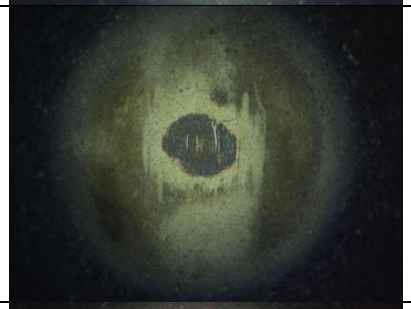	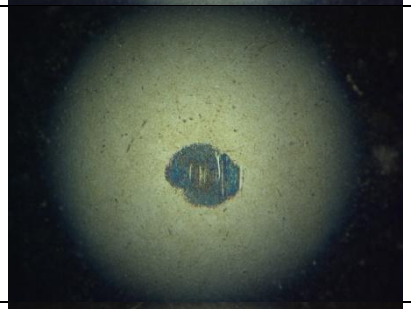	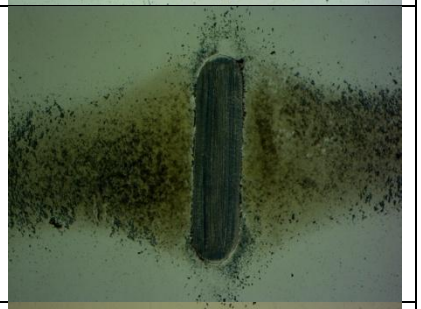
2,29 kPa	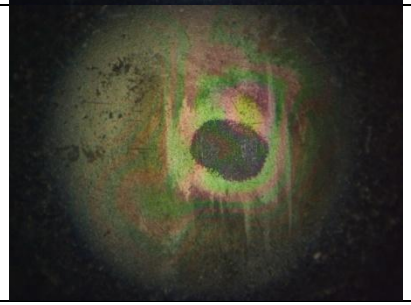	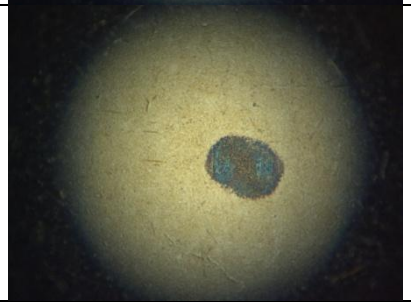	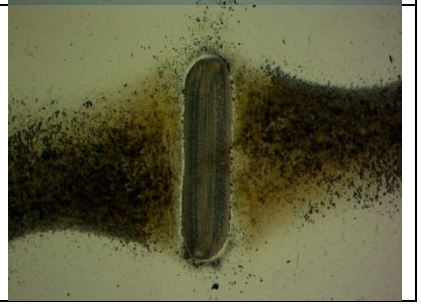

Appendix C

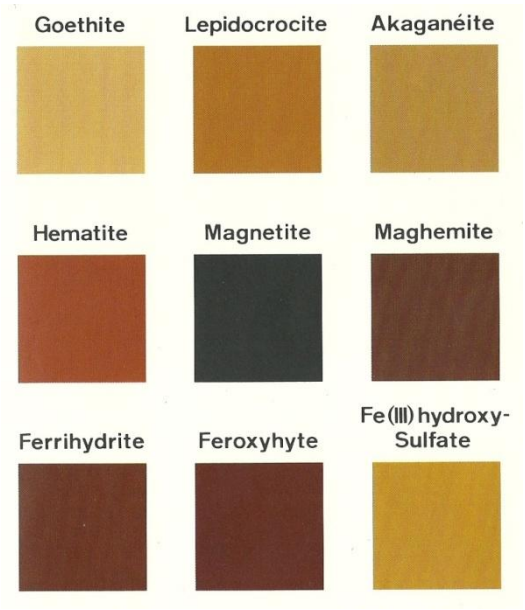

Figure C.1: The typical colours of iron oxides (Schwertmann & Cornell 1991).

In Figure C.2 the conductivity of wüstite is displayed which is the inverse of resistivity. At room temperature wüstite has a resistivity closer to, but lower than hematite. Other oxides are also presented in this figure.

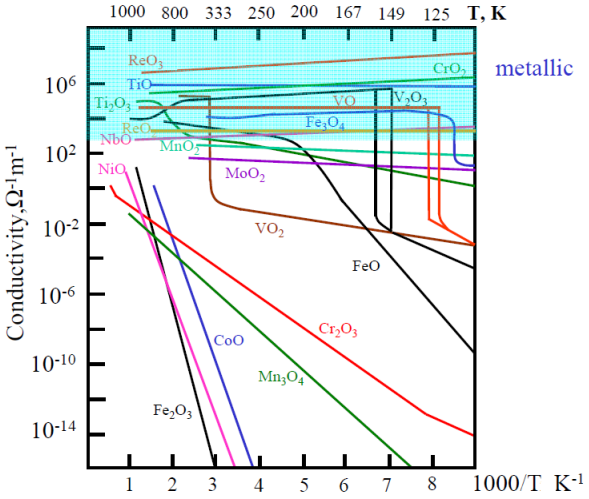

Figure C.2: Conductivity of wustite and other metal oxides (Schaumberg, 1994).

Table C.1: Characteristics of iron oxides (Cornell & Schwertmann, 2007: 4 - 5).

Oxides		Mass % O	Crystallographic system	Formula unit cell	Octahedral occupancy	Anion packing	Density (g/cm3)	Hardness	
Wustite (FeO	Iron(II)	22,27	Cubic	4		Ccp	5,9 – 5,99	5	Non- stoichiometric, oxygen deficient. Black.
Magenetite (Fe_3O_4)	Iron (II,III)	27,64	Cubic	8		ccp [111]	5,18	5,5	
Hematite (α-Fe_2O_3)	Iron (III)	30,06	hexagonal or Rhombohedral	6	2/3	Hcp [001]	5,26	6,5	Very stable
Maghemite (γ-Fe_2O_3)	Iron (III)		Cubic or Tetragonal	8		Ccp [111]	4,87	5	Cation deficient sites
β and ε Fe_2O_3			Orthorhombic (ε)						Rare, Synthetic

Table C.2: Characteristics of iron hydroxides (Cornell & Schwertmann, 2007: 4 - 5).

Hydroxides		Mass %		Formula unit cell	Octahedral Occupancy		Density (g/cm3)	Hardness	
$Fe(OH)_2$	Iron (II)		Hexagonal			Hcp			White. Not a mineral
(Bernalite) $Fe(OH)_3$	Iron (III)		Orthorhombic	8	1/2		3.32		Greenish mineral

Table C.3: Characteristics of iron oxyhydroxides (Cornell & Schwertmann, 2007: 4 - 5). The oxyhydroxides consist of a Fe ion surrounded by three O^{2-} ions and three OH^{-} ions.

Oxyhydroxides		Mass %		Formula unit cell	Octahedral occupancy	Anion packing	Density (g/cm3)	Hardness	
Goethite α-FeOOH			Orthorhombic	4	1/2 (2 rows filled 2 rows empty)	Hcp [001]	4,26	5 – 5,5	Thermodynamically stable at ambient T
Akaganeite β-FeOOH			Monoclinic	8	1/2	Bcp			Occurs rarely in nature
Lepidocrocite γ-FeOOH			Orthorhombic No structure typically	4	1/2	Ccp [015]	4,09	5	
δ-FeOOH			Hexagonal			Hcp [001]			Synthetic form
Feroxyhyte δ'-FeOOH			Hexagonal No structure Typically	2	1/2	Hcp [001]	4,2		Mineral form. Differ from δ-FeOOH in cation ordering
High pressure FeOOH			Orthorhombic						>8 Gpa, Laboratory prepared only
Ferrihydrite $Fe_5HO_8.4H_2O$ (preliminary formula)	2- line (also known as hydrous ferric oxide), 6- line		Hexagonal	4	< 2/3	Hcp [001]	3,96		Exists only as nano-crystals. Unstable. Composition variability w.r.t. OH and H_2O More disordered than 6-line More crystalline than 2-line

Other species include green rusts and Schwertmannite but are not included due to their foreign inclusions.

Table C.4: The porosity and specific surface area of some iron oxides and oxyhydroxides (Cornell & Schwertmann, 2007: 95 - 110).

Iron oxide	Porosity	Specific surface area (m^2/g)
Goethite (α)	• Micropores reported • Meso & macropores (ocasionally reported)	• 8-200 (Natural & synthetic)
Lepidocrocite (γ)	• Micro, Meso and Macro porous	• 15-260 (Synthetic) • >100 (Obtained in the presence of some organics
δ-FeOOH Feroxyhyte (δ')	• Micro/meso interparticle porosity reported	• 20-300 (Synthetic)
Ferrihydrite $Fe_5HO_8.4H_2O$ (preliminary formula)	• Mostly micro porous. It is believed that organic material promotes aggregation of particles.	• 200-400 (Using BET method) • 100-700 (Discrepancies due to the aggregated structure resulting in interparticle porosity)
Magenetite (Fe_3O_4)	• Non porous	• 4 (Via reduction of hematite) • 100 (Precipitation)
Hematite (α-Fe_2O_3)	• Meso/macro porous (formed via dehydroxylation below 500-600 °C) • Micro porous (Solution grown) Porosity is more prevalent in cubic than in spherical crystals.	• <5 (Produced at 800-900 °C) • Up to 200 (Dehydroxylation products < 500-600 °C) • 10-90 (Grown from solution < 100°C) • 0.7-12.4 (Sol-gel method)
Maghemite (γ-Fe_2O_3)	• Non porous (From magnetite oxidation) • Meso porous (From lepidocrocite dehydration)	• 8-130 (If topotactic reaction surface area is close to that of precursor oxide) • 98 (From fine magnetite) • 20 (Goethite→hematite→magnetite→maghemite) • 50-130 (From lepidocrocite) • 5.8-9.8 (Magnetite→hematite)

Calculating oxide and oxyhydroxide stability

The stability of iron oxides or any other reaction for that case depends on the chemical potential of the species in the system. Reactions occur in a manner as to result in the lowest chemical potential. Therefore reactions that favour a decrease in free energy, resulting in products with lower energy than the reactants, will occur naturally. The change in free energy at equilibrium is zero. In Equation C.1 below the change in free energy under standard conditions can be seen as the difference between the free energy of the products and the reactants **(**Cornell & Schwertmann, 2007: 185-186).

$$\Delta G_r^0 = \Delta G_f^0{}_{\text{products}} - \Delta G_f^0{}_{\text{reactants}} \qquad \text{(C.1)}$$

In Table C.5 the free energies, enthalpies and entropies of formation of the iron oxides are presented. The same is presented in Table C.6 for ions and other species. Note these are averaged values from various sources in the reported source. Standard deviation based on averaged values is also indicated if multiple sources were used. These values can be used to see the "relative" stability of these compounds. For oxides other than hematite, magnetite, wüstite and goethite values should be seen as estimates rather than absolute values.

The total free energy is related to the reaction quotient through Equation C.2 below.

$$\Delta G_r = \Delta G_r^0 + RTLnQ \qquad \text{(C.2)}$$

Once equilibrium is reached the total free energy change is zero and Equation C.2 reduces to Equation C.3. from which the extent of the reaction (Equilibrium constant K) can now be determined using the standard free energy of reactions shown previously in Table C.5 and C.6.

$$\Delta G_r^0 = -RTLnK \qquad \text{(C.3)}$$

If reaction data is at a temperature other than the standard temperature, the Equilibrium constants at the two different constants can be related through the well known van't Hoff equation. Note however that when using the van't Hoff equation it is advisable to take into account the dependency of ΔH on temperature. These dependencies can be found in the source materials for some of the iron oxides (Cornell & Schwertmann, 2007: 186).

Table C.5: the free energies, enthalpies and entropies of formation of the iron oxides (Cornell & Schwertmann, 2007: 187).

Iron oxide	ΔG_f^0 (kJ/mol)	ΔH_f^0 (kJ/mol)	ΔS_f^0 (kJ/mol.K)
FeOOH			
Goethite (α)	-488.1 ± 3.82	-561.1 ± 2.55	60.44 ± 0.08
Akaganeite (β)	-752.7	-557.6	
Lepidocrocite (γ)	-482.0 ± 6.08	-555.5 ± 1.27	62.5
δ-FeOOH Feroxyhyte (δ')			
Ferrihydrite $Fe_5HO_8.4H_2O$ (preliminary formula)	-705.5 ± 9.19		
Wustite (FeO)	-248.17 ± 5.05	-269.15 ± 4.03	57.43 ± 4.80
Magenetite (Fe_3O_4)	-1014.6 ± 1.80	-1117.89 ± 1.96	146.2 ± 0.36
Hematite (α-Fe_2O_3)	-743.75 ± 1.93	-825.53 ± 2.18	88.14 ± 1.29
Maghemite (γ-Fe_2O_3) tetr Cubic	-711.14 -723.9 -752.1	 -809.25 ± 4.88 -809.05 ± 4.60	 87.4 91.4
$Fe(OH)_2$	-485.1 ± 1.27	-568.9 ± 0.14	83.75 ± 5.88

Table C.6: the free energies, enthalpies and entropies of formation of ions and other compounds (Cornell & Schwertmann, 2007: 188).

Ion/compound	ΔG_f^0 (kJ/mol)	ΔH_f^0 (kJ/mol)	ΔS_f^0 (kJ/mol.K)
Fe^{3+}	-14.86 ± 3.74	-48.68 ± 1.31	-285 ± 11.31
Fe^{2+}	-78.8	-89.1	-138
$FeOH^+$	-277.3		
$Fe(OH)^{2+}$	-234.9 ± 7.78	-324	-29.2
$Fe(OH)_2^+$	-438		
$Fe(OH)_2^{4+}$	-467.3		
$Fe(OH)_4^-$	-829.8 ± 21.5	-1050	74
H_2O	-238.2		
OH-	-157.5	-230	-10.75
H^+	0		
H_2	0	0	130.6
O_2 g			205
O_2 aq	21.81 ± 7.76	-11.7	111
Fe	0	0	27.3

Appendix D

The following information is specific to the experimental setup:

- Ultrasonic bath used to clean specimens: Model PS-40, Utrasonic power 240 W.
- Optical microscope: Axio scope A1 supplied by Carl Zeiss (Pty) Ltd. Including digital microscopy camera Axiocam ERc 5s.

Test specimens

- HFRR test specimens, batch V521/38 (Disks) and batch 4655 (Balls), supplied by PCS Instruments.
- SRV test specimens, batch 901181301053 and 312081612059 (Disks) and batch 90.01.51 (Balls) supplied by Optimol Instruments.